

Studies of spin dynamics in 122 transition metal arsenides using inelastic neutron scattering technique

by

Aashish Sapkota

A dissertation submitted to the graduate faculty
in partial fulfillment of the requirements for the degree of

DOCTOR OF PHILOSOPHY

Major: Condensed Matter Physics

Program of Study Committee:
Robert J. McQueeney, Co-major Professor
Alan I. Goldman, Co-major Professor
Andreas Kreyssig
Paul C. Canfield
Sanjeevi Sivasankar
Gordon J. Miller

The student author, whose presentation of the scholarship herein was approved by the program of study committee, is solely responsible for the content of this dissertation. The Graduate College will ensure this dissertation is globally accessible and will not permit alterations after a degree is conferred.

Iowa State University

Ames, Iowa

2018

Copyright © Aashish Sapkota, 2018. All rights reserved.

TABLE OF CONTENTS

LIST OF TABLES	v
LIST OF FIGURES	vii
ACKNOWLEDGEMENTS	xii
ABSTRACT	xiii
CHAPTER 1 OVERVIEW	1
CHAPTER 2 INTRODUCTION	4
2.1 Superconductivity: An overview	4
2.2 A brief introduction to the iron-based superconductors	8
2.3 ThCr_2Si_2 -type structure of ATM_2As_2 : $\text{TM} = \text{Mn, Fe, Co}$	9
2.4 Diverse magnetism in ATM_2As_2	10
2.4.1 J_1 - J_2 model in a square-lattice	13
2.5 Chemical substitution as a tuning parameter	16
2.5.1 Superconductivity in AFe_2As_2	16
2.5.2 Insulator-metal transition in $\text{Ba}_{1-x}\text{K}_x\text{Mn}_2\text{As}_2$	19
2.6 Motivation	20
CHAPTER 3 A REVIEW OF PROPERTIES OF ATM_2As_2	23
3.1 ATM_2As_2 : $\text{TM} = \text{Fe}$	23
3.1.1 Structure, magnetism, and superconductivity in AFe_2As_2	23
3.1.2 Spin fluctuations in AFe_2As_2	28
3.1.3 Effect of Cobalt substitution at the Fe site	32
3.1.4 Unique properties of CaFe_2As_2	38
3.2 ATM_2As_2 : $\text{TM} = \text{Co}$	43
3.2.1 Crystal structure	44
3.2.2 Magnetism	44
3.2.3 Spin fluctuations in SrCo_2As_2 : A big surprise	45
3.3 ATM_2As_2 : $\text{TM} = \text{Mn}$	48
3.3.1 Crystal structure and insulating ground state	48
3.3.2 Ferromagnetic order in $\text{Ba}_{1-x}\text{K}_x\text{Mn}_2\text{As}_2$	49

CHAPTER 4	EXPERIMENTAL TECHNIQUE	50
4.1	Direct and Reciprocal space	50
4.2	A general description of scattering	54
4.2.1	Elastic Scattering	54
4.2.2	Inelastic Scattering	55
4.3	Neutron Scattering	57
4.3.1	Nuclear scattering	59
4.3.2	Magnetic scattering	64
4.4	Neutron scattering instruments	71
4.4.1	Neutron generation	73
4.4.2	Time-of-flight instrument	74
4.4.3	Triple-axis spectrometer	79
CHAPTER 5	DOPING EVOLUTION OF SPIN DYNAMICS IN $\text{Ca}(\text{Fe}_{1-x}\text{Co}_x)_2\text{As}_2$	84
5.1	Introduction	84
5.2	Experimental Details	86
5.3	Spin dynamics evolution in the orthorhombic-antiferromagnetic state	90
5.3.1	Convolution with instrumental resolution	94
5.4	Spin dynamics evolution in the high-temperature paramagnetic state	96
5.4.1	Fitting procedure of the paramagnetic spin fluctuations using the diffusive model	100
5.5	Anomalous suppression of the spin fluctuations at low-temperatures for $x = 0.030$.	100
5.6	Spin resonance in the superconducting state for $x = 0.030$	102
5.7	Discussion of the results	103
CHAPTER 6	EXTREMELY ANISOTROPIC SPIN FLUCTUATIONS IN $\text{CaCo}_{1.86}\text{As}_2$. .	109
6.1	Introduction	109
6.2	Experimental Details	110
6.3	Results and analysis	112
6.3.1	Heisenberg Model	113
6.3.2	Diffusive model	115
6.4	Discussion of the ARCS results	122
6.4.1	Evolution of spin fluctuations with the frustration parameter (η)	127
6.4.2	Spin fluctuations below 10 meV: ARCS results	127
6.5	Spin fluctuations below 10 meV: MACS results	129
6.5.1	Experimental Details	129
6.5.2	Results and analysis	131
6.5.3	Discussion	131
6.6	Derivation of the diffusive model for other magnetic orders	134

6.6.1	Diffusive model for the stripe-type antiferromagnet	134
6.6.2	Diffusive model for the Néel-type antiferromagnet	136
CHAPTER 7 EFFECTS OF HOLE DOPING ON SPIN DYNAMICS OF $\text{Ba}_{1-x}\text{K}_x\text{Mn}_2\text{As}_2$		138
7.1	Experimental details and preliminary sample characterization	139
7.2	Results and analysis	140
7.2.1	Energy spectrum of the spin waves	144
7.2.2	Spin gap and its evolution with doping	149
7.2.3	Heisenberg model and other relevant quantities	153
7.2.4	Fits to the Heisenberg model	155
7.3	Discussion of the results	159
7.3.1	Additional information related to the data analysis	164
CHAPTER 8 SUMMARY AND FUTURE WORK		170
BIBLIOGRAPHY		173

LIST OF TABLES

Table 2.1	Stability conditions for three types of collinear magnetic ground states according to the J_1 - J_2 model	15
Table 3.1	Comparison of lattice parameters, magnetic moments and transition temperatures in AFe_2As_2	25
Table 3.2	Comparison of spin-wave velocities and spin-gap in AFe_2As_2	29
Table 3.3	Lattice parameters of ACo_2As_2 compounds.	44
Table 4.1	Basic properties of neutron	58
Table 4.2	ARCS instrument parameters	76
Table 5.1	Lattice parameters for $x = 0.026$ and 0.030 at temperatures corresponding to the inelastic neutron scattering measurement	89
Table 5.2	Comparison of spin gap and spin-wave velocities for $x = 0$ and 0.026	93
Table 5.3	Instrumental resolution δQ for Q cuts for the measurement in the AFM state performed by rotating the sample	96
Table 5.4	Comparison of the parameters of the diffusive model in Eq. (5.6) of the $\text{Ca}(\text{Fe}_{1-x}\text{Co}_x)_2\text{As}_2$ data with the corresponding values for parent compound CaFe_2As_2	98
Table 5.5	Comparison of fit parameters of $T = 90, 20$ and 6 K data for $\text{Ca}(\text{Fe}_{1-x}\text{Co}_x)_2\text{As}_2$, $x = 0.030$	102
Table 6.1	Fit values of the parameters in the diffusive model	120
Table 6.2	Stiffness constants obtained for the ARCS and MACS data	131

Table 7.1	Rough correspondence between relative change of $k_{\text{B}}T_{\text{N}}$ and $\langle E \rangle$ with doping in $\text{Ba}_{1-x}\text{K}_x\text{Mn}_2\text{As}_2$	149
Table 7.2	Doping evolution of the spin gap Δ and energy scale Γ of the spin waves in $\text{Ba}_{1-x}\text{K}_x\text{Mn}_2\text{As}_2$	152
Table 7.3	Energy scales and magnetic parameters of $\text{Ba}_{1-x}\text{K}_x\text{Mn}_2\text{As}_2$ as a function of composition	162
Table 7.4	Parameters (U , F) employed in the background estimates for constant- energy Q cuts	165

LIST OF FIGURES

Figure 2.1	Resistance of mercury with temperature	5
Figure 2.2	Structure of five families of iron-based superconductors	8
Figure 2.3	Conventional unit cell of ThCr_2Si_2	10
Figure 2.4	Stripe-type magnetic order in AFe_2As_2 compounds in the orthorhombic unit cell of 122 system	11
Figure 2.5	A-type antiferromagnetic order in $\text{CaCo}_{1.86}\text{As}_2$	12
Figure 2.6	Magnetic structure of BaMn_2As_2	13
Figure 2.7	Phase diagram of J_1 - J_2 model	14
Figure 2.8	Phase diagrams of the $\text{Ba}(\text{Fe}_{1-x}\text{Co}_x)_2\text{As}_2$ and $\text{Ca}(\text{Fe}_{1-x}\text{Co}_x)_2\text{As}_2$	18
Figure 2.9	Doping evolution of T_N and ordered moment for $\text{Ba}_{1-x}\text{K}_x\text{Mn}_2\text{As}_2$	20
Figure 3.1	Tetragonal and orthorhombic unit cell of AFe_2As_2 compounds	24
Figure 3.2	Experimental signatures of structural and magnetic transition in resistivity, susceptibility and heat capacity measurements	26
Figure 3.3	Experimental signatures of structural and magnetic transitions from x-ray and neutron diffraction	27
Figure 3.4	Spin fluctuations in CaFe_2As_2	30
Figure 3.5	Spin fluctuations in BaFe_2As_2	31
Figure 3.6	Signature of the competition between magnetism and SC	34
Figure 3.7	Fermi surface in 122 compounds and its evolution with cobalt doping	35
Figure 3.8	Evolution of low-energy spin fluctuations in $\text{Ba}(\text{Fe}_{1-x}\text{Co}_x)_2\text{As}_2$ with increas- ing Co doping	37
Figure 3.9	Spin resonance in superconducting $\text{Ba}(\text{Fe}_{1-x}\text{Co}_x)_2\text{As}_2$	39

Figure 3.10	Phase diagram of CaFe_2As_2 with annealing temperature showing correspondence with pressure	40
Figure 3.11	Temperature dependence of c-axis dilation for $\text{Ca}(\text{Fe}_{1-x}\text{Co}_x)_2\text{As}_2$ annealed at 400 °C	42
Figure 3.12	Interlayer pnictogen distance and magnetic ground states in ATM_2X_2 . . .	43
Figure 3.13	Results of band structure calculations and magnetization measurement of ACo_2As_2 compounds.	46
Figure 3.14	Spin fluctuations of SrCo_2As_2 measured using inelastic neutron scattering .	47
Figure 4.1	A simple cubic three-dimensional Bravais lattice	51
Figure 4.2	One-dimensional direct and reciprocal lattice	51
Figure 4.3	A Conventional and primitive unit cell of a body-centered tetragonal Bravais lattice	53
Figure 4.4	Vector diagram of an elastic scattering with an Ewald circle of radius $k = 2\pi/\lambda$	55
Figure 4.5	Vector diagram of an inelastic scattering	56
Figure 4.6	Geometry for scattering experiment	59
Figure 4.7	Coordinates of nucleus and neutron	61
Figure 4.8	Spin waves in a ferromagnet	68
Figure 4.9	A schematic of spin waves in an itinerant system illustrating the decay of spin waves in the Stoner continuum region	70
Figure 4.10	Schematic illustrating the process of an excitation creation and annihilation in a scattering system during the inelastic neutron scattering	72
Figure 4.11	Time–distance diagram for a direct–geometry and an inverse–geometry spectrometers	75
Figure 4.12	Schematics of the ARCS instrument and the spallation process	77
Figure 4.13	Time–distance diagram for the ARCS spectrometer	78
Figure 4.14	Schematic of a triple-axis spectrometer	80
Figure 4.15	Schematic of the MACS instrument	82

Figure 5.1	Phase diagram of $\text{Ba}(\text{Fe}_{1-x}\text{Co}_x)_2\text{As}_2$ illustrating the crossover of the spin dynamics from spin waves to the diffusive spin fluctuations near the coexistence region of AFM and SC	85
Figure 5.2	Phase diagram of $\text{Ca}(\text{Fe}_{1-x}\text{Co}_x)_2\text{As}_2$ annealed at 400 °C, and results of magnetization measurement and temperature dependence of c lattice parameter for $x = 0.026$ and 0.030 compounds	87
Figure 5.3	Co-aligned $\text{Ca}(\text{Fe}_{1-x}\text{Co}_x)_2\text{As}_2$ $x = 0.030$ samples	88
Figure 5.4	Inelastic neutron scattering cross-section for $\text{Ca}(\text{Fe}_{1-x}\text{Co}_x)_2\text{As}_2$ $x = 0.026$ at $T = 20$ K in the AFM state	91
Figure 5.5	One dimensional cuts along the LO and TR directions for $x = 0.026$ sample in the AFM state	92
Figure 5.6	Spin-wave dispersion along the TR, LO, and c directions for $x = 0.026$ sample in AFM state	93
Figure 5.7	Energy cuts for $x = 0.026$ sample in the AFM state for the determination of spin gap Δ	94
Figure 5.8	Paramagnetic spin fluctuations in $\text{Ca}(\text{Fe}_{1-x}\text{Co}_x)_2\text{As}_2$ ($x = 0.026$ and 0.030) measured at $T = 90$ K with $E_i = 49.75$ meV	97
Figure 5.9	E and Q cuts at $\mathbf{Q}_{\text{stripe}}$ for $x = 0.026$ and 0.030 at $T = 90$ and 20 K with $E_i = 49.75$ meV	99
Figure 5.10	Paramagnetic spin fluctuations in $\text{Ca}(\text{Fe}_{1-x}\text{Co}_x)_2\text{As}_2$ ($x = 0.030$) measured at $T = 90, 20$ and 6 K with $E_i = 49.75$ meV	101
Figure 5.11	E cuts at $\mathbf{Q}_{\text{stripe}}$ for $x = 0.030$ measured at $T = 20$ and 6 K with $E_i = 49.75$ meV	103
Figure 5.12	Illustration of spin fluctuations evolution in $\text{Ca}(\text{Fe}_{1-x}\text{Co}_x)_2\text{As}_2$	104
Figure 6.1	Spatial anisotropy of spin fluctuations for different magnetic ordering	111
Figure 6.2	Inelastic neutron scattering spectra of $\text{CaCo}_{1.86}\text{As}_2$ measured at $T = 8$ K at ARCS	114

Figure 6.3	Spin-wave spectrum calculated using the local-moment Heisenberg model with damped simple harmonic oscillator	116
Figure 6.4	Arrangement of spins/moments in $\text{CaCo}_{1.86}\text{As}_2$ in the Co-plane	118
Figure 6.5	Constant-energy cuts and dynamical susceptibility of the data fitted with the diffusive model.	121
Figure 6.6	Estimation of $S J_1 $ from the fit of the energy transfer and half width at half maximum (δ) of the transverse cuts.	122
Figure 6.7	Spin fluctuations in $\text{CaCo}_{1.86}\text{As}_2$: Experimental INS Data vs Diffusive model	123
Figure 6.8	Coupling of spins for maximally frustrated stripe-type AFM and FM/A-type spin dynamics	125
Figure 6.9	Phase diagram of J_1 - J_2 model showing $\text{CaCo}_{1.86}\text{As}_2$ close to the maximum frustration	126
Figure 6.10	Evolution of the spin fluctuations with the frustration parameter (η) for stripe-type, FM/A-type and Néel-type magnetic ordering	128
Figure 6.11	Constant-energy slices below 10 meV	129
Figure 6.12	Low-energy spin fluctuations ≤ 10 meV in $\text{CaCo}_{1.86}\text{As}_2$ measured at MACS spectrometer at NIST	130
Figure 6.13	Cuts along the (H, H) direction through $(0, 0, -3)$ peak and the corresponding dispersion plot	132
Figure 6.14	Cuts along the $(0, 0, L)$ direction	133
Figure 6.15	Two-dimensional arrangement of spins/moments in stripe-type order	134
Figure 6.16	Two-dimensional arrangement of spins/moments in Néel-type order	136
Figure 7.1	X-ray diffraction data for polycrystalline $\text{Ba}_{1-x}\text{K}_x\text{Mn}_2\text{As}_2$ with $x = 0, 0.125$, and 0.25 at room temperature	141
Figure 7.2	Magnetization data for polycrystalline samples of $\text{Ba}_{1-x}\text{K}_x\text{Mn}_2\text{As}_2$ as a function of magnetic field at various temperatures	142

Figure 7.3	Magnetic susceptibility data for polycrystalline samples of $\text{Ba}_{1-x}\text{K}_x\text{Mn}_2\text{As}_2$ taken at a field of 3 T as a function of temperature	143
Figure 7.4	Inelastic neutron scattering data from a powder sample of $\text{Ba}_{1-x}\text{K}_x\text{Mn}_2\text{As}_2$ measured with $E_i = 144.7$ meV and $T = 8$ K	145
Figure 7.5	Magnetic low-angled and phonon high-angled spectra obtained after scaling for $\text{Ba}_{1-x}\text{K}_x\text{Mn}_2\text{As}_2$	147
Figure 7.6	Magnetic spectra for $\text{Ba}_{1-x}\text{K}_x\text{Mn}_2\text{As}_2$ as a function of energy	148
Figure 7.7	Low-energy inelastic neutron scattering spectra of the $\text{Ba}_{0.75}\text{K}_{0.25}\text{Mn}_2\text{As}_2$ sample showing a spin gap	150
Figure 7.8	Energy cuts from $E_i = 74$ meV data for the determination of the spin gap for each concentrations	151
Figure 7.9	Inelastic neutron scattering spectra of $\text{Ba}_{1-x}\text{K}_x\text{Mn}_2\text{As}_2$ for both the raw data and calculated using linear spin wave theory of the Heisenberg model .	157
Figure 7.10	Constant energy cuts of BaMn_2As_2 along with the fits to the Heisenberg spin wave model	160
Figure 7.11	Constant-energy cuts for different compositions of $\text{Ba}_{1-x}\text{K}_x\text{Mn}_2\text{As}_2$	161
Figure 7.12	Powder-averaged spin wave scattering from MnO	166
Figure 7.13	Region of $SJ_1 - SJ_2$ parameter space delineated by boundaries of v_{ab} from 165 to 210 meV Å	168
Figure 7.14	Goodness of the fit, χ^2	169

ACKNOWLEDGEMENTS

I would like to take this opportunity to express my sincere gratitude to all, whose support and guidance made it possible to complete this arduous journey with wonderful experiences.

First and foremost, I would like to thank my major professors Robert J. McQueeny and Alan I. Goldman for their invaluable guidance, support, and encouragement throughout my Ph.D. Additionally, I would like to thank all the past and present members of our x-ray and neutron scattering group for all the stimulating discussions and sleepless nights spent together at the beamline. Special thanks to Andreas Kreyssig and Benjamin Ueland for their patience, guidance and wonderful discussions.

I would also like to thank my collaborators, David C. Johnston and his group, Paul C. Canfield and his group, and Ni Ni for their support. Special thanks to Anna E. Böhmer, Sangeetha Nediadathathanadhan, Vivek K. Anand and Abhishek Pandey for their wonderful crystals which made this thesis possible.

I am also deeply thankful to instrument scientists from Argonne National Laboratory and Oak Ridge National Laboratory. Without their support, my work would not have been complete. I am also thankful to my committee members for their support and guidance.

Finally, I would like to thank my parents, my wife, my brother and my sister for their years of support and love.

This work was supported by the U.S. Department of Energy, Office of Basic Energy Sciences, Division of Materials Sciences and Engineering at the Ames Laboratory under contract number DE-AC02-07CH11358. The Ames Laboratory is operated for the U.S. Department of Energy by Iowa State University.

ABSTRACT

The diverse physical properties and interrelationship between various ground states offer a rich physics to explore in 122 ATM_2As_2 ($A = \text{Ca, Sr, Ba}$ and $TM = 3d$ transition metals). This thesis discusses three examples of the 122 ATM_2As_2 compounds, $TM = \text{Fe, Co and Mn}$, where the focus is to understand their diverse magnetic properties and interplay between the magnetism and electronic properties including superconductivity. Therefore, the spin dynamics (spin fluctuations) of these compounds were studied using inelastic neutron scattering technique.

$CaFe_2As_2$ and the derived compounds are the first system discussed in this work. In this compound, correlation between the magnetism and superconductivity was studied. $CaFe_2As_2$ belongs to the 122 AFe_2As_2 family of high- T_c iron-based superconductors, where previous studies suggest that the overdamped spin dynamics are necessary for superconductivity. The $CaFe_2As_2$ compound has some unique features compared to other members of AFe_2As_2 compounds, therefore presents a different scenario to study this relationship. A study performed using the inelastic neutron scattering on various Co substituted $CaFe_2As_2$ compounds are discussed. The results verify the link between the overdamped spin dynamics and superconductivity. In addition, the results also indicate that some peculiar features are present in the spin fluctuations of $Ca(Fe_{1-x}Co_x)_2As_2$ compounds. These peculiar features seem to be consistent with the unique magnetostructural properties of $Ca(Fe_{1-x}Co_x)_2As_2$ compounds.

Another compound discussed in this thesis is $CaCo_{1.86}As_2$, which is in the collapsed tetragonal phase and exhibits magnetic ground state, unlike its AFe_2As_2 counterparts. Inelastic neutron scattering measurements performed on this compound revealed extremely anisotropic spin fluctuations along the two directions of the reciprocal space. The result suggests that the $CaCo_{1.86}As_2$ is a unique example of highly-frustrated square-lattice system.

The final compound discussed is the K substituted BaMn_2As_2 , i.e. $\text{Ba}_{1-x}\text{K}_x\text{Mn}_2\text{As}_2$ compounds. K substitution (hole doping) in BaMn_2As_2 changes the insulating ground state of the parent BaMn_2As_2 compound to the metallic state. Previous measurements of these compounds indicate that the hole doping induces itinerant ferromagnetism that coexists with the local moment antiferromagnetism of the parent BaMn_2As_2 compound. To further understand the effects of hole doping on magnetism, inelastic neutron scattering measurements were performed on $\text{Ba}_{1-x}\text{K}_x\text{Mn}_2\text{As}_2$ compounds with $x = 0, 0.125$ and 0.25 . The results suggest minor changes in the spin fluctuations with the hole doping, i.e. minor changes up to hole carrier concentrations of 12.5% per Mn ion (i.e. $x = 0.25$). This is consistent with the idea that the charge transport and antiferromagnetism are decoupled in the $\text{Ba}_{1-x}\text{K}_x\text{Mn}_2\text{As}_2$ compounds, i.e. the doped holes have small effects on the antiferromagnetism.

CHAPTER 1 OVERVIEW

The discovery of high-temperature (high- T_c) superconductivity in the iron-based compounds[1, 2] was surprising because magnetic materials such as Fe were considered to be incompatible with superconductivity[3]. The high- T_c in these compounds triggered an extensive research and a central theme of the research has been to understand the interplay between magnetism and superconductivity. Studies so far suggest an intimate relationship between magnetism and superconductivity and spin fluctuations are believed to play an important role in the pairing of the electrons for superconductivity.

A chemical substitution is a commonly employed method to tune physical properties in the iron-based superconductors. The 122 family ($A\text{Fe}_2\text{As}_2$, $A = \text{Ca, Ba, Sr}$) of iron-based superconductors, in which chemical substitution induces superconductivity, has been extensively studied because of early availability of large and homogeneous single crystal. Inelastic neutron scattering measurements of spin fluctuations of these compounds have revealed many crucial features, which linked the spin fluctuations to superconductivity. However, even after a decade of intensive research, a complete understanding of superconductivity is yet to be achieved and there is still a debate about the importance of the spin fluctuations for superconductivity. Therefore, further studies are necessary to pinpoint the necessary and sufficient conditions for superconductivity.

In particular, substitution of the Fe by either Co/Ni is a way to realize superconductivity in 122 $A\text{Fe}_2\text{As}_2$ compounds[3, 4]. A systematic study of spin fluctuations in Co or Ni-doped BaFe_2As_2 compound suggests that the spin fluctuations with overdamped dynamics are required for superconductivity[3, 5]. A part of this thesis discusses the evolution of spin fluctuations with Co-substitution in CaFe_2As_2 compound of the iron-based superconductors. CaFe_2As_2 , which is unique (the strongest magnetostructural coupling) among the members of $A\text{Fe}_2\text{As}_2$ compounds,

presents a different scenario to study the evolution of spin fluctuations with Co-substitution and verify the link between the overdamped spin fluctuations and superconductivity.

In search for the unconventional superconductors, other non-Fe based 3d transition-metal 122 compounds (ATM_2As_2) were also studied. These studies revealed the rich and diverse physical properties in ATM_2As_2 compounds. For example, the $CaCo_{1.86}As_2$ compound, which is in collapsed tetragonal phase (discussed in details in section 3.2.1 of chapter 3) at ambient pressure, undergoes magnetic ordering[6], unlike AFe_2As_2 compounds, which are non-magnetic in the collapsed tetragonal state[7]. Similarly, $SrCo_2As_2$, which belongs to ACo_2As_2 group, does not order magnetically down to ≈ 2 K, but an inelastic neutron scattering measurement revealed the presence of spin fluctuations similar in character as in AFe_2As_2 compounds[8]. The result motivated further study of spin fluctuations in the $CaCo_{1.86}As_2$ compound and find out if the spin fluctuations are only associated with its magnetic ground state or also display characters similar to $SrCo_2As_2$ and AFe_2As_2 compounds.

$BaMn_2As_2$ is another interesting compound because it shares properties with both copper- and iron-based high- T_c superconductors[9]. Hence, there is possibility of a superconducting ground state on substitution, and K substitution (hole-doping) at the Ba site of $BaMn_2As_2$ was employed. The substitution drives the system from an insulating to a metallic ground state, but without superconductivity. Also, in contrast to the high- T_c superconductors, magnetic order of the parent $BaMn_2As_2$ compound seems to be robust against the substitution. An inelastic neutron scattering measurement was performed on the $Ba_{1-x}K_xMn_2As_2$ compounds to find out more about the correlation between the magnetism and chemical substitution.

Layout of the thesis is as follows. Chapter 2 provides an overview of superconductivity, discusses properties of ATM_2As_2 , $TM = Mn, Fe$ and Co compounds and highlights the motivation. Chapter 3 is an extensive review of the properties of these three ATM_2As_2 compounds. Chapter 4 discusses about the neutron scattering technique in details. Chapter 5, 6 and 7 discuss the results of the inelastic neutron scattering measurements performed on $Ca(Fe_{1-x}Co_x)_2As_2$, $CaCo_{1.86}As_2$ and

$\text{Ba}_{1-x}\text{K}_x\text{Mn}_2\text{As}_2$ compounds, respectively. Finally, Chapter 8 summarizes the results and discusses future work.

CHAPTER 2 INTRODUCTION

2.1 Superconductivity: An overview

Superconductivity is a phenomenon where the resistivity of a material falls to zero below a certain critical temperature T_c , therefore the material can carry electrical current without any discernible dissipation. This indicates their potential application in the electricity transport. However, no superconductors at room temperature and ambient pressure have been discovered.

The phenomenon of superconductivity was first discovered by Heike Kamerling Onnes in 1911 [10, 11]. He showed that the resistance of mercury (Hg) falls to zero below the critical temperature, $T_c = 4.2$ K, as shown in Fig. 2.1. Next, Meissner and Ochsenfeld in 1933 discovered that the perfect diamagnetism is a distinguishing characteristic of superconductivity[12]. They found that a superconducting material expels the magnetic field below T_c , as long as the applied magnetic field is below a critical value H_c . This phenomenon is called the Meissner effect. Above the critical field H_c , the superconductivity is destroyed. Perfect diamagnetism is mostly observed in the elemental superconductors, but there are superconductors that allow partial penetration of the magnetic flux for certain values of magnetic field. Therefore, superconductors are classified as being one of the two types: (i) type I and (ii) type II. For type II superconductors there are two critical values: (i) H_{c1} (lower critical field) and (ii) H_{c2} (upper critical field). The flux is completely expelled from the sample below H_{c1} , but there is some penetration between H_{c1} and H_{c2} , where the superconducting and the normal regions coexist. Type II superconductors have some applications, such as for the design of a high-field magnet because their upper critical field can be 3 orders of magnitude higher than type I superconductors[13].

After their discovery, many unsuccessful attempts were made to understand superconductivity and there are also some inadequate theories such as the ones developed by Frölich and

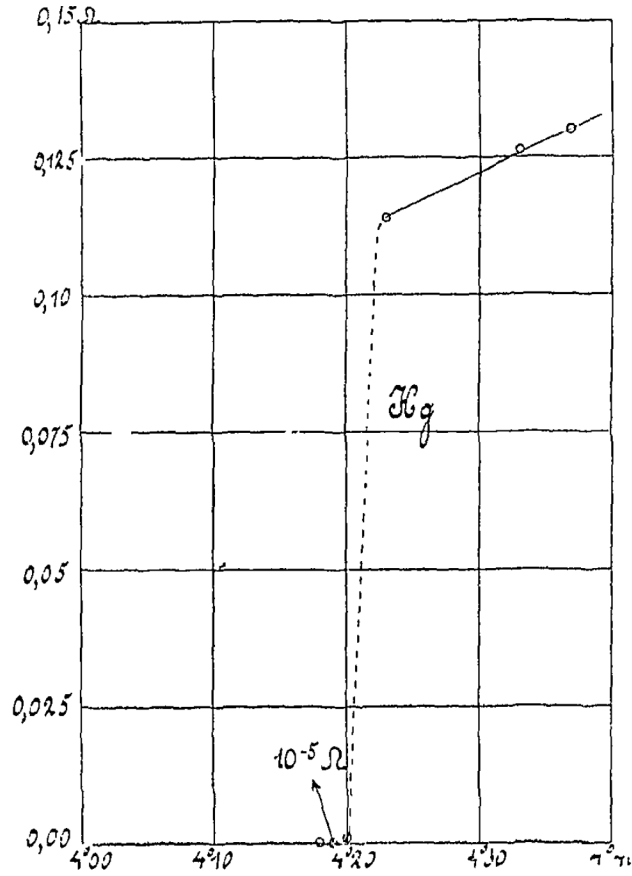


Figure 2.1 Temperature dependence of resistance of the mercury. The figure illustrates the rapid suppression of the resistance below 4.2 K. The disappearance of resistance at low temperature is the property of superconductivity. The figure is reproduced from Ref. [14].

Bardeen[15]. Frölich[16] and Bardeen[17], independently, considered the interaction between electrons and lattice vibrations to explain superconductivity and successfully explained the isotope effect [$T_c(H_c) \propto M^{-1/2}$, M is the isotopic mass][17, 18]. However, these theories are inadequate to explain other properties of superconductivity[15, 19]. It was only in 1957, 46 years after the discovery of superconductivity, that a microscopic theory explaining superconductivity was published by J. Bardeen, L. N. Cooper and J. R. Schrieffer[19, 20] called the BCS theory.

In BCS theory, it is shown that a weak attractive interaction, which is mediated by the lattice vibration (phonons) causes electrons near the fermi surface, to form bound pairs. These bound pairs are called Cooper pairs and the electrons of a pair occupy states with equal and opposite momenta and spins ($\mathbf{k}\uparrow$ and $-\mathbf{k}\downarrow$). Thus, Cooper pairs are bosons and form a Bose-Einstein condensate, which means all of them occupy a single energy level ground state at absolute zero temperature. BCS theory predicts that a minimum energy of $E = 2\Delta(T)$ is required to break a Cooper pair. Here, $\Delta(T)$ is the energy gap at $T < T_c$ and because of the requirement of an energy of at least $2\Delta(T)$ to break a pair, electrons of the superconductor become immune to effects such as scattering from impurities and defects that creates resistance in a normal metal.

In the weak coupling limit, the BCS theory predicts T_c and $\Delta(0)$ from the Debye frequency ω_D , electronic density of states at Fermi energy $N(0)$ and electron phonon coupling (V) as[12, p. 56, 63]:

$$k_B T_c = 1.134 \hbar \omega_D \exp\left(\frac{-1}{N(0)V}\right) \quad (2.1)$$

$$\Delta(0) = 2 \hbar \omega_D \exp\left(\frac{-1}{N(0)V}\right) \quad (2.2)$$

The ratio of Eq. (2.1) and (2.2) gives $\frac{\Delta(0)}{k_B T_c} = 1.764$ [12], and is a characteristic value for BCS superconductors.

Even though electron-phonon interactions are considered in the BCS theory, the pairing can occur due to an attractive potential of any form and strength. The large numbers of superconductors

whose properties can be described using the BCS theory and electron-phonon interaction are called "conventional superconductors".

There exist many superconductors, where the interactions between electrons required to form Cooper pairs cannot be explained by an exchange of bosonic phonons. These superconductors are called "unconventional superconductors" [21] and BCS theory falls short when explaining their properties. Heavy fermion [22, 23], cuprate [24], and iron-based superconductors [3, 25, 26] belong to this class. The interactions responsible for the pair binding are still under debate in this class of superconductors. So, there are many potential candidates: spin fluctuations [21], orbital fluctuations [27], valence fluctuations [28]. Nevertheless, spin fluctuations are the favorite candidate, when superconductivity is in close proximity to magnetism [21].

CeCu₂Si₂, a heavy fermion compound, is the first example of an unconventional superconductor, which was reported in 1979 with a $T_c = 0.6$ K [23, 29]. Next benchmark was discovery of high-temperature superconductivity in the copper-based family (cuprates) Ba-doped La₂CuO₄ with a $T_c \propto 35$ K [21, 30], reported in 1989. This discovery challenged the view that the upper limit of T_c is about 25 – 30 K, which is held by many physicists between 1976 and 1986 for the BCS superconductors [31], where the weak electron-phonon interactions form the pairing in the metals. Later, the highest T_c in this material reached 134 K for HgBa₂Ca₂Cu₃O_{8+ δ} at ambient pressure and 164 K at 31 GPa [32]. In 2008, iron-based family of high-temperature unconventional superconductors was discovered starting with the observation of a $T_c = 26$ K in LaFeAsO_{1- x} F _{x} [2]. This discovery was significant as it further undermined the conventional wisdom that magnetic elements (such as iron) are detrimental to superconductivity. The highest T_c attained in this family so far is 109 K in a single-layer of FeSe on a substrate of SrTiO₃ [33].

In these three classes of unconventional superconductors, the presence of competing ground states and the proximity of superconductivity to magnetism are some of the common features in their phase diagram. So, understanding the magnetism, its role and interplay with superconductivity is essential to understand superconductivity in these materials. In particular, the proximity suggests that spin fluctuations mediate the electron pairing and so far extensive research has been

carried out to understand them. Inelastic neutron scattering is an extensively used technique to investigate the spin dynamics.

2.2 A brief introduction to the iron-based superconductors

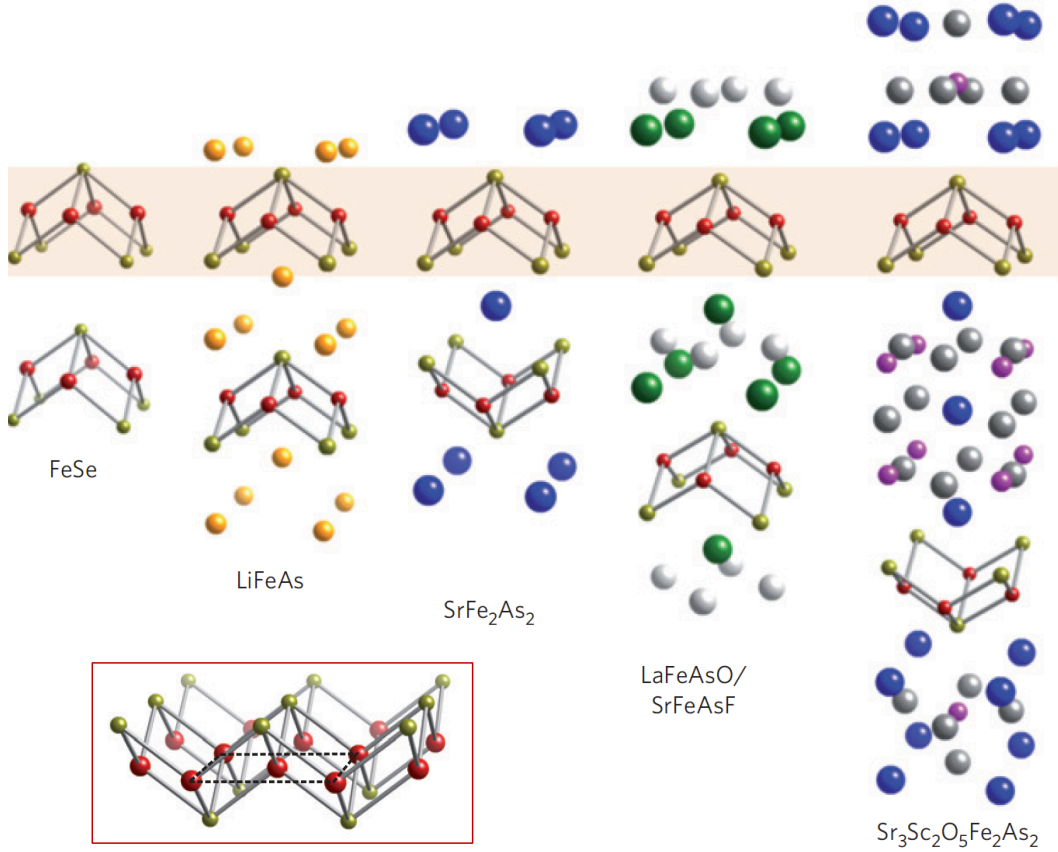


Figure 2.2 Structures of five families of Fe-based superconductors. Red spheres are the Fe atoms that are shown to be tetrahedrally bonded to Se/As (chalcogen/pnictogen:Ch/Pn) and this FePn/Ch structure shaded in the figure and shown in the inset is a common feature in all Fe-based superconductors. The figure is reproduced from Ref. [34].

The iron-based superconductors are defined as a compound that not only contains iron (Fe) but superconductivity involves Fe 3d electrons[21]. As discussed in the Section 2.1 above, this

undermines the conventional wisdom that magnetic elements (such as iron) are detrimental to superconductivity. LaFePO with $T_c = 5$ K is the first iron-based superconductor discovered in 2006[1], however, the interest in this class was invigorated only after discovery of superconductivity in LaFeAsO $_{1-x}$ F $_x$ with $T_c = 26$ K in 2008[2]. Since then, several members have been discovered and classified into several structural families, denoted by the stoichiometric chemical ratio in their undoped parent compound. 1111, 111, 122, 11, 10-3-8, 1144 are few examples of such group. In all these structural families, square planar layer of a Fe, which is tetrahedrally coordinated to the pnictogens (Pn = As, P) or chalcogens (Ch = S, Se, Te), as shown in Fig. 2.2 is the common feature. 11 (such as FeSe[35]), 1144 (such as CaKFe $_4$ As $_4$ [36]) are superconductors below T_c in their stoichiometric compounds, however, 10-3-8[such as Ca $_{10}$ (Pt $_3$ As $_8$)(Fe $_2$ As $_2$) $_5$ [37]] 1111[2] and 122[25, 26] becomes superconductor with either chemical doping or pressure.

Even though the era of Fe-based superconductors began with the 1111 family, the 122 family has been extensively studied due to the early availability of large and high-quality single crystals[25]. Large single crystals make them suitable for microscopic studies employing the neutron scattering technique. AFe $_2$ As $_2$ ($A =$, Ca, Ba, Sr) compounds are the parent compounds of 122 Fe-arsenide superconductors and do not show superconductivity at ambient pressure.

2.3 ThCr $_2$ Si $_2$ –type structure of ATM $_2$ As $_2$: TM = Mn, Fe, Co

ThCr $_2$ Si $_2$ crystallizes into the body-centered tetragonal structure with $I4/mmm$ space group and was first reported in 1965[38]. Since then, a large number of compounds (> 700)[39] with similar structure have been discovered. The conventional unit cell of ThCr $_2$ Si $_2$ is shown in Fig. 2.3 and the Wyckoff positions of Th, Cr and Si are $2a$ (0, 0, 0), $4d$ (0, 0.5, 0.25) and $4e$ (0, 0, z), respectively[38]. A very simple description of the structure is that it is a layered compound with atomic layers perpendicular to the c axis which are stacked in the sequence of Th-Si-Cr-Si-Th-. Another description is that the layers of Th are separated along the c direction by edge sharing Cr $_2$ Si $_2$ layers. This is the common structure for all the 122 compounds discussed in this thesis.

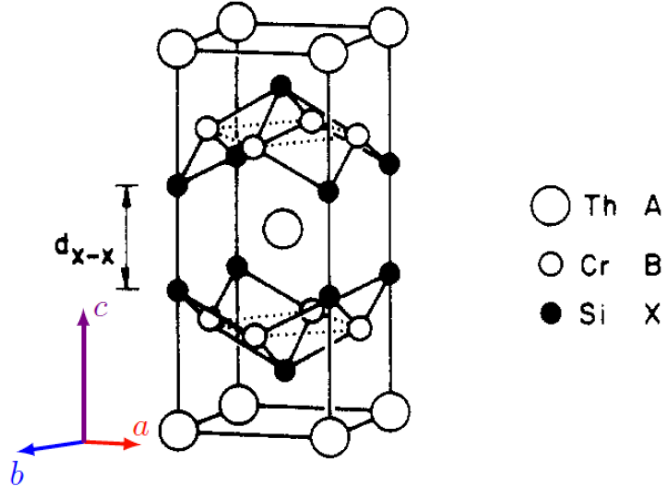


Figure 2.3 Conventional unit cell of ThCr_2Si_2 . Figure is reproduced from Ref.[40]

2.4 Diverse magnetism in ATM_2As_2

The discovery of high- T_c in AFe_2As_2 compounds with either chemical substitution or pressure motivated studies of other 122 compounds with $\text{TM} \neq \text{Fe}$. As mentioned above, these studies discovered a large number of 3d transition metal 122 compounds with diverse and novel physical properties. The diversity is also apparent in their magnetic properties and I will discuss the different magnetic ground states of ATM_2As_2 , $\text{TM} = \text{Mn}, \text{Fe}$ and Co , in this section. Understanding their magnetism and its correlations/interplay with other physical properties/ground states is the motivation of the work discussed in this thesis.

AFe_2As_2 compounds undergoes a structural transition to an orthorhombic phase at lower temperature and generally the structural transition is followed by a magnetic transition to the stripe-type AFM order, which is characterized by ferromagnetic (FM) correlations of spins along the orthorhombic \mathbf{b} direction and AFM along the orthorhombic \mathbf{a} and \mathbf{c} directions as shown in Fig. 2.4. Stripe-type AFM order is represented by an AFM propagation vector of $\boldsymbol{\tau}_{\text{stripe}} = (\frac{1}{2}, \frac{1}{2}, 1)$, in a reciprocal space, with respect to the high-temperature tetragonal unit cell and $(1, 0, 1)$ with respect to low-temperature orthorhombic unit cell[26, 41]. The reciprocal lattice vectors for a crystal sys-

tem are discussed in chapter 4. The structural and magnetic transitions for different members of $A\text{Fe}_2\text{As}_2$ compounds are discussed in detail in section 3.1.1 of chapter 3. Also, the spin dynamics of these compounds are studied using inelastic neutron scattering technique and are discussed in details in section 3.1.2 of chapter 3.

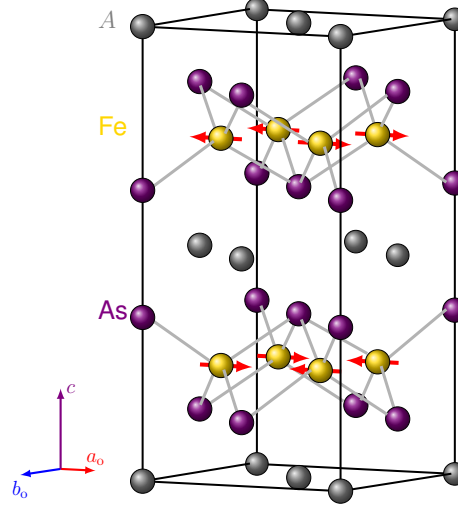


Figure 2.4 Low-temperature orthorhombic unit cell of $A\text{Fe}_2\text{As}_2$ ($A = \text{Ca}, \text{Sr}, \text{Ba}$) and the stripe-type antiferromagnetic order with Fe moment along the a_0 direction. The orthorhombic unit cell is rotated by 45° with respect to the tetragonal unit cell of $A\text{Fe}_2\text{As}_2$ compounds as shown in Fig. 3.1. The figure is created using the figure in Ref. [42] as a guideline.

$\text{CaCo}_{1.86}\text{As}_2$ compound is in the collapsed tetragonal phase at ambient pressure than its Fe counterparts (see section 3.2.1 for the structural description). Here, I am using the chemical formula with 7% vacancy at the Co site, which is the case for the compound studied in this thesis. Microscopic details about the magnetic order in $\text{CaCo}_{1.86}\text{As}_2$ were obtained from neutron diffraction measurements, both powder and single crystals measurements[6]. The results suggest that $\text{CaCo}_{1.86}\text{As}_2$ undergoes an AFM transition at $T_N = 52$ K, below which the compound shows A-type AFM order, which means that the Co moments are aligned ferromagnetically in the plane and antiferromagnetically along the c axis direction, as shown in Fig 2.5. Furthermore, the Co moments are directed along the c axis consistent with the interpretation of the susceptibility data

shown in Fig. 3.13. The Co moment size is calculated to be $< 0.6 \mu_B$ from both the neutron diffraction and magnetization measurements[6]. The small moment supports an itinerant nature of magnetism in $\text{CaCo}_{1.86}\text{As}_2$.

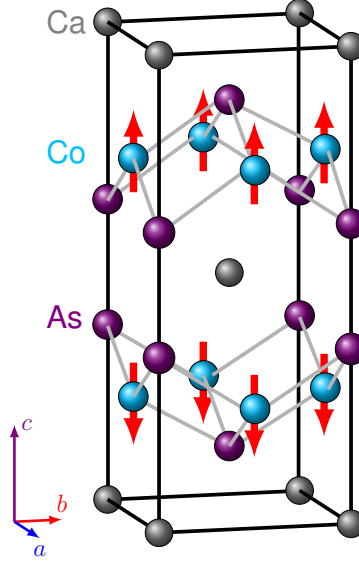


Figure 2.5 Body-centered tetragonal structural and magnetic unit cell of $\text{CaCo}_{1.86}\text{As}_2$. The red arrows show the Co moment direction in the A-type AFM structure. The figure is created using the figure in Ref. [6] as a guideline.

BaMn_2As_2 orders into a collinear Néel- (G- or checkerboard) type antiferromagnetic (AFM) structure below $T_N = 625(1)$ K with an ordered moment (μ) of $3.88(4)\mu_B/\text{Mn}$ (at 10 K)[43]. The G-type magnetic structure of BaMn_2As_2 is illustrated in Fig. 2.6, which shows that the nearest-neighbor Mn moments are antiparallel with each other in the plane and along the c axis. The ordered moment direction is along the c axis. The high spin state of $S = 5/2$ is expected for Mn that has an oxidation state of +2 corresponding to the d^5 electronic configuration. For this spin state, the ordered moment of $5 \mu_B/\text{Mn}$ is expected, however, the measured ordered moment of $3.88(4)\mu_B$ is small and the reduction has been discussed due to effects of the quantum fluctuations[9] and hybridization between Mn d and As p orbitals[44]. The large ordered moment and the insulating ground state infer with the local-moment antiferromagnetism in BaMn_2As_2 . This ground state is

in contrast to itinerant magnetic ordering of AFe_2As_2 compounds[26] but is similar to cuprates[45].

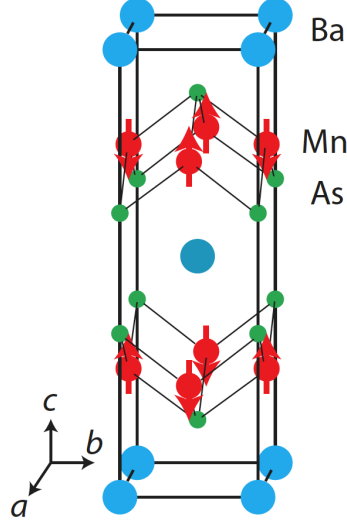


Figure 2.6 Crystallographic and magnetic unit cell of BaMn_2As_2 illustrating the arrangement of the Mn moment. The red arrows corresponds to the direction of the magnetic moment at Mn site. The figure is reproduced from Ref. [9].

2.4.1 J_1 – J_2 model in a square-lattice

Magnetism in ATM_2As_2 compounds is governed mainly by the d elements, which form a square-lattice in the tetragonal structure. As discussed above, these compounds exhibit diverse magnetic ground states and are of both local and itinerant nature. Irrespective of their nature, the magnetism can be minimally described by considering Heisenberg nearest-neighbor (J_1), next-nearest-neighbor (J_2) magnetic exchange interactions between the magnetic ions of the square-lattice in the \mathbf{ab} plane and nearest-neighbor (J_c) along the \mathbf{c} directions.

Neutron scattering technique has been a useful tool to map out the magnetic order in these compounds. The values of J s are obtained from the fits of the different models with the inelastic neutron scattering spectra[8, 9, 26, 46–49]. The values of J_c with respect to in-plane exchange interactions are significantly small for all these compounds indicating that the system are quasi-

two-dimensional (quasi-2D) in terms of magnetism[9, 26]. So, the J_1 and J_2 , defined in the square-lattice of the $3d$ TM, are the minimum requirements to describe the magnetism in these systems.

In this J_1 – J_2 model, the relative strengths and signs of J_1 and J_2 stabilize the different magnetic ground states. The condition for three different magnetic ground states are given in the Table 2.1.

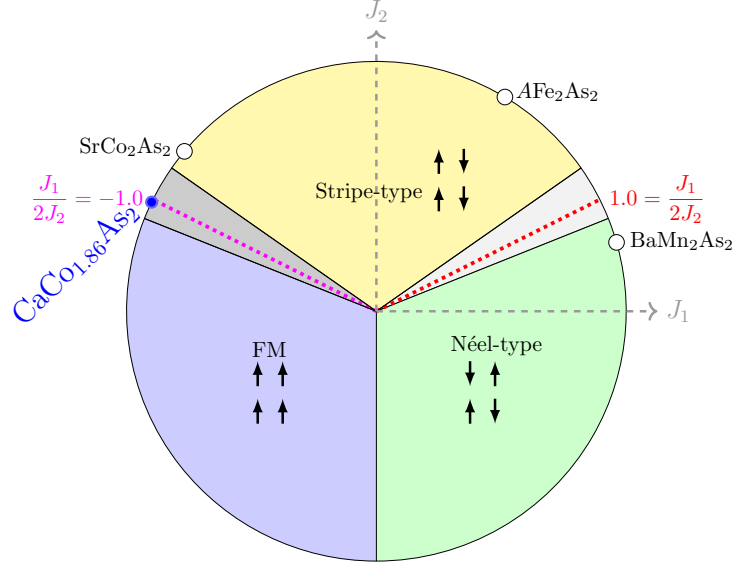


Figure 2.7 Phase diagram of J_1 – J_2 model illustrating the region of stripe-type (yellow), ferromagnetic (FM) (light blue) and Néel-type (light green). The shaded gray (both dark and light) areas correspond to the region where the magnetic ordering is absent. $\eta = \frac{J_1}{2J_2}$ is the frustration parameter with maximum frustration corresponding to 1 or -1 (red or maroon dotted line). Solid circle on the circumference corresponds to the position of AFe_2As_2 [26], SrCo_2As_2 [8], $\text{CaCo}_{1.86}\text{As}_2$ [50] and BaMn_2As_2 [51] based upon the ratio $\frac{J_2}{J_1}$ obtained from the fits to the inelastic neutron scattering data. The figure is created using the figure in the Ref. [26] as a guideline.

These conditions are consistent with the J 's obtained from the inelastic neutron scattering experimental data for stripe-type in AFe_2As_2 [26, 46–49], Néel-type in BaMn_2As_2 [9] and stripe-type in SrCo_2As_2 [8].

Figure 2.7 shows the J_1 – J_2 phase diagram for three magnetic ground states. Each points on the circumference of the circle represents the different ratio of J_2 to J_1 . The ratio defines the frustration

Table 2.1 Stability conditions for three types of collinear magnetic ground states according to the J_1 – J_2 model. The table is reproduced from the Ref. [26].

Ground state	Condition on J_1	Condition on J_2
Ferromagnet	$J_1 < 0$	$-J_1 > 2J_2$
Stripe	no restriction	$ J_1 < 2J_2$
Néel	$J_1 > 0$	$J_1 > 2J_2$

parameter, $\eta = \frac{J_1}{2J_2}$, and different values of η indicates the different degree of frustration. The maximum frustration occurs when $\eta = 1$ or -1 , which is represented by the dashed grey line in the figure. Here, the two magnetic ground-states on the either side compete and magnetic order is suppressed. The shaded gray part in the figure corresponds to the region where the magnetic order is suppressed. AFe_2As_2 [26] and SrCo_2As_2 [8] compounds which have stripe-type magnetism with antiferromagnetic (AFM) and ferromagnetic (FM) J_1 (i.e. $J > 0$ for AFM and $J < 0$ for FM), respectively, are on the opposite side of the stripe-type region. SrCo_2As_2 has only stripe-type spin dynamics but not long-range order and its suppression is likely due to combined effects of weak electronic correlations and moderate magnetic frustration.

For a square-lattice system, a possibility of the spin liquids has been discussed for the case of maximum frustration, i.e. $\eta = 1$ or -1 [26, 52, 53]. Spin liquid is a state, arising due to magnetic frustration, where long-range magnetic order is absent down to $T = 0$ K. A system in the spin liquid state is expected to show exotic phenomena[54, 55]. However, there are no examples of square-lattice system near this region of maximum frustration[50]. Therefore, the J_1 – J_2 phase diagram in Fig. 2.7 provides an interesting insight into the possibility of tuning the compounds on either side of the maximum frustration towards it. One way of finding a potential candidate of the maximum frustration is by tuning the ratio of J_1 to J_2 and a chemical substitution could be a way to achieve that. For example, $\text{CaCo}_{1.86}\text{As}_2$ compound, which is discussed in chapter 6 and is very close to maximum frustration, can be tuned further by doping either Ca by Sr or Co by Fe towards this exotic physics.

In the light of possible exotic physics, this is an additional motivation for a systematic studies of these 122 compounds. The inelastic neutron scattering measurement on the $\text{CaCo}_{1.86}\text{As}_2$ compound discussed in chapter 6 finds the system close to this interesting ratio of J_2 to J_1 .

In the end, the J_1 – J_2 phase diagram discussed above is limited to the collinear magnetism of the 122 compounds and related square-lattice system. Besides these, there are various other interesting magnetic orders, both collinear and non-collinear in iron pnictides, such as spin-vortex crystal order in $\text{CaKFe}_4\text{As}_4$ [36, 56], bicollinear magnetism in FeTe [3, 57, 58]. These magnetic orders cannot be explained by J_1 – J_2 model and it may require additional terms such as the higher order exchange interactions, anisotropic terms (such as biquadratic coupling), etc, in the Hamiltonian to explain their magnetism. The inclusion of these additional terms would expand the above discussed phase diagram and an example of this elaborated phase diagram has been discussed in Ref. [59]. Even though J_1 – J_2 model is not enough to explain all the magnetic orders observed in different members of iron-based superconductors, I am going to limit my discussion to the J_1 – J_2 model in this thesis because it is a minimal model to describe the magnetism of the compounds of interest of this thesis.

2.5 Chemical substitution as a tuning parameter

Chemical substitution is commonly employed method to tune the physical properties of the ATM_2As_2 compounds and provides an opportunity to study the competition and correlation between various ground states. Besides chemical substitution, pressure is also commonly employed tuning parameter that induces superconductivity in these systems[26].

2.5.1 Superconductivity in AFe_2As_2

In AFe_2As_2 , chemical substitution (also refer to as chemical doping) suppresses the AFM order and induces superconductivity[4, 60–63]. The chemical substitution/doping can be categorized into three types: (i) hole doping, (ii) electron doping, and (iii) isovalent doping, depending upon whether the substituting element introduces less, extra or zero extra electrons, respectively. Superconductivity is realized in AFe_2As_2 by all three methods. In addition, the doping can be done at

all available atomic sites, with various elements in the periodic table, thus, creating a significantly large number of routes to achieve superconductivity. Therefore, it is cumbersome to discuss all of them in details here. So, for further discussion, I will focus on the cobalt substitution at Fe site in case of BaFe_2As_2 and CaFe_2As_2 . BaFe_2As_2 is a representative compound of 122 system, where extensive studies have been performed and will serve as a reference for $\text{Ca}(\text{Fe}_{1-x}\text{Co}_x)_2\text{As}_2$, which is the compound of interest for this thesis.

The appearance of superconductivity after significant suppression of the magnetic order with increasing Co-substitution is apparent in the phase diagrams shown in the Fig. 2.8 for $\text{Ba}(\text{Fe}_{1-x}\text{Co}_x)_2\text{As}_2$ and $\text{Ca}(\text{Fe}_{1-x}\text{Co}_x)_2\text{As}_2$ compounds. A major difference between the phase diagrams is the presence of a microscopic coexistence region of the antiferromagnetic and superconducting ground states in $\text{Ba}(\text{Fe}_{1-x}\text{Co}_x)_2\text{As}_2$ and its absence in $\text{Ca}(\text{Fe}_{1-x}\text{Co}_x)_2\text{As}_2$. Antiferromagnetic order and superconducting ground state are well-separated by a strong-first order phase boundary in $\text{Ca}(\text{Fe}_{1-x}\text{Co}_x)_2\text{As}_2$. Additional discussions about the phase diagrams are presented in the section 3.1.3 of chapter 3.

Inelastic neutron scattering measurements on $\text{Ba}(\text{Fe}_{1-x}\text{Co}_x)_2\text{As}_2$ compounds have provided important insights into the relationship between spin fluctuations and superconductivity[3, 5]. The resonance-like feature observed in the spectra of spin fluctuations in the superconducting region suggests an unconventional nature of superconductivity, where the spin fluctuations mediates the pairing mechanism[41, 65, 66]. Additionally, a systematic study of the evolution of spin fluctuations in $\text{Ba}(\text{Fe}_{1-x}\text{Co}_x)_2\text{As}_2$ with increasing x , i.e. Co content, found that the spin fluctuations of the parent BaFe_2As_2 compound changes its nature smoothly from the spin waves like character to the overdamped (diffusive) spin fluctuations in the near beginning of the coexistence region[5]. The evolution of the spin dynamics from the spin-wave type character to the diffusive dynamics for $\text{Ba}(\text{Fe}_{1-x}\text{Co}_x)_2\text{As}_2$ is illustrated in the Fig. 3.8. The appearance of the overdamped spin fluctuations and superconductivity coexist which suggests that the overdamped spin fluctuations are necessary for the pairing mechanism.

$\text{Ca}(\text{Fe}_{1-x}\text{Co}_x)_2\text{As}_2$, which lacks this coexistence region, presents a different scenario to study the correlation between the overdamped spin fluctuations and superconductivity. The absence of

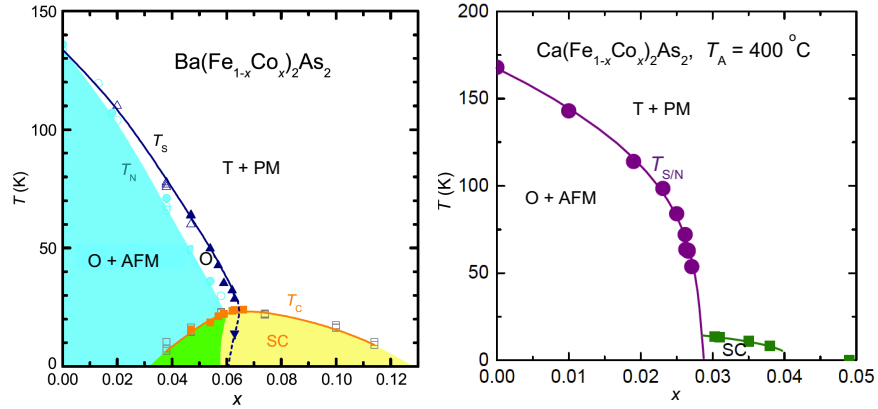


Figure 2.8 Phase diagrams of the $\text{Ba}(\text{Fe}_{1-x}\text{Co}_x)_2\text{As}_2$ and $\text{Ca}(\text{Fe}_{1-x}\text{Co}_x)_2\text{As}_2$ with increasing cobalt doping. They show that T_S and T_N gets suppressed with increasing cobalt doping. The phase transition from high-temperature tetragonal (T) and paramagnetic (PM) to low-temperature orthorhombic (O) and antiferromagnetic (AFM) phase remains coupled and suppressed abruptly in $\text{Ca}(\text{Fe}_{1-x}\text{Co}_x)_2\text{As}_2$, unlike in $\text{Ba}(\text{Fe}_{1-x}\text{Co}_x)_2\text{As}_2$. In addition, there is no coexisting region of antiferromagnetism and superconductivity in $\text{Ca}(\text{Fe}_{1-x}\text{Co}_x)_2\text{As}_2$, as present in $\text{Ba}(\text{Fe}_{1-x}\text{Co}_x)_2\text{As}_2$. The phase diagram for $\text{Ba}(\text{Fe}_{1-x}\text{Co}_x)_2\text{As}_2$ is reproduced from Ref. [4] and has been established from the resistivity and magnetization[60], neutron diffraction[64] and x-ray diffraction[4] measurements. The phase diagram of $\text{Ca}(\text{Fe}_{1-x}\text{Co}_x)_2\text{As}_2$ is from the magnetization measurement performed for the $\text{Ca}(\text{Fe}_{1-x}\text{Co}_x)_2\text{As}_2$ samples annealed at 400°C .

the superconducting region in the antiferromagnetic state suggests that the overdamped spin fluctuations should also be absent in the antiferromagnetic region of the phase diagram. In addition, the strong first order suggests that changes in the physical properties are abrupt in $\text{Ca}(\text{Fe}_{1-x}\text{Co}_x)_2\text{As}_2$ and likely occurs only across the phase boundary. Therefore, one can expect that the spin dynamics in the antiferromagnetic state remain similar with increasing x . The inelastic neutron scattering measurement performed on $\text{Ca}(\text{Fe}_{1-x}\text{Co}_x)_2\text{As}_2$ to find the nature of the evolution of the spin fluctuations and their link with superconductivity is discussed in chapter 5.

2.5.2 Insulator-metal transition in $\text{Ba}_{1-x}\text{K}_x\text{Mn}_2\text{As}_2$

BaMn_2As_2 compound shares properties with both the iron- and copper-based superconductors[9]. Therefore, one can expect that substitution might have effects similar to these two classes of superconductors, i.e. suppression of the magnetism and appearance of superconductivity. Different routes of substitution have been employed so far but without any sign of SC. In addition, the substitution of Mn by transition metals and As site by Sb incur a problem of miscibility or causes relatively negligible changes in properties[67, 68].

A success story in this regard is the K (potassium) substitution at the Ba site, i.e. hole doping. It has been found that $\text{Ba}_{1-x}\text{K}_x\text{Mn}_2\text{As}_2$ compounds with $x \geq 0.016$ are metal[69] indicating that the system is driven towards metallicity (insulator to metal transition), as found in cuprates. However, the significant suppression of AFM order for superconductivity observed in both the cuprates and AFe_2As_2 compounds has not been achieved, at least up to $x = 0.40$, and consistently superconductivity is absent[69, 70]. The T_N decreases only slightly up to $x = 0.40$, i.e. 480 K and the magnetic moment μ per Mn is almost constant, as shown in Fig. 2.9. This indicates that the G-type order of BaMn_2As_2 is robust against the electron-doping or metallicity and is inconsistent with the expectations based upon the significant hybridization between Mn and As orbitals in BaMn_2As_2 [51]. Interestingly, for K concentration ≥ 0.16 , $\text{Ba}_{1-x}\text{K}_x\text{Mn}_2\text{As}_2$ shows itinerant ferromagnetic order that coexist with the G-type AFM order[70]. The ferromagnetic order is suggested to be originated from

the As 4p conduction bands from a x-ray magnetic circular dichroism experiment[71]. This suggests that the charge transport and local-moment G-type order are decoupled in BaMn_2As_2 .

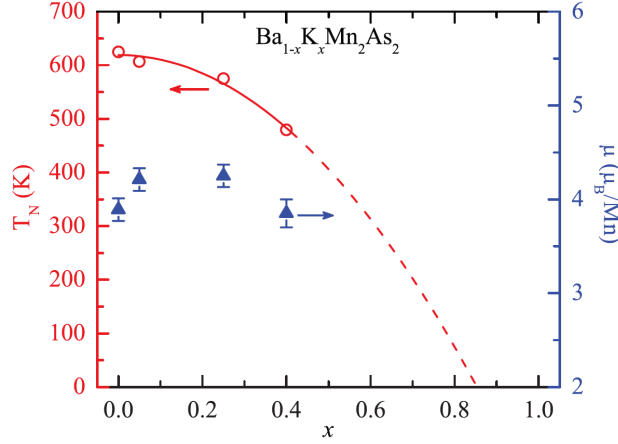


Figure 2.9 Doping evolution of T_N and ordered moment for $\text{Ba}_{1-x}\text{K}_x\text{Mn}_2\text{As}_2$. The solid (dashed) line is fit (extrapolation) using the second-order polynomial of x and provides a rough estimation of concentration at which magnetism is suppressed. The figure is reproduced from Ref. [69].

In order to further understand the effects of the hole-doping on the local-moment antiferromagnetism in BaMn_2As_2 compound, spin excitations in three different compounds of $\text{Ba}_{1-x}\text{K}_x\text{Mn}_2\text{As}_2$ $x = 0, 0.125$ and 0.25 , were studied using inelastic neutron scattering and the results are discussed in the chapter 7.

2.6 Motivation

Diverse physical properties, among which is the high- T_c superconductivity, are motivation behind studying different members of $122 \text{ ATM}_2\text{As}_2$ compounds, with $\text{TM} = 3d$ elements and $A = \text{Ca}, \text{Sr}, \text{Ba}$. Among different ATM_2As_2 compounds, there is diversity in magnetism as well as in its interplay/correlation with other physical properties. Understanding these diverse magnetic properties and its correlations is an ongoing effort to understand many novel properties, such as high- T_c superconductivity.

So, the aim of this thesis is to understand the diverse magnetic properties of the three compounds $\text{Ca}(\text{Fe}_{1-x}\text{Co}_x)_2\text{As}_2$, $\text{CaCo}_{1.86}\text{As}_2$ and $\text{Ba}_{1-x}\text{K}_x\text{Mn}_2\text{As}_2$ by studying their spin dynamics (spin fluctuations). Moreover, in $\text{Ca}(\text{Fe}_{1-x}\text{Co}_x)_2\text{As}_2$ and $\text{Ba}_{1-x}\text{K}_x\text{Mn}_2\text{As}_2$ compounds, the focus is on understanding the correlation between their magnetism and electronic properties. Inelastic neutron scattering technique is a powerful tool to study the spin fluctuations of a condensed matter system and it is employed to study the spin dynamics of these three compounds. The results for $\text{Ca}(\text{Fe}_{1-x}\text{Co}_x)_2\text{As}_2$, $\text{CaCo}_{1.86}\text{As}_2$ and $\text{Ba}_{1-x}\text{K}_x\text{Mn}_2\text{As}_2$ are discussed in the chapters 5, 6 and 7, respectively.

In particular, the phase diagram of the $\text{Ca}(\text{Fe}_{1-x}\text{Co}_x)_2\text{As}_2$ is different than the extensively studied $\text{Ba}(\text{Fe}_{1-x}\text{Co}_x)_2\text{As}_2$ compound. Therefore, it presents a different scenario to study the evolution of spin fluctuations and understand its importance for superconductivity. Inelastic neutron scattering measurements were performed on two different compounds of $\text{Ca}(\text{Fe}_{1-x}\text{Co}_x)_2\text{As}_2$ i.e. $x = 0.026$ and 0.030 , to validate the link between the overdamped spin fluctuations and superconductivity that was discovered in the $\text{Ba}(\text{Fe}_{1-x}\text{Co}_x)_2\text{As}_2$ compounds. In addition, the study also highlights some key differences in the spin fluctuations of $\text{Ca}(\text{Fe}_{1-x}\text{Co}_x)_2\text{As}_2$ from $\text{Ba}(\text{Fe}_{1-x}\text{Co}_x)_2\text{As}_2$ that arises due to the unique properties of CaFe_2As_2 .

Similarly, spin fluctuations in three $\text{Ba}_{1-x}\text{K}_x\text{Mn}_2\text{As}_2$ compounds, $x = 0, 0.125$ and 0.25 were studied to understand the correlation between the local antiferromagnetism and charge transport/metallic property. The metallic property is tuned by chemical substitution/hole doping. Earlier studies of the static magnetic order point towards the robust antiferromagnetism against hole doping. The inelastic measurement of the spin fluctuations discussed in this thesis provides additional detail about the effects of the hole doping on the magnetism.

As discussed above in section 2.4, $\text{CaCo}_{1.86}\text{As}_2$ is unique than its 122 AFe_2As_2 counterparts as it undergoes magnetic ordering in the collapsed tetragonal phase. Another surprise in ACo_2As_2 family is that the spin fluctuations in SrCo_2As_2 compound, discussed in section 3.2.3 of chapter 3, are found to be similar in character (i.e. stripe-type spin fluctuations) as in AFe_2As_2 compounds, even though the SrCo_2As_2 does not order magnetically (at least up to ≈ 2 K) and shows instability

towards ferromagnetism. Hence, it is interesting to see if the spin fluctuations of the $\text{CaCo}_{1.86}\text{As}_2$ possess the similar character as SrCo_2As_2 and AFe_2As_2 compounds.

In addition, from the inelastic neutron scattering spectra, the values of J s for each of these compounds can be obtained and discussed in terms of J_1 – J_2 model.

CHAPTER 3 A REVIEW OF PROPERTIES OF ATM_2As_2

3.1 ATM_2As_2 : TM = Fe

As discussed in Chapter 2, high-temperature superconductivity (SC) in these compounds led to enormous interests in them. It is a topical problem because a microscopic theory describing their origin has not been developed, yet. On the other hand, some technical properties like isotropic upper critical field make them promising materials for technological use[25]. This section discusses properties of AFe_2As_2 compounds in details.

3.1.1 Structure, magnetism, and superconductivity in AFe_2As_2

The parent compounds are metallic and paramagnetic (PM) with body-centered tetragonal (T) crystallographic structure ($I4/mmm$) at room temperature (~ 300 K) and ambient pressure. Generally, a structural phase transition into an orthorhombic (O) phase ($Fmmm$) occurs upon cooling through a temperature T_S [72–74]. In orthorhombic phase $a_o \neq b_o \neq c_o$, whereas in T phase $a = b \neq c$. The structural transition is accompanied by the onset of stripe-type antiferromagnetic (AFM) order below the Néel temperature T_N [26, 41]. Figure 3.1 shows high-temperature T unit cell with no magnetic order and low-temperature O unit cell with spins at Fe site indicating the magnetic order.

The stripe-type AFM order is characterized by ferromagnetic correlations of spins along the orthorhombic \mathbf{b} direction and antiferromagnetic along orthorhombic \mathbf{a} and \mathbf{c} directions as shown in Fig. 3.1. In addition, the stripe-type AFM order is represented by an AFM propagation vector of $\boldsymbol{\tau}_{\text{stripe}} = (\frac{1}{2}, \frac{1}{2}, 1)$, in reciprocal space, with respect to the high-temperature T unit cell and $(1, 0, 1)$ with respect to low-temperature orthorhombic unit cell[26, 41]. The reciprocal lattice vectors for a crystal system are discussed in Chapter 4.

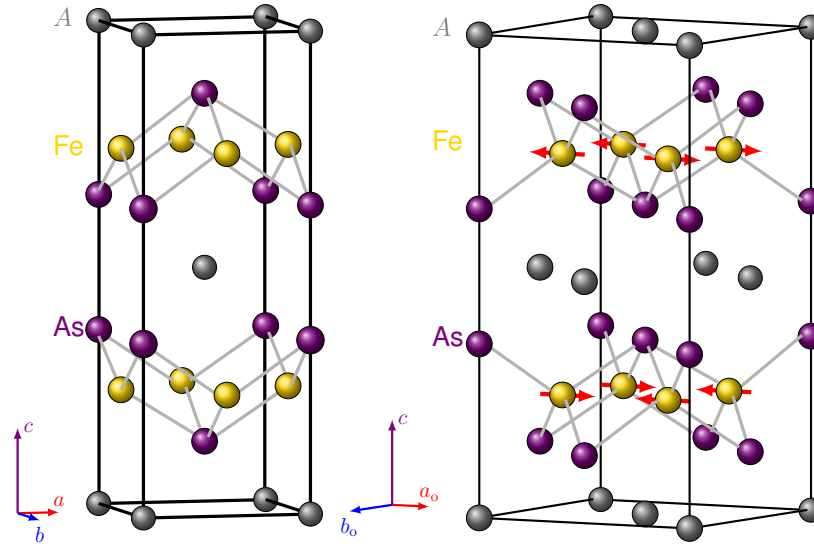


Figure 3.1 High-temperature tetragonal and low-temperature orthorhombic unit cell of $A\text{Fe}_2\text{As}_2$ ($A = \text{Ca}, \text{Sr}, \text{Ba}$). The orthorhombic unit cell is rotated by 45° with respect to tetragonal unit cell and illustrates the stripe-type antiferromagnetic ordering with Fe moment along the a_o direction. The figures are created using the figure in Ref. [26, 42] as a guideline.

Signatures of the structural and magnetic transitions were observed in the resistivity, susceptibility and heat capacity measurements as shown in Fig. 3.2[25]. In addition, microscopic information about these transitions were obtained using x-ray and neutron diffraction techniques. The structural transition has been quantified from the splitting of nuclear Bragg peaks as shown in Fig. 3.3 and the order parameter called distortion parameter δ is defined as $\delta = \frac{a_o - b_o}{a_o + b_o}$, which is 0 in tetragonal phase as $a = b$ and increases below T_S . Below T_N , magnetic Bragg peaks at the wave-vector $\mathbf{Q}_{\text{stripe}} = (\frac{m}{2}, \frac{n}{2}, l)$ with m, n and l odd integers, as shown in Fig. 3.3(b) were observed in the neutron diffraction measurements. Here, \mathbf{Q} is the momentum transfer in reciprocal space and is defined as $\mathbf{Q} = (H, K, L) = \frac{2\pi}{a}H\hat{\mathbf{i}} + \frac{2\pi}{b}K\hat{\mathbf{j}} + \frac{2\pi}{c}L\hat{\mathbf{k}}$ with respect to the tetragonal $I4/mmm$ unit cell.

Even though all three AFe_2As_2 compounds have same structural properties, they show different lattice parameters, magnetic moments, T_S and T_N . These values are listed in the Table 3.1. Also, the nature of these structural and magnetic transitions are different in CaFe_2As_2 , SrFe_2As_2 and BaFe_2As_2 . The structural and magnetic transitions are strongly coupled and is first order for CaFe_2As_2 and SrFe_2As_2 with $T_{S/N} \sim 170$ K[42, 72] and 200 K[73, 75], respectively. However, in case of BaFe_2As_2 the second-order structural transition occurs at $T_S = 134.5$ K, which is followed by the first-order AFM transition at $T_N = 133.75$ K[74]. The occurrence of almost simultaneous structural and magnetic transition infers the strong coupling between magnetism and structure in these systems[42, 74]. The first-order transition is characterized by a jump at the transition temperature whereas the second-order transition shows smooth change in the order parameter.

Table 3.1 Comparison of lattice parameters, magnetic moments and transition temperatures in AFe_2As_2 .

	a, c (Å)	μ (μ_B)	T_S (K)	T_N (K)	References
CaFe_2As_2 ¹	3.879(3), 11.740(3)	0.80(5)	≈ 173	≈ 173	[42]
BaFe_2As_2	3.963, 13.02	0.87(3)	134.5	133.75	[60, 74, 76]
SrFe_2As_2 ²	3.926(3), 12.298(1)	0.94(4)	≈ 220	≈ 220	[73, 75]

¹ For CaFe_2As_2 the lattice parameters have variations for different growth procedure and post growth thermal treatment[77]. The result presented here are for Sn-flux grown sample.

² The $T_{S/N}$ in SrFe_2As_2 varies from ≈ 198 –220 K in different studies [73, 75].

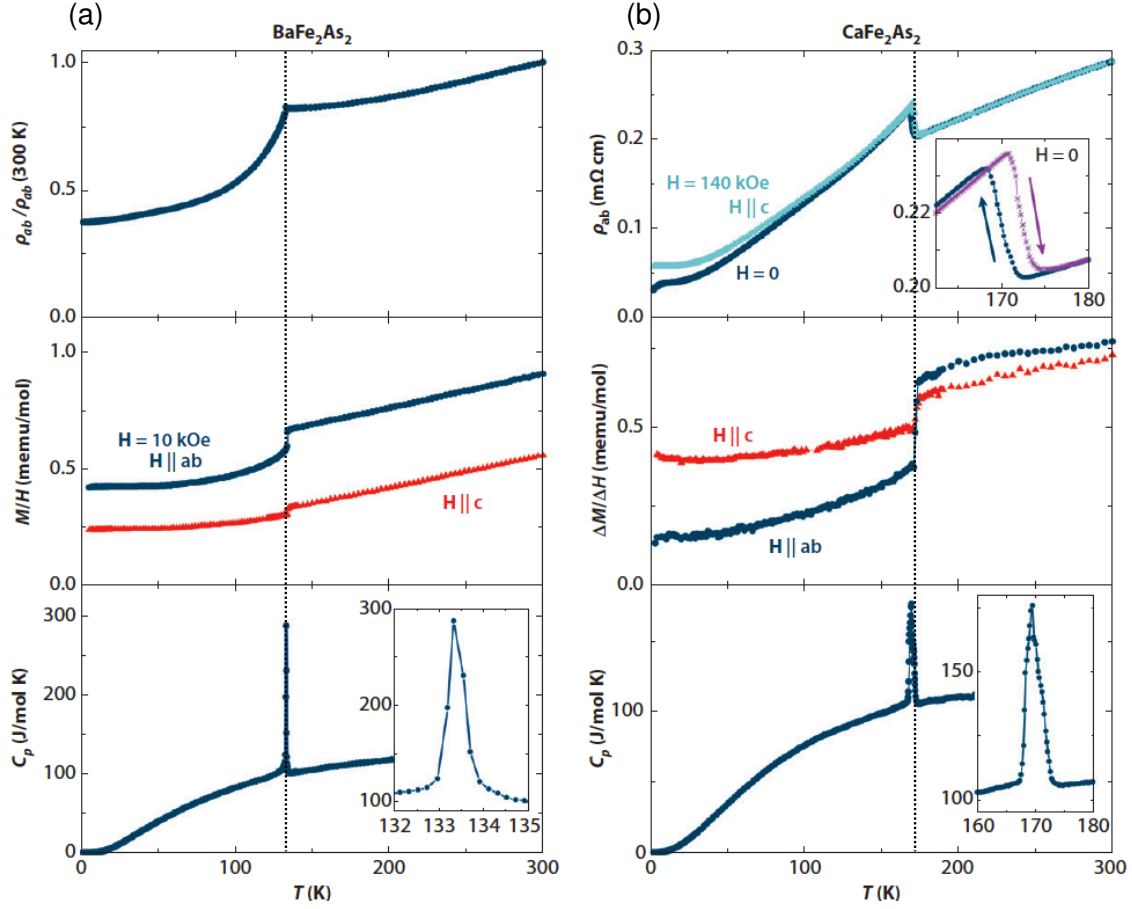


Figure 3.2 (a), (b) Signatures of coupled structural and magnetic transition from the resistivity, susceptibility and heat capacity measurements for BaFe_2As_2 and CaFe_2As_2 , respectively. The dotted black lines are guide for the eyes and correspond to the transitions. The figure is reproduced from Ref. [25].

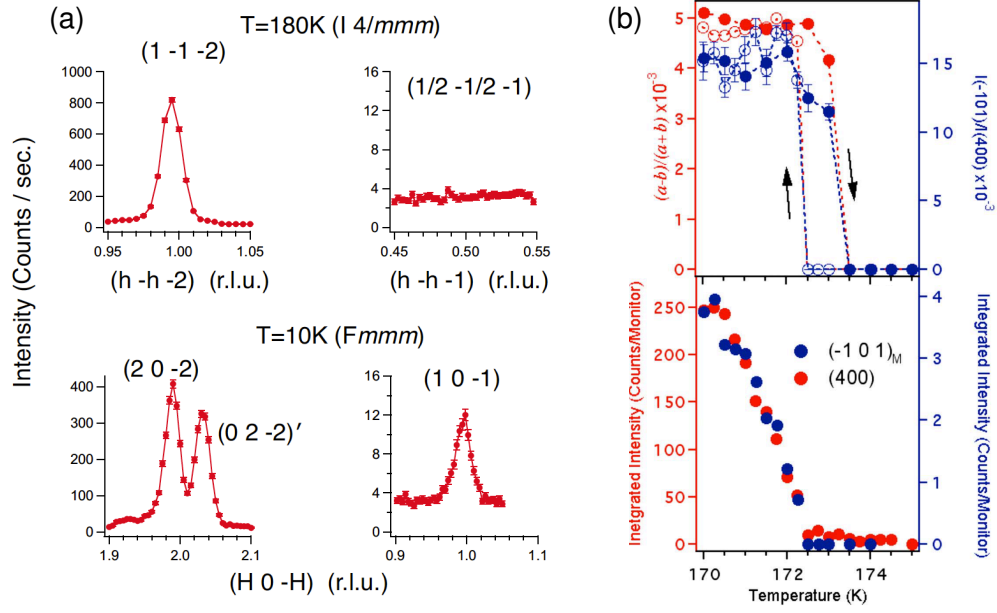
CaFe₂As₂

Figure 3.3 (a) Results from neutron diffraction measurements showing nuclear peaks $(1, 1, -2)_T$ above $T_{S/N}$ in the tetragonal state splits into $(2, 0, -2)_O$ and $(0, 2, -2)_O$ in the orthorhombic state as a signature of the structural transition. From the lattice parameters obtained from the center of these peaks, a plot of the distortion parameter δ in (b) is generated. In some AFe_2As_2 compounds, δ was also obtained using the x-ray diffraction, where similar splitting of the Bragg peaks were observed. Similarly, the measurement of the magnetic Bragg peak $(1/2, 1/2, -1)_T = (1, 0, -1)_O$ is observed below T_N and the integrated intensity of these peaks are shown in (b) as the order parameter. The figure is reproduced from Ref. [42]

3.1.2 Spin fluctuations in AFe_2As_2

Spin fluctuations are regarded as the mediator for the pairing in Fe-arsenide superconductors, therefore it is necessary to fully understand their properties to understand their importance for superconductivity. The early availability of large, homogeneous crystals of AFe_2As_2 compounds made it possible to study spin fluctuations using inelastic neutron scattering measurements.

With some differences in the details, there are common features in the spin fluctuations spectra of all three AFe_2As_2 [26, 47, 49, 78, 79] compounds. Some of the features observed in these compounds are discussed below:

1. Spin fluctuations are found to be centered at $\mathbf{Q}_{\text{stripe}} = (\frac{m}{2}, \frac{n}{2}, l)$, with m , n and l odd integers, both in the AFM ordered and PM state.
2. Spin waves in the AFM ordered state are found to be gapped with sharp excitations that extend in energy ≈ 200 meV [3, 46, 78] as shown in Fig. 3.4 and 3.5. The spin gap is due to single-ion anisotropy.
3. Spin waves are three-dimensional (3D) in these compounds unlike quasi-two-dimensional in cuprates [46]. Furthermore, among AFe_2As_2 compounds, spin waves in CaFe_2As_2 compound are comparatively more 3D [26].
4. Spin wave velocities along the a_o and b_o directions in the ordered states are anisotropic. The anisotropy is apparent as an elliptical INS spectra as shown in Fig. 3.5. This spatial anisotropy in scattering persists in the PM state as well and is tied to the anisotropy in magnetic correlation length [79, 80].
5. Above T_N , in the PM state, the low-energy spin fluctuations are no more sharp, well-defined and gapped as found in the AFM ordered state. The spin fluctuations are characterized by the overdamped dynamics with significant broadening in \mathbf{Q} . The broadening in \mathbf{Q} is related to the shorter-correlation of Fe spins. In addition, the spin fluctuations develops more two-dimensional (2D) character with weak interlayer coupling in the PM state [80, 81].

6. The high-energy spectra near the Brillouin zone boundary are diffusive and remain identical both above and below T_N [78, 79].
7. The low-energy spin fluctuations (i.e. close to the zone center) are described by the local-moment Heisenberg model, where the exchange interactions between the nearest-neighbor and next-nearest-neighbor interactions are considered. On the other hand, the high-energy excitations close to the zone boundary are discussed with substantial damping due to decay of spin fluctuations in stoner continuum, which is relevant at high energies[47, 78]. On contrary, there are also results which suggest the absence of any substantial damping at higher energies[49] supporting the local-moment description of spin fluctuations in AFe_2As_2 compounds. This suggests that both the nature (itinerant and local) should be considered while describing the spin fluctuations in these compounds[3].

Spin-wave velocities along three crystallographic orthorhombic directions and spin gap, for AFe_2As_2 compounds, obtained from the fits of the inelastic neutron scattering spectra to the Heisenberg model are listed in the Table 3.2. The velocity along the \mathbf{c} direction measures the strength of the interlayer interactions and its ratio with in-plane velocity provides the dimensionality of the magnetism. The ratio is maximum for $CaFe_2As_2$ indicating that it is the most three-dimensional among AFe_2As_2 compounds. The parameters are almost similar for all three compounds.

Table 3.2 Comparison of spin-velocities and spin-gap in AFe_2As_2 compounds where velocities are calculated using the exchange constants using the equations in Ref. [26]. The exchange constants used in the calculations for $CaFe_2As_2$, $BaFe_2As_2$, and $SrFe_2As_2$ are from Refs. [47],[79], and [78], respectively.

	v_{a_o} (meVÅ)	v_{b_o} (meVÅ)	v_c (meVÅ)	v_c/v_{a_o}	Δ (meV)
$CaFe_2As_2$	534	386	246	0.46	6.9
$BaFe_2As_2$	490	315	163	0.33	9.8
$SrFe_2As_2$	418	337	164	0.40	6.5

A major difference between the spin dynamics in $BaFe_2As_2$ and other two compounds is that the ring-like feature observed at higher energies for $CaFe_2As_2$, as shown in Fig. 3.4, is absent in

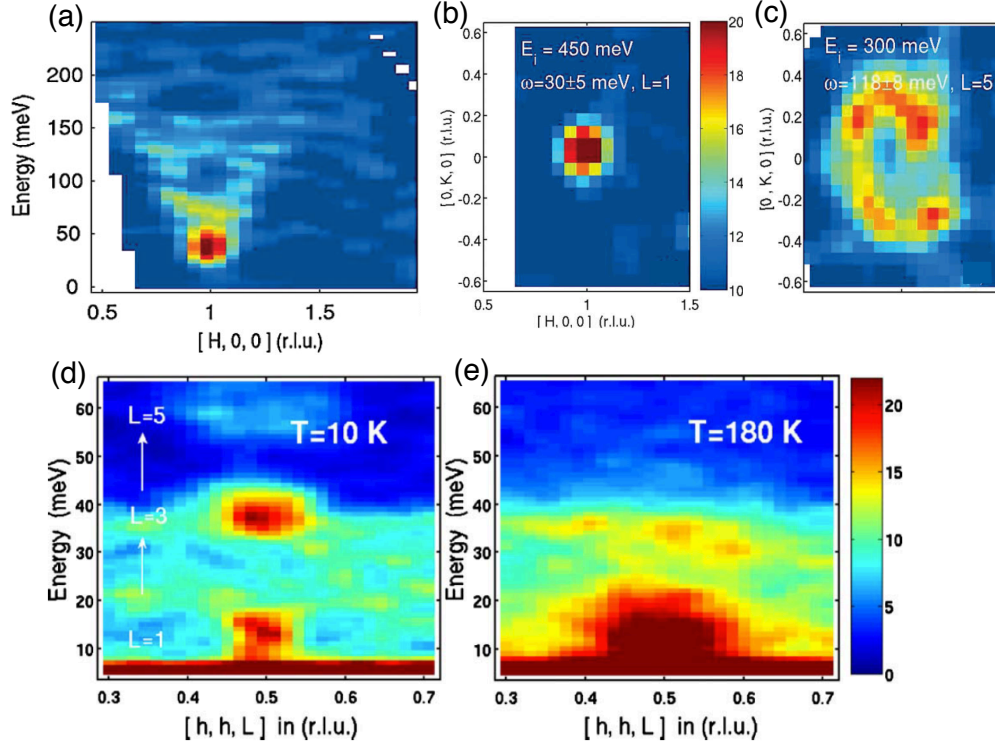


Figure 3.4 (a)-(d) Spin fluctuations of CaFe_2As_2 in the AFM state and (e) the PM state. (a) Spin waves are found to be extended in energy above 150 meV. (b) and (c) Constant-energy (Q) cuts showing spin waves sharp in \mathbf{Q} for low-energy and nearly ring-like feature with small ellipticity for high-energy, respectively. The small ellipticity indicates the presence of anisotropic spin-wave velocities along the corresponding directions. (d) and (e) Comparison of the spin fluctuations above and below T_N . Figures show that the scattering spectra sharp in \mathbf{Q} (i.e. $[h, h, L]$) below T_N becomes broad above T_N , which is consistent with the diffusive character. The figure is reproduced from Refs. [47] and [80].

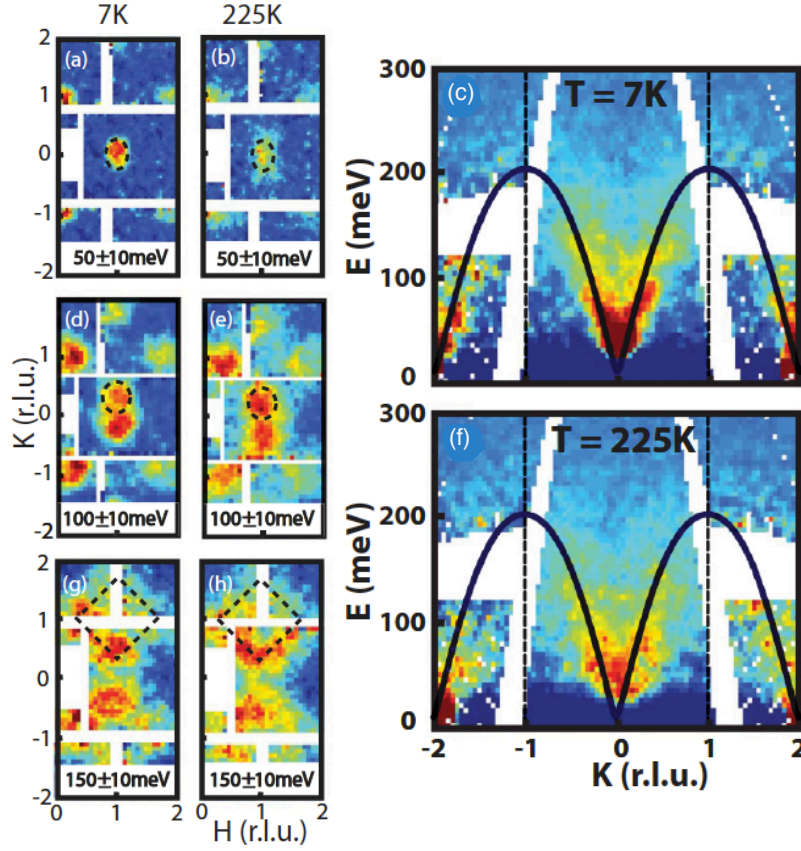


Figure 3.5 Spin fluctuations of BaFe_2As_2 at different temperatures, both below (AFM phase) and above (PM phase) $T_N \sim 140$ K. (a), (d), (g), Constant-energy slices in the AFM phase and (b), (e), (f) in the PM phase. The dashed ellipses are guide for the eye to compare the two temperatures data. (c), (f) Slices showing energy dependence of spin fluctuations. The spectra are found up to ≈ 200 meV in both the AFM and PM phases. In addition, the low-energy spectra close to zone center ($\mathbf{K} = 0$) become broader above T_N . The black line is dispersion plot obtained using the Heisenberg model and the parameters, which are obtained from fit to the inelastic data. The figure is reproduced from Refs. [82].

BaFe₂As₂. In BaFe₂As₂, the spectra split into two peaks at higher energies as shown in Fig. 3.5(d) and (e)[48].

3.1.3 Effect of Cobalt substitution at the Fe site

The Co substitution at Fe site suppresses the AFM order in all three AFe₂As₂ members. In case of BaFe₂As₂, the nearly simultaneous T_S and T_N split clearly with increasing Co substitution and become second order[4, 74, 83], as shown in Fig. 2.8. The suppression of T_S and T_N is gradual with Co substitution. Furthermore, the magnetic moment $\mu = 0.87 \mu_B$ for parent compound BaFe₂As₂ [or Ba(Fe_{1-x}Co_x)₂As₂ with $x = 0$] is significantly reduced to $0.2 \mu_B$ for Ba(Fe_{1-x}Co_x)₂As₂ $x = 0.047$, which has $T_N = 47$ K[83]. However, the strongly coupled magneto-structural (structural and magnetic) transition in CaFe₂As₂ remains coupled with increasing Co substitution, as shown in Fig. 2.8, and disappearance of $T_{S/N}$ is abrupt. Also, the magnetic moment $\mu = 0.8 \mu_B$ [42] for parent CaFe₂As₂ compound reduces by very small amount in Ca(Fe_{1-x}Co_x)₂As₂ compounds with increasing x , that shows AFM order.

In Ba(Fe_{1-x}Co_x)₂As₂, the superconducting and AFM states coexist for certain Co-concentration as shown in the phase diagram in Fig. 2.8[4]. On the other hand, the presence of the strong first-order magnetostructural transition effectively forbids the coexistence of AFM and SC states in Ca(Fe_{1-x}Co_x)₂As₂[84]. In case of tin (Sn) flux grown sample, there are reports of coexistence of SC and the AFM state in Ca(Fe_{1-x}Co_x)₂As₂ as well, but, the issue of reproducibility and inhomogeneity in Sn-flux grown samples indicate the possibility of mixed phases[77, 85]. Therefore, the AFM and SC could arise from the different parts of the heterogeneous sample. The phase diagram shown in Fig. 2.8 is for self-flux (FeAs as a flux) grown sample and it illustrates the absence of the coexistence in Ca(Fe_{1-x}Co_x)₂As₂. In addition, in self-flux grown Ca(Fe_{1-x}Co_x)₂As₂ the post growth treatment (annealing/quenching) should be taken into consideration as the annealing and quenching affects the property and phase diagram looks different with annealing temperatures[77, 84, 85]. The sample used in our work is annealed at 400 °C, hence the phase diagram of Ca(Fe_{1-x}Co_x)₂As₂

discussed in this thesis is for this annealing temperature only. The transition temperature $T_{S/N}$ for CaFe_2As_2 annealed at 400 °C is ~ 170 K similar as Sn-flux grown samples[86].

The coexistence of superconducting and AFM states in $\text{Ba}(\text{Fe}_{1-x}\text{Co}_x)_2\text{As}_2$ provides an opportunity to study the interplay between magnetism and SC, and have provided useful insights into these systems. The anomalous suppression of the orthorhombic distortion below T_c and observation of re-entrant behavior manifested the interplay between structure and SC[4]. This is discussed as an indirect consequence of competition between magnetism and SC. In addition, the decrease of magnetic intensity below T_c , as shown in Fig. 3.6 indicates the competition between magnetism and SC[83] as well as provides strong evidence of microscopic coexistence of AFM and SC. Furthermore, the two-band itinerant model showed that the coexistence is possible only in unconventional pairing of Cooper pairs with the sign changing state (s^{+-})[64]. s^{+-} means superconducting order parameter has isotropic gaps on the hole and electron bands but with different signs (phase changes by π).

3.1.3.1 Fermi surface nesting and magnetism

In iron-arsenide superconductors, Fe d bands predominantly govern the physical properties[26]. Iron in AFe_2As_2 compounds is in the +2 oxidation state with d^6 electronic configuration and localized case of Fe d -electrons in the high spin state $S = 2$ suggests Fe moment of $\mu = gS\mu_B = 4\mu_B$. However, relatively small Fe moment (μ) is observed as shown in Table 3.1. This observation along with the fact that 122 compounds are metallic suggest that the AFM order is the spin-density-wave (SDW) order that arises from the itinerant electron. In itinerant systems, nesting between Fermi surfaces can drive system towards SDW instability and it has been discussed that the Fermi nesting between the hole and electron Fermi surface sheets drives the system towards SDW ordering in AFe_2As_2 .

In AFe_2As_2 compounds, nearly-circular hole and elliptical electron pockets are present at the Fermi level at the center [$\Gamma = \mathbf{Q} = (0, 0)$] and the corner [$X = \mathbf{Q} = (\frac{1}{2}, \frac{1}{2})_T$] of the Brillouin zone, respectively, as shown in the Fig. 3.7(a). Angle-resolved photoemission spectroscopy (ARPES)

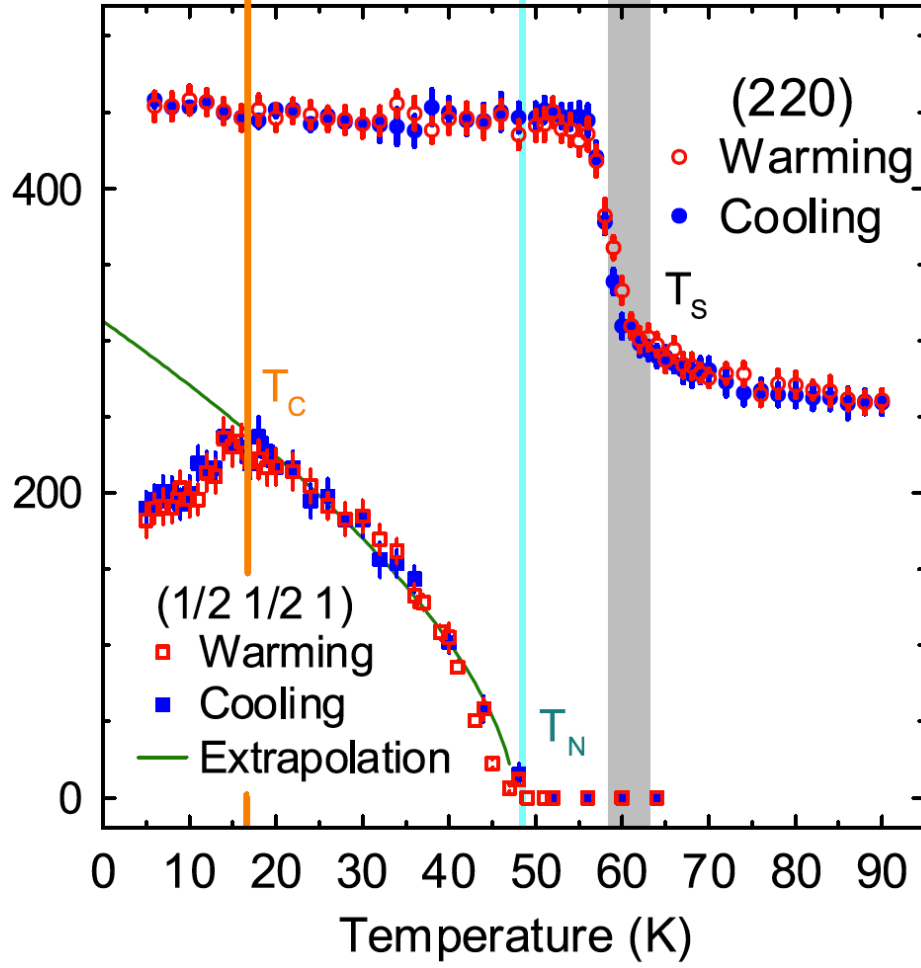


Figure 3.6 Results of neutron diffraction measurement on $\text{Ba}(\text{Fe}_{1-x}\text{Co}_x)_2\text{As}_2$ $x = 0.047$ showing that the intensity of magnetic peak $(1/2, 1/2, 1)$ decreases below T_c . This indicates that SC and magnetism competes for same electrons. The figure is reproduced from Ref. [83].

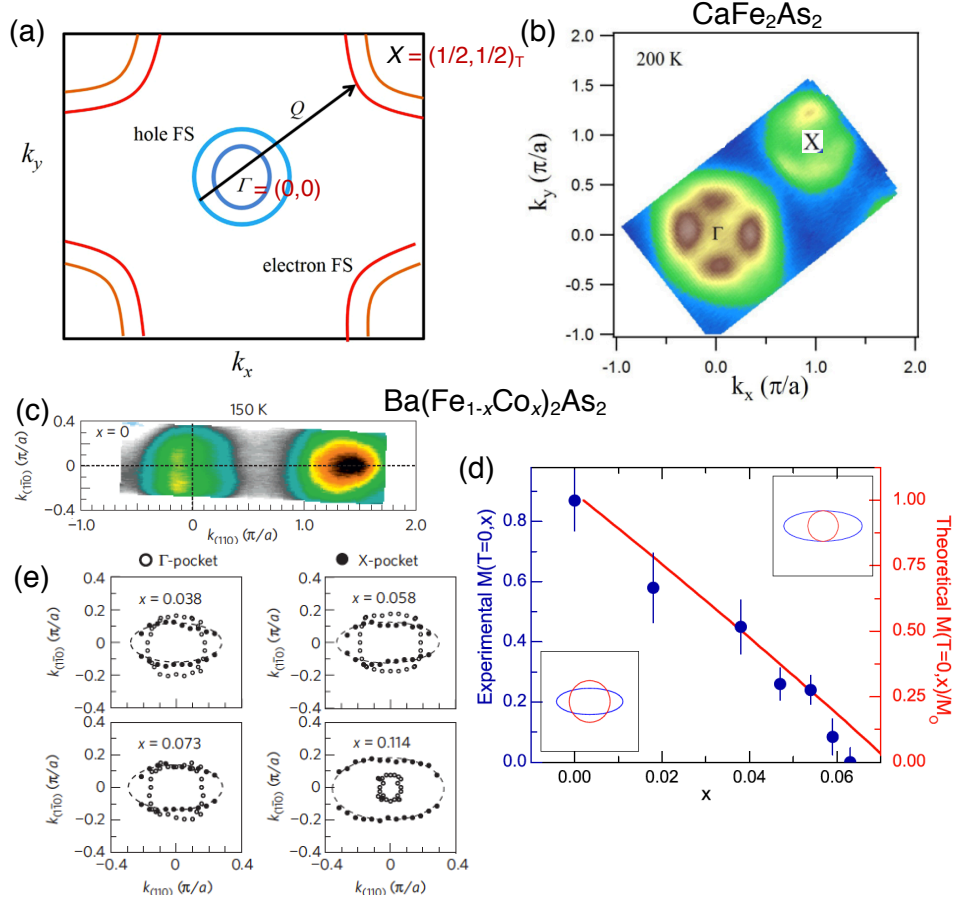


Figure 3.7 (a) Schematics of Fermi surface showing 2 nearly-circular hole and elliptical electron pockets at $\Gamma = \mathbf{Q} = (0,0)$ and $X = \mathbf{Q} = (\frac{1}{2}, \frac{1}{2})_{\Gamma}$ separated by the wave-vector $\mathbf{Q} = (\frac{1}{2}, \frac{1}{2})$. (b) and (c) ARPES data for CaFe_2As_2 and BaFe_2As_2 compounds in the tetragonal phase, showing the hole and electron pockets at the Γ and X positions. (d) Figure illustrates the decrease in the Fe moment size with increasing Co concentration in $\text{Ba}(\text{Fe}_{1-x}\text{Co}_x)_2\text{As}_2$ for both the experimental value and theoretical calculation. The inset shows the hole pocket (red circle) shrinks and electron pocket (blue circle) enlarges with increasing doping. (e) ARPES measurement showing the similar feature in $\text{Ba}(\text{Fe}_{1-x}\text{Co}_x)_2\text{As}_2$ with increasing x . Here, the X -pocket are shifted by $\mathbf{Q} = (\frac{1}{2}, \frac{1}{2})$ for better comparison. The figure is reproduced from (a) Ref. [87], (b) Ref. [88], (c) and (e) Ref. [89], and (d) Ref. [64].

measurements confirm their presence and shape for both CaFe_2As_2 [90] and BaFe_2As_2 [89, 90], as shown in Fig. 3.7(b) and (c), respectively. Significant parts of the hole pockets are connected to the electron pockets by an in-plane wavevector $\mathbf{Q} = (\frac{1}{2}, \frac{1}{2})$ [89, 90], which means that these regions of the hole and electron Fermi surfaces overlap on shifting one of them by $(\frac{1}{2}, \frac{1}{2})$, as shown in Fig. 3.7(e). The condition is described as Fermi surface nesting between the hole and electron pockets by in-plane nesting vector of $\mathbf{Q} = (\frac{1}{2}, \frac{1}{2})$. The nesting gives the peak in the susceptibility at the corresponding wavevector, hence, drives the system towards spin-density-wave (SDW) ordering with wavevector $\mathbf{Q} = (\frac{1}{2}, \frac{1}{2})$, i.e. stripe-type AFM order. The back folding, hybridization and the reconstruction of the bands observed in both CaFe_2As_2 and BaFe_2As_2 in the ARPES measurements are consistent with the AFM order[89, 90]. With increasing Co doping, the size of the Fermi surface changes, i.e. electron pocket enlarges and hole pocket shrinks, which detunes the Fermi surface, thus, consequently the nesting condition. The detuning of the nesting condition with increasing doping is considered to be responsible for the suppression of the SDW order in these compounds[64]. This is illustrated in Fig. 3.7(d) and (e).

3.1.3.2 Evolution of the Spin fluctuations with Co doping in $\text{Ba}(\text{Fe}_{1-x}\text{Co}_x)_2\text{As}_2$

In order to understand the interplay between magnetism and SC, it is necessary to understand the evolution of spin dynamics from the AFM ordered state to the SC states. The evolution has been systematically studied in the Co-doped BaFe_2As_2 compounds[5]. It has been found that the high-energy (> 80 meV[3, 5]) spin fluctuations remain insensitive with doping, but the low-energy spin fluctuations show significant changes[3, 5, 91]. The spin fluctuations are always found to be originated/centered at $\mathbf{Q}_{\text{stripe}}$ wavevector. The well-defined and gapped spin waves, of the parent compound, that have 3D character and small damping evolve into the gapless and diffusive spin fluctuations with more 2D character. The changes occur smoothly near beginning of the coexistence region of AFM and superconducting states in $\text{Ba}(\text{Fe}_{1-x}\text{Co}_x)_2\text{As}_2$ and the appearance of the diffusive spin dynamics is concomitant with the onset of SC. The appearance of the diffusive spin fluctuations in the AFM ordered state ($T > T_c$) in the coexistence region and their absence

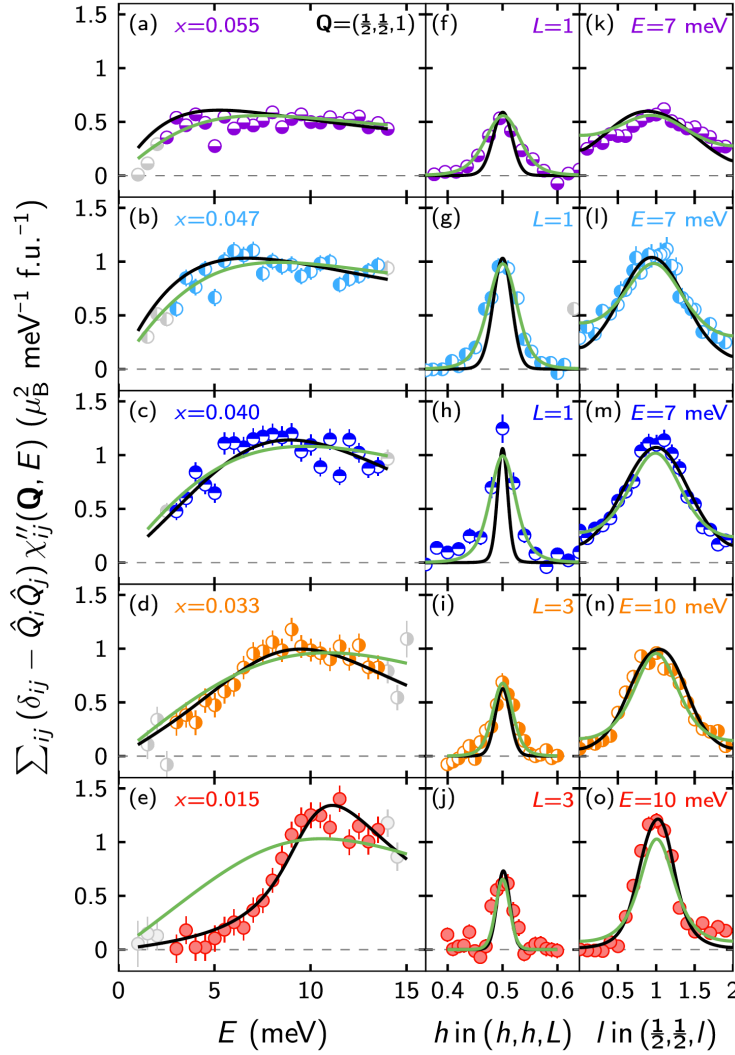


Figure 3.8 Inelastic neutron scattering results showing the evolution of low-energy spin fluctuations in $\text{Ba}(\text{Fe}_{1-x}\text{Co}_x)_2\text{As}_2$. (a)–(e) Energy cuts at $\mathbf{Q}_{\text{stripe}} = (\frac{1}{2}, \frac{1}{2}, 1)$ showing the gapped spin fluctuations become gapless with increasing Co-concentration. (f)–(j) and (k)–(o) Constant-energy scans along the in-plane direction (h, h, l) and c direction, respectively. The cuts show that sharp peaks at lower concentration become broader diffusive spin fluctuations. Black line is fit to the damped spin-wave model and light green line to the diffusive model. The lower Co-concentration data fits better with the spin-wave model and the higher with the diffusive model. The $x = 0.040$ to 0.055 for $\text{Ba}(\text{Fe}_{1-x}\text{Co}_x)_2\text{As}_2$ lies in the coexistent region and the measurement is performed at $T_c < T < T_N$. The figure is reproduced from Ref. [5].

(low-energy spin fluctuations) in the overdoped superconducting $\text{Ba}(\text{Fe}_{1-x}\text{Co}_x)_2\text{As}_2$ $x = 0.14$ [92] and non-superconducting $x = 0.24$ [92] suggest that the diffusive spin fluctuations are necessary for the SC. Furthermore, the suppression of the low-energy spin fluctuations with increasing doping towards the overdamped side and its complete suppression in higher-doped non-superconducting sample is also observed in $\text{Ba}(\text{Fe}_{1-x}\text{Ni}_x)_2\text{As}_2$ [93] compounds as well. This strongly infers that the low-energy spin fluctuations are necessary for the existence of SC. The evolution of the spin dynamics from the spin-wave type character to the diffusive dynamics for $\text{Ba}(\text{Fe}_{1-x}\text{Co}_x)_2\text{As}_2$ is illustrated in the Fig. 3.8.

In addition to the above discussed changes in the low-energy spectra with increasing Co-concentration, there is a prominent feature in the spectra below T_c in the superconducting phase. Below T_c , a spin-resonance peak in the spin fluctuations spectra appears at $\mathbf{Q}_{\text{stripe}}$ position. It is peak at low-energy, called resonance energy (E_{res}), as shown in Fig. 3.9 and appears due to depletion of spectral weight of the lower-energy spin fluctuations and its redistribution to the resonance peak. In these compounds, the resonance peak is formed at $E_{\text{res}} \leq 2\Delta$ [41, 65, 66], similar to the cuprates[66].

It has been discussed that the presence of spin resonance suggests the sign changing, i.e. s^{+-} , symmetry of the superconducting order parameter in iron-arsenide superconductors and further indicates the unconventional nature of SC with the spin fluctuations as the mediator for pairing[41, 94, 95]. In addition, the results of the phase sensitive tunneling measurements in iron-based superconductors[21] and the two-band itinerant model describing the coexistence in $\text{Ba}(\text{Fe}_{1-x}\text{Co}_x)_2\text{As}_2$ compounds[64] favor the s^{+-} gap structure.

3.1.4 Unique properties of CaFe_2As_2

Additional interesting properties of CaFe_2As_2 compound are (1) the most sensitivity to pressure (among AFe_2As_2 compounds), (2) strict necessity of non-hydrostatic pressure for SC[7, 96, 97] (unlike BaFe_2As_2 and SrFe_2As_2 [98–100]), and (3) strong dependence of physical properties on the post-growth thermal treatments[77, 84].

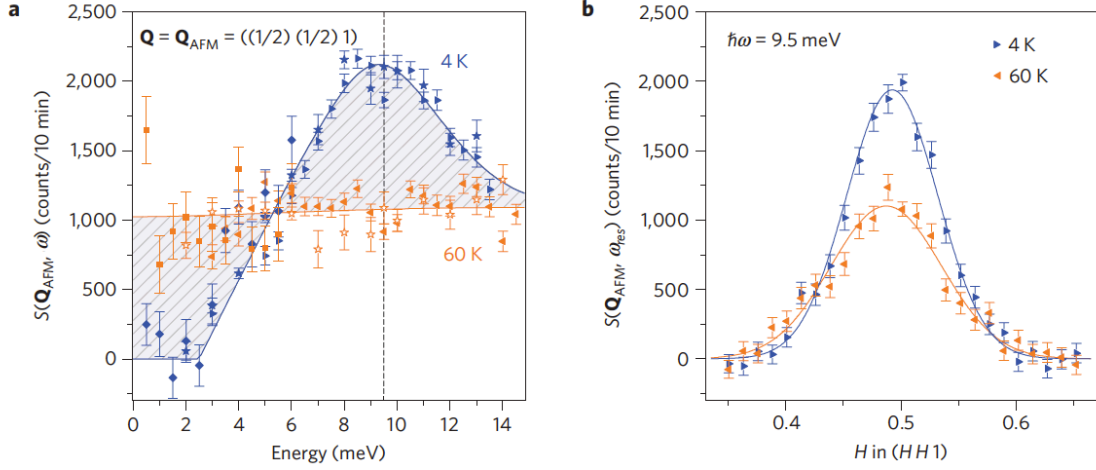


Figure 3.9 Spin fluctuations spectra of Ba(Fe_{0.925}Co_{0.075})₂As₂ ($T_c = 25$ K) in the normal ($T = 60$ K) and the superconducting state $T = 4$ K). (a) Energy cuts showing spin-resonance peak in the superconducting state at $E_{\text{res}} = 9.5$ meV at $\mathbf{Q}_{\text{stripe}} = (\frac{1}{2}, \frac{1}{2}, 1)$. The spectral weight of the low-energy spin fluctuations is depleted in the superconducting state in comparison to the normal state. (b) Constant-energy cuts showing the peak centered at $\mathbf{Q}_{\text{stripe}} = (\frac{1}{2}, \frac{1}{2}, 1)$ and enhanced for the superconducting state. The figure is reproduced from Ref. [65].

CaFe₂As₂ undergoes structural transition to the collapsed tetragonal (cT) state with an application of the modest pressure of 1.6 GPa at ambient temperature[7], which is much smaller in comparison to 10 GPa[101] and 17–22 GPa[102] for SrFe₂As₂ and BaFe₂As₂, respectively. Furthermore, the pressure of ~ 0.3 GPa is sufficient to make the transition to cT phase at 50 K. On the other hand, in case of non-hydrostatic pressure, multi phases (O, T and cT phases) are stabilized in the crystal and SC appears from the remaining orthorhombic or tetragonal phases[98, 103].

In addition, for the self-flux grown sample, it has been discovered that the physical properties of CaFe₂As₂ compounds depend upon the post-growth thermal treatment, annealing and quenching[77, 84]. The cT phase can be stabilized at ambient pressure in Ca(Fe_{1-x}Co_x)₂As₂ compounds with proper annealing and quenching protocol. It has been discussed that the strain, caused by nanoscale precipitates present in these samples, is controlled by annealing and quenching process, and consequently changes properties similar to pressure[86]. The Fig. 3.10 below shows the correlation between the annealing temperature and pressure. The effects of annealing have been studied

in the $\text{Ca}(\text{Fe}_{1-x}\text{Co}_x)_2\text{As}_2$ compounds and a three dimensional phase diagram with annealing as an additional axis has been produced[77]. The phase diagram contains T/PM, O/AFM, T/PM/SC, and non-magnetic/cT phases and provides additional routes to study the interplay between these ground states.

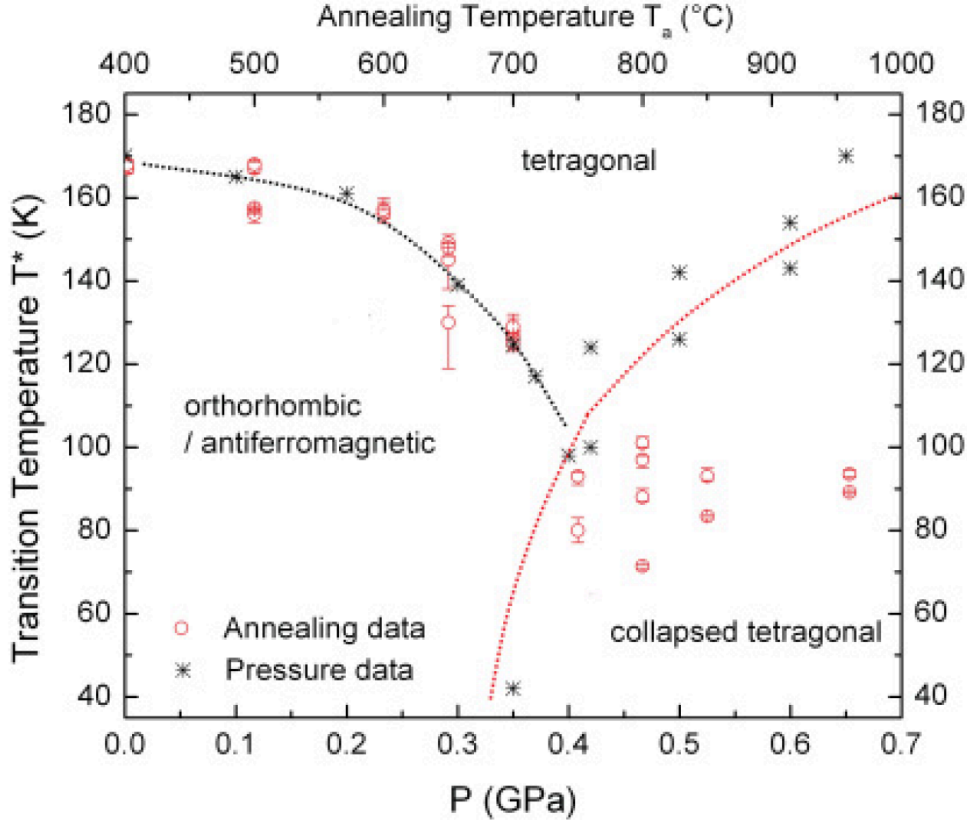


Figure 3.10 Phase diagram of CaFe_2As_2 with annealing temperature T_a showing correspondence with pressure (P). T^* is the transition temperature from T/PM phase to AFM/O phase for lower annealing temperature (700°C , or ~ 0.35 GPa) and T/PM to non-magnetic/cT phase for higher annealing temperature ($> 750^\circ\text{C}$ or > 0.35 GPa). The figure is reproduced from Ref. [86].

During the transformation to the cT phase in CaFe_2As_2 , c lattice parameter reduces by nearly 9.5% (i.e. from 11.74 to 10.63 Å at 300 K)[7]. The cT phase is characterized by the quenching of the Fe moment[104, 105], as a consequence of which a complete absence of the stripe-type antiferromagnetic order has been observed in the neutron diffraction experiments[7]. Spin fluctuations are

also found to be absent in the cT phase[106, 107] and absence of the SC in this phase[77] presents another strong evidence in support of necessity of spin fluctuations for SC.

In Ref. [7], the absence of the magnetic order has been discussed in terms of decrease in the density of states with the shift of Fe 3d bands to the lower energies than the Fermi level. The band structure calculation shows that the generalized susceptibility displays a peak at the AFM wave-vector $(\frac{1}{2}, \frac{1}{2}, 1)$ in the tetragonal phase as an indication of the AFM instability, and in the cT phase this is suppressed significantly to be able to drive the system towards magnetic ordering. Consistent with this, ARPES measurement and DFT calculations show that the hole bands, present at the Γ point, sink below the Fermi energy in the cT state[87, 108]. Consequently, the nesting condition is lost and this leads to the quenching of the Fe moment and magnetism[87, 108]. Changes in the electronic structure and Fe moment are gradual with increasing pressure, i.e. system going towards cT phase with decreasing c .

Additionally, the quenching of the Fe moment in the cT phase is also associated with the formation of the interlayer As–As bonds along c , which decreases in size. This indicates a strong magnetoelastic coupling of the As–As distance to the magnetic moment size (i.e. to the magnetism). The magnetoelastic coupling is present even in the ambient-pressure tetragonal (uncollapsed) phase as suggested by density functional theory (DFT) calculations[105] and the measurements of phonon[109, 110]. The anomalies in phonon are observed in T CaFe_2As_2 compound, unlike BaFe_2As_2 , and are associated with the compound's proximity to the cT phase[110]. The nature of spin dynamics in the two extremes T and cT phase is known and the DFT calculation suggested a correlation between the decrease in Fe moment and c [105]. Hence, it is interesting to map the evolution of spin dynamics with decreasing c in the T phase and draw correlation between the magnetoelastic coupling and spin dynamics.

For these measurements, $\text{Ca}(\text{Fe}_{1-x}\text{Co}_x)_2\text{As}_2$ compounds are perfect, because $\text{Ca}(\text{Fe}_{1-x}\text{Co}_x)_2\text{As}_2$ annealed at 400 °C show monotonic decrease in c for $x \geq 0.029$, as shown in Fig. 3.11. The decrease in c lattice parameter is $\approx 2.5\%$ for $\text{Ca}(\text{Fe}_{1-x}\text{Co}_x)_2\text{As}_2$ $x = 0.029$ and higher for higher Co concentration[111]. This allows the study of spin dynamics evolution towards the cT phase at ambi-

ent pressure by changing the temperature only. Also, this is amiable for inelastic neutron scattering measurement as the disadvantages of the pressure experiment, for example higher background and limitations in the sample volume introduced by a pressure cell, are absent.

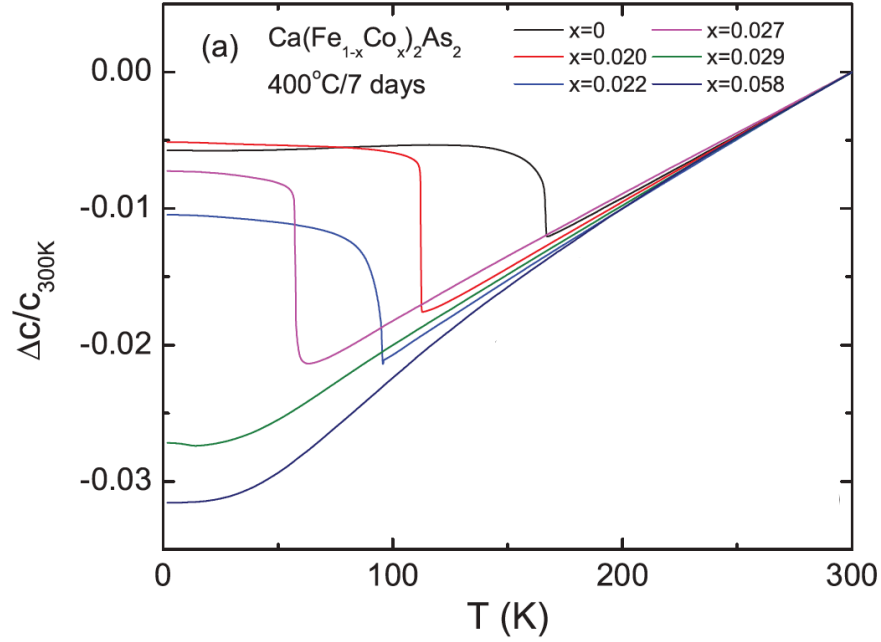


Figure 3.11 Temperature dependence of c-axis dilation for $\text{Ca}(\text{Fe}_{1-x}\text{Co}_x)_2\text{As}_2$ annealed at 400 °C. The thermal expansion measurement was performed using a capacitive dilatometer. The figure is reproduced from Ref. [111].

3.1.4.1 Magnetoelastic coupling in 122 compounds

The above discussed magnetoelastic coupling, i.e. As–As (X – X) to magnetism, is not unique to AFe_2As_2 compounds, but are ubiquitous in 122 system. There are plentiful examples of $\text{A}/\text{RTM}_2\text{X}_2$ compounds exhibiting broad spectrum of magnetic ground states that can be tied to the presence or absence of interlayer X – X bond[112, 113]. Figure 3.12 lists some examples of ATM_2X_2 , with TM = Mn, Fe, Co, Ni and X = As and P, that exhibit different magnetic ground states corresponding to the interlayer X – X distance. For example, $\text{A}/\text{RCo}_2\text{P}_2$ exhibits AFM ground states in presence of the interlayer P–P bond and no long-range AFM order/FM ground states/no Co moment in absence of the P–P bond[113].

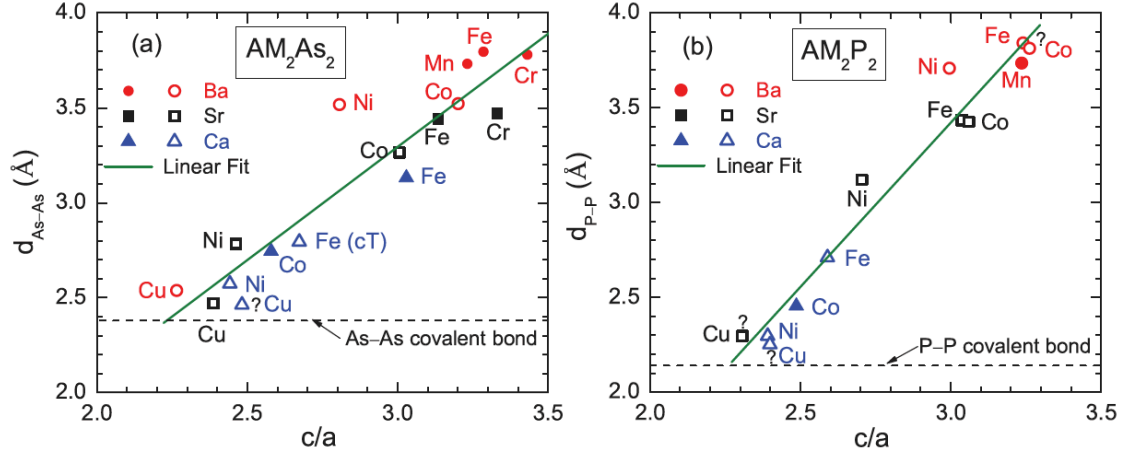


Figure 3.12 (a) Interlayer As-As distance and (b) interlayer P-P distance vs c/a for ATM_2X_2 . The filled symbols are for the compounds with magnetic ground state. The horizontal dashed line represents As-As/P-P single-covalent bond distance. The figure is reproduced from Ref. [114].

The magnetism has been discussed in terms of the oxidation state of TM corresponding to the change in the valence state of X ($=$ As and P) from -3 in the uncollapsed state to -2 due to dimerization in the cT state. This simple rule does explain the absence of magnetism in $SrCu_2As_2$ compound[114], which is in cT state. The valence state for Sr and As_2 are $+2$ and -4 , respectively, indicating that Cu has $+1$ oxidation state, i.e. d^{10} electronic configuration. This means Cu d bands are completely filled, thus bears no magnetism. On the other hand, it is not applicable to all 122 compounds, for example $BaCu_2Sb_2$ where no interlayer bonding between Sb-Sb is possible[114], and is also not sufficient to explain the magnetism in many ATM_2As_2 systems, for example AFe_2As_2 compounds where the details of the electronic structures at the Fermi surface governs the magnetism[26]. However, this serves as a basic guideline for defining magnetism in 122 compounds and highlights the underlying interesting magnetoelastic correlation.

3.2 ATM_2As_2 : TM = Co

ACo_2As_2 compounds are closely related to AFe_2As_2 superconductor family and are end members of extensively studied $A(Fe_{1-x}Co_x)_2As_2$ series. In addition, they are variant of ACo_2P_2 compounds,

which exhibits the above discussed magnetoelastic coupling. In ACo_2P_2 compounds, $CaCo_2P_2$ is in cT phase (i.e. P–P bond present) and exhibits A-type AFM ground state and the T $SrCo_2P_2$ (i.e. no P–P bonding) does not show magnetic ordering. So, the motivation of studying ACo_2As_2 compounds is twofold, understanding the SC and magnetoelastic coupling in 122 system. Moreover, spin fluctuations are crucial part of SC and their complete understanding, not only in the superconducting region of the phase diagram of AFe_2As_2 compounds but also on the either sides, is necessary. In addition, the nature of spin fluctuations in A/RCo_2X_2 systems that exhibit broad spectrum of the magnetoelastic coupling is yet to be explored.

3.2.1 Crystal structure

Similar to AFe_2As_2 compounds, they are metals and crystallizes into the body-centered tetragonal structure ($I4/mmm$ crystal symmetry)[115–117], but $CaCo_2As_2$ exhibits slight variation. $CaCo_2As_2$ is in cT phase (small c and c/a ratio in Table 3.3) at 300 K and ambient pressure. Unlike AFe_2As_2 , they remain tetragonal down to low temperature ≈ 5 K[115] and do not undergo structural transition to orthorhombic or any other structural symmetry. Lattice parameters of these compounds at 300 K and ambient pressure are listed in the Table. 3.3.

Table 3.3 Lattice parameters of ACo_2As_2 compounds at 300 K. The table is reproduced from Ref. [115].

	$a = b$ (\AA)	c (meV \AA)	c/a	d_{As-As}
$CaCo_2As_2$	3.9831(2)	10.2732(6)	2.5792(3)	2.745(4)
$BaCo_2As_2$	3.958(5)	12.67(2)	3.201(9)	3.52
$SrCo_2As_2$	3.9466(2)	11.773(1)	2.9831(4)	3.327(7)

3.2.2 Magnetism

As ACo_2As_2 compounds are metals, the magnetism can be expected to arise from the itinerant electrons. However, the nesting condition that drives the SDW ordering in AFe_2As_2 compounds is absent. ARPES measurements in these compounds show electron pockets at $X = \mathbf{Q} = (\frac{1}{2}, \frac{1}{2})_T$ position, but without any hole pockets at $\Gamma = \mathbf{Q} = (0, 0)$ [115, 118]. In addition, both the ARPES

measurement and band structure calculations show large density of states at Fermi energy (E_f), mainly from Co d bands, as shown in Figs. 3.13 (a)–(c) [115–117, 119]. The large density of states $[D(E_f)]$ at E_f in these compounds imply that Stoner criterion $[D(E_f)I > 1, I = 0.8 \text{ eV per spin for } 3d \text{ elements}]$ is strongly exceeded, indicating the instability towards ferromagnetism[115–117]. However, the susceptibility measurement on these compounds show no signature of long-range magnetic ordering for both BaCo_2As_2 and SrCo_2As_2 compounds, as shown in Figs. 3.13 (d)–(e). Moreover, BaCo_2As_2 displays paramagnetic behavior and SrCo_2As_2 shows a broad maximum without any clear signature of transition. On the other hand, susceptibility of $\text{CaCo}_{1.86}\text{As}_2$ compound in Fig. 3.13 (f) show peak at $T_N \approx 52 \text{ K}$, which is a signature of an AFM transition. The susceptibility decreases below T_N in the case where magnetic field is applied along \mathbf{c} direction inferring that Co moments are aligned along the c axis direction. $\text{CaCo}_{1.86}\text{As}_2$ compounds described in the figure was found to have vacancy of $\approx 7\%$ at Co-site, but the structural and magnetic properties are almost similar to CaCo_2As_2 .

3.2.3 Spin fluctuations in SrCo_2As_2 : A big surprise

Even though ACo_2As_2 compounds hint proximity towards ferromagnetism, spin fluctuations measured using inelastic neutron scattering in SrCo_2As_2 reveal very different nature. Surprisingly, the stripe-type spin fluctuations similar to AFe_2As_2 compounds are observed[8]. The stripe spin fluctuations are steeply dispersive and quasi-2D, as shown in Fig. 3.14, and are similar in many aspects with the diffusive spin fluctuations of AFe_2As_2 compounds. The diffusive spin fluctuations are considered important for SC in AFe_2As_2 compounds, therefore indicating a possibility of SC in ACo_2As_2 . On the other hand, the anisotropy of spin fluctuations in SrCo_2As_2 is different than $\text{A}(\text{Fe}_{1-x}\text{TM}_x)_2\text{As}_2$ compounds. Spin fluctuations are elongated along the longitudinal direction in SrCo_2As_2 , unlike transverse elongation observed in $\text{A}(\text{Fe}_{1-x}\text{Co}_x)_2\text{As}_2$. This anisotropy suggest that the nearest-neighbor interactions of spin in SrCo_2As_2 compound is ferromagnetic (FM), which is AFM in AFe_2As_2 compounds. Even though the presence of diffusive stripe-type spin fluctuations suggest the possibility of the spin-fluctuations mediated unconventional SC in these compounds,

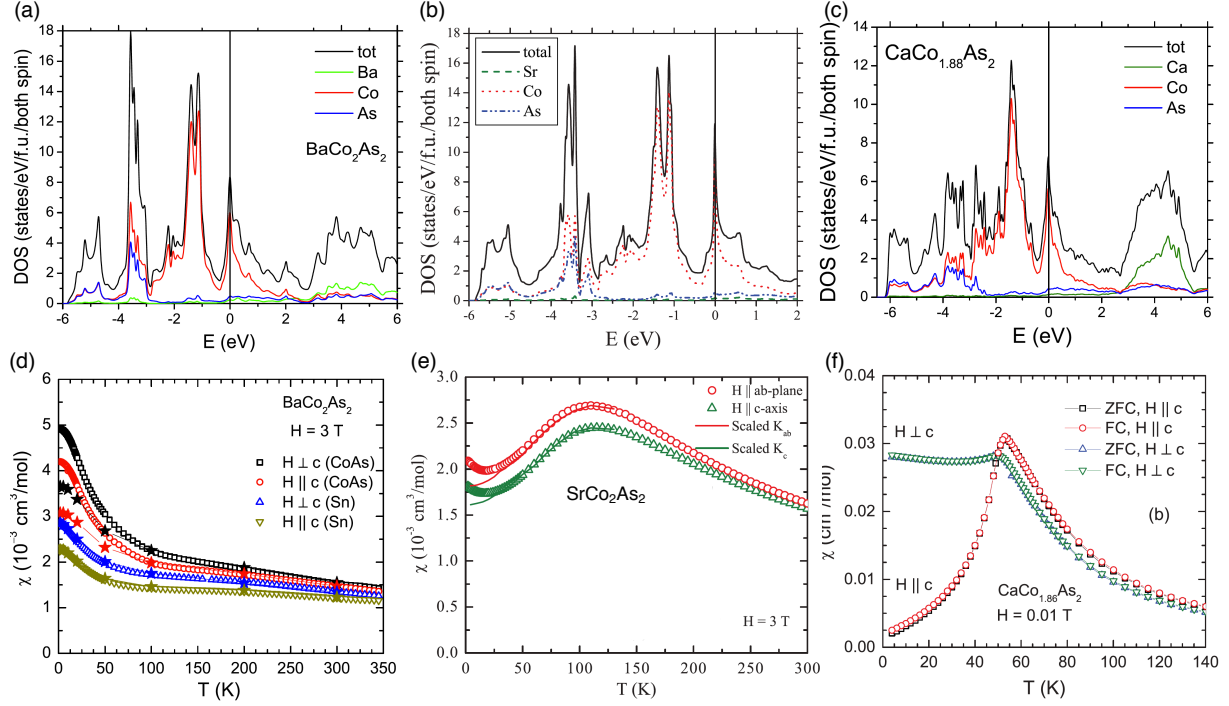


Figure 3.13 (a), (b), (c) Band structure calculations showing large density of states at Fermi energy ($E = 0$), mainly from Co d bands, in BaCo₂As₂, SrCo₂As₂ and CaCo_{1.86}As₂ respectively. (d), (e), (f) Susceptibility (χ) vs temperature (T) for BaCo₂As₂, SrCo₂As₂ and CaCo_{1.86}As₂ respectively. In (d), for BaCo₂As₂ data are from measurements performed on both Sn-flux as well as CoAs-flux grown samples. For all three samples, the results are from the measurements where the external field was applied along both parallel and perpendicular to the c direction. The figure is reproduced from Refs. [115, 116, 119].

the FM nearest-neighbor interactions and close competition of FM fluctuations[8] also indicate a possibility of triplet SC (p-wave) or the suppression of the s-wave SC in SrCo₂As₂ compounds.

The low-energy spin fluctuations are suppressed in Ba(Fe_{1-x}TM_x)₂As₂ (TM = Co, Ni) compounds towards overdoped region and are completely absent in the non-superconducting region of higher Co/Ni concentration[3, 92]. This should be the case for all Co/Ni substituted AFe₂As₂ compounds. In addition, the anisotropy along the transverse direction increases with increasing Co/Ni doping in AFe₂As₂ compounds, in the region of $x < 0.15$ for Ba(Fe_{1-x}TM_x)₂As₂[3, 91].

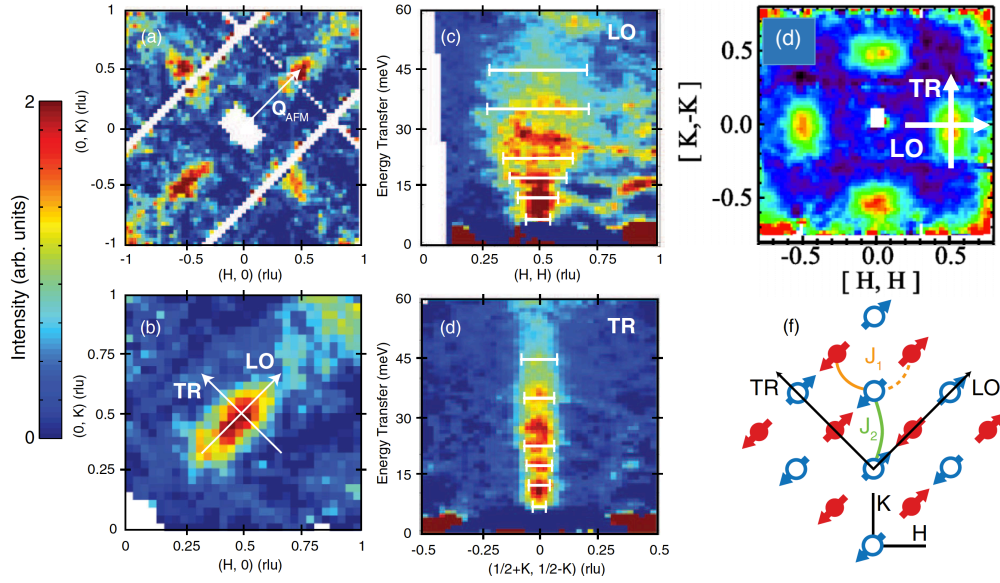


Figure 3.14 (a), (b), (c) and (d) Data of inelastic neutron scattering measurement at $T = 5K$ with incident energy $E_i = 75$ meV. Figures in (a), (b) show spin fluctuations centered at $\mathbf{Q}_{\text{stripe}} = (1/2, 1/2)$ and anisotropic along the longitudinal (LO) and transverse (TR) directions. (c) and (d) Energy dependence of the spin fluctuations in the LO and TR directions, respectively. The white horizontal bars in (c) and (d) are FWHM of a Gaussian fits to constant energy cuts produced from these figures. (e) Constant-energy slice of CaFe_2As_2 compound showing 90° rotated anisotropy in comparison to SrCo_2As_2 . (f) Schematics of the arrangement of spins in stripe-type AFM order and shows the nearest-neighbor (J_1) and next-nearest-neighbor (J_2) exchange interactions. The solid line between nearest-neighbor along the TR direction illustrates FM nearest-neighbor interaction and the dashed line illustrates the frustrated nearest-neighbor interaction along the LO direction. The figure is reproduced from Refs. [8, 107].

Therefore, the appearance of the stripe-type spin fluctuations in the end compound SrCo_2As_2 , but, with completely different anisotropy is a puzzle to be solved.

3.3 ATM_2As_2 : TM = Mn

Among three members of AMn_2As_2 compounds, only BaMn_2As_2 is isostructural to AFe_2As_2 compounds and belongs to ThCr_2Si_2 structural class. So, I am going to discuss BaMn_2As_2 only in this section. The motivation of study of BaMn_2As_2 arises from the fact that it shares properties of both the high-temperature iron-arsenide and cuprate superconductors[9]. Therefore, it is a potential compound to link these two classes of superconductors. In addition, there are other interesting properties observed in other Mn based compounds, for example colossal magnetoresistance in LaMnO_3 [120].

3.3.1 Crystal structure and insulating ground state

As mentioned above, the BaMn_2As_2 crystallizes into the body-centered-tetragonal ThCr_2Si_2 structure, similar to AFe_2As_2 compounds[9]. It remains tetragonal down to low temperature $T = 10$ K[121] without any sign of structural transition and the lattice parameters at 300 K are $a = b = 4.168(4)$ Å and $c = 13.473(3)$ Å[43].

Unlike AFe_2As_2 compounds, it is an insulator as the resistivity is found to increase with decreasing temperature, at least below ≈ 100 K for both MnAs and Sn-flux grown sample[44, 121], and is of order of 10^4 Ωcm at $T \approx 10$ K[44, 121, 122]. The observed metallic behavior at $T > 100$ K is different for differently grown samples and is even absent in the Sn-flux grown sample reported in Ref. [122], implying that the variations in the impurities/defects with the different growth procedure could be the factor. In addition, both the resistivity and optical spectroscopy measurement suggests the band-gap (i.e. energy gap between valence and conduction band) of < 1 eV, which indicates that BaMn_2As_2 is a semiconductor. Typical value of the band gap for semiconductors is < 2 eV[13, p. 562], for example silicon possesses band-gap of 1.12 eV at 300 K[13, p. 566]. Moreover, it is in order of 5.5 eV for insulator like diamond[13, p. 564]. The electronic linear specific

heat coefficient $\gamma = 0$ is obtained from the specific heat measurement and is consistent with the insulating ground state of the compound.

3.3.1.1 Mott-Hund insulator

The insulating ground state of BaMn_2As_2 cannot be described by the conventional band theory (which neglects the electron-electron interactions) because it implies that BaMn_2As_2 with d^5 electronic configuration, i.e. partially-filled d orbitals, should be a metal, but is an insulator. The dynamical mean-field theory calculations reproduced the charge gap similar to the optical measurement in the presence of the electronic correlations parametrized by Hubbard $U = 8$ eV (U = coulomb energy as a consequence of coulomb repulsion between two electrons occupying the same orbital) and Hund's coupling $J_H = 0.9$ eV[122]. This suggests that the significant electron-electron correlation is present in BaMn_2As_2 and leads to the localization of the electrons. This is the definition of a Mott insulator[123, p. 152,155]. Furthermore, as the insulating state is promoted by the Hund's coupling, it is classified as Mott-Hund insulator. For the half-filled bands, like d^5 of Mn in BaMn_2As_2 , the Hund's coupling increases the effective U facilitating the insulating state[124].

3.3.2 Ferromagnetic order in $\text{Ba}_{1-x}\text{K}_x\text{Mn}_2\text{As}_2$

Interestingly, for K concentration $x \geq 0.16$, $\text{Ba}_{1-x}\text{K}_x\text{Mn}_2\text{As}_2$ shows ferromagnetic order that coexist with the G-type AFM order[70]. The significantly larger enhancement of the magnetization for an applied field along the **ab** plane in comparison to that along the **c** direction implies that the FM ordered moment is aligned in the **ab** plane[70, 125]. The origin of this FM order from the canting of the Mn moment has been proposed, but experimental evidences so far oppose it[70]. Recent x-ray magnetic circular dichroism experiment, on $\text{Ba}_{1-x}\text{K}_x\text{Mn}_2\text{As}_2$ $x = 0.040$, which provides element-specific information of the magnetism, supports the picture that ferromagnetism arises from the polarization of the doped holes on the As $4p$ conduction band[71]. Furthermore, the measurement provides the upper limit of $0.02 \mu_B$ for FM order arising due to canting of Mn moment. The value is much smaller than $0.45 \mu_B$ obtained from the magnetization measurement[70].

CHAPTER 4 EXPERIMENTAL TECHNIQUE

4.1 Direct and Reciprocal space

The description of a crystal structure starts with the Bravais lattice, which is the periodic array in which the basis of a crystal is arranged. The basis is an atom, group of atoms or molecules, etc., that repeats themselves in a crystal. Thus, a crystal structure consists of a basis at every lattice point.

In three dimensions, the Bravais lattice is described by three translation vectors \mathbf{a}_1 , \mathbf{a}_2 and \mathbf{a}_3 and all the lattice points are defined by the vector[13, p. 64]

$$\mathbf{R} = n\mathbf{a}_1 + m\mathbf{a}_2 + l\mathbf{a}_3 \quad (4.1)$$

Here, n , m and l are integers, and \mathbf{a}_1 , \mathbf{a}_2 and \mathbf{a}_3 are primitive vectors (or equivalently direct lattice vectors). The choice of the primitive vectors is not unique for a Bravais lattice. Figure 4.1 shows a three-dimensional simple cubic Bravais lattice.

The crystal system can also be defined using the reciprocal lattice, which is the Fourier transform of the direct lattice. Figure 4.2 shows a one-dimensional (1-D) direct lattice chain with the primitive vector $\mathbf{a}_1 = a\hat{x}$ and the corresponding reciprocal lattice chain with the primitive vector $\mathbf{b}_1 = \frac{2\pi}{a}\hat{x}$. The figure shows that a 1-D direct lattice chain with a period “ a ” can be defined by the Fourier (reciprocal) space of another 1-D lattice chain, but with the period $\frac{2\pi}{a}$.

The arrangement of the lattice points in the direct lattice of period “ a ” can be defined by a function

$$g(x) = \sum_{n=-\infty}^{\infty} \delta(x - na) \quad (4.2)$$

Here, n is an integer and $g(x)$ vanishes everywhere except at $x = na$. The function describing the corresponding Fourier (reciprocal) space lattice can be obtained from the Fourier transform of

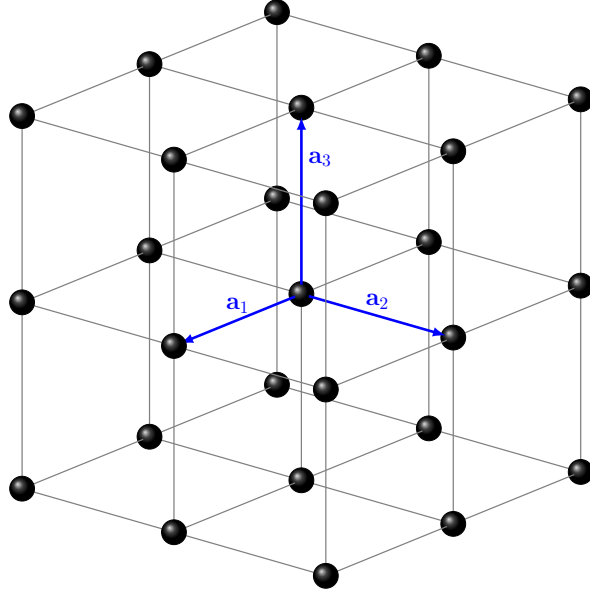


Figure 4.1 A simple cubic three-dimensional Bravais lattice with three mutually perpendicular primitive vectors of equal magnitude. Each cubes in the figure is a primitive unit cell with the side a . The figure is reproduced from Ref. [13, p. 65].

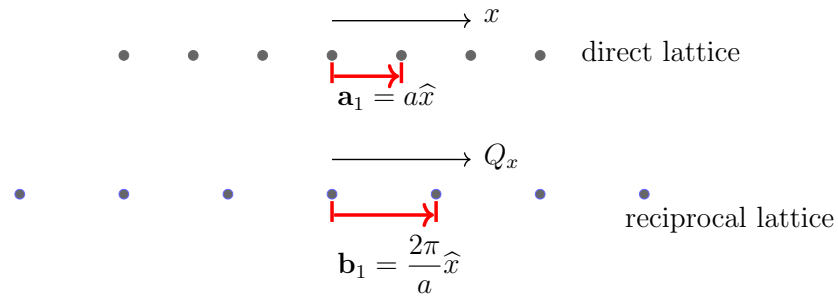


Figure 4.2 One-dimensional direct and reciprocal lattice with periodicity a and $\frac{2\pi}{a}$.

Eq. (4.2),

$$f(Q_x) = \int_{-\infty}^{\infty} e^{iQ_x x} \sum_{n=-\infty}^{\infty} \delta(x - na) dx \quad (4.3)$$

which gives

$$f(Q_x) = \frac{2\pi}{a} \sum_{m=-\infty}^{\infty} \delta(Q_x - m \frac{2\pi}{a}) \quad (4.4)$$

Here, m is an integer and $f(Q_x)$ vanishes except at $Q_x = m \frac{2\pi}{a}$. This suggests that the arrangement of the lattice points in the Fourier-space is periodic with a period which is inversely proportional to the period in real space.

The above relationships can be expanded to the three-dimensional lattice. For example, for a simple Bravais cubic lattice (direct lattice) with sides “ a ”, there corresponds a reciprocal lattice with the primitive vectors \mathbf{b}_1 , \mathbf{b}_2 and \mathbf{b}_3 of magnitude $2\pi/a$.

The relationship between the primitive reciprocal lattice vectors \mathbf{b}_1 , \mathbf{b}_2 and \mathbf{b}_3 and the primitive direct lattice vectors \mathbf{a}_1 , \mathbf{a}_2 and \mathbf{a}_3 is given by

$$\mathbf{b}_1 = 2\pi \frac{\mathbf{a}_2 \times \mathbf{a}_3}{\mathbf{a}_1 \cdot (\mathbf{a}_2 \times \mathbf{a}_3)}, \quad \mathbf{b}_2 = 2\pi \frac{\mathbf{a}_3 \times \mathbf{a}_1}{\mathbf{a}_1 \cdot (\mathbf{a}_2 \times \mathbf{a}_3)}, \quad \mathbf{b}_3 = 2\pi \frac{\mathbf{a}_1 \times \mathbf{a}_2}{\mathbf{a}_1 \cdot (\mathbf{a}_2 \times \mathbf{a}_3)} \quad (4.5)$$

with $\mathbf{b}_i \cdot \mathbf{a}_j = 2\pi \delta_{ij}$. The reciprocal lattice points are defined by a vector,

$$\mathbf{G} = h\mathbf{b}_1 + k\mathbf{b}_2 + l\mathbf{b}_3 \quad (4.6)$$

Here, \mathbf{G} is the reciprocal lattice vector and is often represented as $\mathbf{G} = (h, k, l)$ in reciprocal length units (r.l.u.).

The reciprocal lattice vector is related to the set of parallel and equidistant planes in the direct lattice, where (h, k, l) are the Miller indices[13, p. 91] of the direct lattice planes. These planes intersect the unit cell axis in the real space at $1/h, 1/k, 1/l$. In Ref. [13, p. 90], it is discussed that for a family of lattice planes separated by the distance d in a direct space, there are reciprocal lattice vectors perpendicular to these planes. The shortest length of these vectors is $2\pi/d$. Therefore, a set of direct lattice planes can be represented by the lattice points in the reciprocal space. This picture simplifies the visualization of the scattering process by using the Ewald’s sphere in reciprocal

space, which is illustrated in Figs. 4.4 and 4.5. In addition, the Bragg spots observed in a diffraction experiment can be represented by (h, k, l) points in a reciprocal space, from which the arrangement of the atoms in real space can be extracted.

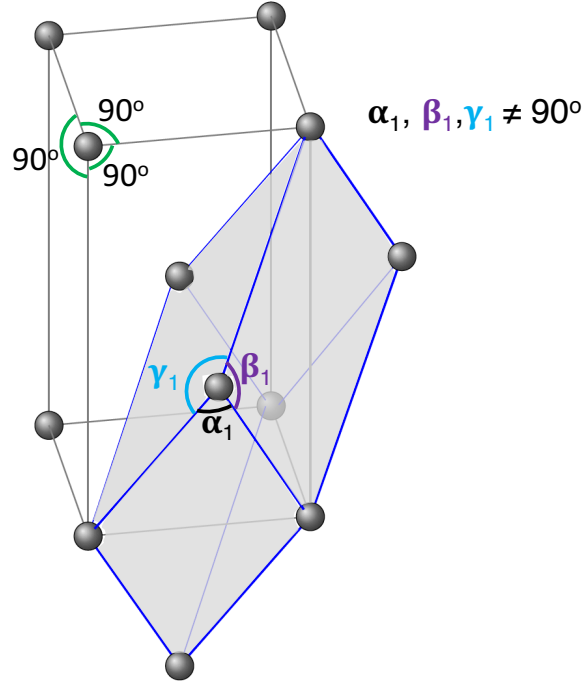


Figure 4.3 A Conventional (gray edges) and a smaller primitive unit cell (shaded region with blue edges) of a body-centered tetragonal Bravais lattice. The figure is reproduced from Ref. [13, p. 73].

Instead of describing the crystal structure by the smallest-volume primitive unit cell, they are often described by a conventional unit cell. The symmetry of the lattice is easier to visualize with a conventional unit cell. This is illustrated by Fig. 4.3, which shows that the four-fold rotational symmetry present in the conventional unit cell is not apparent in the primitive unit cell.

The 122 compounds in this thesis also possess a body-centered tetragonal structure and a conventional unit cell is used to represent the crystal structure. The conventional unit cell is described by three orthogonal non-primitive lattice vectors $\mathbf{a} = a\hat{\mathbf{i}}$, $\mathbf{b} = b\hat{\mathbf{j}}$, and $\mathbf{c} = c\hat{\mathbf{k}}$, where a , b and c are lattice constants. The corresponding reciprocal lattice vectors, using Eq. (4.5), are

$\mathbf{a}^* = \frac{2\pi}{a}\hat{\mathbf{i}}$, $\mathbf{b}^* = \frac{2\pi}{b}\hat{\mathbf{j}}$, and $\mathbf{c}^* = \frac{2\pi}{c}\hat{\mathbf{k}}$. The reciprocal lattice vectors discussed in this thesis are then defined as $\mathbf{Q} = (H, K, L) = H\mathbf{a}^* + K\mathbf{b}^* + L\mathbf{c}^*$.

4.2 A general description of scattering

Scattering is a well-known technique used to explore the microscopic properties of a condensed matter system. The common probes are electrons, x-ray and neutrons, which have wavelengths comparable to the inter-atomic distances of a condensed matter system ($\approx 1 \text{ \AA}$). The scattering experiments are governed by the laws of momentum and energy conservation:

$$\mathbf{Q} = \mathbf{k}_f - \mathbf{k}_i \quad (4.7)$$

$$E = \hbar\omega = E_i - E_f \quad (4.8)$$

Here, \mathbf{k}_i and \mathbf{k}_f are the wavevectors of the incident and scattered particle, respectively, E_i and E_f are the corresponding energies. \mathbf{Q} is known as the scattering vector, and $\hbar\mathbf{Q}$ and E are momentum and energy transferred to the sample, respectively.

Basically, the scattering process can be classified into the two categories, elastic and inelastic scattering.

4.2.1 Elastic Scattering

In case of elastic scattering, no energy is transferred or absorbed from the scattering system (crystal), $|\mathbf{k}_f| = |\mathbf{k}_i| = k$. For elastic scattering from a periodic crystal, the scattering vector \mathbf{Q} is equal to the reciprocal-lattice vector \mathbf{G} , then the Eq. (4.7) becomes

$$\mathbf{G} = \mathbf{Q} = \mathbf{k}_f - \mathbf{k}_i \quad (4.9)$$

Using the cosine law and Fig. 4.4, the above equation becomes

$$|\mathbf{G}| = |\mathbf{Q}| = 2k \sin \theta \quad (4.10)$$

Substituting, $|\mathbf{G}| = 2\pi/d$ [13, p. 90], where d is the interplanar spacing and $k = 2\pi/\lambda$, we get

$$\lambda = 2d \sin \theta \quad (4.11)$$

This is the famous Bragg's law. Elastic scattering is illustrated in Fig. 4.4. The diffraction peaks corresponding to the reciprocal lattice vectors \mathbf{G} will be observed if the reciprocal lattice points connected by this vector lie on the circumference of the circle. In three-dimensions, the Ewald's sphere illustrates the diffraction process.

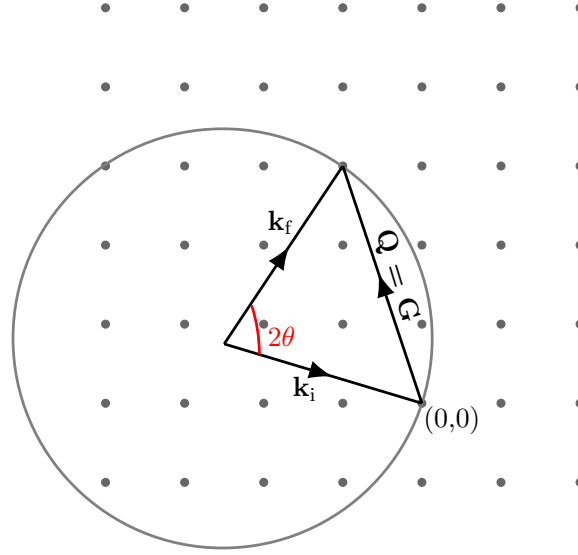


Figure 4.4 Vector diagram of an elastic scattering with an Ewald circle of radius $k = 2\pi/\lambda$. The dots represent reciprocal-lattice points in a two-dimensional reciprocal space. The figure is created using the figure in Ref. [126, p. 14] as a guideline.

4.2.2 Inelastic Scattering

In the case of inelastic scattering, energy is either transferred to or absorbed from the scattering system (crystal) by the scattered particle or wave, so $|\mathbf{k}_f| \neq |\mathbf{k}_i|$. The energy lost or gained by the incident particle or wave is illustrated in Fig. 4.5, and is equivalent to the energy gained or lost by the scattering system. Additionally, the energy loss and gain by the incident particle or wave is associated with the creation and annihilation of an excitation in the crystal.

Both elastic and inelastic scattering techniques have been employed to investigate various microscopic properties of the condensed-matter system. Elastic scattering provides the structural information associated with both the chemical and magnetic ordering and inelastic scattering stud-

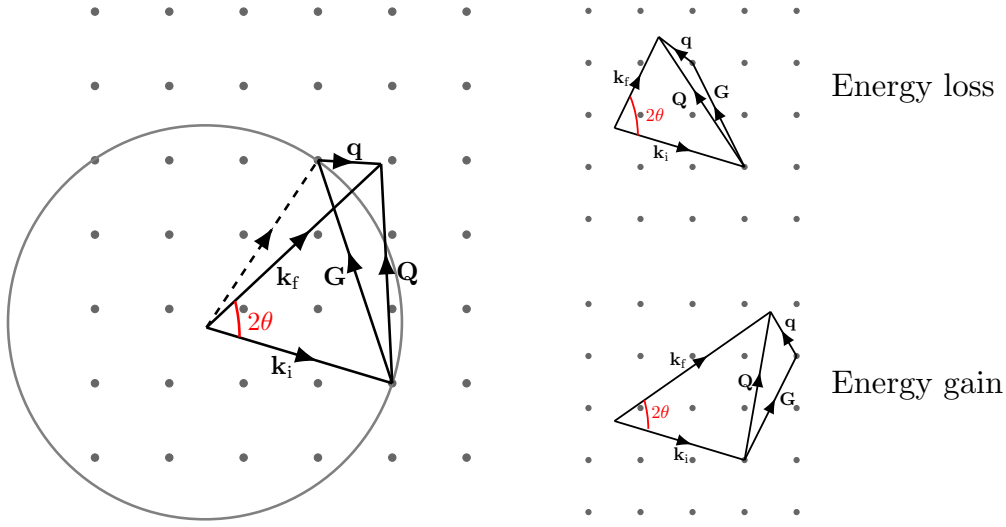


Figure 4.5 Vector diagram of an inelastic scattering showing the cases of the energy gain and loss by an incident particle. Here, $\mathbf{Q} = \mathbf{G} + \mathbf{q}$, where \mathbf{G} is the reciprocal lattice vector and \mathbf{q} is a vector within the first Brillouin zone. Brillouin zone is discussed in Ref. [13, p. 89] and physical quantities like phonon, electron and magnon dispersions repeat over each Brillouin zone[126, p. 32]. The figure is created using the figure in Ref. [126, p. 14 and 15] as a guideline.

ies the dynamics (such as phonons and magnons) of the scattering system. Neutrons are one of the extensively used probes for study of the microscopic properties, so the following sections discussed the neutron scattering in details .

4.3 Neutron Scattering

The following are the basic properties, as discussed in Ref. [127], which make neutrons a useful probe:

- The wave-particle duality of a neutron with a de Broglie wavelength ($\lambda = \frac{h}{p}$, where h = Planck constant and p is the momentum of the neutron) on the order of the inter-atomic spacing of a solid is exploited to obtain microscopic information.
- The charge less nature of the neutron allows for deep penetration through many materials making them a bulk probe.
- Energy of a neutron with a wavelength of an order of 1\AA is in the range of meV. It is in the same order of many excitations of a condensed matter system. This allows easily approachable energy resolution of $\approx 10\%$, in contrast to the $\approx 10^{-5}\%$ of x-ray. Consequently, the information about a system's dynamics can be achieved by measuring the energy lost or gained by neutrons during a scattering process.
- The $\frac{1}{2}$ spin of a neutron means that it has a magnetic moment which will interact with the magnetic moment of a condensed matter system via dipole interactions. This is the vital property that makes it an ideal probe to study a magnetism.

The above mentioned properties mean that neutron scattering is a very powerful technique for exploring the microscopic properties of a magnetic system. Despite these advantages, there are also some limitations associated with this technique, for example, a sample with a large mass is required because of the weak interactions and low flux. Some basic properties of the neutron are listed in Table 4.1:

Table 4.1 Basic properties of neutron. In the table, $\mu_N = \frac{e\hbar}{2m_p}$ is the nuclear magneton. e and m_p are the charge and rest mass of the proton, respectively.

mass (m)	$1.675 \times 10^{-27} \text{ kg}$
charge	0
spin	$\frac{1}{2}$
magnetic dipole moment (μ_n)	$-1.913 \mu_N$

A scattering cross section is the quantification of the interaction of a neutron with the scattering system. In any neutron scattering experiment, an incident beam of neutrons, defined by the wavevector \mathbf{k} and flux Φ (number of neutrons per unit time through per unit area perpendicular to the beam direction), interacts with the scattering system and is scattered in many directions. These directions are specified by the spherical polar angles (θ and ϕ) as shown in Fig. 4.6. Detectors, which subtend a solid angle $d\Omega$ at the sample position, measure the neutrons scattered along the specific polar directions θ and ϕ . The rate at which neutron with an energy between E and $E + dE$ arrives at the detector located at (θ, ϕ) is known as the partial differential cross-section:

$$\frac{d^2\sigma}{d\Omega dE} = \frac{\left(\begin{array}{c} \text{number of neutrons scattered per second into a small solid angle } d\Omega \\ \text{in the direction } \theta, \phi \text{ with the final energy between } E \text{ and } E + dE \end{array} \right)}{\Phi d\Omega dE} \quad (4.12)$$

A unit analysis of the above definition gives area as the dimension of σ . The detector which counts all the neutrons irrespective of their energy measures a differential scattering cross section, which is defined as

$$\frac{d\sigma}{d\Omega} = \frac{\text{number of neutrons scattered per second into a small solid angle } d\Omega \text{ in the direction } \theta, \phi}{\Phi d\Omega} \quad (4.13)$$

The differential cross-section and the partial differential cross-section are related by

$$\frac{d\sigma}{d\Omega} = \int_0^\infty \left(\frac{d^2\sigma}{d\Omega dE} \right) dE \quad (4.14)$$

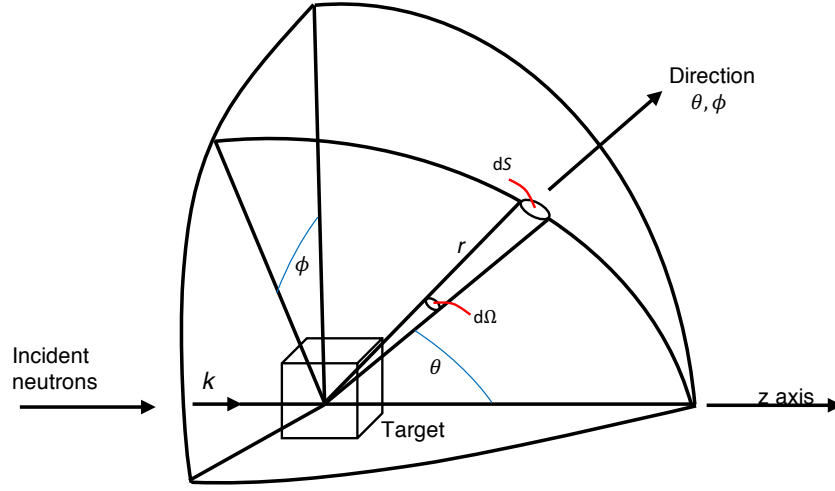


Figure 4.6 Geometry for scattering experiment. The figure is reproduced from Ref. [127, p. 5]

Finally, the integral of the differential scattering cross-section in terms of the solid angle $d\Omega$ gives the total scattering cross-section

$$\sigma = \int \left(\frac{d\sigma}{d\Omega} \right) d\Omega \quad (4.15)$$

which is the total number of neutrons scattered per second over all angles per unit incident flux.

The neutrons can interact with a nucleus via the strong force and the magnetic moments via the dipole-dipole interaction. The former is called the nuclear scattering and the latter is magnetic scattering. Here, I will discuss the theoretical aspects of these scattering process by starting with a simple model of scattering from a single fixed nucleus and eventually scattering from a crystal, both the nuclear and magnetic scattering. In doing so, I will follow Ref. [127] and Ref. [126], so please refer to them for the mathematical details.

4.3.1 Nuclear scattering

For neutron scattering by a fixed nucleus, the nuclear forces responsible for scattering is on the order of 10^{-14} to 10^{-15} m and much smaller than the wavelength of thermal neutrons, which is on the order of 10^{-10} m. This implies that scattering is isotropic and the scattered wave is spherically

symmetric[127, p. 7]. The wavefunction corresponding to the incident neutrons can be represented by a plane wave,

$$\psi_i = e^{ikz} \quad (4.16)$$

Here, z is the direction of the incident beam with wavevector k . Similarly, the wavefunction for the scattered neutron at a point r is a spherically symmetric wave represented as

$$\psi_f = \frac{b}{r} e^{ikr} \quad (4.17)$$

Here, b is the scattering length and is the characteristics of the scattering nucleus. It is different among different atoms and between isotopes of the same atoms. Furthermore, it is a complex quantity and the imaginary part corresponds to absorption of neutron by the scattering system.

Next, v is the velocity of incident neutrons and it is considered to be same after scattering. The number of neutrons scattered through area dS per unit time is $v dS |\psi_f|^2 = v b^2 d\Omega$ and flux of the incident neutron is $\Phi = v |\psi_i|^2 = v$. Therefore, the cross-section $\frac{d\sigma}{d\Omega}$ corresponding to the above scattering is

$$\frac{d\sigma}{d\Omega} = \frac{v b^2 d\Omega}{\Phi d\Omega} = b^2 \quad (4.18)$$

and the corresponding total scattering is

$$\sigma_{\text{tot}} = 4\pi b^2 \quad (4.19)$$

Scattering from a condensed matter system where the change of the state of both the neutron and scattering system is considered. The corresponding differential scattering cross-section can be obtained using the Fermi's Golden Rule, which gives the partial differential cross-section as

$$\left(\frac{d^2\sigma}{d\Omega dE_f} \right)_{\lambda \rightarrow \lambda'} = \frac{k_f}{k_i} \left(\frac{m}{2\pi\hbar} \right)^2 |\langle k_f \lambda' | V | k_i \lambda \rangle|^2 \delta(E_\lambda - E'_\lambda + E_i - E_f) \quad (4.20)$$

Here, λ and λ' , k_i and k_f , E_i and E_f , and E_λ and E'_λ are the initial and final states of the scattering system, initial and final wavevectors, initial and final energy of the neutron, and initial and final energy of the system, respectively. V is the potential due to a nucleus, and here it is considered to be of short range and described by the form,

$$V_j(x_j) = \frac{2\pi\hbar^2}{m} b_j \delta(x_j) \quad (4.21)$$

for the j th nucleus with scattering length b_j . x_j is the position of the neutron with respect to the j th nucleus as shown in Fig. 4.7

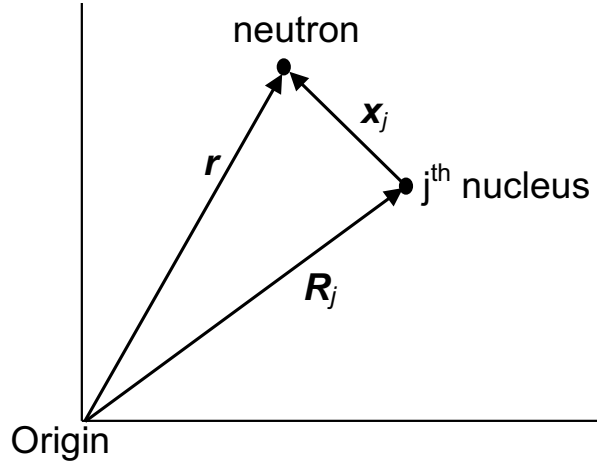


Figure 4.7 Coordinates of nucleus and neutron. The figure is reproduced from Ref. [127, p. 11]

Finally, the basic expression for the partial differential cross-section is obtained in Squires[127, p. 20] as

$$\left(\frac{d^2\sigma}{d\Omega dE_f} \right) = \frac{k_f}{k_i} \frac{1}{2\pi\hbar} \sum_{jj'} b_j b_{j'} \int_{-\infty}^{\infty} \langle e^{-i\mathbf{Q} \cdot \mathbf{R}_{j'}(0)} e^{i\mathbf{Q} \cdot \mathbf{R}_j(t)} \rangle \times e^{-i\omega t} dt \quad (4.22)$$

where, \mathbf{Q} is the momentum transfer and $\hbar\omega = E$ is the energy transfer defined in Eqs. (4.7) and (4.8), and \mathbf{R}_j is the position of the j th nucleus as shown in Fig. 4.7.

The partial differential scattering is the sum of the coherent and incoherent parts as shown below,

$$\frac{d^2\sigma}{d\Omega dE_f} = \left(\frac{d^2\sigma}{d\Omega dE_f} \right)_{\text{coh}} + \left(\frac{d^2\sigma}{d\Omega dE_f} \right)_{\text{inc}} \quad (4.23)$$

The coherent part is equivalent to the case where all the scattering lengths in the system is identical to \bar{b} and the incoherent scattering arises from the random fluctuations of the scattering length at different sites. Common causes of the random fluctuations are the presence of different isotopes at different sites and nucleus with nonzero spin I . The different isotopes have different scattering lengths and similar is the case for the spin $I + 1/2$ and $I - 1/2$ of a nucleus-neutron system. The number of the spin states associated with these two spins of a nucleus-neutron system is different.

The coherent scattering is defined as

$$\left(\frac{d^2\sigma}{d\Omega dE_f} \right)_{\text{coh}} = \frac{\sigma_{\text{coh}}}{4\pi} \frac{k_f}{k_i} \frac{1}{2\pi\hbar} \sum_{jj'} \int_{-\infty}^{\infty} \langle e^{-i\mathbf{Q} \cdot \mathbf{R}_{j'}(0)} e^{i\mathbf{Q} \cdot \mathbf{R}_j(t)} \rangle \times e^{-i\omega t} dt \quad (4.24)$$

$$= N \frac{\sigma_{\text{coh}}}{4\pi} \frac{k_f}{k_i} S(\mathbf{Q}, \omega) \quad (4.25)$$

where, N is the number of the nuclei, $\sigma_{\text{coh}} = 4\pi(\bar{b})^2$, and the $S(\mathbf{Q}, \omega)$ is the scattering function defined as

$$S(\mathbf{Q}, \omega) = \frac{1}{N 2\pi\hbar} \sum_{jj'} \int_{-\infty}^{\infty} \langle e^{-i\mathbf{Q} \cdot \mathbf{R}_{j'}(0)} e^{i\mathbf{Q} \cdot \mathbf{R}_j(t)} \rangle \times e^{-i\omega t} dt \quad (4.26)$$

Eq. (4.24) indicates that the coherent scattering possesses the correlation between the positions of the same nucleus at different times and different nucleus at different times. This gives the interference effects.

Similarly, the incoherent scattering is defined as

$$\left(\frac{d^2\sigma}{d\Omega dE_f} \right)_{\text{inc}} = \frac{\sigma_{\text{inc}}}{4\pi} \frac{k_f}{k_i} \frac{1}{2\pi\hbar} \sum_j \int_{-\infty}^{\infty} \langle e^{-i\mathbf{Q} \cdot \mathbf{R}_j(0)} e^{i\mathbf{Q} \cdot \mathbf{R}_j(t)} \rangle \times e^{-i\omega t} dt \quad (4.27)$$

where, $\sigma_{\text{inc}} = 4\pi(\bar{b}^2 - (\bar{b})^2)$. The incoherent scattering cross-section depends only upon the correlation between the positions of the same nucleus at different times and does not give the interference effect.

4.3.1.1 Coherent elastic nuclear scattering: Bragg's law

Elastic scattering means that $\hbar\omega = 0$ and $k_f = k_i$. Considering the displacement of the atoms from the equilibrium position for a Bravais lattice[127, p. 26], we can see that Eq. (4.24) becomes

$$\left(\frac{d^2\sigma}{d\Omega dE_f}\right)_{\text{coh, el}} = \frac{\sigma_{\text{coh}}}{4\pi} N \frac{(2\pi)^3}{v_o} e^{(-2W)} \delta(\hbar\omega) \sum_{\mathbf{G}} \delta(\mathbf{Q} - \mathbf{G}) \quad (4.28)$$

Here, W is the Debye-Waller factor, which originates due to the thermal fluctuations of the atoms about their equilibrium positions, \mathbf{G} is a reciprocal-lattice vector, and v_o is the unit cell volume. The differential scattering cross-section can be obtained by integrating Eq. (4.28) with respect to E_f :

$$\left(\frac{d\sigma}{d\Omega}\right)_{\text{coh, el}} = \frac{\sigma_{\text{coh}}}{4\pi} N \frac{(2\pi)^3}{v_o} e^{(-2W)} \sum_{\mathbf{G}} \delta(\mathbf{Q} - \mathbf{G}) \quad (4.29)$$

This infers that the scattering occurs only when $\mathbf{Q} - \mathbf{G} = 0$, which is also the condition given in Eq. (4.10), and therefore must be the Bragg's law of diffraction. For the case of a non-Bravais lattice, i.e. a crystal with more than one atom per unit cell, the position of the j th atom in the unit cell is \mathbf{d}_j and the elastic coherent scattering is

$$\left(\frac{d\sigma}{d\Omega}\right)_{\text{coh, el}} = N \frac{(2\pi)^3}{v_o} \sum_{\mathbf{G}} \delta(\mathbf{Q} - \mathbf{G}) |F_N(\mathbf{G})|^2 \quad (4.30)$$

where, $F_N(\mathbf{G}) = \sum_j \bar{b}_j e^{i\mathbf{Q} \cdot \mathbf{d}_j} e^{(-W_j)}$ is the nuclear unit-cell structure factor.

On the other hand, the elastic incoherent scattering is

$$\left(\frac{d\sigma}{d\Omega}\right)_{\text{inc, el}} = \frac{\sigma_{\text{inc}}}{4\pi} N e^{(-2W)} \quad (4.31)$$

The Debye-Waller factor in the equation depends upon the mean-square displacement of the atoms and on Q , therefore it is the sole component with \mathbf{Q} dependence. However, for low Q and low

temperature (T), this gives almost a uniform background and the incoherent scattering contribution decreases monotonically with increasing Q and T .

4.3.2 Magnetic scattering

Magnetic scattering is the scattering of a neutron, which is a spin $\frac{1}{2}$ particle, from the magnetic moment of the scattering system due to the dipole-dipole interaction. The magnetic moment of a scattering system is associated with the spin and orbital angular momentum of its unpaired electrons. The magnetic dipole moment of a neutron is $-\gamma\mu_N\boldsymbol{\sigma}$, where $\gamma = 1.913$, $\mu_N = \frac{e\hbar}{2m_p}$, and $\boldsymbol{\sigma}$ are the gyromagnetic ratio, nuclear magneton, and Pauli spin operator for the neutron, respectively[127, p. 129].

The differential scattering cross-section after considering the spin state of a neutron is given by

$$\left(\frac{d^2\sigma}{d\Omega dE_f}\right)_{\sigma\lambda\rightarrow\sigma'\lambda'} = \frac{k_f}{k_i} \left(\frac{m_n}{2\pi\hbar}\right)^2 |\langle k_f\sigma'\lambda' | V_m | k_i\sigma\lambda \rangle|^2 \delta(E_\lambda - E'_\lambda + E_i - E_f) \quad (4.32)$$

Here, V_m is the potential of a neutron in the magnetic field due to both the spin and orbital angular momentum of an electron and is defined as

$$V_m = -\boldsymbol{\mu}_N \cdot \mathbf{B} = -\gamma\mu_N\boldsymbol{\sigma} \cdot (\mathbf{B}_s + \mathbf{B}_L) \quad (4.33)$$

where, \mathbf{B}_s and \mathbf{B}_L are the magnetic fields corresponding to the spin and orbital momentum of an electron. They are defined as

$$\mathbf{B}_s = -\frac{2\mu_B\mu_0}{4\pi} \text{curl}\left(\frac{\mathbf{s} \times \hat{\mathbf{R}}}{\mathbf{R}^2}\right) \quad (4.34)$$

$$\mathbf{B}_L = -\frac{2\mu_B\mu_0}{4\pi\hbar} \left(\frac{\mathbf{p} \times \hat{\mathbf{R}}}{\mathbf{R}^2}\right) \quad (4.35)$$

where \mathbf{p} is the momentum of an electron.

In Ref. [127], Eq. (4.32) is further evaluated using the Eqs. (4.33), (4.34) and (4.35). Finally, the cross-section for the magnetic scattering is expressed in terms of the time-dependent angular

momentum operators $S_l^\beta(t) = \exp(iHt/\hbar)S_l^\beta \exp(-iHt/\hbar)$, where H is the Hamiltonian of a scattering system. Considering the electrons are localized, the partial differential cross-section for the scattering from a monoatomic magnetic system is

$$\begin{aligned} \frac{d^2\sigma}{d\Omega dE_f} = & N \frac{k_f}{k_i} \frac{(\gamma r_o)^2}{2\pi\hbar} \left[\frac{gF(\mathbf{Q})}{2} \right]^2 e^{-2W} \sum_{\alpha\beta} (\delta_{\alpha\beta} - \hat{\mathbf{Q}}_\alpha \hat{\mathbf{Q}}_\beta) \sum_l e^{i\mathbf{Q}\cdot\mathbf{l}} \\ & \times \int_{-\infty}^{\infty} \langle e^{-i\mathbf{Q}\cdot\mathbf{u}_0(0)} e^{i\mathbf{Q}\cdot\mathbf{u}_l(t)} \rangle \langle \mathbf{S}_0^\alpha(0) \mathbf{S}_l^\beta(t) \rangle e^{-i\omega t} dt \end{aligned} \quad (4.36)$$

Here, $\langle \rangle$ is the thermal average, r_o is the classical radius of an electron, g is the Landé splitting factor which is 2 for a spin-only system and $F(\mathbf{Q})$ is the magnetic form factor. Both g and $F(\mathbf{Q})$ are ion specific. $\hat{\mathbf{Q}}$ is the unit vector along \mathbf{Q} , α and β corresponds to the x , y , or z coordinates and $\delta_{\alpha\beta}$ is the Kronecker delta function. $\mathbf{u}_l(t)$ is the displacement of the l^{th} nucleus from its equilibrium position. During the derivation of the above equation, the magnetization interaction vector $\mathbf{S}_\perp = \hat{\mathbf{Q}} \times (\mathbf{S} \times \hat{\mathbf{Q}})$ was used and this implies that only the component of \mathbf{S} perpendicular to \mathbf{Q} contributes to the scattering.

4.3.2.1 Elastic magnetic scattering

For elastic scattering, $\hbar\omega = 0$ and the matrix elements $\langle \mathbf{S}_0^\alpha(0) \mathbf{S}_0^\beta(t) \rangle$ become time-independent. So, Eq. (4.36) becomes

$$\frac{d^2\sigma}{d\Omega dE_f} = N(\gamma r_o)^2 \left[\frac{gF(\mathbf{Q})}{2} \right]^2 e^{-2W} \sum_{\alpha\beta} (\delta_{\alpha\beta} - \hat{\mathbf{Q}}_\alpha \hat{\mathbf{Q}}_\beta) \sum_l e^{i\mathbf{Q}\cdot\mathbf{l}} \langle \mathbf{S}_0^\alpha \rangle \langle \mathbf{S}_l^\beta \rangle \delta(\hbar\omega) \quad (4.37)$$

Integrating the Eq. (4.37) with respect to E_f gives the differential scattering cross section as

$$\left(\frac{d\sigma}{d\Omega} \right)_{\text{el}} = N(\gamma r_o)^2 \left[\frac{gF(\mathbf{Q})}{2} \right]^2 e^{-2W} \sum_{\alpha\beta} (\delta_{\alpha\beta} - \hat{\mathbf{Q}}_\alpha \hat{\mathbf{Q}}_\beta) \sum_l e^{i\mathbf{Q}\cdot\mathbf{l}} \langle \mathbf{S}_0^\alpha(0) \rangle \langle \mathbf{S}_l^\beta \rangle \quad (4.38)$$

Next, consider an ideal paramagnet where the magnetic moments are uncorrelated and randomly oriented, the differential scattering cross section in zero magnetic field is

$$\left(\frac{d\sigma}{d\Omega}\right)_{\text{el}} = N \frac{2}{3} (\gamma r_o)^2 \left[\frac{gF(\mathbf{Q})}{2}\right]^2 e^{-2W} S(S+1) \quad (4.39)$$

Here, S is the magnitude of the spin and is limited to the paramagnetic phase of a system where exchange coupling between the moments is negligible.

Next, for the elastic magnetic scattering from a magnetically ordered system, the differential scattering cross section is given by

$$\left(\frac{d\sigma}{d\Omega}\right)_{\text{el}} = N_{\text{M}} (\gamma r_o)^2 \frac{(2\pi)^3}{v_{\text{M}}} \sum_{\mathbf{G}_{\text{M}}} \delta(\mathbf{Q} - \mathbf{G}_{\text{M}}) \times |\mathbf{F}_{\text{M}}(\mathbf{G}_{\text{M}})|^2 \quad (4.40)$$

where $\mathbf{F}_{\text{M}}(\mathbf{G}_{\text{M}})$ is the magnetic structure factor and is defined as

$$\mathbf{F}_{\text{M}}(\mathbf{G}_{\text{M}}) = \sum_j e^{i\mathbf{G}_{\text{M}} \cdot \mathbf{r}_j} \frac{g}{2} F_j(G_{\text{M}}) e^{-2W_j} \langle [\hat{\mathbf{G}}_{\text{M}} \times (\mathbf{S}_j \times \hat{\mathbf{G}}_{\text{M}})] \rangle \quad (4.41)$$

Here, the subscript M corresponds to a magnetic unit cell which can be different from the chemical unit cell. $F_j(G_{\text{M}})$ is the magnetic form factor. \mathbf{G}_{M} is the reciprocal lattice vector of the magnetic structure and can be written as $\mathbf{G}_{\text{M}} = \mathbf{G} + \boldsymbol{\tau}$. $\boldsymbol{\tau}$ is the propagation vector of the magnetic structure and characterizes its periodicity[128, p. 17].

4.3.2.2 Inelastic magnetic scattering

Similar to nuclear inelastic scattering, where neutron can scatter after an exchange of energy with phonons [127, p. 43], collective excitations of spins in a magnetically ordered system can scatter neutrons. These collective excitations are called spin waves[127, p. 155]. The spin waves arise due to the fluctuations of the relative orientation of individual magnetic moments as a consequence of thermal energy and quantum zero-point fluctuations. Spin waves are quantized bosons and are often referred to as magnons. Its energy relative to the ground state is $n\hbar\omega$. Spin waves exhibit dispersion with respect to the wavevector \mathbf{q} within a Brillouin zone. A neutron can absorb or loose energy to the scattering system causing $n \rightarrow n \pm 1$, change in the energy, for a spin wave.

From the general equation of magnetic scattering given by Eq. (4.36), the partial differential equation for the inelastic magnetic cross-section for neutron scattering is

$$\frac{d^2\sigma}{d\Omega dE_f} = N \frac{k_f}{k_i} \frac{(\gamma r_o)^2}{\hbar} \left[\frac{gF(\mathbf{Q})}{2} \right]^2 e^{-2W} \sum_{\alpha\beta} (\delta_{\alpha\beta} - \hat{\mathbf{Q}}_\alpha \hat{\mathbf{Q}}_\beta) S^{\alpha\beta}(\mathbf{Q}, \omega) \quad (4.42)$$

where, $S^{\alpha\beta}(\mathbf{Q}, \omega)$ is the spin-spin correlation function of the system and is defined as

$$S^{\alpha\beta}(\mathbf{Q}, \omega) = \frac{1}{2\pi} \int_{-\infty}^{\infty} \sum_l e^{i\mathbf{Q} \cdot \mathbf{l}} \times \langle \mathbf{S}_0^\alpha(0) \mathbf{S}_l^\beta(t) \rangle e^{-i\omega t} dt \quad (4.43)$$

In Ref. [127, p 156] the Heisenberg Hamiltonian with the linear spin-wave theory is used to describe the magnetic excitations (spin waves) in a magnetic system. Here, $\alpha = \beta = z$ are the spins (moments) direction (longitudinal direction) and $S^z(t) = S^z(0)$, which indicates that the longitudinal component of the spins contributes to the elastic scattering only. $\alpha = \beta = x/y$ are the deviation directions of the spins/moments (transverse direction) which contribute to the magnon creation and annihilation process. The $(\delta_{\alpha\beta} - \hat{\mathbf{Q}}_\alpha \hat{\mathbf{Q}}_\beta) S^{\alpha\beta}(\mathbf{Q}, \omega)$ in Eq. (4.42) is evaluated and leads to the result

$$\sum_{\alpha\beta} (\delta_{\alpha\beta} - \hat{\mathbf{Q}}_\alpha \hat{\mathbf{Q}}_\beta) S^{\alpha\beta}(\mathbf{Q}, \omega) = \frac{1}{2} S_{\text{SW}}(\mathbf{Q}, \omega) (1 + \hat{\mathbf{Q}}_z^2) \quad (4.44)$$

Using the result in Eq. (4.44) the partial differential cross-section in Eq. (4.44) becomes

$$\frac{d^2\sigma}{d\Omega dE_f} = \frac{k_f}{k_i} (\gamma r_o)^2 \frac{(2\pi)^3}{v_o} \frac{1}{2} S_{\text{SW}}(\mathbf{Q}, \omega) (1 + \hat{\mathbf{Q}}_z^2) \left[\frac{gF(\mathbf{Q})}{2} \right]^2 e^{-2W} \quad (4.45)$$

For the spin waves in a ferromagnet, as shown in the Fig. 4.8, the partial differential scattering cross-section is

$$\begin{aligned} \frac{d^2\sigma}{d\Omega dE_f} = & \frac{k_f}{k_i} (\gamma r_o)^2 \frac{(2\pi)^3}{v_o} \frac{1}{2} S (1 + \hat{\mathbf{Q}}_z^2) \left[\frac{gF(\mathbf{Q})}{2} \right]^2 e^{-2W} \\ & \times \sum_{\mathbf{G}, \mathbf{q}} [\delta(\mathbf{Q} - \mathbf{q} - \mathbf{G}) \delta(\hbar\omega_{\mathbf{q}} - \hbar\omega) \langle n_{\mathbf{q}} + 1 \rangle \\ & + \delta(\mathbf{Q} + \mathbf{q} - \mathbf{G}) \delta(\hbar\omega_{\mathbf{q}} + \hbar\omega) \langle n_{\mathbf{q}} \rangle] \end{aligned} \quad (4.46)$$

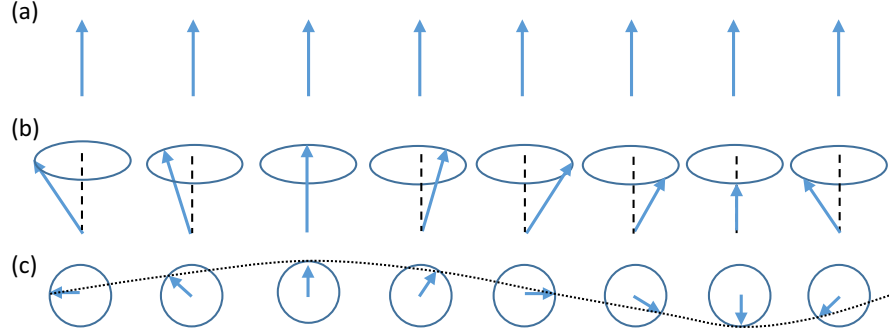


Figure 4.8 Spin waves in a ferromagnet. (a) Arrangement of the spins in a ferromagnet in the ground state. The direction of the spins are assumed to be along the z axis. (b) Precession of the spins on the surface of the cones about the vertical axis with each subsequent spin advancing with a constant phase. (c) Projection of the spin motion in the transverse direction (xy plane) showing a wave-like pattern. The figure is created using the figure in Ref. [127, p. 166] as a guideline.

Here, the thermal average $n_{\mathbf{q}} = \frac{1}{e^{\hbar\omega/k_{\text{B}}T} - 1}$. The first term in the summation in Eq. 4.46 corresponds to the creation and the second term to the annihilation of a magnon. The two δ -functions in the first term in the above equation along with the relationship of \mathbf{Q} in Eq. (4.7) and (4.8) give the condition for the inelastic scattering process as

$$\frac{\hbar^2}{2m}(k_{\text{i}}^2 - k_{\text{f}}^2) = \hbar\omega_{\mathbf{q}} \quad (4.47)$$

$$k_{\text{f}} - k_{\text{i}} = \mathbf{G} + \mathbf{q} \quad (4.48)$$

The spin wave gains energy $\hbar\omega_{\mathbf{q}}$ which is equivalent to the decrease in the kinetic energy of the neutron. Above equations suggest that the magnon dispersion relation can be obtained by measuring k_{i} and k_{f} of a magnetic peak. For a cubic/linear chain ferromagnet with a nearest-neighbor interactions only, the dispersion relation for a small \mathbf{q} is given by $\hbar\omega_{\mathbf{q}} = Dq^2$ with $D = 2JSa^2$, where J is the exchange energy. Similarly, for an antiferromagnetic chain the dispersion relation is given by $\hbar\omega_{\mathbf{q}} = 4|J|Saq$.

The condition for the magnon annihilation and energy gain by the neutron is given by the second term in the summation in Eq. (4.46).

The delta functions in Eq. (4.46) implies the infinite correlation and non-interaction (no decay and infinite life-time of the excitations). However, in a real system, the magnetic correlation length is finite and the magnon decays due to interactions with phonons, magnons, etc. Therefore excitations have finite life-time. The dissipation is often taken into account by considering the damped harmonic oscillator model[126, p. 29], where the delta function in Eq. (4.46) is replaced with the lorentzians,

$$\delta(\hbar\omega_{\mathbf{q}} \pm \hbar\omega) \rightarrow \frac{1}{\pi} \frac{\hbar\Gamma_{\mathbf{q}}}{(\hbar\omega \pm \hbar\omega_{\mathbf{q}})^2 + (\hbar\Gamma_{\mathbf{q}})^2} \quad (4.49)$$

Here, $\Gamma_{\mathbf{q}}$ is the half-width at half maximum of the peak and is called the damping coefficient. It measures the life-time of the excitations. The damped harmonic oscillator model with the Heisenberg-Hamiltonian has been used to describe the longer-wavelength spin fluctuations in AFe_2As_2 systems[46, 49, 81].

The inelastic neutron scattering cross-sections for the spin waves discussed above are obtained using localized picture and should not be appropriate for itinerant systems (such as the transition metal compounds, AFe_2As_2 , ACo_2As_2 compounds discussed in this work). However, as mentioned above and in section 3.1.2 of chapter 2, a model based upon the Heisenberg-Hamiltonian is able to describe the spin waves in AFe_2As_2 compounds at small q (i.e. low-energy excitations). Therefore, the Heisenberg model is a reasonable phenomenological description of the low-energy spin waves of itinerant systems but some modifications, such as the inclusion of damping terms are usually required.

Additionally for the itinerant system, spin waves decay into the particle-hole excitations at high energy on entering the Stoner continuum as shown in Fig. 4.9. This gives rise to broad and diminished neutron scattering intensity. Therefore, there should be inclusion of this damping while interpreting the neutron scattering data. A phenomenological model called diffusive model[65, 80, 91] takes into account of this damping and has been used in AFe_2As_2 compounds to describe spin fluctuations of the nearly ordered system. This model has been used to describe the paramagnetic

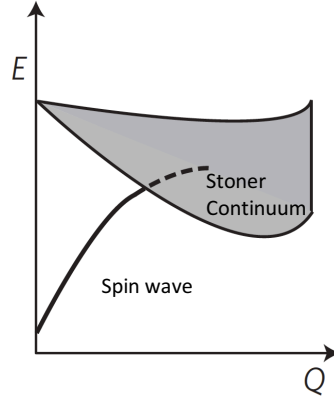


Figure 4.9 A schematic of spin waves in an itinerant system illustrating the decay of spin waves in the Stoner continuum region. The figure is reproduced from Ref. [49].

spin fluctuations of both the $\text{Ca}(\text{Fe}_{1-x}\text{Co}_x)_2\text{As}_2$ and $\text{CaCo}_{1.86}\text{As}_2$ compounds in chapters 5 and 6, where a detailed description can be found.

4.3.2.3 Dynamical susceptibility

The magnetic scattering cross-section can also be expressed in terms of the magnetic susceptibility tensor $\chi_{\alpha\beta}(\mathbf{Q}, \omega)$ [26], defined as

$$\mathbf{M}_\alpha(\mathbf{Q}, \omega) = \chi_{\alpha\beta}(\mathbf{Q}, \omega) \mathbf{H}_\beta(\mathbf{Q}, \omega) \quad (4.50)$$

Here, $\mathbf{M}_\alpha(\mathbf{Q}, \omega)$ is the Fourier transform of the response (magnetization) of a system to the periodically varying magnetic field in both space and time. $\mathbf{H}_\beta(\mathbf{Q}, \omega)$ is the Fourier transform of this magnetic field along the β direction and $\chi_{\alpha\beta}(\mathbf{Q}, \omega)$ is the coefficient of the linear response and is a complex quantity.

The $\chi_{\alpha\beta}(\mathbf{Q}, \omega)$ is also called dynamical susceptibility and can be written in the real and imaginary part as

$$\chi_{\alpha\beta}(\mathbf{Q}, \omega) = \chi'_{\alpha\beta}(\mathbf{Q}, \omega) + i\chi''_{\alpha\beta}(\mathbf{Q}, \omega) \quad (4.51)$$

The imaginary part is the dissipative response to the field and the fluctuation-dissipation theorem relates it to the spin-spin correlation function in Eq. (4.43) by[3]

$$S^{\alpha\beta}(\mathbf{Q}, \omega) = \frac{\hbar}{\pi(g\mu_B)^2} \frac{1}{1 - e^{-\hbar\omega/k_B T}} \chi''_{\alpha\beta}(\mathbf{Q}, \omega) \quad (4.52)$$

4.3.2.4 Principle of detailed balance

The principle of the detailed balance is

$$S(-\mathbf{Q}, -\omega) = e^{-\hbar\omega/k_B T} S(\mathbf{Q}, \omega) \quad (4.53)$$

This relates the intensity of the scattering processes in which the neutron loses (excitation creation, $E = \hbar\omega > 0$) and gains (excitation annihilation, $E = \hbar\omega < 0$) energy. The intensities of these two processes are related by the Boltzmann factor $e^{-\hbar\omega/k_B T}$, which is also defined as the probability of a system being at an energy state $\hbar\omega$ with respect to the ground state ($\hbar\omega = 0$). A schematic of the excitation creation and annihilation processes are shown in Fig. 4.10. For the temperature $k_B T < \hbar\omega_0$, the intensity corresponding to the excitations annihilation is smaller than that of creation. The two intensities become equivalent when $k_B T \gg \hbar\omega_0$.

4.4 Neutron scattering instruments

This section discusses the neutron scattering instruments in general and the ones where inelastic neutron scattering measurements were carried out for the compounds discussed in this work. All three experiments on $\text{Ca}(\text{Fe}_{1-x}\text{Co}_x)_2\text{As}_2$, $\text{CaCo}_{1.86}\text{As}_2$ and $\text{Ba}_{1-x}\text{K}_x\text{Mn}_2\text{As}_2$ were performed on the wide angular-range chopper spectrometer (ARCS) at the Spallation Neutron Source (SNS) at Oak Ridge National Laboratory (ORNL). An additional measurement on the $\text{CaCo}_{1.86}\text{As}_2$ focused on the low energy (< 10 meV) spin fluctuations was carried out at the Multi Axis Crystal Spectrometer (MACS) at the NIST Center for Neutron Research.

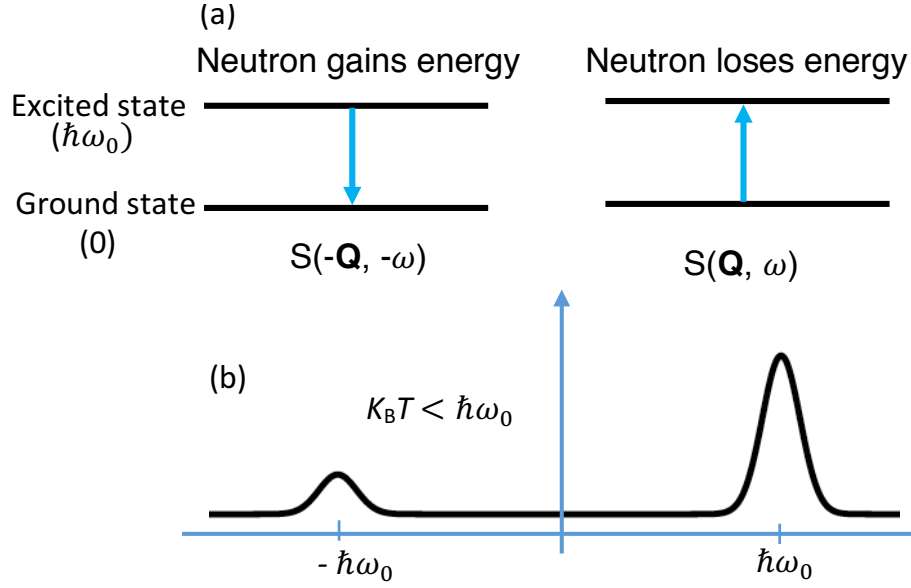


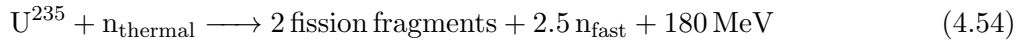
Figure 4.10 Schematic illustrating the process of an excitation creation and annihilation in a scattering system during the inelastic neutron scattering. (a) The transition of the scattering system between the ground and excited states with an energy gap of $\hbar\omega_0$. The arrow showing the transition from the excited state to the ground state corresponds to the annihilation process, in which the neutron absorbs energy equivalent to $\hbar\omega_0$. Similarly, the second case where the arrow shows the transition from the ground to the excited state corresponds to the excitation creation process, in which the neutron loses energy to the scattering system. (b) Comparison of the inelastic neutron scattering intensity for the creation and the annihilation process at the temperature less than $\hbar\omega_0/k_B$. The figure is created using figure in [127, p. 69] as a guideline.

4.4.1 Neutron generation

Neutrons are not stable in their free states and decay into a proton, an electron and an antineutrino. The mean lifetime of a free neutron is about 886 seconds, which is sufficient time to perform neutron scattering measurements. Spontaneous fission and spallation are two common methods for generating neutrons for scattering experiments[126, p. 4].

4.4.1.1 Fission

The spontaneous fission of U^{235} after absorption of a slow neutron produces neutrons in a nuclear reactor with the following reaction



The process releases 180 MeV of energy per fission and the neutrons released are highly energetic (\sim MeV). These neutrons are then thermalized by a moderator. Light water (H_2O) or heavy water (D_2O) at $T \approx 315$ K are commonly used moderators in a reactor. The moderated thermal neutrons are then used for further chain reaction, whereas more neutrons are produced than required to sustain the continuous reaction. So, some of them are extracted through horizontal beam tubes for neutron experiments. The energy distribution of thermal neutrons follows the Maxwell-Boltzmann distribution with an energy peak at ~ 25 meV corresponding to the temperature of the moderator. For the production of low energy neutrons, additional moderators at lower temperatures are used. For example, liquid hydrogen at ~ 20 K is used at the NIST center of neutron research. Nuclear reactors are generally continuous source of the neutrons, but the choppers can be used in a spectrometer to produce pulsed neutrons, at the cost of the time-averaged flux.

4.4.1.2 Spallation

A spallation neutron source, such as SNS at ORNL, produce neutrons from bombarding a heavy target by highly-energetic particles. At SNS, a mercury (Hg) target is bombarded by accelerated protons. The short proton pulses, which are on the order of μs at SNS, are used to produce pulsed

neutrons. The target is excited in this process and then de-excites to the ground state after releasing neutrons along with additional nucleons, photons and neutrinos. Similar to the nuclear reactors, water moderators are used to produce the room-temperature neutrons and liquid hydrogen at 20 K to produce the cold neutrons. In either case, some of the fast and epithermal neutrons escape the moderators. These higher-energy epithermal neutrons can be used to measure the dynamics on the order of eV. Fast neutrons should be eliminated as they contribute to the background/noise and can also give spurious peaks

4.4.2 Time-of-flight instrument

As the name suggests, the time-of-flight of a neutron is used to calculate its energy. The velocity of a neutron is obtained by measuring the time taken by a neutron to travel the known distance. For this, it is necessary to define the start time, and for pulsed source chopper spectrometers, the start time or the zeroth of the flight $t = 0$ is the time at which the proton pulse hits the heavy target. The energy (E_n) and velocities (v) of neutron are related by $E_n = \frac{1}{2}m_n v^2$, where m_n is the mass of a neutron. Therefore, the energy of the incident and scattered neutron can be calculated from the corresponding velocities. Consequently, this gives the energy gain or loss by the neutron ($E = \hbar\omega$), so Q is obtained from the scattering angle and energy of the detected neutrons. As discussed above, these two information are needed to map the magnetic excitations.

The time-of-flight instruments are the direct-geometry or the inverse-geometry spectrometers based upon whether the time-of-flight of the incident neutron (k_i) or the scattered neutron (k_f) is measured. Time-distance diagram for the direct-geometry and the inverse-geometry time-of-flight spectrometers are illustrated in Fig. 4.11.

4.4.2.1 Direct-geometry spectrometer

In direct-geometry spectrometers, the incident energy of a neutron is defined by a monochromator (choppers in pulsed source). The incident neutrons are scattered both elastically and inelastically from the sample and arrive at the detector at different times. This difference in the travel

time from a sample to a detector is used to determine the final energy E_f . The energy transfer is given by the difference of the final and incident energies, as in Eq. (4.7), and the momentum transfer Q is obtained using Eqs. (4.7) and (4.8), which give

$$\frac{\hbar^2 Q^2}{2m} = 2E_i - E - 2 \cos \phi [E_i(E_i - E)]^{\frac{1}{2}} \quad (4.55)$$

where ϕ is the scattering angle between the incident and scattered neutrons.

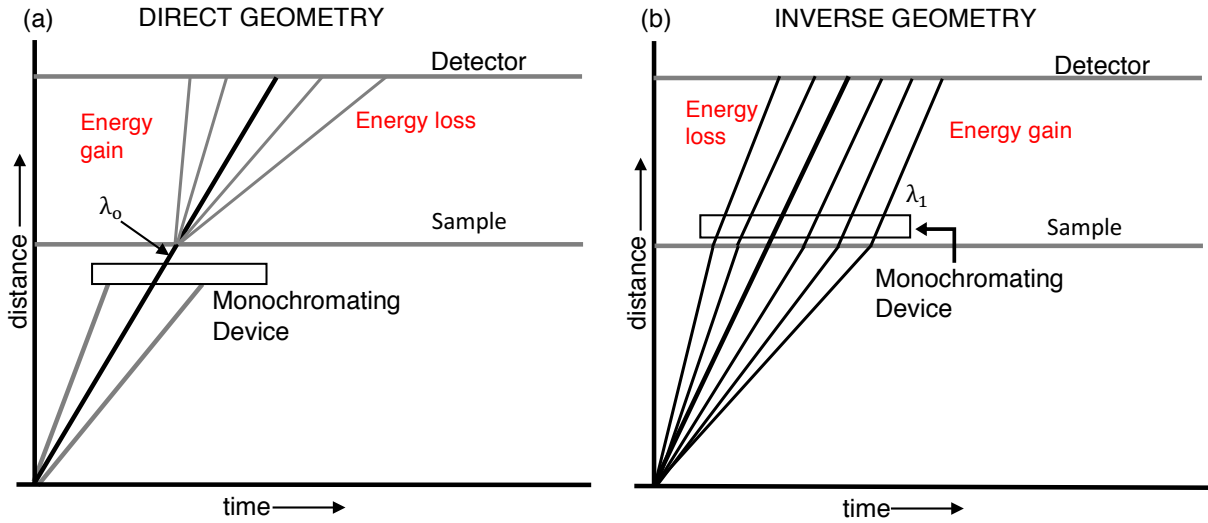


Figure 4.11 (a) and (b) Time–distance diagram for a direct–geometry and an inverse–geometry spectrometers, respectively. Energy gain and loss in the figures correspond to the energy gain and loss by the neutrons to the sample. λ_0 in (a) and λ_1 in (b) are the wavelengths of the incident and scattered neutrons, respectively, defined by the monochromating devices (choppers). The figure is reproduced from Ref. [129, p. 214]

4.4.2.2 Inverse-geometry spectrometer

For an inverse–geometry spectrometer, the monochromator is after a sample, and thus the incident neutrons on the sample have range of energies or arrival times. The neutrons arriving at different times are scattered from the sample. The scattered neutrons travel towards the detector with a same speed, i.e. known flight-time after the monochromator. Similar as above, the momentum transfer Q in this case is given by

$$\frac{\hbar^2 Q^2}{2m} = 2E_f + E - 2 \cos \phi [E_f(E_f + E)]^{\frac{1}{2}} \quad (4.56)$$

4.4.2.3 ARCS

ARCS is a wide angular-range chopper spectrometer at SNS. It is a direct-geometry, time-of-flight spectrometer and the time taken by the neutrons to reach the detector is used to calculate the velocities of the scattered neutrons from the sample. A schematic of the ARCS instrument is shown in Fig. 4.12 and the time–distance diagram is illustrated in Fig. 4.13. In addition, the instrument parameters are given below in Table 4.2.

Table 4.2 ARCS instrument parameters. The table is reproduced from the Ref. [130].

Incident energy range, E_i (meV)	15–1500
Energy resolution ΔE for elastic scattering	3.0% to 5.0% of E_i
Moderator to T_0 chopper distance (m)	8.77
Moderator to Fermi chopper distance (m)	11.61
Fermi chopper to sample distance (m)	1.99
Sample to detector distance (m)	3.0 to 3.5
Moderator to beam monitor 1 (m)	11.83
Moderator to beam monitor 2 (m)	18.50

The required velocity/energy of incident neutrons on a sample is acquired with the combination of the rotation of T_0 and the Fermi-chopper, which are phased according to the source frequency. The T_0 chopper is located after the moderator and opens slightly after each source pulse as shown in the time–distance diagram in Fig. 4.13. So, it blocks the prompt radiation as well as the high-energy neutrons that can contribute to the background. It has a wide opening ($8.5 \times 8.5 \text{ cm}^2$ [130]) and allows a wide-range of neutron energies to pass through it.

The energy (or k_i) of the neutrons incident on a sample is defined by the Fermi chopper, which is accordingly phased to the source pulse. It consists of curved neutron transmitting slits separated by absorbing walls. It has the rotation axis perpendicular to the beam direction. In this configuration, only neutrons with the intended velocities can traverse the curved path without being absorbed. Hence, this produces neutrons with a well-defined energy.

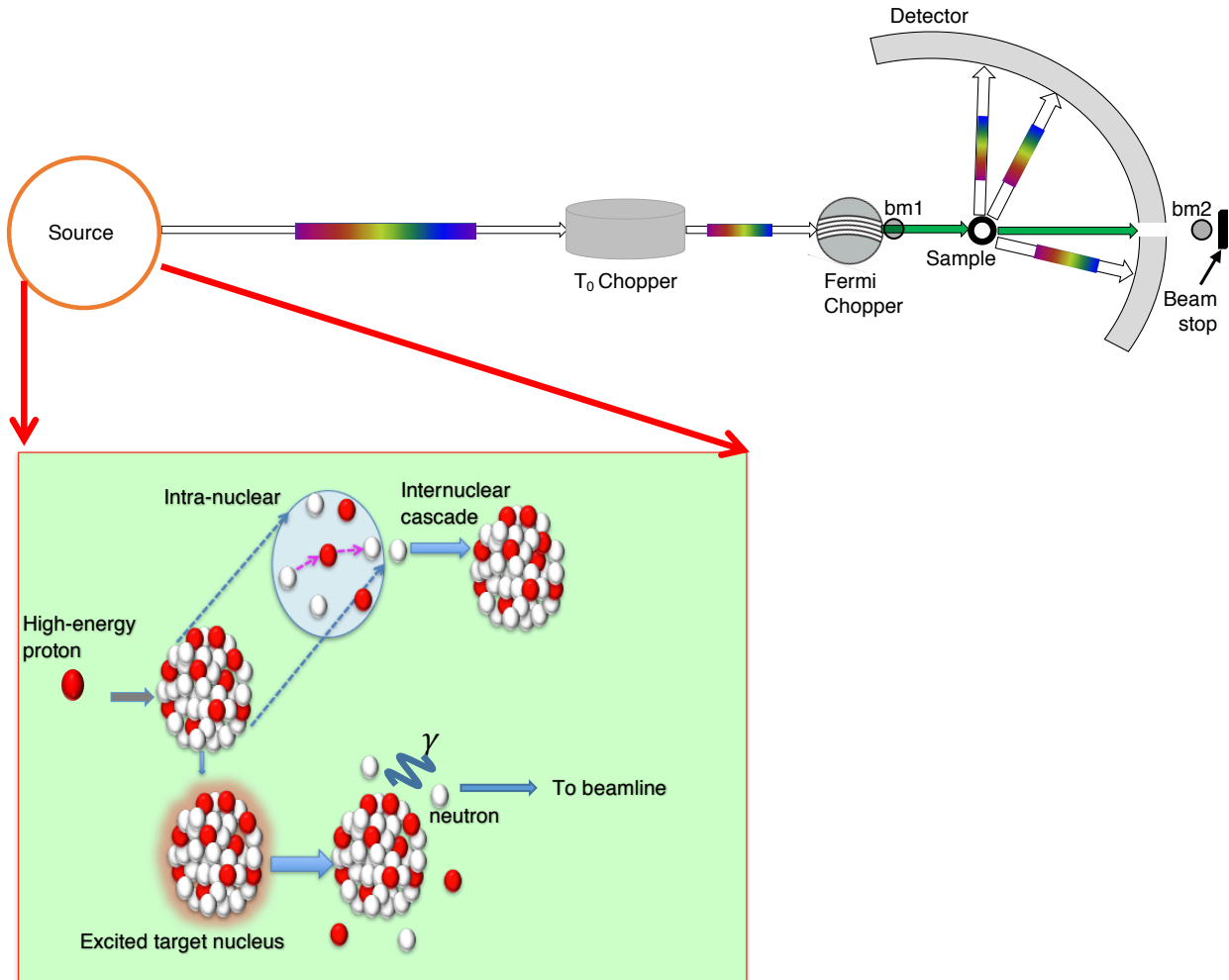


Figure 4.12 Schematics of the ARCS instrument and the spallation process. Two choppers, T_0 (T zero) and Fermi chopper, are shown in the figure. The multicolor patched arrows on the neutron beam path represent the neutrons with a broad range of the velocities/energies. The single colored arrows on the beam path represent the neutron with single-defined energy. bm1 and bm2 are two beam monitors after the Fermi chopper and before beam stop, respectively. The spallation process is shown in the inset. It shows the two processes that occur after the bombardment with the energetic protons. In the first one (lower one), the neutrons, along with the other products, are released after bombardment via process of excitement and de-excitment of the traget nucleus. Simultaneously, second process (upper one), illustrates the cascade of an internuclear processes due to the energetic particles knocked off from the target nucleus. The figure is created using the information in the Ref. [130] and the Fermi chopper in the figure is obtained from the Ref. [131].

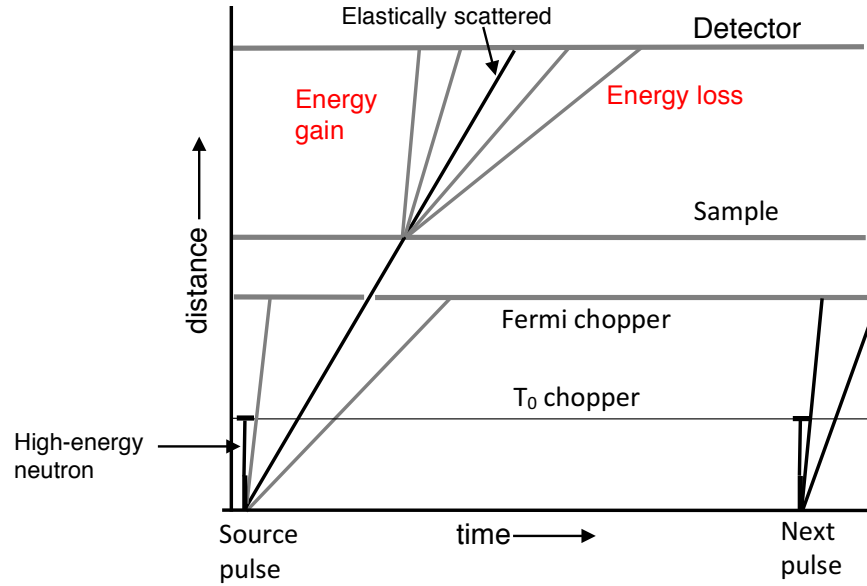


Figure 4.13 Time–distance diagram for the ARCS spectrometer. The thick lines in the T₀ chopper is used to highlight the instant, at which it absorbs the high-energy neutrons and prompt radiation. The figure is reproduced from Ref. [129, p. 209]

There are additional components in the ARCS beam path. There are neutron guides which reflect the neutrons below a certain critical energy and decrease the loss of neutron flux during the long flight. There are motorized slits which defines the size of the beam at the sample environment. There are two beam monitors, the first one is right after the Fermi chopper and the second one is before the heavy concrete beam stop. They are for the calculation of the energy of the neutrons incident upon the sample. From the fits of the peaks of the beam monitors, time-of-flight of the incident neutrons at these positions are obtained. The time difference provides the time-of-flight of the incident neutrons between the two monitors, for which the distance is known. From this information, the velocity and energy of the incident neutrons are calculated.

The scattered neutrons from the sample are detected using He³ linear position sensitive detectors which spans the horizontal angles from -27° to 135° and vertical angles from -27° to 26° . This wide angular coverage and the time-of-flight technique allows measurement of a large range of the reciprocal space efficiently. Furthermore, the data are recorded in these detectors as a function of

a two-dimensional scattering angle and the time of arrival. For the measurement done with the incident neutron fixed along a certain crystallographic direction, as in the majority of the measurements discussed in this thesis, only three components of the four-dimensional (\mathbf{Q}, E) space are independent, i.e. only three-dimensional manifold of the four-dimensional (\mathbf{Q}, E) space is measured. To map spin fluctuations in four-dimensional (\mathbf{Q}, E) space, the measurement is performed by rotating the sample.

Even though the ARCS instrument is very efficient at providing a broad map of the spin fluctuations/excitations, there are other instruments that are more effective in the case of the focused measurements at a particular \mathbf{Q} and E , for example triple-axis spectrometers at nuclear reactors. In addition, the energy resolution of low- E measurements at these instruments are better than at ARCS operated with higher incident energies ($E \geq 75$ meV). So the measurements at ARCS are usually complemented by measurements at these other instruments. This is the case for our measurement on $\text{CaCo}_{1.86}\text{As}_2$, where the information about spin fluctuations below 10 meV was acquired by measurement at the MACS (Multi axis crystal spectrometer), a cold neutron spectrometer at the NIST Center for Neutron Research.

4.4.3 Triple-axis spectrometer

The triple-axis spectrometer (TAX) is a popular instrument used at neutron reactors for neutron scattering measurements. The triple-axis gets its name from the three axis of rotation of the monochromator, the sample, and the analyzer, as shown in Fig. 4.14. The monochromator defines the energy of the incident neutrons on the sample. For this, it Bragg diffracts a polychromatic/white neutron beam [i.e neutrons with the wide range of energies(or wavelengths)] coming from the reactor source. The Bragg's diffraction condition is $\lambda = 2d_{\text{hkl}} \sin \theta_{\text{M}}$, where $2\theta_{\text{M}}$ is the angle between the incident white beam and diffracted neutron beam with particular wavelength, and d_{hkl} is the distance between the reflecting crystallographic planes. So, by choosing a reflection from the fixed planes (i.e. d_{hkl} constant) of the monochromator crystal and by rotating it to change θ_{M} , a different wavelength (or energies) for the incident beam is selected. Vertically focusing pyrolytic

graphite (PG002) crystals are used at the HB3 triple-axis spectrometer at the High-flux Isotope reactor (HFIR) at ORNL and is an example of a monochromator.

Incident neutrons with a well-defined energy are then scattered both elastically and inelastically from the sample. Similar to the monochromator crystal, the analyzer crystal Bragg reflects the neutron with certain final energy or wavelength. These diffracted neutrons are then detected by the detectors. Generally, a point in (\mathbf{Q}, E) space is measured at a time.

There are two general methods of the measurement in the TAX: (i) Constant- \mathbf{Q} , where the momentum transfer is held fixed and the energy transfer is varied, and (ii) constant- E (energy) scan, where scans along the reciprocal space of the sample are done with constant energy transfer. For the constant- E scan, the incident and final energies of the neutron are kept fixed.

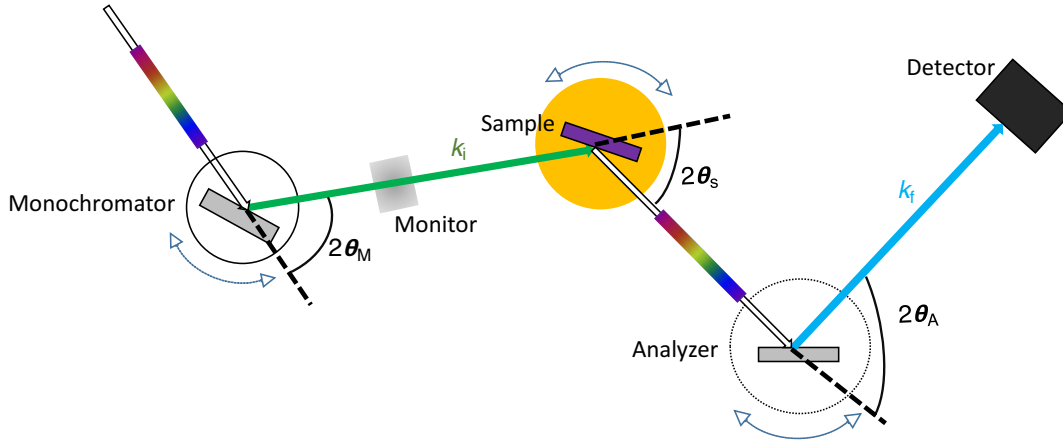


Figure 4.14 Schematic of a triple-axis spectrometer, top view. The curved two headed arrows at the monochromator, sample and analyzer indicate the axes of the rotation, which is perpendicular to the plane.

In addition, there are other components, (i) low-efficiency monitor to measure the intensity of the incident neutrons, (ii) collimators such a Soller collimator which consists of slits separated by the neutron absorbing walls to limit the angular divergence of the beam, and (iii) filters to suppress the higher-order neutrons. The collimators are commonly placed before monochromators, between

the monochromator and sample, between the sample and analyzer, and between the analyzer and detector.

The Bragg diffraction from the monochromator and analyzer, which selects the incident energy ($k_i = \frac{2\pi}{\lambda_i}$) and final energy ($k_f = \frac{2\pi}{\lambda_f}$), respectively, also allows the higher-order neutrons ($\frac{\lambda_{i/f}}{n}$, $n = 2, 3, \dots$) to pass through them. They can produce spurious peaks in the measured data. Thus, it is necessary to effectively suppress these higher-order neutrons. So various types of filters are used for this task. Depending upon the energy of the neutron used in the scattering, some of the common filters are PG, Be, and BeO filters. For example, at HB3 spectrometer at HFIR, PG filters are used when the instrument is operated at $E_f = 14.7$ meV. For this energy, the PG filters have significant transmission and suppression of the primary and higher-order neutrons, respectively[126].

4.4.3.1 MACS: High intensity cold neutron spectrometer

MACS (Multi axis crystal spectrometer) is a cold neutron spectrometer at the NIST Center for Neutron Research, which is a nuclear reactor source. The neutrons are generated as discussed above in Section 4.4.1 and the liquid hydrogen at 20 K is used as a moderator. The instrument is optimized for enhanced neutron flux at a sample by using a doubly focusing monochromator. Figure 4.15 show a schematic of MACS.

The rotating beam shutter is the first component right after the biological shielding of the reactor and is followed by Be filters cooled at 77 K. The filters are used to suppress higher-order neutrons by using the condition $\lambda_{\text{cutoff}} = 2d_{\text{max}}$ [126, p. 78]. The cooling of the filters helps to suppress the scattering of the neutrons due to thermal phonons of the filters, and thus improving the transmission through them. The Be filters are used for incident energies less than 5 meV, otherwise no filter (called open condition) is employed. After the Be filter, two radial collimators, which can be used in multiple ways, are available to limit the horizontal beam divergence. This consequently controls the incident beam energy resolution. The opening of the variable aperture after the collimators can be varied up to the 35×35 cm² and this define the beam size at the monochromator.

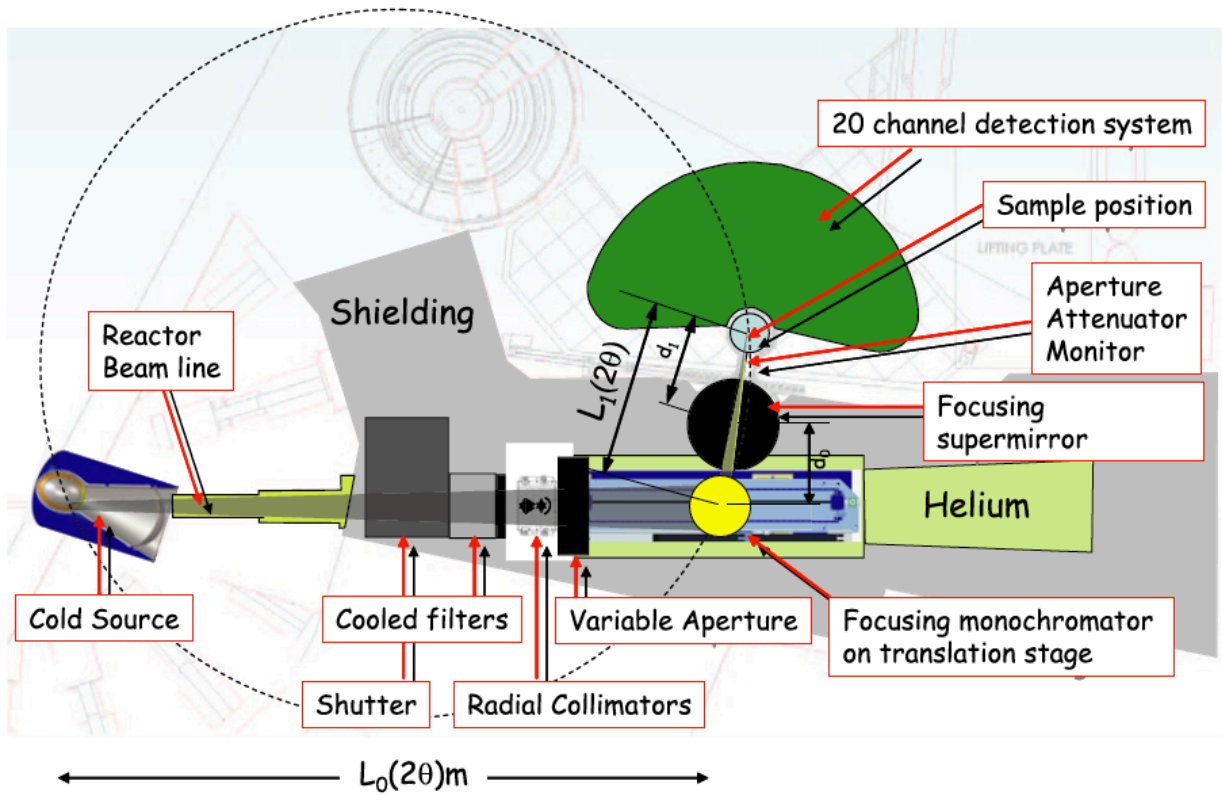


Figure 4.15 Schematic (top view) of the MACS instrument at the NIST Center for Neutron Research. The dashed circle is the Rowland circle that passes through the center of the source, the monochromator and the sample. The figure is reproduced from Ref. [132].

The double focusing monochromator is on the beam path to produce the monochromatic beam. It consists of an array of 357 pyrolytic graphite (PG) crystals attached to thin aluminum blades to facilitate the bending and rotation for both vertical and horizontal focusing. The doubly focusing enhances the flux at the sample position and provides up to 5×10^8 neutrons $\text{cm}^{-2} \text{s}^{-1}$ on a 8 cm^2 sample area[132]. This is nearly 40 times more flux than the SPINS cold neutron spectrometer at NIST[132]. The super mirror guides are after the monochromator to decrease the loss of neutron flux along the flight path.

The beam size at the sample is defined by the horizontal and vertical slits right before it. Finally, 20 detector channels, shown as a green kidney-shaped component in Fig. 4.15, after the sample position detect the scattered neutrons. Each channel has three different options for filters (Be, BeO or graphite), which are cooled to less than 77 K to reduce transmission losses from inelastic phonon scattering. Soller collimator follows the filter providing four different collimation settings, $60'$, $90'$, $36'$ and open. Next, the vertically focusing double PG crystal analyzers define the final energy, E_f . The final energy can be between 2.5 to 20 meV[132]. There are two detectors in each of the detector channels, (i) a diffraction detector that views the sample directly is behind the first analyzer and measures the diffraction peak and (ii) a spectroscopic detector which measures the neutrons reflected from the second analyzer. Each channel is separated by 8° and covers 152° in one settings, hence allowing broad \mathbf{Q} coverage.

Measurements at MACS can be carried out effectively for two different settings, (i) different final energies for each analyzer, (ii) broad \mathbf{Q} scans for a common final energy. MACS with its enhanced intensity at the sample is useful for the small samples or samples with weak scattering cross sections, and one can also benefit from the broad \mathbf{Q} and E scans available.

CHAPTER 5 DOPING EVOLUTION OF SPIN DYNAMICS IN

$\text{Ca}(\text{Fe}_{1-x}\text{Co}_x)_2\text{As}_2$

Part of the content of this chapter is from the manuscript accepted for publication in Physical Review B.[133].

5.1 Introduction

As discussed in chapters 2 and 3, in “122” iron-arsenide superconductors ($A\text{Fe}_2\text{As}_2$, with $A = \text{Ca}, \text{Sr}, \text{Ba}$), superconductivity (SC) lies in a close proximity to magnetism[25, 26, 134], and appears in the presence of substantial spin fluctuations, which is centered at a wavevector characterized by an antiferromagnetic (AFM) propagation vector $\boldsymbol{\tau}_{\text{stripe}} = (\frac{1}{2} \frac{1}{2} 1)$ [26, 41]. The SC appears after significant suppression of the AFM order by either chemical substitution[4, 61–63, 72] or pressure[96–98, 101, 102]. Therefore, the close proximity of the AFM order and SC in these compounds, and the presence of spin fluctuations in their superconducting (SC) state suggest an intimate relationship between the magnetism and SC. In particular, the spin fluctuations present in the SC state are considered as a necessary component of the SC pairing mechanism[5].

This necessitates the thorough understanding of spin fluctuations in 122 compounds and extensive studies have been done using the inelastic neutron scattering (INS) technique. INS studies of $\text{Ba}(\text{Fe}_{1-x}\text{TM}_x)_2\text{As}_2$ (TM= Co, Ni)[135, 136] in superconducting state find spin resonance in spin fluctuations spectra, which is an indication of the unconventional nature of SC[137] and also suggests that spin fluctuations mediate pairing of electrons for superconductivity[41]. In addition, in $\text{Ba}(\text{Fe}_{1-x}\text{Co}_x)_2\text{As}_2$, it has been found that with increasing Co-doping (i.e. x), spin dynamics evolve smoothly from the well-defined, gapped spin waves to the diffusive (overdamped) spin fluctuations as shown in Fig. 5.1. The evolution of the diffusive spin fluctuations coincides with the onset of

SC, hence providing an evidence of a requirement of the diffusive (overdamped) spin fluctuations for SC[5].

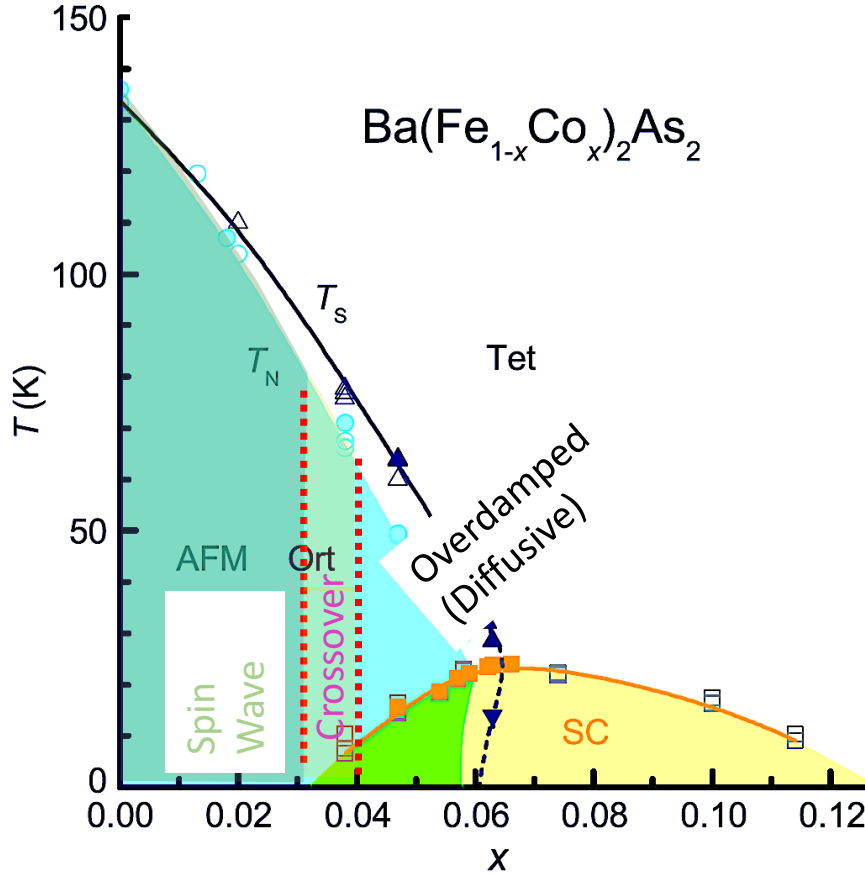


Figure 5.1 Phase diagram of $\text{Ba}(\text{Fe}_{1-x}\text{Co}_x)_2\text{As}_2$ illustrating the crossover of the spin dynamics from spin waves to the diffusive spin fluctuations near the coexistence region of AFM and SC. The figure is produced using the phase diagram in Ref. [4] and the doping evolution information of the spin dynamics from Ref. [5].

This chapter discusses INS results on a variant compound $\text{Ca}(\text{Fe}_{1-x}\text{Co}_x)_2\text{As}_2$, which presents a different scenario than $\text{Ba}(\text{Fe}_{1-x}\text{Co}_x)_2\text{As}_2$ compound. CaFe_2As_2 is unique among the members of AFe_2As_2 , because of its strongly coupled first ordered magnetostructural transition[25, 42, 72] and extreme sensitivity to pressure[7]. This strong first order magnetostructural coupling persists with electron-doping in $\text{Ca}(\text{Fe}_{1-x}\text{Co}_x)_2\text{As}_2$ and the suppression of $T_{S,N}$ is abrupt. Moreover, the strong first-order transition effectively forbids the microscopic coexistence of AFM and SC phases

in $\text{Ca}(\text{Fe}_{1-x}\text{Co}_x)_2\text{As}_2$ [84]. These situations are different than in $\text{Ba}(\text{Fe}_{1-x}\text{Co}_x)_2\text{As}_2$ [4], where the almost coupled structural and magnetic transitions for BaFe_2As_2 split further and become second order with increasing Co-concentration and the suppression of T_S and T_N is gradual [4, 74]. Also, the AFM and superconducting states coexist microscopically in $\text{Ba}(\text{Fe}_{1-x}\text{Co}_x)_2\text{As}_2$ [4]. Therefore, it is interesting to see how this strong magnetoelastic coupling affects the nature of spin dynamics in $\text{Ca}(\text{Fe}_{1-x}\text{Co}_x)_2\text{As}_2$ and whether the diffusive spin fluctuations are absent in the AFM state following the absence of the coexisting region of superconducting and AFM states. This will present another evidence of the link between the diffusive spin fluctuations and SC.

Additionally, in section 3.1.4 of chapter 3, presence of another type of magnetoelastic coupling in CaFe_2As_2 compound has been discussed. In CaFe_2As_2 compound, the As-As distance is strongly coupled with the magnetic moment in CaFe_2As_2 compound in the collapsed tetragonal (cT) phase. In the cT phase, there is a quenching of the magnetic moment and is associated with the formation of the interlayer As-As bonds. Relevance of this magnetoelastic coupling in tetragonal (T) CaFe_2As_2 has been indicated by the density functional theory (DFT) [105] and anomalies in the phonon spectrum of the T phase of CaFe_2As_2 , which have been associated with the compound's proximity to the cT phase [110]. However, it is unknown whether the coupling of As-As distance to the magnetic moment size affects the nature of spin dynamics or SC in uncollapsed state. The question is addressed by performing INS measurement on $\text{Ca}(\text{Fe}_{1-x}\text{Co}_x)_2\text{As}_2$ $x = 0.030$, which shows strong decrease in c with decreasing temperature [111], as shown in Fig. 5.2(d), but is uncollapsed. This is a favorable situation for studying the effects of the coupling between the As-As distance and the magnetism on the spin dynamics in the uncollapsed state.

5.2 Experimental Details

To address all the questions discussed above, inelastic neutron scattering measurements were performed on $\text{Ca}(\text{Fe}_{1-x}\text{Co}_x)_2\text{As}_2$ with two values of x as close to the phase boundary between AFM and SC states as practically possible, given the requirement of the homogenous crystals with large mass. Single crystals of $\text{Ca}(\text{Fe}_{1-x}\text{Co}_x)_2\text{As}_2$ were grown using the FeAs self flux and were annealed

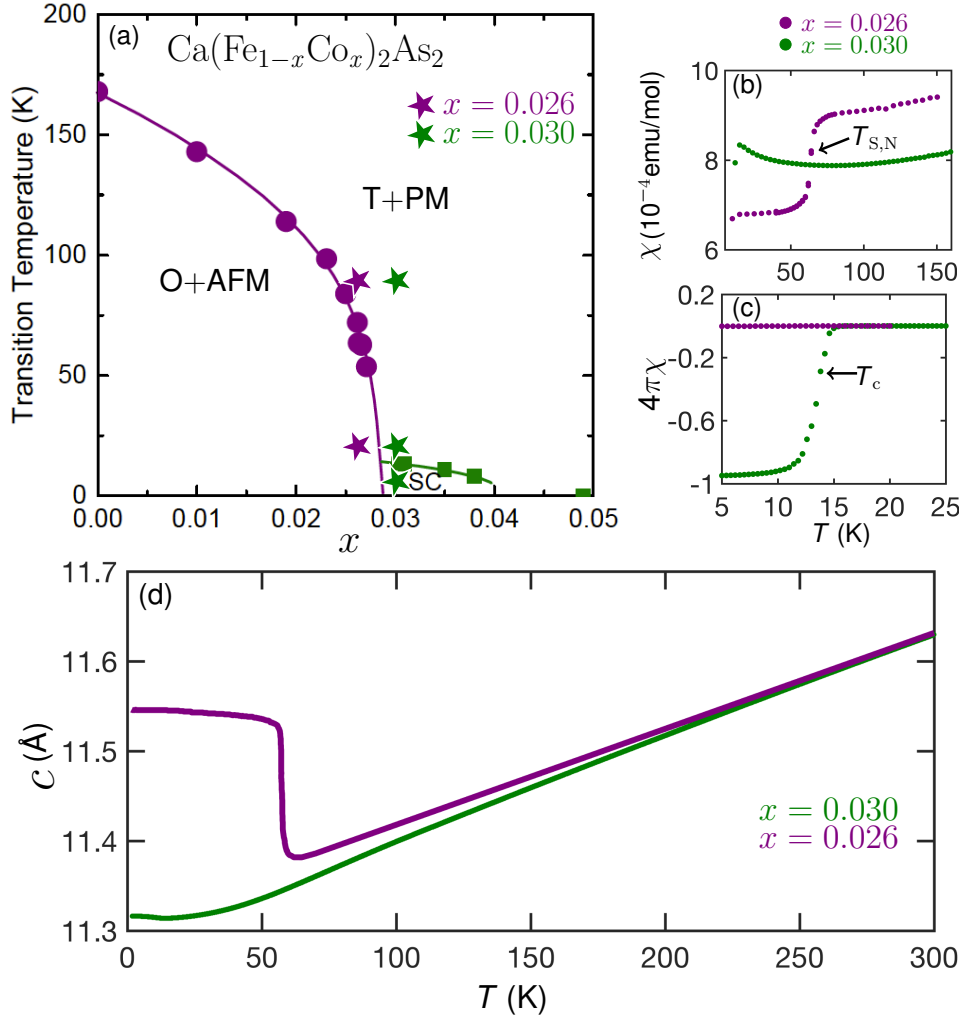


Figure 5.2 (a) Phase diagram of $\text{Ca}(\text{Fe}_{1-x}\text{Co}_x)_2\text{As}_2$ annealed at 400 °C showing the coupled structural and magnetic transition from high-temperature tetragonal (T) and paramagnetic (PM) phase to the orthorhombic (O) and antiferromagnetic (AFM) phase, as well as the superconducting (SC) region. Stars in (a) represent where the INS measurements were performed. (b) and (c) Magnetization data illustrating the T-O and AFM transition at $T_{\text{S,N}}$ for $x = 0.026$ (purple circles) and the superconducting transition at T_c for $x = 0.030$ (green circles). (d) Temperature dependence of the c lattice parameter for $x = 0.026$ (purple line) and 0.030 (green line). The lattice parameter for 300 K is obtained from the center of the (0, 0, 8) diffraction peak. The temperature dependence plot for $x = 0.026$ is derived using this lattice parameter at 300 K and dilatometry data of $x = 0.027$ given in Ref. [111]. The temperature dependence plot for $x = 0.030$ is derived similarly, using the dilatometry data for $x = 0.029$ given in Ref. [111]. The figure is reproduced from Ref. [133].

postgrowth at $T = 400\text{ }^{\circ}\text{C}$, which ensures the absence of the cT phase, at all temperature at ambient pressure, which is present in the quenched (as-grown) samples[84, 138]. The cobalt concentration of $x = 0.026 \pm 0.001$ and 0.030 ± 0.001 was determined from elemental analysis performed using wavelength dispersive x-ray spectroscopy (WDS). Magnetization measurements performed on a single crystal of $x = 0.026$, shown in Fig. 5.2(b) and 5.2(c), show magnetostructural transition at $T_{S,N}$ only and similar measurement on $x = 0.030$ shows superconducting transition below T_c . So the compounds, as represented by stars in the phase diagram of Fig. 5.2(a), are representative of the low-temperature AFM and SC phases.



Figure 5.3 Example of a co-alignment. 14 single crystals of $\text{Ca}(\text{Fe}_{1-x}\text{Co}_x)_2\text{As}_2$ $x = 0.030$ are mounted on aluminum fingers using aluminum wires.

For INS measurements, 10 to 14 crystals were co-aligned in the horizontal (H, H, L) tetragonal scattering plane for $x = 0.026$ and 0.030 , respectively. The co-aligned picture of the $x = 0.030$ is shown in Fig. 5.3. The mosaic of the co-alignment is characterized by full widths at half maximum (FWHM) of less than 1.3° . The INS measurements were performed on the ARCS spectrometer[130] at the Spallation Neutron Source at Oak Ridge National Laboratory. The samples were cooled using a closed-cycle He cryostat. Measurements were carried out with the incident neutron beam along \mathbf{c} with incident energies of $E_i = 49.75$ meV at $T = 20$ and 90 K for both concentrations, and with $E_i = 49.75$ meV at $T = 6$ K for $x = 0.030$, and $E_i = 73.9$ and 238.4 meV at $T = 20$ K for $x = 0.026$. In addition, for $x = 0.026$, a measurement at $T = 20$ K with $E_i = 73.9$ meV was made while rotating the crystal about its vertical axis in 1° steps over a range of 145° .

Table 5.1 Lattice parameters for $x = 0.026$ and 0.030 at temperatures corresponding to the inelastic neutron scattering measurement. The values are obtained using the dilatometry data of $x = 0.027$ and $x = 0.029$ given in Ref. [111] and the lattice parameters at 300 K from the diffraction measurement.

	$x = 0.026$	$x = 0.026$	$x = 0.030$	$x = 0.030$	$x = 0.030$
	$T = 90$ K	$T = 20$ K	$T = 90$ K	$T = 20$ K	$T = 6$ K
$a = b$ (Å)	3.92	3.91	3.89	3.90	3.90
c (Å)	11.40	11.56	11.39	11.31	11.31

Here, the momentum transfer is defined as $\mathbf{Q} = (H - K, H + K, L) = (2\pi/a)(H - K)\hat{\mathbf{i}} + (2\pi/a)(H + K)\hat{\mathbf{j}} + (2\pi/c)L\hat{\mathbf{k}}$ with respect to the tetragonal $I4/mmm$ unit cell. At ambient temperature, $c = 11.63$ Å, and $a = 3.91$ and 3.88 Å for $x = 0.026$ and 0.030 , respectively, and the lattice parameters at the temperatures of the measurement is given in the Table 5.1. In this notation, the reciprocal lattice vectors for stripe-type AFM order are $\mathbf{Q}_{\text{stripe}} = (\frac{m}{2}, \frac{n}{2}, l)$ with m , n and l odd integers. Data were visualized using the MSLICE[139] and HORACE[140] software packages. Incoherent nuclear scattering from a vanadium standard was used to normalize the data and we report the dynamical structure factor $S(\mathbf{Q}, E)$ in the units of mbarn/sr-meV-f.u., where E is neutron energy transfer, sr is steradians and f.u. is formula unit. The values determined using this method

is accurate within the 20–30% of the actual values. Wherever possible the data are averaged over the four symmetry equivalent quadrants of the basal plane to improve statistics.

5.3 Spin dynamics evolution in the orthorhombic-antiferromagnetic state

A well-defined and gapped spin waves, centered at $\mathbf{Q}_{\text{stripe}}$ and extended up to high energy, characterize the spin dynamics in the O-AFM state of parent CaFe_2As_2 $x = 0$ [46, 47]. In addition, the spin dynamics are three dimensional with conical dispersion in the \mathbf{ab} plane. Comparison of the results of INS measurement on $\text{Ca}(\text{Fe}_{1-x}\text{Co}_x)_2\text{As}_2$ $x = 0.026$ with parent CaFe_2As_2 depicts the spin dynamics evolution in the O-AFM state.

Figures in 5.4 illustrate the scattering from the spin waves in the AFM state of $\text{Ca}(\text{Fe}_{1-x}\text{Co}_x)_2\text{As}_2$ $x = 0.026$ measured at $T = 20$ K ($T/T_N \approx 0.3$). The spin waves are centered at the $\mathbf{Q}_{\text{stripe}}$ position as observed in the parent CaFe_2As_2 [47]. The scattering at the lower energies are sharp in \mathbf{Q} as shown in Q slices in Fig. 5.4(f), longitudinal (LO) slices in Figs. 5.4(a),(h), and transverse (TR) slices in Figs. 5.4(b),(i) and the dispersion plot along the $(-0.5, -0.5, L)$ in Fig. 5.4(g). Figures suggest the steep dispersion extending up to high energies along all three crystallographic directions and the ring-like feature in Q slices of Figs. 5.4(c), (d), (j), (n), and (o) is expected for a conical dispersion in the \mathbf{ab} plane. The observed small ellipticity in the rings along the TR and LO direction is due to differences in the spin-wave velocities along these directions.

For the quantification of the data, one-dimensional (1D) cuts were made for the Q slices in Fig. 5.4 along the TR and LO directions. The results for the $L \geq 3$ are shown in Fig. 5.5, where the plots are fitted using two Gaussian lineshapes. From the center of the peaks obtained from the fits, dispersion plots along the TR and LO directions are obtained as shown in Figs. 5.6(a) and (b), respectively. For $L = 1$, a single peak is observed which is fit with a Gaussian lineshape and the determined peak center and the FWHM is represented by the blue filled circle and errorbar, respectively, in both Figs. 5.6(a) and (b). The dispersion plot along the $[0, 0, L]$, shown in Fig. 5.6(c), are obtained by making Q cuts in the slice in Fig. 5.4(g) and fitting the resulting single peak with a Gaussian lineshape convoluted with the instrumental resolution. The details

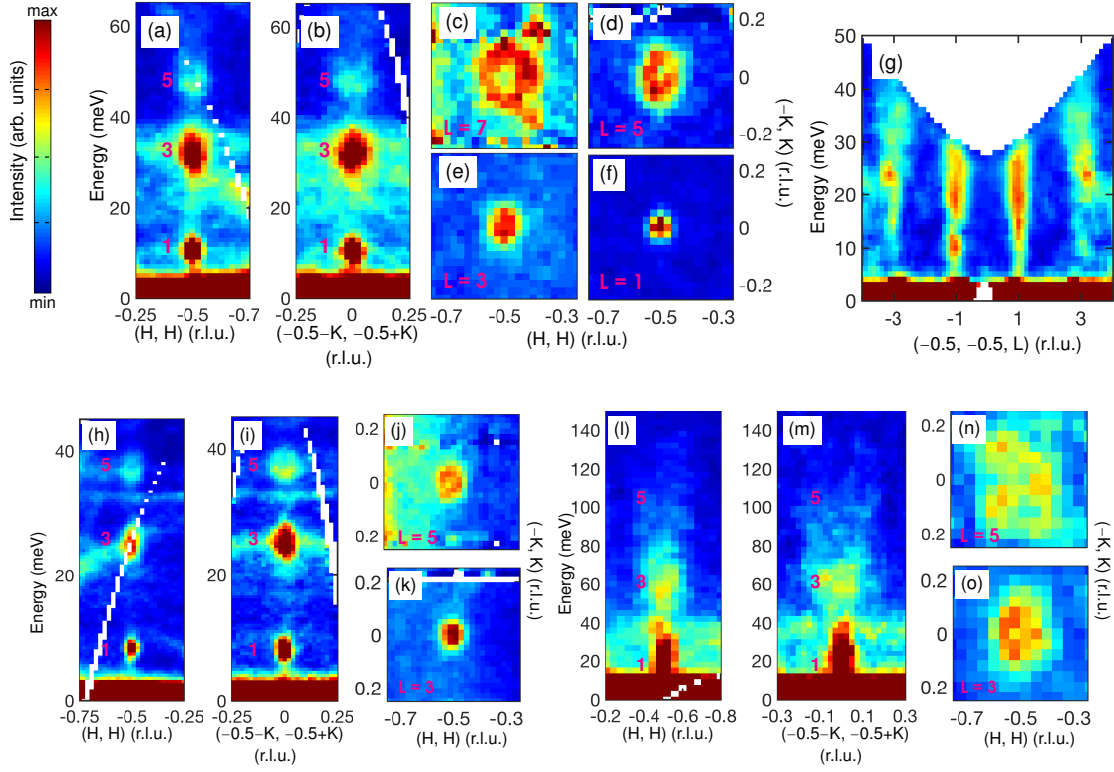


Figure 5.4 Inelastic neutron scattering cross-section for $\text{Ca}(\text{Fe}_{1-x}\text{Co}_x)_2\text{As}_2$ $x = 0.026$ at $T = 20$ K in the AFM state. Data in (a)–(f) and (h)–(o) are measured with incident beam fixed along the crystallographic c direction, and in (g) coaligned set was rotated about the vertical axis perpendicular to the beam direction, i.e. rotating the sample about $(-K, K)$ with an angular step of 1° over the range of 15° – 160° . Incident energies for the measurement were $E_i = 73.9, 49.75$ and 238.4 meV for (a)–(g), (h)–(k) and (l)–(o), respectively. Energy dependence slices of the data along the longitudinal (LO) direction $[H, H]$ in (a), (h) and (l) are obtained after averaging over the range of $\pm 0.1, \pm 0.05$ and ± 0.15 r.l.u., respectively, along the transverse (TR) direction. Energy dependence slices of the data along the TR direction $[-K, K]$ in (b), (i) and (m) are obtained after averaging over the range of $\pm 0.1, \pm 0.05$ and ± 0.1 r.l.u., respectively, along the LO direction. Constant-energy (Q) slices in (c)–(f) are obtained after averaging over $E = 59$ – $63, 45$ – $51, 30$ – $34, 8$ – 12 meV, respectively, (j), (k) over $E = 35$ – $39, 23$ – 27 meV, respectively, and (n), (o) over $E = 97$ – $108, 59$ – 70 meV, respectively. Part of the figure is from Ref. [133].

about the instrumental resolution and convolution is discussed in the end of this Section at 5.3.1. The velocities of the spin waves along the respective directions are obtained from the fits of these dispersion plots using the dispersion model

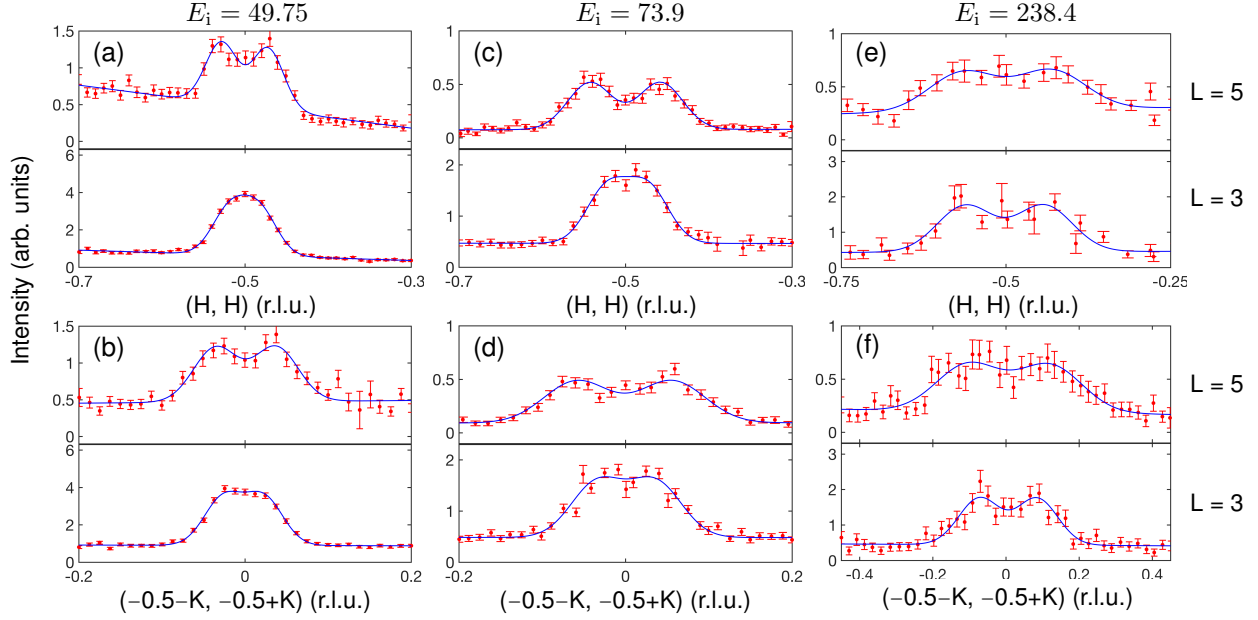


Figure 5.5 One dimensional cuts along the LO and TR directions obtained for the Q slices shown in Figs. 5.4. Blue lines are fit to the two Gaussian lineshapes.

$$E(\mathbf{q}) = \sqrt{\Delta^2 + v_{\text{LO}}^2 q_{\text{LO}}^2 + v_{\text{TR}}^2 q_{\text{TR}}^2 + v_c^2 q_c^2}, \quad (5.1)$$

where, v_{LO} , v_{TR} , and v_c are spin wave velocities along the LO, TR, and c directions, respectively, and $\mathbf{q} = \mathbf{Q} - \mathbf{Q}_{\text{stripe}}$. Δ in the Eq. (5.1) is the spin gap and was determined by fitting the E (energy) cut at $\mathbf{Q}_{\text{stripe}}$ as shown in Fig. 5.7(b), using the Eq. (5.2). The fit yielded $\Delta = 5.3 \pm 1.5$ meV. The velocities obtained from the fits to Eq. (5.1) are listed in Table 5.2, along with the corresponding values of $x = 0$.

$$S(Q, E) = \frac{AE'\Gamma}{\Gamma^2 + E'^2} \quad (5.2)$$

where E' is given by

$$E' = \frac{1}{\sqrt{2}} \left[\left((E^2 - \Gamma_s^2 - \Delta^2)^2 + 4E^2\Gamma_s^2 \right)^{1/2} + (E^2 - \Gamma_s^2 - \Delta^2) \right]^{1/2}. \quad (5.3)$$

Here, A is the lineshape amplitude, E is the energy transfer, Δ is the spin gap, Γ_s is a damping constant that describes the sharpness of the gap, and Γ is the energy scale of the spin fluctuations.[141]

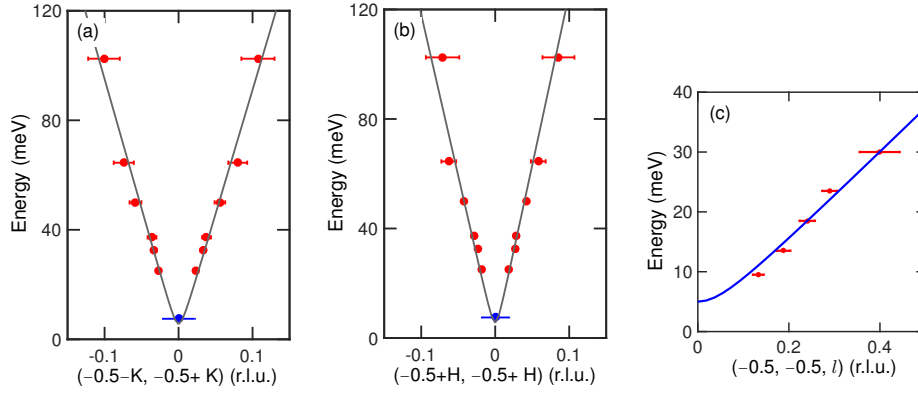


Figure 5.6 Spin-wave dispersion along the TR, LO, and $[0, 0, L]$ directions. The solid lines are fits to Eq. (5.1). l in $(-0.5, -0.5, l)$ in (c) represents the half width at half maximum of peaks centered at $(0.5, 0.5, 1)$ or $(0.5, 0.5, 3)$. The dispersion data along $[0, 0, L]$ provide a lower bound of the spin-wave velocity along L . The figure is reproduced from Ref. [133].

Table 5.2 Comparison of spin gap and spin-wave velocities for $x = 0$ and 0.026. The table is reproduced from Ref. [133].

	$x = 0$	$x = 0$	$x = 0.026$
	Ref. [47]	Ref. [49]	
Δ (meV)	7	6.8	5.3 ± 1.5
v_{LO} (meVÅ)	534	498	520 ± 20
v_{TR} (meVÅ)	386	347	400 ± 17
v_c (meVÅ)	246	259	137 ± 4
v_c/v_{LO}	0.46	0.52	0.26 ± 0.01

The fit shows that all the parameters spin gap, in-plane velocities (v_{LO} , v_{TR}) are almost similar to that of the parent compound except for the decrease in the interlayer velocity v_c and the ratio v_c/v_{LO} . The decrease suggests the relative decrease of the strength of the interlayer interaction

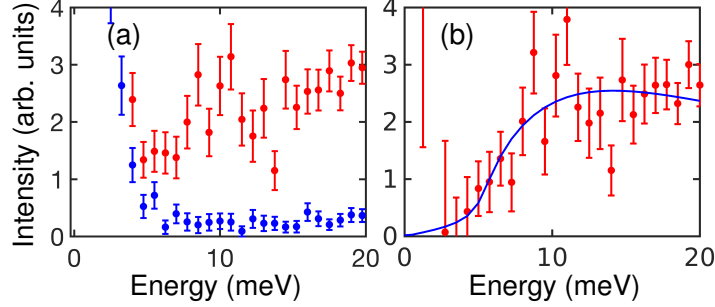


Figure 5.7 Energy cuts of $x = 0.026$ in Fig. 5.4(g) measured at $T = 20$ K. (a) Cut at $(-0.5, -0.5, -1)$ (red symbols) and background cut at $(-0.6, -0.6, -1)$ (blue symbol) obtained after averaging over the LO and TR directions by ± 0.05 r.l.u. The cut shown in (b) is obtained after subtracting both the background cut and the elastic Bragg peak from cut at $(-0.5, -0.5, -1)$. To subtract the Bragg peak, the elastic peak remained after subtracting cut at $(-0.6, -0.6, -1)$ from cut at $(-0.5, -0.5, -1)$ is fit with a PseudoVoigt lineshape and the fit is subtracted. Blue line is fit to a model described in Eq. (5.2) used to determine the spin gap Δ . The figure is reproduced from Ref. [133].

and dimensionality of the magnetism with increasing x in $\text{Ca}(\text{Fe}_{1-x}\text{Co}_x)_2\text{As}_2$. The evolution of the spin dynamics from anisotropic 3D spin waves to quasi-two dimensional (2D) spin fluctuations with increasing Co doping is similar to $\text{Ba}(\text{Fe}_{1-x}\text{Co}_x)_2\text{As}_2$ [135]. Additionally, no diffusive spin fluctuations are observed in $\text{Ca}(\text{Fe}_{1-x}\text{Co}_x)_2\text{As}_2$ $x = 0.026$ despite that it has T_N similar to $\text{Ba}(\text{Fe}_{1-x}\text{Co}_x)_2\text{As}_2$ with $x \approx 0.040$ [60], wherein the diffusive spin fluctuations are observed in the AFM state [5]. In $\text{Ba}(\text{Fe}_{1-x}\text{Co}_x)_2\text{As}_2$ the appearance of diffusive spin fluctuations corresponds to the region where the AFM order and SC states coexist microscopically and such coexistence region is absent in $\text{Ca}(\text{Fe}_{1-x}\text{Co}_x)_2\text{As}_2$. Hence, the result suggest that, unlike $\text{Ba}(\text{Fe}_{1-x}\text{Co}_x)_2\text{As}_2$, there will be no diffusive spin fluctuations in the AFM state of $\text{Ca}(\text{Fe}_{1-x}\text{Co}_x)_2\text{As}_2$ and accordingly present another evidence of the requirement of the diffusive spin fluctuations for the existence of SC.

5.3.1 Convolution with instrumental resolution

The data in Fig. 5.4(g) from which the dispersion along $[0, 0, L]$ is determined do not show two resolvable spin-wave branches. This is due to the instrumental resolution. To account for

broadening due to the resolution, the peak in a Q cut of data from Fig. 5.4(g) is fit to a Gaussian lineshape convoluted with another Gaussian lineshape that represents the instrumental resolution. The FWHM of the Gaussian lineshape for the resolution is calculated using [142],

$$\delta Q = \frac{1}{Q} [Q_x^2 (\delta Q_x)^2 + Q_y^2 (\delta Q_y)^2]^{1/2}, \quad (5.4)$$

where

$$\begin{aligned} \delta Q_x = \frac{m_n}{\hbar} \left\{ \frac{1}{L_1^2} (v_i^2 + v_f^2 \frac{L_2}{L_3} \cos 2\theta)^2 \delta t_p^2 \right. \\ \left. + \frac{1}{L_1^2} (v_i^2 + v_f^2 \frac{L_1 + L_2}{L_3} \cos 2\theta)^2 \delta t_c^2 \right. \\ \left. + (\frac{v_f^2}{L_3} \cos 2\theta)^2 \delta t_d^2 + (v_f \sin 2\theta)^2 (\delta 2\theta)^2 \right\}^{1/2}, \end{aligned}$$

and

$$\begin{aligned} \delta Q_y = \frac{m_n}{\hbar} \left\{ \frac{v_f^2 L_2}{L_1 L_3} \sin 2\theta)^2 \delta t_p^2 \right. \\ \left. + (\frac{v_f^2}{L_1} \frac{L_1 + L_2}{L_3} \sin 2\theta)^2 \delta t_c^2 \right. \\ \left. + (\frac{v_f^2}{L_3} \sin 2\theta)^2 \delta t_d^2 + (v_f \cos 2\theta)^2 (\delta 2\theta)^2 \right\}^{1/2}. \end{aligned}$$

Here, δQ , $\delta Q_{x,y}$, Q , and $Q_{x,y}$ have units of \AA^{-1} , v_i and v_f are initial and final velocities of the neutron, L_1 , L_2 and L_3 are the distances from the moderator to the Fermi chopper, the Fermi chopper to the sample, and the sample to the detector, respectively, δt_p , δt_c , and δt_d are time spreads associated with neutron travel through the moderator and Fermi chopper, and the uncertainty associated with the sample position, respectively. Here, x and y represents the direction parallel and perpendicular to the incident beam direction. The sample width is taken to be 3 cm, which approximates the extent of the co-aligned single-crystal sample. Values of the resolution δQ for data at (0.5, 0.5, 1) and (0.5, 0.5, 3) are shown in Table 5.3.

Using the corresponding value of δQ given in Table 5.3 as the width of the Gaussian lineshape representing the instrumental resolution, a peak in a Q cut is fit to:

$$I(q) = \frac{A}{2\pi\sigma_1\sigma_2} \int_{-\infty}^{\infty} e^{-q^2/2\sigma_1^2} e^{-(q'-q)^2/2\sigma_2^2} dq', \quad (5.5)$$

where, I is the neutron-scattering intensity, and σ_1 and σ_2 represents the standard deviation of the peak corresponding to the signal of interest and the instrumental resolution, respectively.

Table 5.3 Instrumental resolution δQ for Q cuts centered at $(0.5, 0.5, 1)$ for E up to 23.5 meV and $(0.5, 0.5, 3)$ for E up to 30 meV, with $E_i = 73.9$ meV. The table is reproduced from Ref. [133].

E (meV)	9	13.5	18.5	23.5	30
δQ (\AA^{-1})	0.08	0.08	0.08	0.09	0.08

5.4 Spin dynamics evolution in the high-temperature paramagnetic state

In this section, INS measurements performed in the PM phase at $T = 90$ K for $x = 0.026$ ($T/T_N \approx 1.4$) and $x = 0.030$ are compared with that of the parent $x = 0$ compound discussed in Ref. [80]. Similar to the parent compound, scattering due to spin fluctuations originates from $\mathbf{Q}_{\text{stripe}}$, appears broader in E as well as \mathbf{Q} as shown in Fig. 5.8, and possesses different broadening along the LO and TR directions, which indicates anisotropic in-plane magnetic correlations. The broadening is due to a combination of shorter-lived spin dynamics, weaker interlayer interactions, and shorter-range in-plane correlations of the Fe moments.

These are characteristics of diffusive spin fluctuations and can be described by the diffusive model discussed in Refs. [107] and [80] for the spin dynamics in the PM phase of the parent compound. The model considers the anisotropic in-plane correlations along with overdamped dynamics originating due to the decay of spin-fluctuations into particle-hole excitations. The resulting imaginary part of the dynamical susceptibility is

$$\chi''(\mathbf{q} + \mathbf{Q}_{\text{stripe}}, E) = \frac{\gamma\chi_0 E}{E^2 + \gamma^2 \left\{ (q_x^2 + q_y^2 + \eta q_x q_y) a^2 + \left(\frac{a}{\xi}\right)^2 + \eta_c [1 + \cos(\pi L)] \right\}^2}, \quad (5.6)$$

where $\mathbf{q} = \mathbf{Q} - \mathbf{Q}_{\text{stripe}}$, $q^2 = q_x^2 + q_y^2 + q_c^2$, χ_0 is the staggered susceptibility, γ denotes the damping coefficient originating from decay of spin fluctuations into particle-hole excitations, ξ is

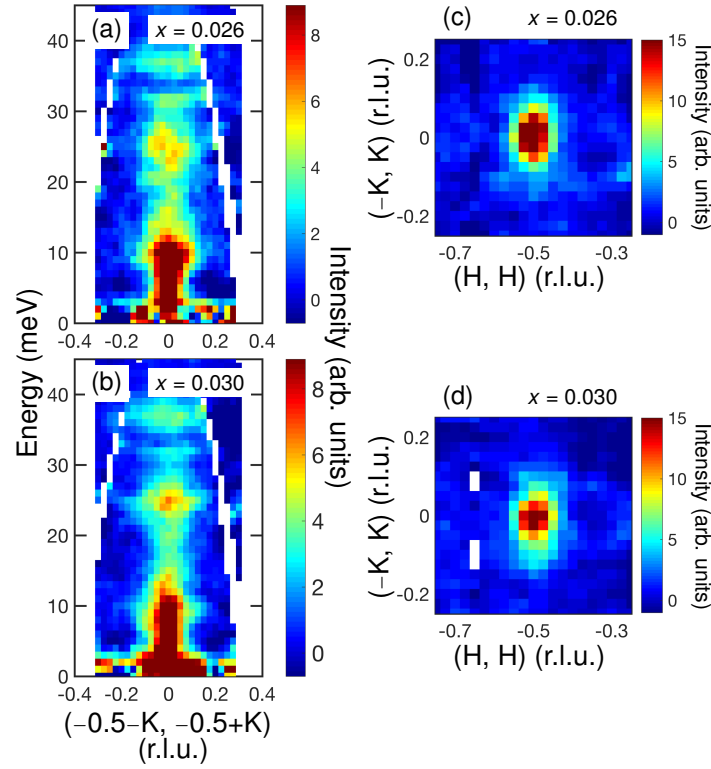


Figure 5.8 Paramagnetic spin fluctuations in $\text{Ca}(\text{Fe}_{1-x}\text{Co}_x)_2\text{As}_2$ ($x = 0.026$ and 0.030) measured at $T = 90$ K with $E_i = 49.75$ meV. (a) and (b) Transverse slices of the background subtracted data through $(-0.5, -0.5)$ averaged over the LO direction by ± 0.06 r.l.u., for $x = 0.026$ and 0.030 , respectively. An isotropic background has been estimated and subtracted as discussed in Ref. [91]. (c) and (d) Q slices of the background subtracted data averaged over the $E = 5.5\text{--}9.5$ meV, for $x = 0.026$ and 0.030 , respectively. The black lines along the LO and the TR direction in (c) of different length illustrates the anisotropic peak width. The figure is reproduced from Ref. [133].

the magnetic correlation length, η represents the anisotropy of the in-plane magnetic correlation length, and $\eta_c = J_c\chi_0$ gives the strength of the interlayer spin correlations.

The fluctuation dissipation theorem relates the imaginary part of dynamical susceptibility to the dynamical structure factor by,

$$S(\mathbf{Q}, E) = (r_0)^2 \frac{f^2(\mathbf{Q})}{2\pi\mu_B^2} \frac{\chi''(\mathbf{q} + \mathbf{Q}_{\text{stripe}}, E)}{1 - e^{-E/kT}}, \quad (5.7)$$

where $(r_0)^2 = 290.6 \text{ mbarns sr}^{-1}$ and $f(\mathbf{Q})$ is the magnetic form factor for Fe^{2+} . The E and Q cuts, for $x = 0.026$ and 0.30 at $T = 90 \text{ K}$ and for $x = 0.030$ at $T = 20 \text{ K}$, shown in Figs. 5.9, were simultaneously fit to Eqs. (5.6) and (5.7). The results of the fits are listed in Table 5.4 along with values for CaFe_2As_2 taken from Refs. [80, 107].

The size of the fluctuating moment (or spectral weight) per Fe atom is estimated by using the fitted values in Table 5.4 and the equation

$$\langle m^2 \rangle = \frac{1}{2} \frac{3}{\pi} \frac{\int \chi''(\mathbf{Q}, E) (1 - e^{-E/kT})^{-1} d\mathbf{Q} dE}{\int d\mathbf{Q}}, \quad (5.8)$$

Similar to the parent compound [80], the integration is done in the orthorhombic zone defined by the ranges $0 \leq Q_x \leq \frac{2\sqrt{2}\pi}{a}$, $\frac{-\sqrt{2}\pi}{a} \leq Q_y \leq \frac{\sqrt{2}\pi}{a}$ and $0 \leq Q_z \leq \frac{4\pi}{c}$, and an upper energy cutoff of $\sim 200 \text{ meV}$ is used. The calculated values for $\sqrt{\langle m^2 \rangle}$ are given in Table 5.4.

Table 5.4 Comparison of the parameters of the diffusive model in Eq. (5.6) of the $\text{Ca}(\text{Fe}_{1-x}\text{Co}_x)_2\text{As}_2$ data and the corresponding values for CaFe_2As_2 [80, 107] along with fluctuating moment per Fe calculated using the fit parameters. The table is reproduced from Ref. [133].

	$x = 0$	$x = 0$	$x = 0.026$	$x = 0.030$
	Ref. [80], $T = 180 \text{ K}$	Ref. [107], $T = 150 \text{ K}$	$T = 90 \text{ K}$	$T = 90 \text{ K}$
$\chi_0(\mu_B^2 \text{ meV}^{-1} \text{ f.u.}^{-1})$	0.20 ± 0.05	—	0.14 ± 0.01	0.15 ± 0.01
η	0.55 ± 0.36	1.0 ± 0.2	0.88 ± 0.14	0.90 ± 0.13
$\Gamma(\text{meV})$	10.0	14.3 ± 0.8	7.8 ± 0.5	9.8 ± 0.5
$\gamma(\text{meV})$	43 ± 5	37 ± 2	41 ± 3	41 ± 3
$\xi (\text{\AA})$	7.9 ± 0.1	6.4 ± 0.2	9.0 ± 0.2	8.0 ± 0.2
$\sqrt{\langle m^2 \rangle} (\mu_B/\text{Fe})$	0.71 ± 0.09	—	0.60 ± 0.02	0.63 ± 0.02

The fit parameters for $T = 90 \text{ K}$ of $x = 0.030$ and $x = 0.026$ are similar with each other within the error bar and are similar with those for $x = 0$ at $T = 150$ and 180 K . This shows that

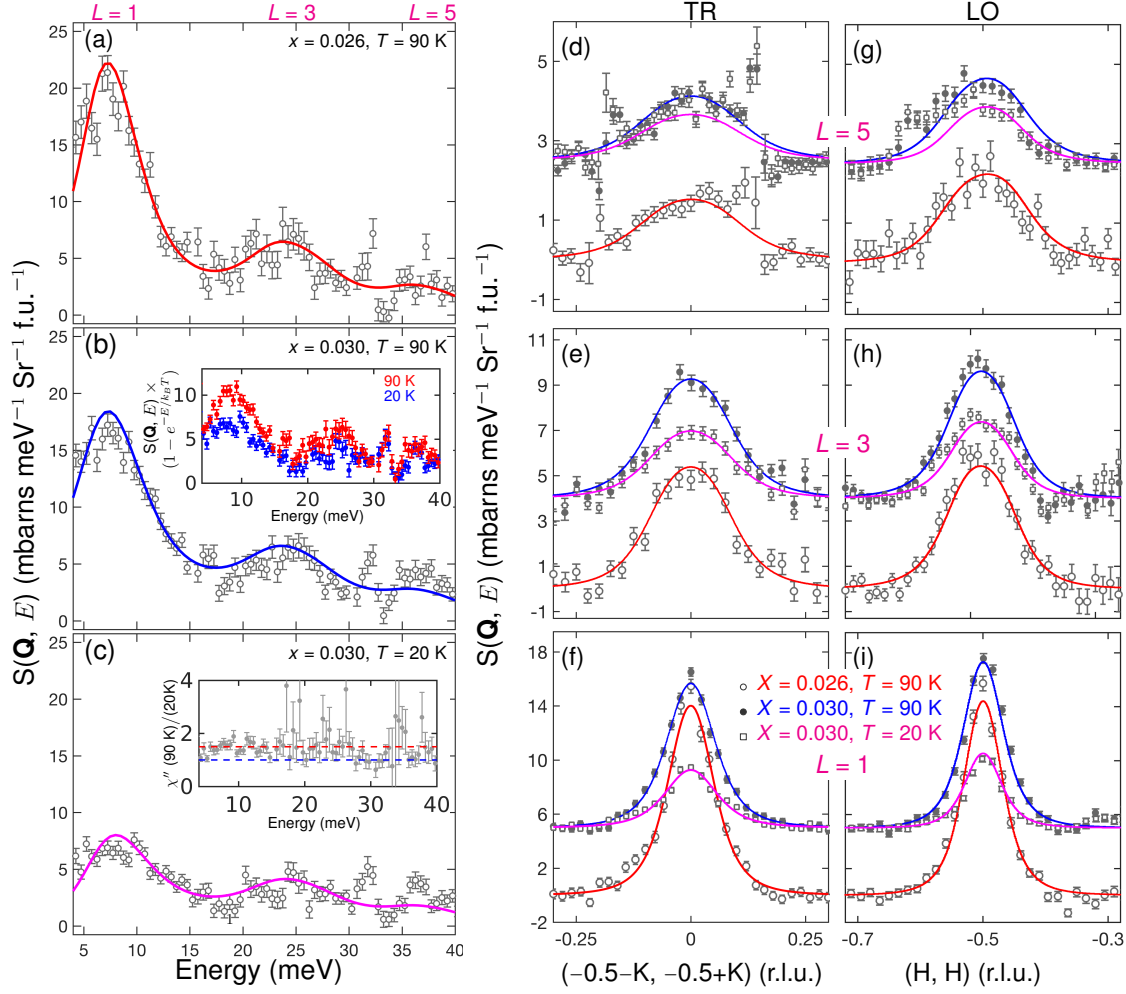


Figure 5.9 E and Q cuts at $\mathbf{Q}_{\text{stripe}}$ for $x = 0.026$ and 0.030 at $T = 90$ and 20 K with $E_i = 49.75$ meV and \mathbf{c} fixed along the incident beam. Data are subtracted by an isotropic background, similar to Ref. [91], for E cuts and averaged over ± 0.03 r.l.u. in both the LO and TR directions. A fitted background has been subtracted for Q cuts and the cuts are taken at energy transfers corresponding to $L = 1, 3$, and 5 . The in-plane anisotropy of the scattering is apparent from the difference in the width of the scattering along the LO and TR directions. Red, blue, and magenta lines are fits using the model discussed in the text with the parameters in Tables 5.4 and 5.5. Cuts for different values of L are shifted by arbitrary offsets for clarity. The inset to (b) shows bose-factor corrected E cuts for $x = 0.030$ at $T = 90$ K (red circle) and 20 K (blue circle). The inset to (c) shows the ratio of the $T = 90$ and 20 K data shown in the inset to (b). Dashed red and blue horizontal line is a guide for the ratio 1.5 and 1 , respectively. The figure is reproduced from Ref. [133].

the diffusive spin dynamics in the PM phase at higher temperatures are relatively insensitive to Co-doping. This is different than the case of $\text{Ba}(\text{Fe}_{1-x}\text{Co}_x)_2\text{As}_2$ for which Landau damping (i.e. γ) increases with increasing x [5, 91].

5.4.1 Fitting procedure of the paramagnetic spin fluctuations using the diffusive model

For the fits of the E and Q cuts in Fig. 5.9, η was determined from the width of the Q cuts in the TR and LO directions for $L = 1$ shown in Fig. 5.9(f) and (i). The Q cuts were fit to a Gaussian line shape, and the corresponding magnetic correlation length was determined from the fitted FWHM (κ) using $\xi \approx \frac{a}{\sqrt{2}} \times \frac{1}{2\pi} \times \frac{2.3548}{\kappa}$. η was then determined from the magnetic correlation lengths using the relation $\eta = 2 \frac{\xi_{\text{LO}}^2 - \xi_{\text{TR}}^2}{\xi_{\text{LO}}^2 + \xi_{\text{TR}}^2}$ and is kept fixed throughout the fitting.

The protocol for the fits follows. First, the E cuts in Fig. 5.9 were fit by keeping η_c fixed at a value in the range from 0.1 to 0.6. The Lorentzian width $[\Gamma = \gamma(\frac{a}{\xi})^2]$ obtained from the fits was then kept fixed in subsequent fitting of the Q cuts shown in Fig. 5.9. Fits of the Q cuts for different values of L and along different directions (LO and TR) produced almost identical values of χ_0 and ξ . Due to the interrelated nature of χ_0 and ξ , the average of χ_0 from all of the fits was then kept fixed to the values in Table 5.4 and the data were fit again by varying ξ . During the entire fitting procedure (i.e. for χ_0 fixed and free), ξ is found within ± 0.5 of the average value shown in Table 5.4. Finally, the best fit values of η_c ($0.1 < \eta_c < 0.25$) was determined from the chi-squared analysis of the fits where only η_c was varied.

5.5 Anomalous suppression of the spin fluctuations at low-temperatures for $x = 0.030$

Figure 5.9 also shows the E and Q cuts of the diffusive spin fluctuations for $x = 0.030$ at 20 K ($T/T_c \approx 1.4$) and illustrates the decrease in intensity at 20 K in comparison to the 90 K. The inset to Fig. 5.9(b) shows the background subtracted data after correcting by the Bose factor and illustrates that χ'' decreases upon cooling down to $T = 20$ K. The inset to Fig. 5.9(c) presents

the ratio of χ'' at $T = 90$ K to that at 20 K, and shows that the 20 K data decrease by a scale factor of nearly 1.5 for all energy transfers < 30 meV. In addition, TR energy dependence slices in Figure 5.10 for $x = 0.030$ at three temperatures $T = 90$, 20 and 6 K also indicate diffusive spin fluctuations with small intensity at 20 and 6 K than 90 K.

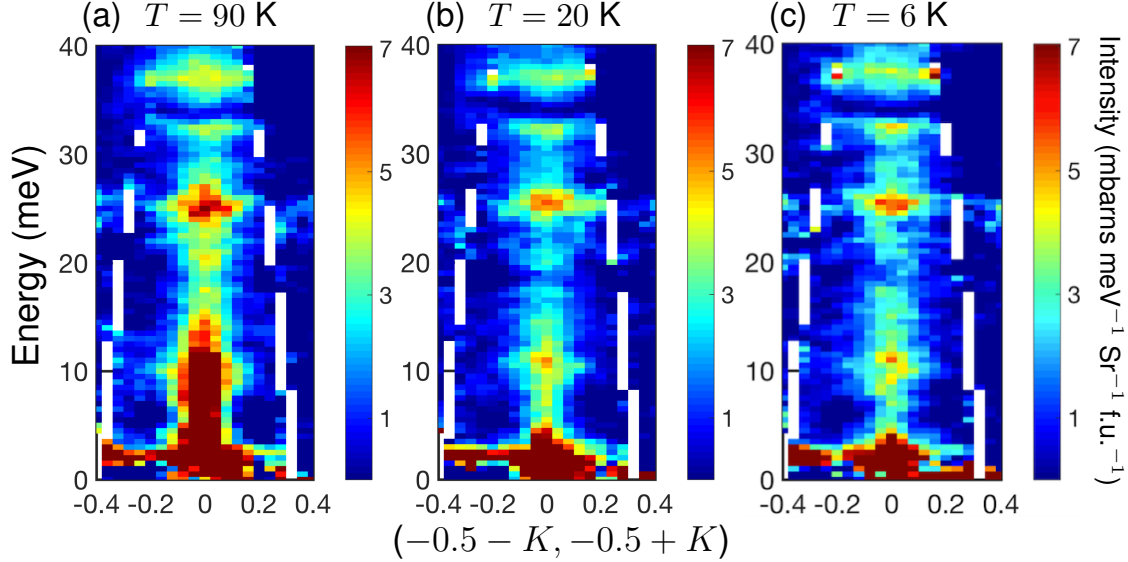


Figure 5.10 Paramagnetic spin fluctuations in $\text{Ca}(\text{Fe}_{1-x}\text{Co}_x)_2\text{As}_2$ ($x = 0.030$) measured at $T = 90, 20$ and 6 K with $E_i = 49.75$ meV. (a)–(c) Transverse slices of the background subtracted data through $(-0.5, -0.5)$ averaged over the LO direction by ± 0.06 r.l.u., for $x = 0.030$, at 90, 20 and 6 K, respectively. An isotropic background has been estimated and subtracted as discussed in Ref. [91]. The intensity is in absolute unit and is of the same range for all three figures.

The suppression of the spectral weight with decreasing temperature is peculiar than the ones observed in CaFe_2As_2 [80] and SC $\text{Ba}(\text{Fe}_{1-x}\text{Co}_x)_2\text{As}_2$ [65], where the spectral weight decreases with increasing temperature corresponding to the decrease in the magnetic correlation length. The diffusive spin fluctuations and the suppression of 20 K are quantified by fitting the data using the diffusive model and the results of the best fit are listed in Table 5.5.

The result shows that parameters from fits of the diffusive model to the $T = 20$ K data compare well with those for 90 K, except for a decrease of χ_0 , which indicates a loss of fluctuating Fe moment. The calculation of the fluctuating Fe moment from these fit values gives $\sqrt{\langle m^2 \rangle} =$

$(0.50 \pm 0.02 \mu_B)/\text{Fe}$, which is a decrease of nearly 21% at 20 K with respect to 90 K. Thus, the observed suppression of spectral weight is associated with the loss of fluctuating Fe moment with decreasing temperature. In addition, similar diffusive spin fluctuations are observed at 6 K in the superconducting state ($T_c \approx 14$ K). The similarity of the E and Q cuts shown in Fig. 5.11 and TR slices in Fig. 5.10 (b) and (c) for $T = 20$ and 6 K suggests that there is no further decrease in intensity for $T < 20$ K. The 6 K data were also fit using the diffusive model following the same procedure as discussed above and the fit parameters are listed in Table 5.5. From these fit parameters, the fluctuating Fe moment of $\sqrt{\langle m^2 \rangle} = (0.47 \pm 0.02 \mu_B)/\text{Fe}$ is calculated for $T = 6$ K.

Table 5.5 Comparison of fit parameters of $T = 90, 20$ and 6 K data for $\text{Ca}(\text{Fe}_{1-x}\text{Co}_x)_2\text{As}_2$, $x = 0.030$. The table is reproduced from Ref. [133].

	$x = 0.030$	$x = 0.030$	$x = 0.030$
	$T = 90$ K	$T = 20$ K	$T = 6$ K
$\chi_0(\mu_B^2 \text{ meV}^{-1} \text{ f.u.}^{-1})$	0.15 ± 0.01	0.09 ± 0.01	0.08 ± 0.01
η	0.90 ± 0.13	1.12 ± 0.30	1.10 ± 0.30
$\Gamma(\text{meV})$	9.8 ± 0.5	9.5 ± 0.8	9.7 ± 0.9
$\gamma(\text{meV})$	41 ± 3	45 ± 4	47 ± 5
$\xi (\text{\AA})$	8.0 ± 0.2	8.5 ± 0.2	8.6 ± 0.2
$\sqrt{\langle m^2 \rangle} (\mu_B/\text{Fe})$	0.63 ± 0.02	0.50 ± 0.02	0.47 ± 0.02

5.6 Spin resonance in the superconducting state for $x = 0.030$

The $x = 0.030$ compound undergoes superconducting transition below $T_c \approx 14$ K and similar to other iron arsenide superconductors[65], spin-resonance peak in the spin fluctuations spectrum is expected below T_c , due to a redistribution of the spectral weight. So, taking $E_{\text{res}} = 4.5k_B T_c$ as the value for the expected resonance energy, as in optimally doped $\text{Ba}(\text{Fe}_{1-x}\text{Co}_x)_2\text{As}_2$ [135], the resonance peak is expected at ≈ 5.4 meV. However, Fig. 5.11 shows the E and Q cuts for the measurement performed at $T = 6$ K, that is below $T_c \approx 14$ K without any sing of enhanced peak corresponding to spin resonance around this and other E .

The absence of the spin resonance in our measurement does not conclude the absence of the spin resonance in $\text{Ca}(\text{Fe}_{1-x}\text{Co}_x)_2\text{As}_2$ as there is another plausible explanation, which is caused by

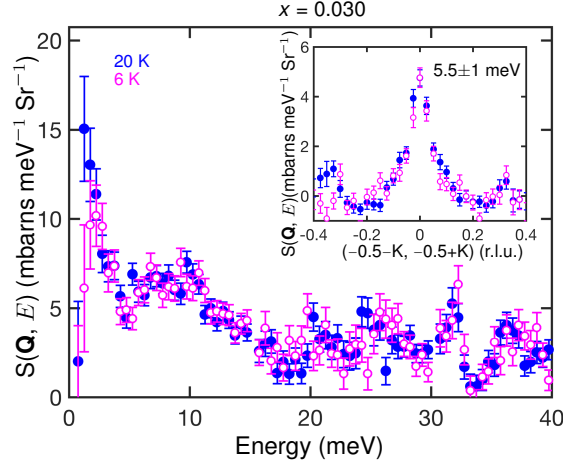


Figure 5.11 E cuts at $\mathbf{Q}_{\text{stripe}}$ for $x = 0.030$ measured at $T = 20$ (filled circle) and 6 K (open circle) with $E_i = 49.75$ meV. Data are subtracted by an isotropic background, similar to Ref. [91], and averaged over ± 0.03 r.l.u. in both the LO and TR directions. The inset shows Q cuts along the TR direction obtained after averaging over $E = 4.5$ – 6.5 meV and along the LO direction by ± 0.05 . Data for $E \leq 4$ meV are dominated by incoherent background scattering. The figure is reproduced from Ref. [133].

the experimental configuration. The measurement were performed with the incident beam kept fixed along the \mathbf{c} , thus, E and L are coupled. In this experimental configuration, $E = 5.4$ meV corresponds to $L = 0.77$ for $E_i = 49.75$ meV and in-plane wavevector of $(0.5, 0.5)$. The resonance peak is expected to center at $L = 1, 3, \dots$ position corresponding to $\mathbf{Q}_{\text{stripe}}$ $(0.5, 0.5)$ in-plane and the value of $L = 0.77$ is shifted away from the optimal $L = 1$ position. Moreover, the stronger 3D character of CaFe_2As_2 (as compared to BaFe_2As_2) [26] suggests that the resonance intensity away from $L = 1$ is strongly suppressed. Thus, another measurement that accesses lower energy transfers at $\mathbf{Q}_{\text{stripe}}$ is required to make a firm conclusion about the existence of a spin-resonance peak.

5.7 Discussion of the results

The results presented above show that: (1) spin excitations centered at $\mathbf{Q}_{\text{stripe}}$ occur in the T-PM, O-AFM, and SC phases of $\text{Ca}(\text{Fe}_{1-x}\text{Co}_x)_2\text{As}_2$; (2) the low-temperature spin dynamics become more 2D with increasing electron doping up to at least $x = 0.030$; (3) well-defined gapped spin

waves with small damping persist in the O-AFM phase up to at least $x = 0.026$; (4) similar diffusive spin fluctuations are present in the T-PM phase for both $x = 0.026$ and 0.030 at $T = 90$ K; (5) similar diffusive spin fluctuations are present in the SC phase of $x = 0.030$ as in the normal T-PM state; (6) For $E < 30$ meV, $\chi''(\mathbf{Q}_{\text{stripe}}, E)$ decreases between $T = 90$ and 20 K for $x = 0.030$. (7) The low-temperature ($T = 20$ K) spin dynamics changes abruptly between O-AFM $x = 0.026$ and T-PM $x = 0.030$, where the change in x is only 0.004 , which appears to be consistent with the strong-first order line separating O-AFM and other phases in $\text{Ca}(\text{Fe}_{1-x}\text{Co}_x)_2\text{As}_2$. Next, these results are compared with those for the closely related electron-doped series $\text{Ba}(\text{Fe}_{1-x}\text{Co}_x)_2\text{As}_2$. Descriptions of the spin dynamics in other related compounds are found in, for example, Ref. [3]. The summary of the results are illustrated in Fig. 5.12.

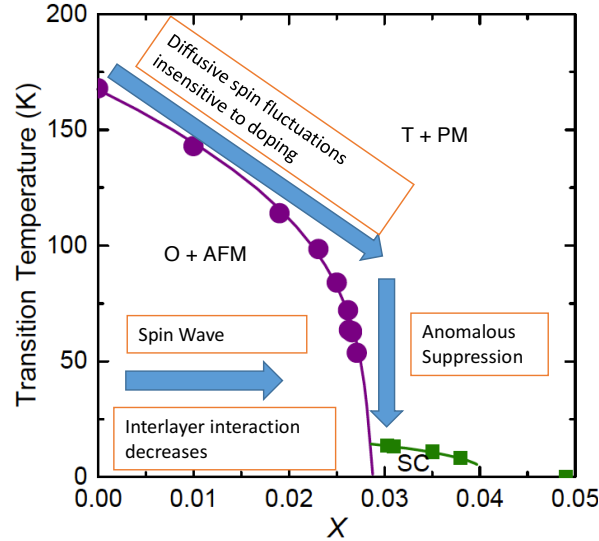


Figure 5.12 Illustration of spin fluctuations evolution in $\text{Ca}(\text{Fe}_{1-x}\text{Co}_x)_2\text{As}_2$. The figure summarizes the results of the inelastic neutron scattering measurement discussed above.

Similar to $\text{Ca}(\text{Fe}_{1-x}\text{Co}_x)_2\text{As}_2$, spin excitations centered at $\mathbf{Q}_{\text{stripe}}$ are found in the T-PM, O-AFM, and SC phases of $\text{Ba}(\text{Fe}_{1-x}\text{Co}_x)_2\text{As}_2$ [65, 81, 91, 143], and the spin dynamics become more 2D with increasing x [5]. However, AFM order and SC microscopically coexist in underdoped $\text{Ba}(\text{Fe}_{1-x}\text{Co}_x)_2\text{As}_2$ over $0.04 \lesssim x \lesssim 0.06$ [64, 83], with the appearance of SC being coincident with

an increase in the damping of spin excitations[5]. As x is increased through the coexistence region, connecting O-AFM and SC phases, a crossover from the well-defined spin waves to the diffusive spin fluctuations occurs [5]. Since $\text{Ca}(\text{Fe}_{1-x}\text{Co}_x)_2\text{As}_2$ does not possess a region of microscopically coexisting AFM order and SC, one may expect that the crossover to diffusive spin fluctuations found for $\text{Ba}(\text{Fe}_{1-x}\text{Co}_x)_2\text{As}_2$ is absent.

The results presented above are consistent with this expectation, as the data show that well-defined spin waves persist in the AFM phase of $\text{Ca}(\text{Fe}_{1-x}\text{Co}_x)_2\text{As}_2$ up to at least $x = 0.026$. One can go a step further by considering that T_N for $x = 0.026$ is similar to T_N for $x \approx 0.040$ $\text{Ba}(\text{Fe}_{1-x}\text{Co}_x)_2\text{As}_2$, which displays diffusive spin dynamics. Thus, despite a similar characteristic energy for the AFM order in both of these compounds, their magnetic-excitation spectra are inherently different, with the striking physical difference between the two compounds being the presence of SC.

Analysis of INS data for $\text{Ba}(\text{Fe}_{1-x}\text{Co}_x)_2\text{As}_2$ also indicates that the crossover from well-defined spin waves to diffusive spin fluctuations with increasing x in its O-AFM phase is concomitant with a suppression of the spin-density-wave gap Δ_{SDW} associated with the itinerant AFM order [5]. Since Δ_{SDW} is proportional to the ordered-magnetic moment μ , [5, 144] changes in μ should reflect changes to Δ_{SDW} , and the size of μ can be used as a determining factor for the appearance of diffusive spin dynamics. μ for $\text{Ba}(\text{Fe}_{1-x}\text{Co}_x)_2\text{As}_2$ decreases from 0.87 to $\approx 0.1 \mu_B/\text{Fe}$ as the composition is varied from $x = 0$ to 0.059[64, 83], which is near the O-AFM to SC phase boundary. On the other hand, μ for $\text{Ca}(\text{Fe}_{1-x}\text{Co}_x)_2\text{As}_2$ changes very little across the O-AFM phase, decreasing from $\mu = 0.8 \mu_B/\text{Fe}$ for $x = 0$ to $\mu = 0.71 \mu_B/\text{Fe}$ for $x = 0.028$ [145], which is near the first-order phase boundary. Hence, the change in Δ_{SDW} across the O-AFM phase of $\text{Ca}(\text{Fe}_{1-x}\text{Co}_x)_2\text{As}_2$ should be much less than for $\text{Ba}(\text{Fe}_{1-x}\text{Co}_x)_2\text{As}_2$, which supports the notion that well-defined spin waves persist throughout the O-AFM state of $\text{Ca}(\text{Fe}_{1-x}\text{Co}_x)_2\text{As}_2$.

The negligible increase in damping of the spin fluctuations in the T-PM phase of $\text{Ca}(\text{Fe}_{1-x}\text{Co}_x)_2\text{As}_2$ with increasing x is in contrast to the sizable increase in damping of the fluctuations seen for $\text{Ba}(\text{Fe}_{1-x}\text{Co}_x)_2\text{As}_2$ [5, 91]. This difference can be understood in terms of changes to the electronic-

band structure due to electron doping. In particular, the shrinking (expansion) of hole (electron) pockets due to the addition of electrons changes the Fermi velocities of electrons and holes connected by $\mathbf{Q}_{\text{stripe}}$, resulting in an increase in damping in $\text{Ba}(\text{Fe}_{1-x}\text{Co}_x)_2\text{As}_2$ [5]. Since the number of electrons introduced into optimally doped $\text{Ca}(\text{Fe}_{1-x}\text{Co}_x)_2\text{As}_2$ is nearly half that for optimally doped $\text{Ba}(\text{Fe}_{1-x}\text{Co}_x)_2\text{As}_2$ [4], the almost constant value of the damping parameter in the T-PM phase of $\text{Ca}(\text{Fe}_{1-x}\text{Co}_x)_2\text{As}_2$ for $x \leq 0.030$ may be the result of smaller changes to its Fermi surface between $x = 0$ and its optimal-doping level.

Similar to $\text{Ca}(\text{Fe}_{1-x}\text{Co}_x)_2\text{As}_2$, diffusive spin fluctuations are found for the T-PM and SC phases of $\text{Ba}(\text{Fe}_{1-x}\text{Co}_x)_2\text{As}_2$. However, as discussed in section 5.6, the limitations of the experimental setup in regards to being able to determine whether or not a spin-resonance peak exists in the SC phase. Next, I am going to discuss the decrease in $\chi''(\mathbf{Q}_{\text{stripe}}, E)$, for $4 \lesssim E < 30$ meV, with decreasing temperature in the T-PM phase of $x = 0.030$ $\text{Ca}(\text{Fe}_{1-x}\text{Co}_x)_2\text{As}_2$.

The decrease in $\chi''(\mathbf{Q}_{\text{stripe}}, E)$ at low energies contrasts with previous results for the T-PM states of CaFe_2As_2 [80] and $\text{Ba}(\text{Fe}_{1-x}\text{Co}_x)_2\text{As}_2$ [65, 146] where $\chi''(\mathbf{Q}_{\text{stripe}}, E)$ generally increases with decreasing temperature. In the T-PM phases of CaFe_2As_2 [80] and $\text{Ba}(\text{Fe}_{1-x}\text{Co}_x)_2\text{As}_2$ [65, 146], the magnetic-correlation length in the **ab** plane increases with decreasing temperature, whereas we find it to be relatively unchanged for $\text{Ca}(\text{Fe}_{0.97}\text{Co}_{0.03})_2\text{As}_2$. The analysis of the data with the diffusive model concluded that the decrease of $\chi''(\mathbf{Q}_{\text{stripe}}, E)$ at low energies with decreasing temperature for $\text{Ca}(\text{Fe}_{0.97}\text{Co}_{0.03})_2\text{As}_2$ is associated with a decrease in the magnitude of the fluctuating Fe moment. Nuclear magnetic resonance (NMR) measurements have also observed a suppression of AFM spin fluctuations in the normal state of SC samples of $\text{Ca}(\text{Fe}_{1-x}\text{Co}_x)_2\text{As}_2$ below a temperature T^* , which is attributed to the opening of a pseudogap [145].

Timusk and Statt define the pseudogap as a partial gapping of the Fermi surface [147], and many theories have been put forth that describe the origin of the pseudogap found for certain high- T_c cuprate superconductors [148, 149]. Among the theories is the case of preformed Cooper pairs, which suggests that the pairing necessary for SC starts at a temperature $T^* > T_c$. NMR data provided the first experimental evidence for the pseudogap in $\text{YBa}_2\text{Cu}_3\text{O}_{6.7}$ by showing a

suppression of the spin-lattice relaxation rate below T^* [150, 151]. INS measurements have observed the development of a spin resonance at $T^* > T_c$, which is associated with the opening of a pseudogap[149, 152].

Signatures of a pseudogap phase are also observed for some iron-arsenide superconductors. For example, a spin-resonance peak is found for $(\text{CaFe}_{1-x}\text{Pt}_x\text{As})_{10}\text{Pt}_3\text{As}_8$ above T_c [153]. Further, the spin-resonance peak occurs at the same values of E for $T^* > T > T_c$ and $T < T_c$, for both the cuprate[154] and iron-arsenide[153] superconductors, and, generally, the magnetic-scattering intensity at values of E lower than the resonance peak is suppressed. In contrast, the suppression of $\chi''(\mathbf{Q}_{\text{stripe}}, E)$ for $\text{Ca}(\text{Fe}_{0.97}\text{Co}_{0.03})_2\text{As}_2$ occurs at values of E much larger than the expected resonance energy of $E_{\text{res}} \approx 5.4$ meV, which differs with previous results for materials displaying a pseudogap[153, 154]. However, as noted above, INS measurements specifically targeting lower values of E at positions corresponding to $\mathbf{Q}_{\text{stripe}}$ are required to make a firm conclusion about the existence of a spin-resonance peak in $\text{Ca}(\text{Fe}_{0.97}\text{Co}_{0.03})_2\text{As}_2$.

Another potential explanation for the decrease in the fluctuating Fe moment lies with the proximity of the $x = 0.030$ sample to the cT phase found for CaFe_2As_2 [7, 104] and related compounds [155, 156]. As discussed in Chapter 2 in section 3.1.4, the cT phase of CaFe_2As_2 is characterized by a decrease in c of $\approx 9.5\%$, with $c = 10.607$ Å in the cT phase at $T = 50$ K [104], and quenching of the Fe magnetic moment [104, 105, 107]. Fig. 5.2(d) shows that c for $x = 0.030$ decreases with decreasing temperature, moving towards the cT phase. If the approach to the cT phase is associated with an increase in the interlayer As-As hybridization[40, 113, 114, 116, 156, 157], then it is possible that the Fe magnetic moment is concomitantly decreasing. Such an effect is shown to be the case for $\text{CaFe}_2(\text{As}_{1-x}\text{P}_x)_2$, $x = 0.033$ and 0.055 , and $\text{Ca}_{0.78}\text{La}_{0.22}\text{Fe}_2\text{As}_2$ [158]. Thus, it is suggested that the suppression of $\chi''(\mathbf{Q}_{\text{stripe}}, E)$ with decreasing temperature for $\text{Ca}(\text{Fe}_{0.97}\text{Co}_{0.03})_2\text{As}_2$ may be due to a decrease in the fluctuating Fe moment tied to the decrease in c . No such suppression in $\chi''(\mathbf{Q}_{\text{stripe}}, E)$ is observed for $x = 0.026$ between $T = 90$ and 20 K, because c increases only weakly upon cooling through $T_{\text{S,N}}$, as shown in Fig. 5.2(d). In fact, for both CaFe_2As_2 and

$\text{CaFe}_2(\text{As}_{0.967}\text{P}_{0.033})_2$ the Fe magnetic moment is found to increase proportionally with c upon cooling through $T_{\text{S,N}}$ [\[158\]](#).

CHAPTER 6 EXTREMELY ANISOTROPIC SPIN FLUCTUATIONS IN $\text{CaCo}_{1.86}\text{As}_2$

*Part of the content of this chapter has been published in Physical Review Letter [Phys. Rev. Lett. **119**, 147201 (2017)] [50].*

6.1 Introduction

As discussed in section 3.2 of chapter 3, $\text{CaCo}_{1.86}\text{As}_2$ is different than its CaFe_2As_2 counterparts, because it is in the collapsed tetragonal (cT) phase at ambient pressure for all temperatures. Additionally, it exhibits magnetism which is quenched in the cT phase of CaFe_2As_2 . Therefore the magnetoelastic coupling of As-As distance to the magnetism, discussed in section 3.1.4 in chapter 3, is different. Also, the observation of stripe-type spin fluctuations in SrCo_2As_2 compound[8] similar to AFe_2As_2 compounds, but with different anisotropy is puzzling because SrCo_2As_2 lacks Fermi-surface nesting[115, 118], that drives magnetism in AFe_2As_2 compound[26]. Moreover, ACo_2As_2 compounds show instability towards ferromagnetism. Therefore, it naturally raises a curiosity about the nature of spin fluctuations in the magnetically ordered $\text{CaCo}_{1.86}\text{As}_2$ compound, which shows A-type antiferromagnetic (AFM) order below $T_N = 52$ K[6].

In addition, in section 2.4.1 of chapter 2, it has been discussed that 122 compounds, that have magnetic ions on a square-lattice, are quasi-two-dimensional (quasi-2D) in terms of magnetism and their magnetism can be minimally described by considering nearest-neighbor (J_1) and next-nearest-neighbor (J_2) magnetic exchange interactions between magnetic ions on a square lattice[46, 49, 159]. In general, the magnetic ground state is determined by the relative strengths of J_1 and J_2 and the system becomes frustrated and ordering in any of these magnetic structures is suppressed when $|J_1| \approx 2J_2$ and $J_2 > 0$ (AFM). A frustration parameter, $\eta = J_1/2J_2$, quantifies the level of the magnetic frustration. Maximum frustration occurs when $\eta = 1$ (-1), and the stripe-type and Néel-

type [stripe-type and ferromagnetic (FM)] ground states compete and the possibility of the exotic physics like spin liquids at maximum frustration has been discussed[26, 52]. In the absence of any examples of insulating square-lattice compound close to this region of the maximum frustration, these quasi-2D, square-lattice metallic systems may have a member with η corresponding to the maximum frustration.

The frustration parameter, η , can be determined experimentally by measuring the spatial anisotropy of the spin fluctuations using inelastic neutron scattering (INS). The spatial distributions of the spin fluctuations in different magnetic ground states depend strongly on η as illustrated in the Fig. 6.1. For example, INS measurements for the parent and doped compositions of AFe_2As_2 compounds find η in the range from 0.3–0.7[79, 91], suggesting the presence of a moderate degree of frustration. The anisotropy of the spin fluctuations of SrCo_2As_2 gives $\eta \approx -0.6$ [8], and indicates a moderate frustration.

This chapter presents the results of the INS measurements of $\text{CaCo}_{1.86}\text{As}_2$ as well as (i) discusses if any peculiar behavior or the stripe-type spin fluctuations, as observed in SrCo_2As_2 , are present, and (ii) determines the degree of the magnetic frustration in $\text{CaCo}_{1.86}\text{As}_2$ from the anisotropy of the spin fluctuations.

6.2 Experimental Details

Single crystals of $\text{CaCo}_{1.86}\text{As}_2$, were grown using Sn flux[6, 116] and possess vacancy of 7% at Co-sites. The vacancies on the Co sites are randomly distributed, as x-ray and neutron diffraction measurements find no evidence for vacancy ordering[6, 116]. INS experiments were performed on the ARCS Spectrometer[130] at the Spallation Neutron Source, at Oak Ridge National Laboratory. Six single crystals of $\text{CaCo}_{1.86}\text{As}_2$ with a total mass of ~ 1.1 g were co-aligned in the $(H, 0, L)$ scattering plane (in tetragonal notation) with the full width at half maximum of less than 4° . The co-aligned set was attached to the cold finger of a closed-cycle He cryostat. The measurements were carried out with the incident beam along the c axis and incident energies of $E_i = 74.02$ and 238.56 meV at $T = 8$ K. Here, we define $\mathbf{Q} = (H-K, H+K, L) = (2\pi/a)(H-K)\hat{\mathbf{i}} + (2\pi/a)(H+K)\hat{\mathbf{j}} + (2\pi/c)L\hat{\mathbf{k}}$

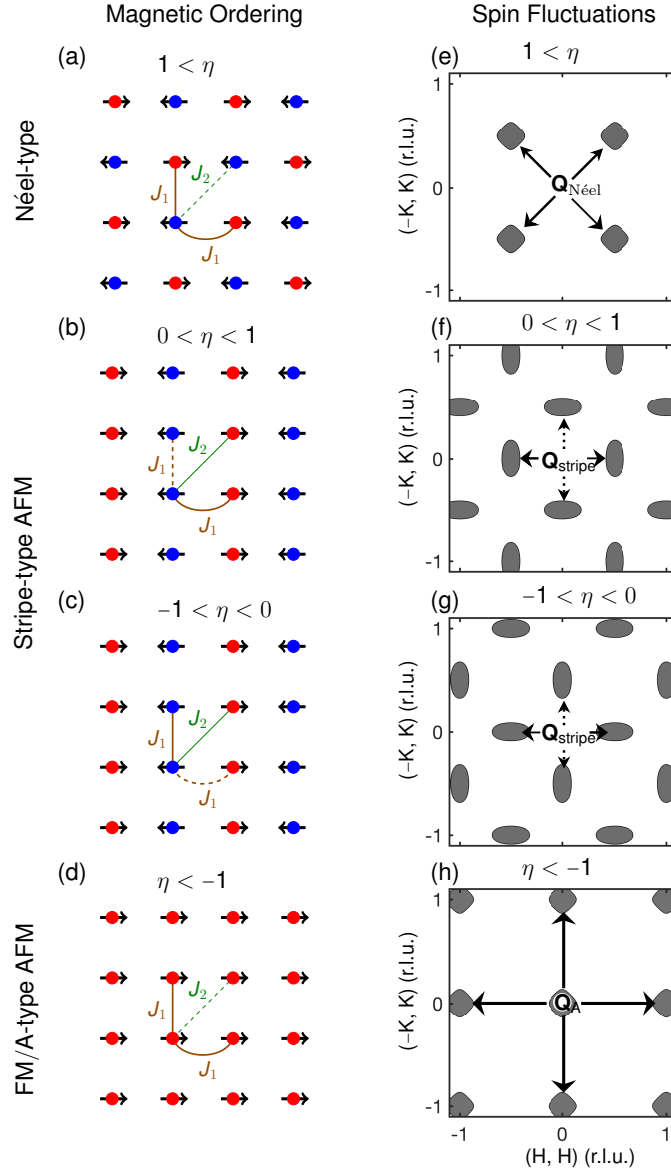


Figure 6.1 (a)–(d) Real space arrangement of spins on a square lattice for: (a) Néel-type, (b),(c) stripe-type AFM and (d) FM/A-type order. Red and blue circles represent transition metals on different magnetic sublattices. Magnetic NN (J_1) and NNN (J_2) interactions are shown where J_1 is AFM in (a) and (b) and FM in (c) and (d) and J_2 is AFM. Dashed lines indicate frustrated interactions when J_2 is AFM. (e)–(h), Spread and positions of spin fluctuations in reciprocal space for finite neutron energy transfer for the corresponding magnetic order. Dotted arrows in (f) and (g) point to spin fluctuations of the domains which have magnetic ordering similar to (b) and (c), respectively, but with alternating chains of blue and red circles along the perpendicular direction. Néel and FM/A-type fluctuations have four-fold anisotropy. Spin fluctuations corresponding to the different magnetic orderings show differences in spatial anisotropy. The figure is reproduced from Ref. [50].

with respect to the tetragonal $I4/mmm$ crystal system, where $a = 3.98 \text{ \AA}$ and $c = 10.27 \text{ \AA}$ at $T = 300 \text{ K}$. In this notation, the reciprocal lattice vectors for stripe and A-type magnetic order are $\mathbf{Q}_{\text{stripe}} = (\frac{1}{2}, \frac{1}{2}, 1) + (m, n, l)$ with m, n integers and l even and $\mathbf{Q}_A = (H - K, H + K, L)$ where $H - K$ and $H + K$ are integers with $|H - K| + |H + K|$ even and L odd. The data were visualized using the MSLICE[139].

6.3 Results and analysis

Figure 6.2 show the raw and background subtracted data of the INS measurements. An isotropic background is estimated as in the Ref. [91] and the procedure followed is, (i) mask the region where the spin fluctuations are expected, and (ii) average the rest of the data from equal Q and E sections. In this case, regions along the longitudinal (LO) directions as shown by white arrows in Fig 6.2 (a) are masked. For A-type AFM order of $\text{CaCo}_{1.86}\text{As}_2$ compound, the spin fluctuations are expected to be centered at $\mathbf{Q}_A = (H - K, H + K) = (0, 0), (1, 1), \dots$ and $L = \text{odd}$. E and L are coupled in the experimental configuration where incident beam is fixed along \mathbf{c} direction. Hence, different $(H - K, H + K)$ points in the Fig. 6.2 corresponds to different L values for same E and similarly, same $(H - K, H + K)$ corresponds to different L values for different E . $(H - K, H + K) = (0, 0)$ is in the direct beam and ARCS does not have any detector to measure spin fluctuations at this position. This corresponds to the white squares in Figure 6.2 (a)–(f) and (i) at $(0, 0)$. So, it is expected to observe the spin fluctuations centered at $(1, 1)$ around E corresponding to the odd values of L .

However, the results are very striking. Constant-energy (Q) slices of the data in Figs. 6.2(a)–(f) and (i) show that the scattering from the spin fluctuations does not occur only around positions corresponding to \mathbf{Q}_A , but extends along the LO direction, crossing positions including $\mathbf{Q}_{\text{stripe}} = (1/2, 1/2)$, at all accessible energies from ~ 10 – 120 meV . In contrast, the scattering along the TR direction is sharp. The energy dependence, in Figs. 6.2 (g), (h) and (j), shows steep dispersion in the TR direction and the scattering extends in energy beyond 100 meV . This broad spin fluctuations along the LO direction infers the weak correlation of the spins along the LO direction. In addition,

the spin fluctuations look broader in E without any appreciable modulation in intensity which implies that the modulation of intensity in L is absent. The result suggests a very weak interlayer interaction or correlation.

So, the spin fluctuations in $\text{CaCo}_{1.86}\text{As}_2$ compound are extremely anisotropic and the feature is unique than observed in any other 122 members. The observed spin fluctuations can be described as a “plane” of scattering in reciprocal space perpendicular to the Co square-lattice planes. This is in sharp contrast to “rods” of scattering expected perpendicular to quasi-two-dimensional planes of spins but similar to the expectation for quasi-one-dimensional spin chains.

Next, to describe the scattering data, two models for A-type AFM are considered. For both the models, only NN (J_1) and NNN (J_2) interactions appropriate for an A-type AFM ground state are considered and the interlayer exchange interaction J_c is neglected. First, I am going to discuss the calculation of the neutron scattering cross-section, corresponding to the values of \mathbf{Q} and E measured by INS, using the linear spin-wave theory approximation to the Heisenberg model. Then, I will discuss the diffusive model, which has been used to describe the overdamped spin fluctuations in a nearly ordered system, for example, on weakly ordered and metallic $\text{Ba}(\text{Fe}_{1-x}\text{Co}_x)_2\text{As}_2$ [5, 65, 91] and paramagnetic CaFe_2As_2 [80].

6.3.1 Heisenberg Model

The Heisenberg Hamiltonian consisting of nearest-neighbor (J_1), next-nearest-neighbor (J_2) and interlayer (J_c) exchange parameters in the $I4/mmm$ cell, is

$$H = J_1 \sum_{\text{NN}, ab} \mathbf{S}_i \cdot \mathbf{S}_j + J_2 \sum_{\text{NNN}, ab} \mathbf{S}_i \cdot \mathbf{S}_j + J_c \sum_{\text{NN}, c} \mathbf{S}_i \cdot \mathbf{S}_j \quad (6.1)$$

The spin-wave dispersion relation for the A-type AFM order (Fig. 2.5), using linear spin-wave approximation of Eq. (6.1), is

$$E(\mathbf{q}) = \sqrt{A_{\mathbf{q}}^2 - B_{\mathbf{q}}^2}, \quad (6.2)$$

where $\mathbf{q} = \mathbf{Q} - \mathbf{Q}_A$ is the reduced wavevector and

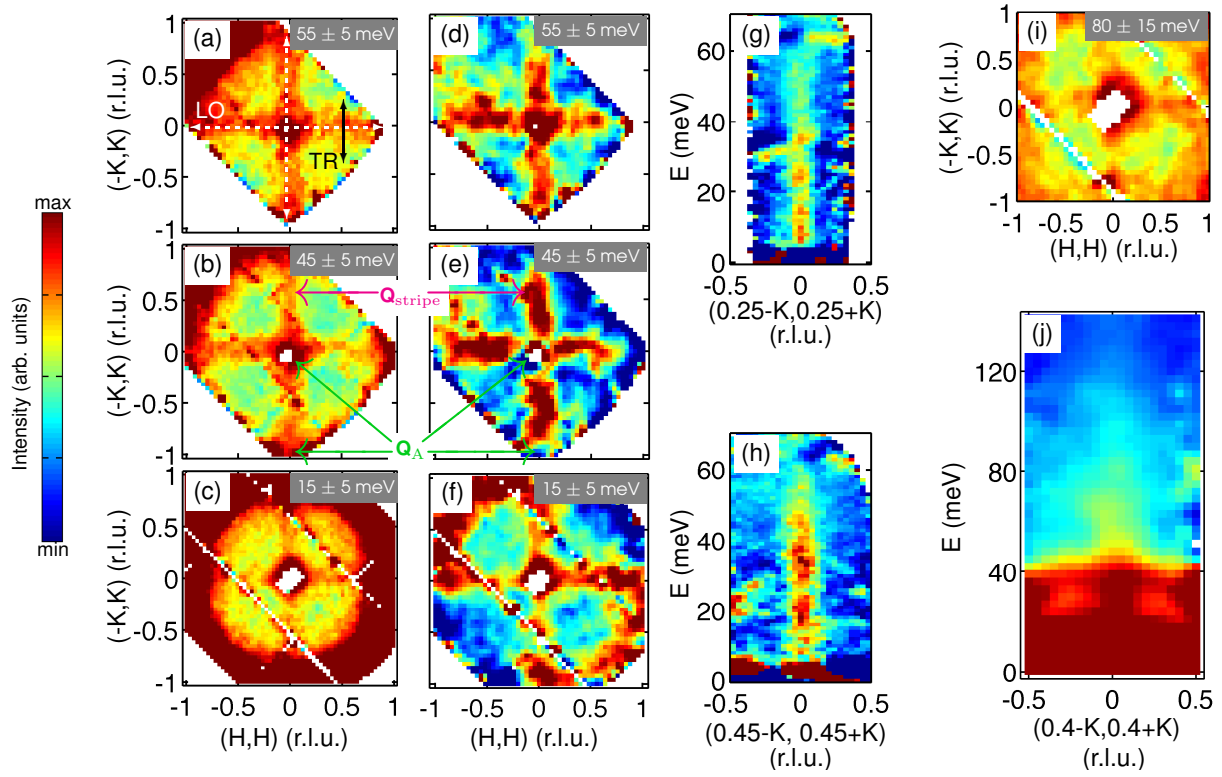


Figure 6.2 Inelastic neutron scattering spectra of $\text{CaCo}_{1.86}\text{As}_2$ measured at $T = 8$ K at ARCS. (a)–(h) Data measured with $E_i = 74.02$ meV and (i)–(j) with $E_i = 238.56$ meV. (a)–(c) Constant-energy (Q) slices of the raw data in (H, H) – $(-K, K)$ plane averaged over energy range of (a) 50–60 meV, (b) 40–50 meV and (c) 10–20 meV. (d)–(f) The background subtracted data averaged over the same energy range respectively. An isotropic background is estimated as discussed in Ref. [91]. White dashed arrows in (a) show longitudinal (LO) direction and black arrow shows transverse (TR) direction. (g)–(h) Transverse slices of the raw data along the $[-K, K]$ direction through $(0.25, 0.25)$ and $(0.45, 0.45)$, respectively. They are obtained after averaging over the LO direction by ± 0.1 r.l.u. and illustrate the energy dependence of the scattering. (i) Q slice of the data in (H, K) plane averaged over energy range of 65–95 meV. (j) Transverse slice of the data along the $[-K, K]$ direction through $(0.4, 0.4)$ showing presence of excitation up to 120 meV. The energy dependence figures are obtained after performing the earlier mentioned background subtraction and are averaged over all four symmetry-related quadrants. The color scale represents intensity in each panels. The maximum/minimum intensity in (a) 1.2/0 (b) 1.65/0 (c) 3.85/0 (d) 0.35/–0.5 (e) 0.55/–0.5 (f) 0.65/–0.8 (g) 0.65/–0.5 (h) 0.65/–0.5 (i) 5.5/0 (j) 1/0 arb. units. The figure is reproduced from Ref. [50].

$$\begin{aligned}
A_{\mathbf{q}} &= 2SJ_c - 4S(J_1 + J_2) + 4S\left\{\frac{J_2}{2}[\cos(2\pi H) + \cos(2\pi K)] + J_1 \cos(\pi H) \cos(\pi K)\right\} \\
B_{\mathbf{q}} &= 2SJ_c \cos(\pi L)
\end{aligned} \tag{6.3}$$

Here too, $J_c = 0$, so, $B_{\mathbf{q}} = 0$ in Eq. (6.3). Next, only the transverse-component contributions to the neutron intensity is considered and $[n(E = \hbar\omega) + 1]\delta[E - E(\mathbf{q})]$, which infers excitations with infinite lifetime, is replaced with $\frac{1}{1 - e^{-E/k_B T}} \times \frac{4}{\pi} \frac{\Gamma E E(\mathbf{q})}{[E^2 - E^2(\mathbf{q})]^2 + 4(\Gamma E)^2}$, which instead considers that the excitations have finite lifetime and can be described by the damped simple harmonic oscillator (DSHO) with inverse lifetime Γ [26, 78, 79]. This gives the inelastic cross-section as

$$\frac{d^2\sigma}{d\Omega dE} = A \frac{k_f}{k_i} \sum_{\alpha, \beta} (\delta_{\alpha\beta} - \hat{Q}_\alpha \hat{Q}_\beta) S^{\alpha\beta}. \tag{6.4}$$

with transverse component of $S(\mathbf{Q}, E)$ as,

$$S(\mathbf{Q}, E) = S_{\text{eff}} \frac{1}{1 - e^{-E/k_B T}} \frac{4}{\pi} \frac{\Gamma E E(\mathbf{q})}{[E^2 - E^2(\mathbf{q})]^2 + 4(\Gamma E)^2}, \tag{6.5}$$

where A is scale factor, S_{eff} is the effective spin.

The inelastic neutron scattering spectra calculated using above Eqns. (6.4) and (6.5) are shown in Fig. 6.3. The result show that for $J_1 \approx 2J_2$, the spin wave collapses along the LO direction, leading to a spin wave anisotropy that is similar to the experimental data at low energies, as shown in Fig. 6.3(e). However, for the higher energy transfers the calculated cross section and INS data show significant differences, as there is no intensity along the LO direction in the calculated cross section as shown in Fig. 6.3 (b) and (e). Therefore, Heisenberg model is not able to capture the essential features of the INS spectra.

6.3.2 Diffusive model

Next, the cross-section is calculated using a model more appropriate for itinerant systems close to magnetic order. In itinerant magnets, the electronic degrees-of-freedom can result in a significant degree of Landau damping of the spin fluctuations due to the scattering of electrons. A diffusive

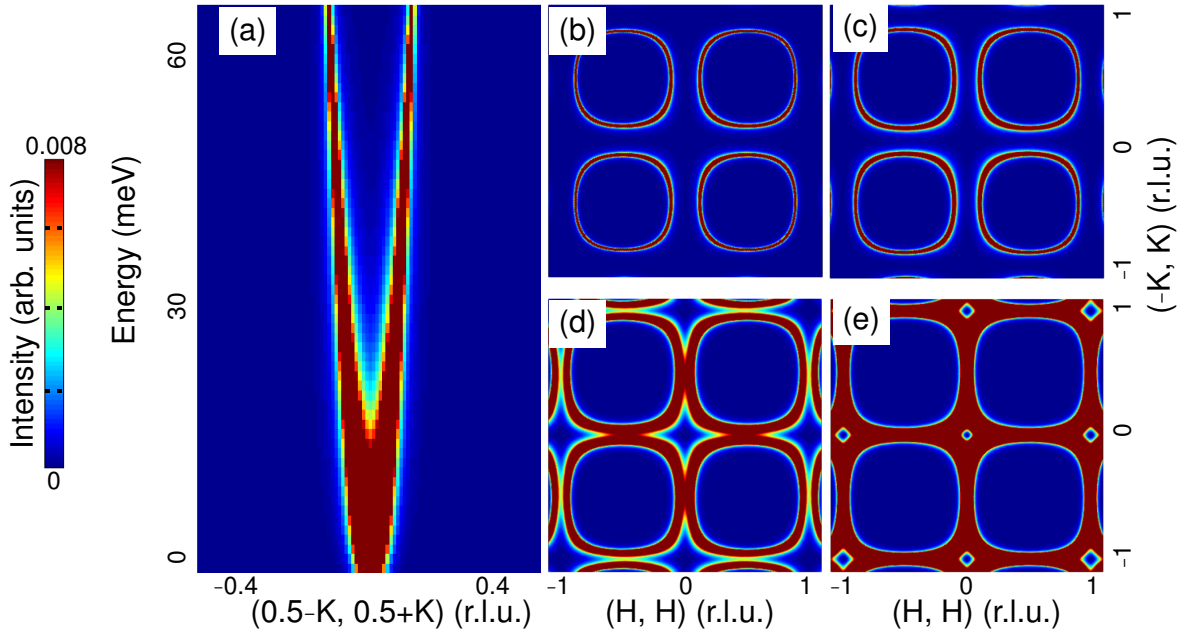


Figure 6.3 (a) Slice showing the energy dependence of spin fluctuations along the TR direction. (b)–(e) Constant-energy slices for energy transfers of (b) 55 ± 5 meV, (c) 45 ± 5 meV, (d) 15 ± 5 meV, and (e) 5.5 ± 4.5 meV. Unlike the experimental data, the figures show a dispersion of the peak at the higher energy transfer with no intensity along the LO direction. The spectrum is obtained with values $SJ_1 = -50$ meV, $SJ_2 = 24.4$ meV and $SJ_c = 0.0$ meV. The figure is reproduced from Ref. [50]

model that describes such overdamped spin fluctuations in a nearly ordered system has been used to describe INS data on weakly ordered and metallic $\text{Ba}(\text{Fe}_{1-x}\text{Co}_x)_2\text{As}_2$ [5, 65, 91] and paramagnetic CaFe_2As_2 [80]. Here too, the weak AFM interlayer interactions is neglected and only intralayer interactions up to NNN is kept.

6.3.2.1 Derivation of the diffusive model for A-type AFM

In the mean-field approximation, the dynamical susceptibility can be written as

$$\chi^{-1}(\mathbf{q}, \omega) = \chi_0^{-1} - [J(0) - J(\mathbf{q})] - i\gamma\omega, \quad (6.6)$$

where, γ is the Landau damping parameter, which is the decay of the spin fluctuations into the particle-hole pair excitations.

$$\chi(\mathbf{q}, \omega) = \chi'(\mathbf{q}, \omega) + i\chi''(\mathbf{q}, \omega), \quad (6.7)$$

From Eq. (6.6), the imaginary part of the dynamical susceptibility is

$$\chi''(\mathbf{q}, \omega) = \frac{\gamma\omega}{\left\{ \chi_0^{-1} + [J(\mathbf{q}) - J(0)] \right\}^2 + \gamma^2\omega^2} \quad (6.8)$$

Lets define $\Gamma = 1/\chi_0\gamma$ (which has units of energy) to obtain

$$\chi''(\mathbf{q}, \omega) = \frac{\chi_0\Gamma\omega}{\Gamma^2\{1 + \chi_0[J(\mathbf{q}) - J(0)]\}^2 + \omega^2} \quad (6.9)$$

The $J(\mathbf{q})$ is obtained by treating the exchange as a sum over pairwise interactions coupled by the exchange J_{ij}

$$J(\mathbf{q}) = \sum_{i,j} J_{ij} e^{i\mathbf{q} \cdot \mathbf{r}_{ij}} \quad (6.10)$$

For NN (J_1) and NNN (J_2) interactions on a square lattice defined in the $I4/mmm$ cell with lattice parameter a as shown in Fig. 6.4,

$$J(\mathbf{q}) = 2J_1 \left\{ \cos[(q_x + q_y)a/2] + \cos[(q_x - q_y)a/2] \right\} + 4J_2 \left\{ \cos[(q_x + q_y)a/2] \cos[(q_x - q_y)a/2] \right\} \quad (6.11)$$

here, x and y directions correspond to the $[1\ 0\ 0]$ and $[0\ 1\ 0]$ directions of the tetragonal $I4/mmm$ crystal system, respectively, and

$$J(0) = 4(J_1 + J_2) \quad (6.12)$$

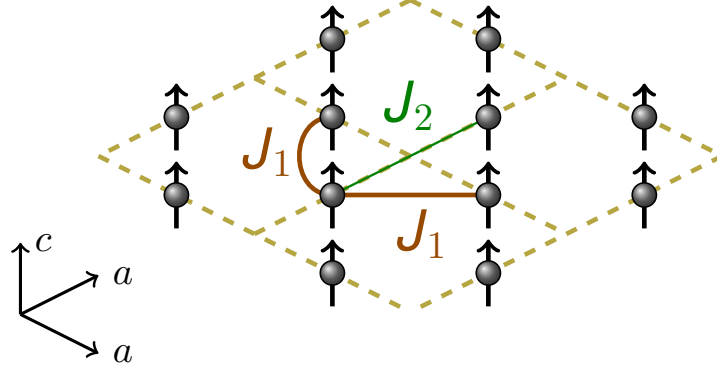


Figure 6.4 Arrangement of spins/moments in $\text{CaCo}_{1.86}\text{As}_2$ in the Co-plane. The figure shows that there are 4 NN and 4 NNN for each Co-moments separated by $(\frac{1}{2}, \frac{1}{2})$ and $(1, 0)$, respectively.

The imaginary part of the dynamical susceptibility then becomes (where $c_{x\pm y} = \cos[(q_x \pm q_y)a/2]$)

$$\chi''(\mathbf{q}, \omega) = \frac{\chi_0 \Gamma \omega}{\Gamma^2 \{1 + \chi_0 [2J_1(c_{x+y} + c_{x-y}) + 4J_2 c_{x+y} c_{x-y} - 4J_1 - 4J_2]\}^2 + \omega^2} \quad (6.13)$$

Now defining the anisotropy parameter $\eta = J_1/2J_2$, which is also the definition of the frustration parameter, and an average correlation length $\xi^2/a^2 = J_2\chi_0$ to obtain

$$\chi''(\mathbf{q}, \omega) = \frac{\chi_0 \Gamma \omega}{\Gamma^2 \{1 + (4\xi^2/a^2)[\eta(c_{x+y} + c_{x-y}) + c_{x+y} c_{x-y} - 2\eta - 1]\}^2 + \omega^2} \quad (6.14)$$

and finally defining

$$q^2 \xi_q^2 = (2\xi/a)^2 [\eta(c_{x+y} + c_{x-y}) + c_{x+y} c_{x-y} - 2\eta - 1]. \quad (6.15)$$

In the itinerant picture relevant for the iron arsenides, η arises from the spatial anisotropy of electronic velocities at the Fermi surface[91, 160].

6.3.2.2 Correlation length and anisotropy parameter

For the LO direction, $\mathbf{q}_{\text{LO}} = (\delta, \delta)$ and $q^2 = 2\delta^2$ and

$$\text{LO} : q^2 \xi_q^2 = (4\xi^2/a^2)(\eta + 1)(\cos \delta a - 1) \quad (6.16)$$

For $\delta a \ll 1$, this gives the expected formula,

$$q^2 \xi_{\text{LO}}^2 \approx -\frac{4\xi^2}{a^2}(\eta + 1)\frac{1}{2}(\delta a)^2 = \xi^2(-\eta - 1)q^2 \quad (6.17)$$

or

$$\xi_{\text{LO}}^2 = \xi^2(-\eta - 1) \quad (6.18)$$

For INS spectra of $\text{CaCo}_{1.86}\text{As}_2$ compound, transverse and longitudinal cuts are made around the stripe wavevector $\mathbf{q}_s = (\frac{\pi}{a}, \frac{\pi}{a})$. Hence, for the transverse cut, $\mathbf{q} = \mathbf{q}_s + \mathbf{k}_{\text{TR}} = \mathbf{q}_s + (\delta, -\delta)$, Eq. (6.17) becomes

$$\text{TR} : k^2 \xi_k^2 = (4\xi^2/a^2)[(1 - \eta)(1 - \cos \delta a) - 2(\eta + 1)] \quad (6.19)$$

for small δa and $k^2 = 2\delta^2$

$$\text{TR} : k^2 \xi_k^2 = k^2 \xi^2(1 - \eta) + 8\xi_{\text{LO}}^2/a^2 \quad (6.20)$$

where, the transverse correlation length is

$$\xi_{\text{TR}}^2 = \xi^2(1 - \eta) \quad (6.21)$$

Using the Eq. (6.18) and (6.21), the formula relating the correlation lengths to the anisotropy is defined as

$$\frac{\xi_{\text{LO}}^2 + \xi_{\text{TR}}^2}{\xi_{\text{LO}}^2 - \xi_{\text{TR}}^2} = \frac{-1 - \eta + 1 - \eta}{-1 - \eta - 1 + \eta} = \eta \quad (6.22)$$

This relationship is strictly only appropriate in the small- q limit for sharp peaks (i.e. where the correlation length can be obtained from the peakwidth), but it is a good estimate even in cases, like our, where the intensity is more broadly distributed.

6.3.2.3 Estimation of the anisotropy parameter from the full width half maximum

In the Section 6.1, it is discussed that the anisotropy parameter η can be independently determined from the spatial anisotropy of the spin fluctuations. η , as shown in the Eq. (6.22), is related to the magnetic correlation lengths. The magnetic correlation length, $\xi_{\text{LO/TR}} \propto \frac{1}{\kappa_{\text{LO/TR}}}$, where $\kappa_{\text{LO/TR}}$ is the full width at half maximum (FWHM) of the peaks along the corresponding direction.

The almost flat peak along the LO direction gives $\xi_{\text{LO}} \approx 0$ and average FWHM of the lowest 3 energies ($\kappa_{\text{TR}} \approx 0.20$ r.l.u.) gives $\xi_{\text{TR}} \approx 4.5$ Å. Hence, $\eta = \frac{\xi_{\text{LO}}^2 + \xi_{\text{TR}}^2}{\xi_{\text{LO}}^2 - \xi_{\text{TR}}^2}$ suggests $\eta \approx -1$.

6.3.2.4 Fit of the data using the diffusive model

So, the INS data were fit using the diffusive model in Eqs. (6.14) and (6.15), as shown in Fig. 6.5. The values of η and ξ_{TR} obtained from the fitting are expected to be close to the values of ≈ 4.5 Å and -1 . The best fit values of the model parameters are listed in Table 6.1 and the data are fit with a constant (\mathbf{Q} -independent) damping parameter [$\Gamma = 20(4)$ meV] and $\eta = -1.03(2)$.

This value of $\eta \approx -1.03$ is close to the value of the maximum frustration based upon J_1 – J_2 model. Therefore, the result infers that $\text{CaCo}_{1.86}\text{As}_2$ is extremely frustrated square-lattice system. The calculated neutron scattering cross sections, using the diffusive model, capture all of the essential features corresponding the INS data shown in Figs. 6.5 and 6.7 $\gtrsim 10$ meV.

Table 6.1 Fit values of the parameters in the diffusive model. The table is reproduced from Ref. [50].

Γ (meV)	η	χ_0 (arb. units)	ξ (Å)	ξ_{TR} (Å)
20(4)	-1.03(2)	3.2(4)	4.1(1)	5.8(5)

Also, from the dispersion relation of the A-type antiferromagnet in Eq. (6.2), with $J_c = 0$, J_1 can be written in terms of the half width at half maximum (δ) along the TR direction at $(H, K) = (0.5, 0.5)$ and E as:

$$S|J_1| = \frac{E}{8\pi^2\delta^2}, \quad (6.23)$$

where δ is in r.l.u. and the fit of the Fig. 6.6 using the Eq. (6.23) gives

$$S|J_1| = 52 \pm 3 \text{ meV}. \quad (6.24)$$

Comparing the energy scale associated with J_1 to that of $T_N = 52$ K, it is found that the energy scale for the A-type AFM order is much smaller than the FM NN exchange energy ($k_B T_N / S|J_1| \approx 0.1$). This ratio, 0.1, is much smaller than the same ratio of the moderately frustrated square lattice

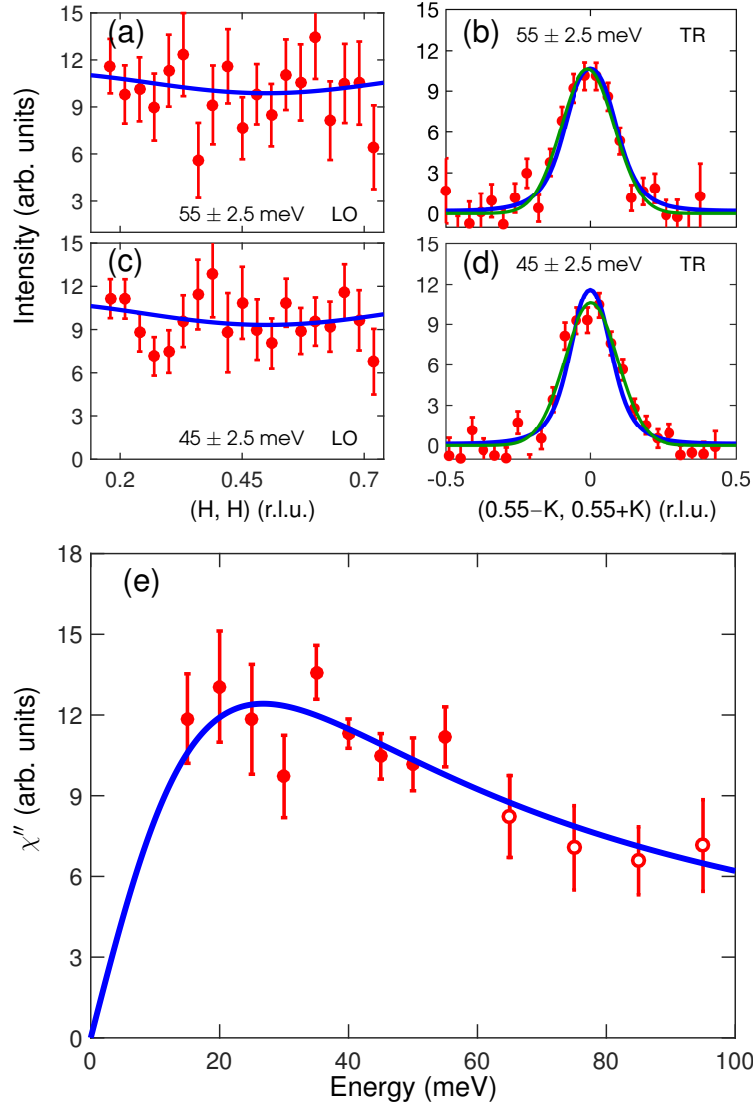


Figure 6.5 Constant-energy cuts and dynamical susceptibility of the data fitted with the diffusive model. (a),(c) LO and (b),(d) TR cuts of data through $(0.55, 0.55)$ at (a), (b) $52.5\text{--}57.5$ meV and (c), (d) $42.5\text{--}47.5$ meV. TR cuts were averaged from $0.3\text{--}0.8$ r.l.u. in the LO direction and LO cuts ± 0.1 r.l.u. in the TR directions. Both data are corrected for the Co^{+1} magnetic form factor after subtracting a background contribution estimated from Gaussian fits to the TR cuts. The single peaked TR cuts is an outcome of the unresolvable broader dispersion branches due to the diffusive nature of the spin fluctuations. The green lines in the TR cuts are fits to a Gaussian lineshape and blue solid lines are fits to the diffusive model. (e) Energy dependence of the imaginary part of the dynamical susceptibility centered at $(0.55, 0.55)$ and averaged along the LO direction from $0.3\text{--}0.8$ r.l.u. Each data point is obtained after fitting the TR cuts with a Gaussian lineshape. The closed symbols are data measured with $E_i = 74.02$ meV and open symbols with $E_i = 238.56$ meV. The figure is reproduced from Ref. [50].

oxides (minimum value in oxides is 0.6)[161] and the iron arsenides (0.7)[47]. Thus $\text{CaCo}_{1.86}\text{As}_2$ orders at a temperature much lower than expected based on the strength of its magnetic interactions. This is a hallmark of strong magnetic frustration.

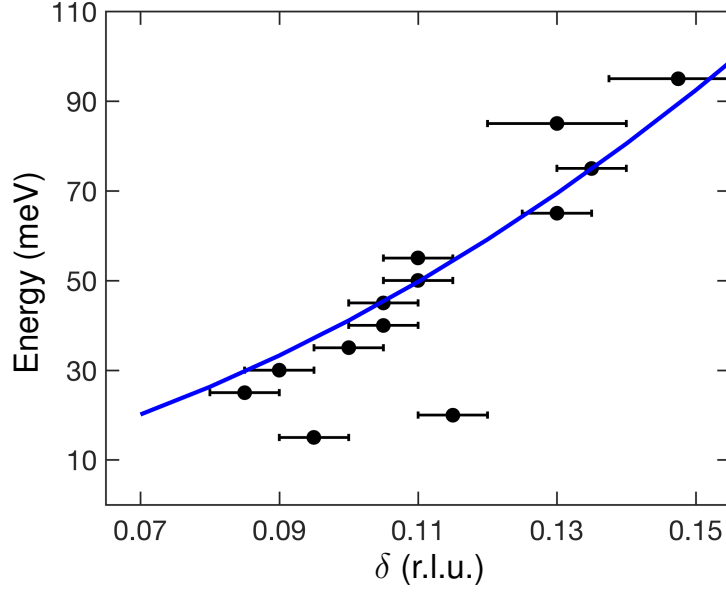


Figure 6.6 Fit of the energy transfer and half width at half maximum (δ) of the TR cuts using the Eq. 6.23 to estimate $S|J_1|$. The figure is reproduced from Ref. [50].

6.4 Discussion of the ARCS results

The results shown above present a unique spin fluctuations in $\text{CaCo}_{1.86}\text{As}_2$ at $E \gtrsim 10$ meV. The spin fluctuations are very sharp along the TR direction and extremely broad along the LO and E/L , indicating extremely weak correlations of spins (Co moments) along LO and L directions. This extreme anisotropy is unique among the 122 compounds. The anisotropy parameter or frustration parameter η obtained from this spatial anisotropy and diffusive model gives value ≈ -1 , which is the case of maximum frustration for square lattice system based upon the J_1 – J_2 model.

The observed planes of scattering instead of rods of scattering expected for the quasi-2D systems, like $\text{CaCo}_{1.86}\text{As}_2$, is consistent with the 1D behavior. These 1D behavior arises due to the frustrated interactions in $\text{CaCo}_{1.86}\text{As}_2$ compound. The frustrated interactions make the effective coupling

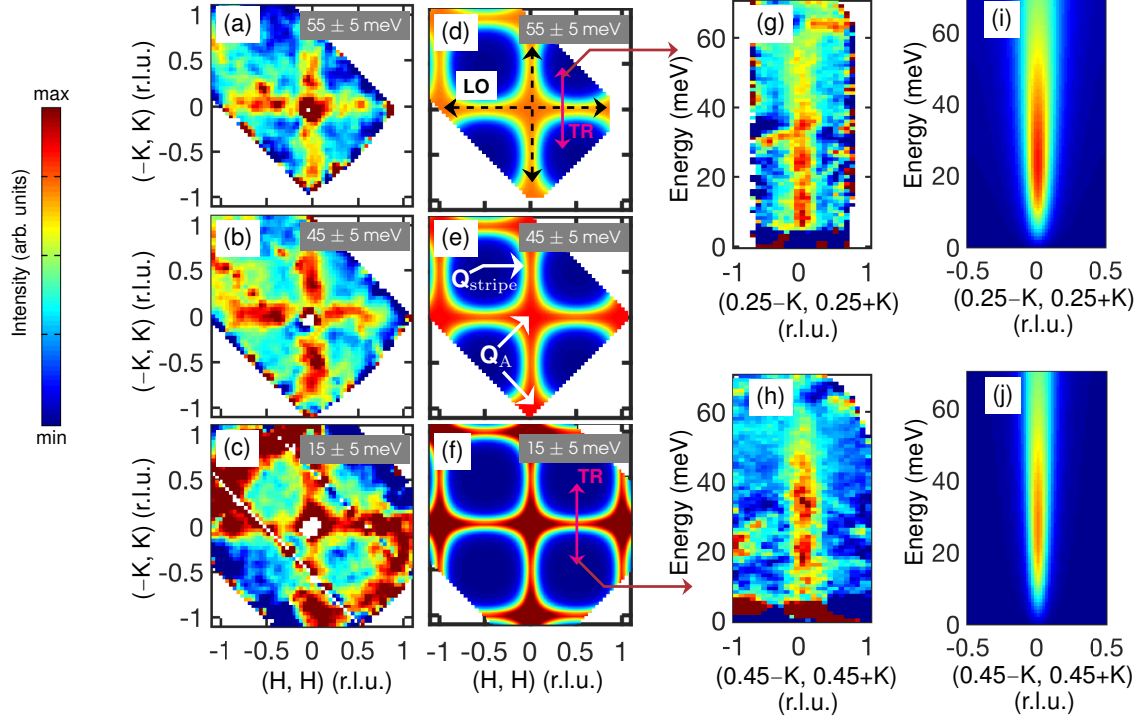


Figure 6.7 Spin fluctuations in $\text{CaCo}_{1.86}\text{As}_2$: Experimental INS Data ($E_i = 75$ meV) vs Diffusive Model. (a)–(c), Constant-energy slices of the background subtracted data (the isotropic background is estimated similar to Ref. [91]) averaged over the energy ranges of 50–60 meV, 40–50 meV and 10–20 meV, respectively. (d)–(f) Corresponding constant-energy slices calculated using the diffusive model and parameters obtained from fitting the data shown in Fig. ?? . In Fig. (d), the black dashed arrows show the LO directions and the maroon arrow shows the TR directions. (g),(h) Transverse slices of the background-subtracted data along the $[-K, K]$ direction through (0.25, 0.25) and (0.45, 0.45) (r.l.u.), respectively, obtained after averaging over the LO direction by ± 0.1 r.l.u. (i),(j) Corresponding energy dependence of the scattering obtained using the diffusive model and parameters of fits to the data in Fig. 6.5. The energy-dependent figures are averaged over all four symmetry-related quadrants. The color scale represents the intensity in each panel. The maximum/minimum intensities in the panels are (a) 0.34/−0.5, (b) 0.42/−0.3, (c) 0.65/−0.15, (d)–(f) 0.43/0, (g) 0.52/−0.45, (h) 0.65/−0.35, (i) and (j) 0.52/0 in arbitrary units. The figure is reproduced from Ref. [50].

along the TR directions in the Co plane to vanish, thus, leading to the 1D behavior of the spin correlations. This is most easily pictured by considering J_1 and J_2 interactions in a single square layer with the stripe-type AFM order, as shown in Fig. 6.8 (a). The stripe-type magnetic structure consists of alternating chains of FM spins oriented in the TR direction [ordering vector $(1/2, 1/2)$] with an effective interchain coupling of $\sim |J_1| - 2J_2$ which goes to zero as $\eta \rightarrow (-1)^+$. Moreover, the cost of flipping one FM chain against another goes to zero and the FM chains decouple. This results in a vanishing dispersion in the LO direction, but the steep dispersion remains in the TR direction as shown in Fig. 6.8 (c) where effective coupling is maximized as $\sim -|J_1| - 2J_2$. Rod-like fluctuations occur as a result of the effective zero coupling along the LO direction as shown in Fig. 6.8 (c).

Starting from the FM side, the spin stiffness goes to zero in all directions as $\eta \rightarrow (-1)^-$, preserving the 4-fold symmetry of the ground state. However, similar to the stripe-type AFM order, the effective coupling between FM chains in the LO direction goes to zero, as shown in Fig. 6.8 (b), and any TR component is steeply dispersive. Thus, the low-energy magnetic spectral weight is confined to a wall along the LO direction [Fig. 6.8 (d)], the scattering signature of a 1D system.

The result is novel because $\text{CaCo}_{1.86}\text{As}_2$ is the first square-lattice compound to exhibit nearly maximum frustration, as shown in Fig. 6.9, and furthermore, it is a metallic (itinerant) system, where the role of magnetic frustration is poorly understood. Figure 6.9 shows that all other compounds both 122 compounds and insulator oxides are far from the maximum frustration region. In addition, the values of η for $\text{CaCo}_{1.86}\text{As}_2$ is close to the region where the possibility of spin liquids has been discussed[52]. So, this results motivate to identify other potential candidates with moderate electronic correlations and a way to do that could be doping as discussed in Section 2.4.1 of Chapter 2. In these potential compounds, novel electronic and/or magnetic phenomena may be found.

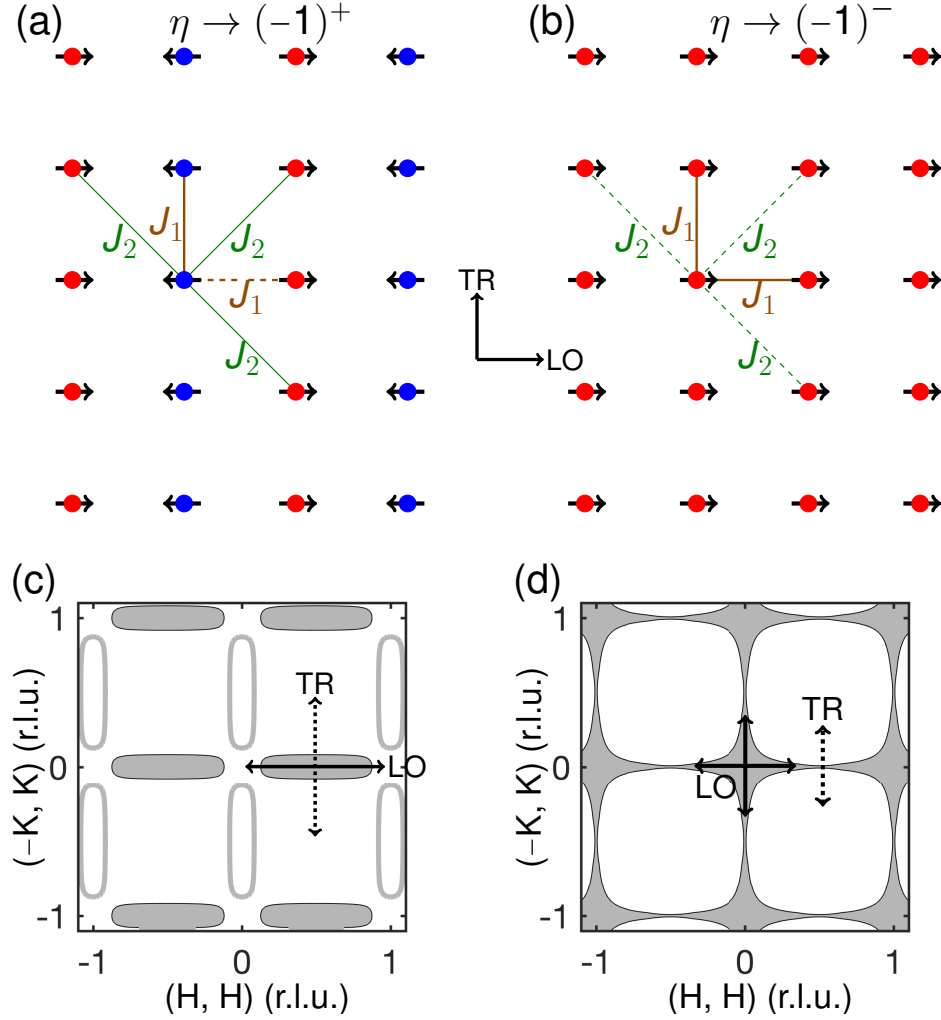


Figure 6.8 (a),(b), Coupling of spins on a square lattice corresponding to stripe-type AFM and FM/A-type spin dynamics, respectively, for an extreme degree of frustration showing effective zero coupling along the LO directions. Red and blue circles represent transition metals on different magnetic sublattices. Magnetic NN (J_1) and NNN (J_2) interactions are shown where J_1 is FM and J_2 is AFM. Stable(frustrated) bonds are denoted by a solid (dashed) lines. (c),(d), Spin fluctuations corresponding to highly frustrated spin interactions in (a) and (b), respectively. The empty rods shown in (c) are due to the twin domain of (a), that has alternating chains of blue and red circles along the perpendicular directions. Both occur with equal populations. The figure is reproduced from Ref. [50].

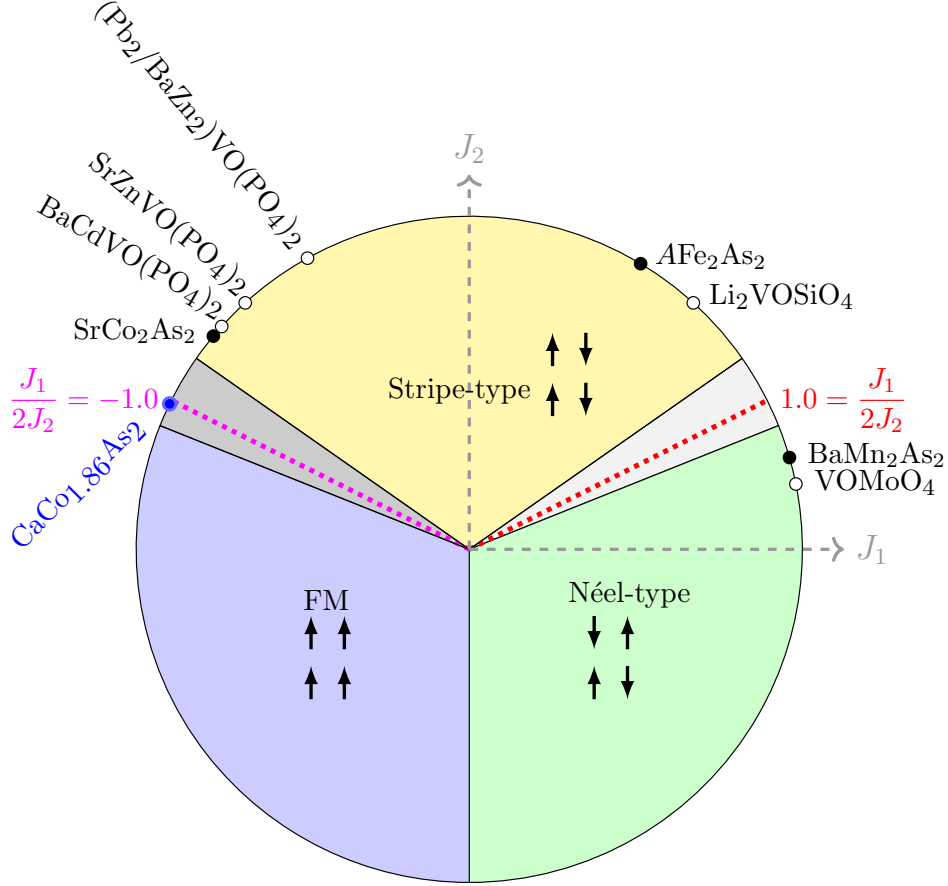


Figure 6.9 Phase diagram of J_1 - J_2 model illustrating that $\text{CaCo}_{1.86}\text{As}_2$ is a unique compound in terms of degree of magnetic frustration. The shaded gray (both dark and light) area corresponds to the region where long-range magnetic ordering is absent. $\eta = \frac{J_1}{2J_2}$ is the frustration parameter with maximum frustration corresponding to 1 or -1 (red or maroon dotted line). Black filled circles on the circumference corresponds to the position of AFe_2As_2 , SrCo_2As_2 and BaMn_2As_2 based upon the ratio $\frac{J_2}{J_1}$ obtained from inelastic neutron scattering data. Similarly, blue filled circle corresponds to $\text{CaCo}_{1.86}\text{As}_2$ based upon the ratio $\frac{J_2}{J_1}$ obtained from inelastic neutron scattering data. Empty circles correspond to well-studied insulator oxides. The figure is created using the figure in Refs. [26, 161] as a guideline.

6.4.1 Evolution of spin fluctuations with the frustration parameter (η)

The diffusive model for $\text{CaCo}_{1.86}\text{As}_2$ compound shows that the calculated INS cross-section are anisotropic for $\eta \approx -1$. Furthermore, the evolution of the anisotropy of the spin fluctuations corresponding to the value of η is calculated using the diffusive model for stripe-type (both $\eta >$ and < 0) and Néel-type. Similar to the imaginary part of dynamical susceptibility in Eq. (6.15), the χ'' for stripe-type and Néel-type are derived and the details of the derivation are discussed in the section 6.6 of this chapter. The result in Fig. 6.10 shows that spin fluctuations becomes extremely anisotropic for all magnetic ground states on approaching the region of maximum frustration. This further confirms that the extremely anisotropic spin fluctuations in INS spectra are signature of the extreme frustration.

6.4.2 Spin fluctuations below 10 meV: ARCS results

The ARCS measurements with the incident energy of 74.02 and 238.56 meV do not provide the clear picture of the nature of the spin fluctuations $\lesssim 10$ meV. The anisotropic spin fluctuations are no more visible below 10 meV, as shown in Fig. 6.11, so the question remains if the spin fluctuations are centered at \mathbf{Q}_A . Figure 6.11, which is the constant-energy slice of the background subtracted data averaged from 5 to 10 meV [$L = 1$ at $E = 5$ meV and $(1, 1)$ for $E_i = 74.02$], indeed show a peak centered at \mathbf{Q}_A . However, a firm conclusion about the nature of the spin fluctuations $\lesssim 10$ meV cannot be made because of the following reasons. The energy resolution (i.e. full width at half maximum) of the elastic peaks for $E_i = 74.02$ meV is nearly ≈ 3 meV, which is much higher for $E_i = 238.56$ meV. Hence, both the tail of the Bragg peaks as well as the incoherent background, have contributions above 5 meV. Also, the $(1, 1, 0)$ position corresponds to nuclear peak, so the dispersion of the phonon arising from these positions could also have some contributions. Therefore, to affirm the nature of the spin fluctuations below 10 meV, we performed another experiment at MACS (Multi Axis Crystal Spectrometer) at NIST neutron research reactor. This instrument is optimized for the measurement with $E_i = 2.1\text{--}20$ meV[132].

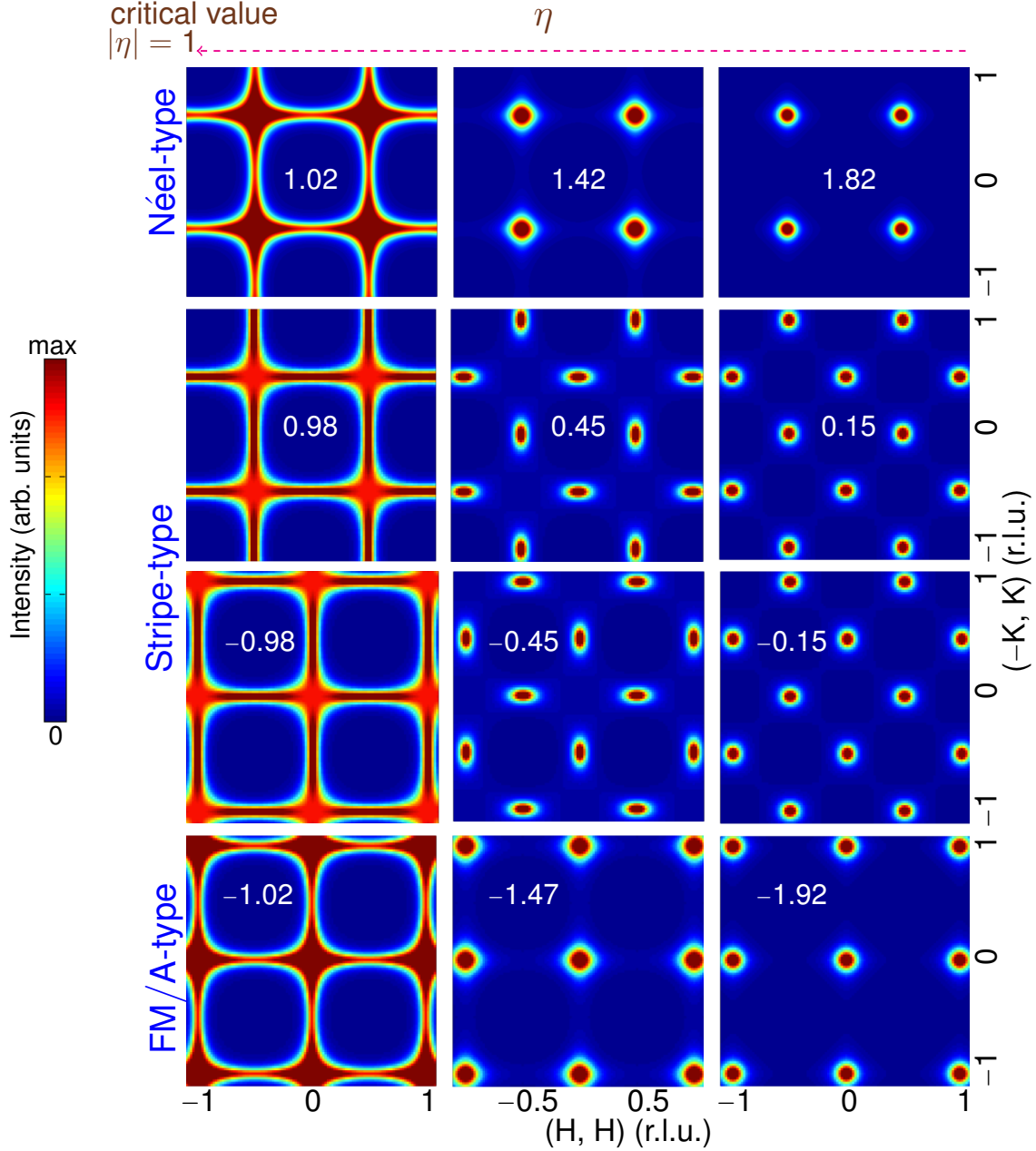


Figure 6.10 Constant energy slices showing INS cross-section calculated using the diffusive model for different magnetic ordering. The spin fluctuations become extremely anisotropic for all ordering with the frustration parameter $|\eta| \rightarrow 1$ (maximum frustration). This supports the fact that extremely anisotropic spin fluctuations are consequence of the system being in a highly-frustrated state. For maximum frustration $\eta = -1$ (1), the spin fluctuations for stripe-type and FM/A-type (Néel-type and stripe-type) become identical. The constant-energy slices are averaged over the energy ranges of 10–20 meV. The figure is reproduced from Ref. [50].

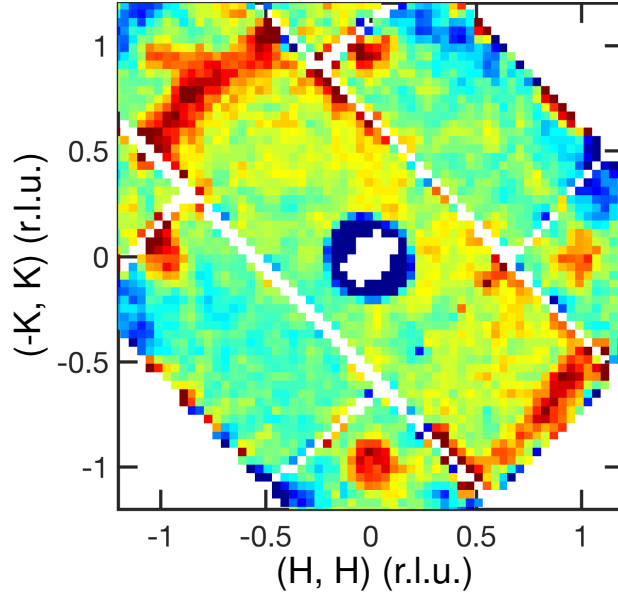


Figure 6.11 Constant-energy slices below 10 meV of the background subtracted data showing a peak centered at $Q_A = (1, 1)$ position. An isotropic background is subtracted after its estimation as discussed in Section 6.3.

6.5 Spin fluctuations below 10 meV: MACS results

6.5.1 Experimental Details

INS experiments were performed at MACS[132] at the NIST-neutron research reactor. Four single crystals of $\text{CaCo}_{1.86}\text{As}_2$, which were selected from the ones measured at ARCS, with a total mass of ~ 0.8 g were co-aligned in the (H, H, L) scattering plane (in tetragonal notation). Orange-cryostat was used to cool the sample. The sample base was attached to the end of a sample stick and inserted into a well filled with helium exchange gas. The measurements were carried out at 1.5 K, with final energy fixed at 5 meV. The configuration of the experimental setting was open before the monochromator, and Be-filter and 90° collimation was used after the sample. The data were visualized using the MSLICE software[162].

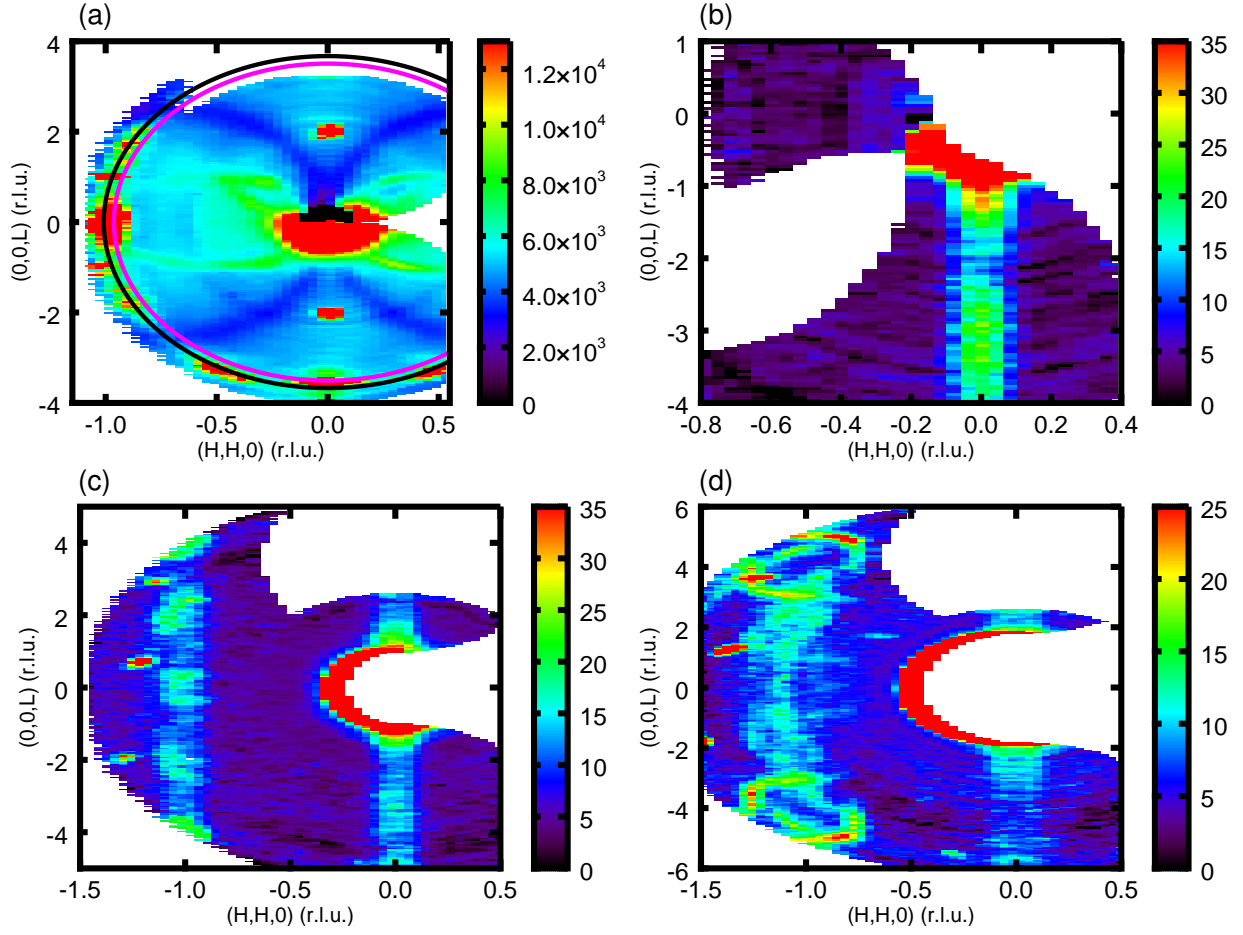


Figure 6.12 Low-energy spin fluctuations in $\text{CaCo}_{1.86}\text{As}_2$ at energy transfers of $E =$ (a) 0, (b) 3, (c) 5 and (d) 10 meV. The results are from the measurements done at $T = 1.5$ K at MACS spectrometer at NIST. Slices are obtained after subtracting the background from the empty-can measurements. In panel (a), the black and magenta rings corresponds to the $(2, 0, 0)$ and $(1, 0, 1)$ of the β -tin. Ring like features in (d) centered at $(1, 1, 4)$ position is from the sample phonon.

6.5.2 Results and analysis

Figure 6.12 shows that the spin fluctuations are centered at \mathbf{Q}_A positions and are consistent with the ARCS result, shown in Fig. 6.11. This infers that the continuum of the spin fluctuations starts at $E > 10$ meV. The cuts along the (H, H) direction, shown in Fig. 6.13 through $(0, 0, -3)$ for 3, 5 and 10 meV, are fit with two Gaussian lineshapes to obtain the center of the peaks. The dispersion plot in the Fig. 6.13 (d) is obtained using these centers. The dispersion plot is then fit with the dispersion equation for ferromagnet in the long-wavelength limit, i.e. $qa \ll 1$ or $\delta\pi \ll 1$:

$$E_q = Dq^2 \quad (6.25)$$

where, D is the stiffness constant. The values of the stiffness constant obtained from the fits to the MACS data is illustrated in the Table 6.2 along with the stiffness constant obtained from the ARCS data. The results indicate a presence of the very steep A-type spin waves at $E \leq 10$ meV.

Table 6.2 Stiffness constants obtained for the ARCS and MACS data, which represents the high and low-energy fluctuations, respectively. D_{LO} for ARCS data is the stiffness constant for the dispersion along the same direction as the MACS data.

D (meVÅ ²) (MACS)	492 ± 14
D_{LO} (meVÅ ²) (ARCS)	12 ± 1
D_{TR} (meVÅ ²) (ARCS)	811 ± 47

Figure 6.14 shows the cuts along the L direction at $(H, H) = (0, 0)$. For $E = 3$ meV, they are peaked at $L = 1, 3, \dots$, as expected for \mathbf{Q}_A . The spin waves appear to be almost L independent above $E \geq 5$ meV.

6.5.3 Discussion

The results show that the spin fluctuations of $\text{CaCo}_{1.86}\text{As}_2$ is centered at \mathbf{Q}_A at $E \leq 10$ meV. So, from the ARCS and MACS results, it is apparent that the continuum of the INS spectra appears $E > 10$ meV and very stiff A-type spin waves are observed at $E \leq 10$ meV. However, the gap energies at $\mathbf{Q}_{\text{stripe}}$ and at other wavevectors than \mathbf{Q}_A have not been established yet, and it is also

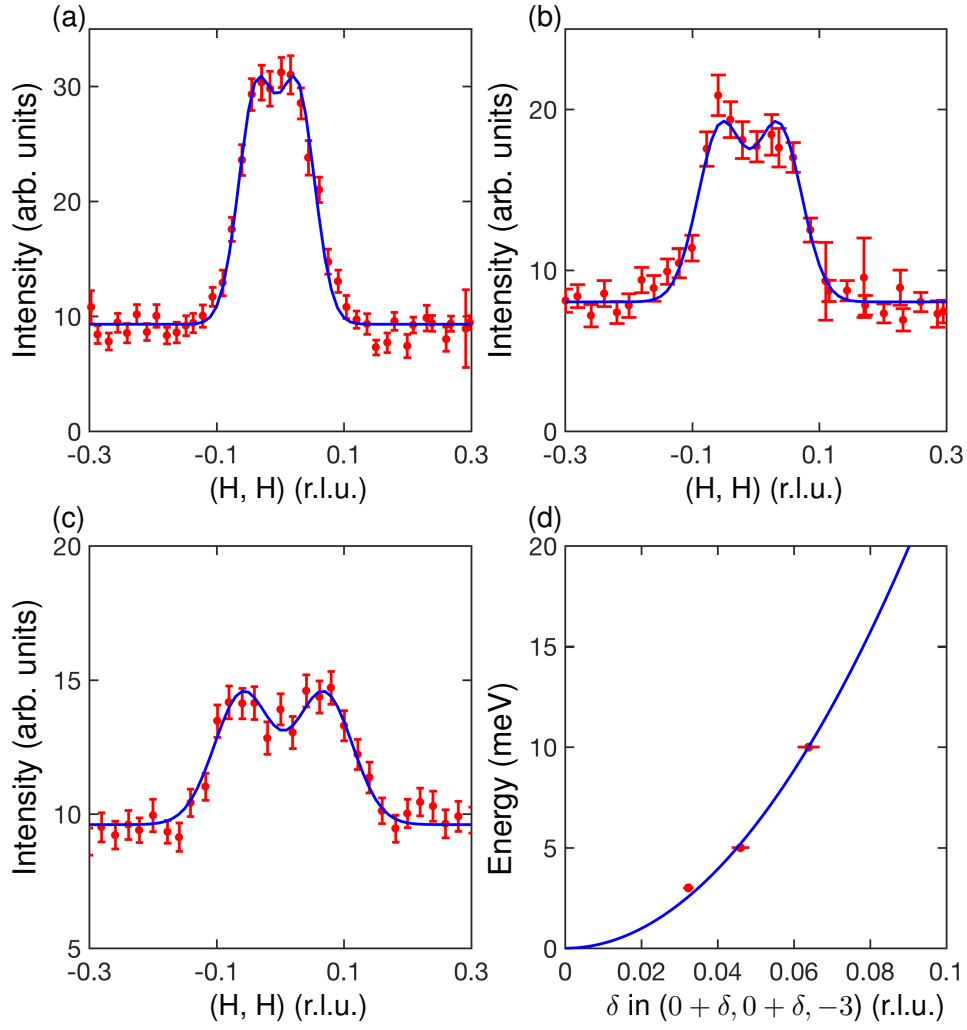


Figure 6.13 (a)–(c) Cuts along the (H, H) direction through $(0, 0, -3)$ peak for 3, 5 and 10 meV, respectively. (d) Corresponding dispersion plot obtained from the center of the peak of the fits to the cuts in (a)–(c) using two Gaussian line-shapes. Blue line is fit to the Eq. (6.25)

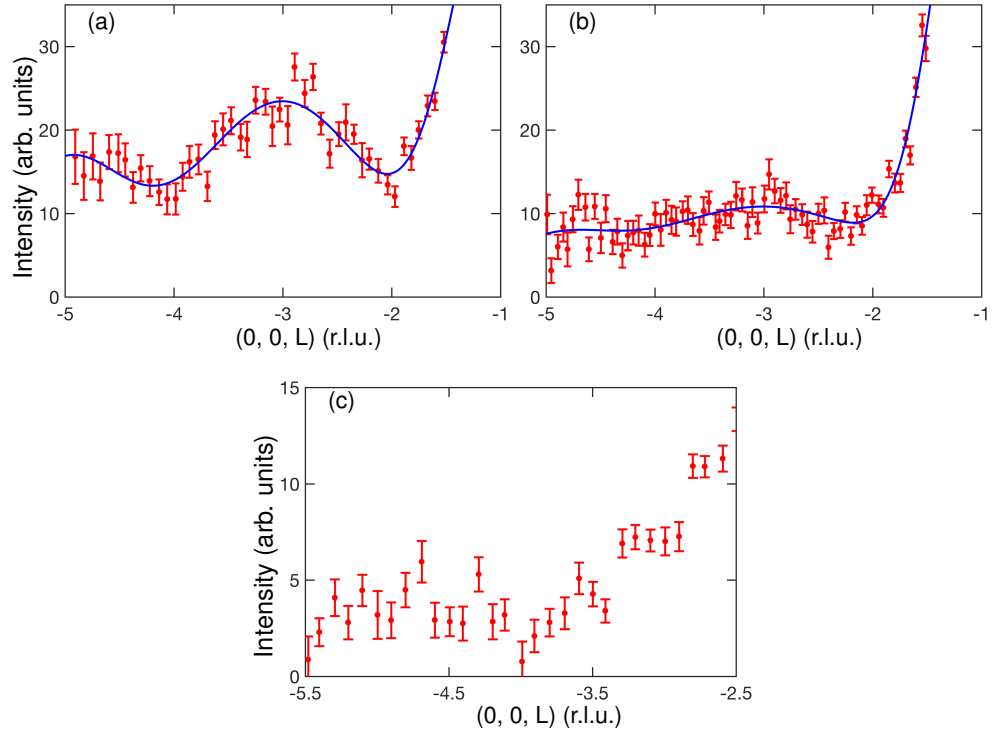


Figure 6.14 (a)–(c) Cuts along the $(0, 0, L)$ direction for $E = 3, 5$ and 10 meV, respectively. The increase in intensity at lower values of L is from the spillage of the direct beams. Blue lines are fit to the Gaussian lineshapes with the peaks centered at odd L .

interesting to find how this stiff spin waves evolve into the continuum. Further experiment for the measurements above 10 meV has already been planned to shed a light upon it.

A rough estimate of SJ_c can be obtained from the half-width at half maximum of the fit to the peaks at odd L as shown in Fig. 6.14. The dispersion relation of A-type in Eq. (6.2) at $(0, 0, L+0.5)$ gives $E = 2SJ_c$, and the half-width at half maximum of the peak fit of $(0, 0, -3)$ at $E = 1$ meV is nearly 0.6 r.l.u., which suggest that the $SJ_c \approx 0.5$ meV. However, the convolution with the instrumental resolution is needed for the better estimation of the peak width. The analysis of the results is ongoing and future detail analysis will be able to provide further insight into the data as well as a better estimation of the exchange parameter, SJ_c .

6.6 Derivation of the diffusive model for other magnetic orders

6.6.1 Diffusive model for the stripe-type antiferromagnet

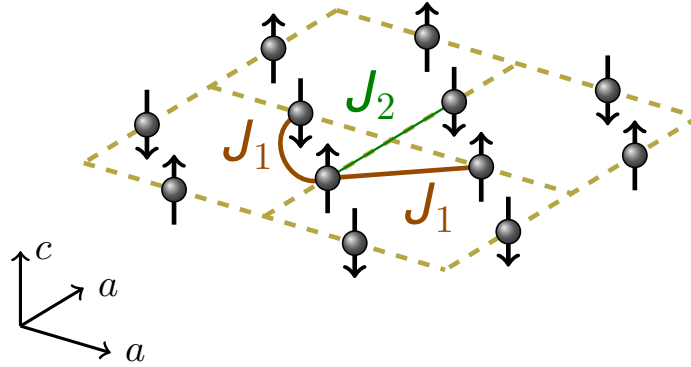


Figure 6.15 Two-dimensional arrangement of spins/moments in stripe-type order.

For stripe-type on a square lattice defined in the $I4/mmm$ cell with lattice parameter a as shown in Fig. 6.15, $J(0) = J(\pi, \pi)$ in Eq. (6.9). So, $J(\pi, \pi)$ for stripe-type is

$$J(0) = -4J_2 \quad (6.26)$$

and $J(\mathbf{q})$ is

$$J(\mathbf{q}) = 2J_1(c_{x+y} + c_{x-y}) + 4J_2(c_{x+y}c_{x-y}) \quad (6.27)$$

So, replacing these values in Eq. (6.9) gives

$$\chi''(\mathbf{q}, \omega) = \frac{\chi_0 \Gamma \omega}{\Gamma^2 \{1 + \chi_0 [2J_1(c_{x+y} + c_{x-y}) + 4J_2 c_{x+y} c_{x-y} + 4J_2]\}^2 + \omega^2} \quad (6.28)$$

Again, defining anisotropy parameter $\eta = J_1/2J_2$, which is also the definition of the frustration parameter, and an average correlation length $\xi^2/a^2 = J_2\chi_o$ to obtain

$$\chi''(\mathbf{q}, \omega) = \frac{\chi_0 \Gamma \omega}{\Gamma^2 \{1 + (4\xi^2/a^2)[\eta(c_{x+y} + c_{x-y}) + c_{x+y}c_{x-y} + 1]\}^2 + \omega^2} \quad (6.29)$$

and defining,

$$q^2 \xi_q^2 = (2\xi/a)^2 [\eta(c_{x+y} + c_{x-y}) + c_{x+y}c_{x-y} + 1]. \quad (6.30)$$

6.6.1.1 Correlation length and anisotropy parameter

For stripe-type, the spin fluctuations are centered at $\mathbf{q}_s = (\frac{\pi}{a}, \frac{\pi}{a})$ and the transverse and longitudinal cuts are made around this wavevector. So, for the LO direction, $\mathbf{q} = \mathbf{q}_s + \mathbf{k}_{LO} = \mathbf{q}_s + (\delta, \delta)$ and $k_{LO}^2 = 2\delta^2$ and

$$\text{LO} : k_{LO}^2 \xi_q^2 = (4\xi^2/a^2)(\eta + 1)(1 - \cos \delta a) \quad (6.31)$$

For $\delta a \ll 1$, this gives

$$k_{LO}^2 \xi_{LO}^2 \approx \frac{4\xi^2}{a^2}(\eta + 1) \frac{1}{2}(\delta a)^2 = \xi^2(\eta + 1)k_{LO}^2 \quad (6.32)$$

or

$$\xi_{LO}^2 = \xi^2(\eta + 1) \quad (6.33)$$

Similarly, for TR direction, $\mathbf{q} = \mathbf{q}_s + \mathbf{k}_{TR} = \mathbf{q}_s + (\delta, -\delta)$ and $k_{TR}^2 = 2\delta^2$ and

$$\text{TR} : k_{TR}^2 \xi_q^2 = (4\xi^2/a^2)(\eta + 1)(1 - \cos \delta a) \quad (6.34)$$

For $\delta a \ll 1$, this gives

$$k_{TR}^2 \xi_{TR}^2 \approx \frac{4\xi^2}{a^2}(1 - \eta) \frac{1}{2}(\delta a)^2 = \xi^2(1 - \eta)k_{TR}^2 \quad (6.35)$$

or

$$\xi_{\text{TR}}^2 = \xi^2(1 - \eta) \quad (6.36)$$

From Eqs. (6.33) and (6.36), the anisotropy parameter η in terms of correlation length is

$$\frac{\xi_{\text{LO}}^2}{\xi_{\text{TR}}^2} = \frac{1 + \eta + 1 - \eta}{1 - \eta} \quad (6.37)$$

On solving, the Eq. (6.37) becomes

$$\eta = \frac{\xi_{\text{LO}}^2 - \xi_{\text{TR}}^2}{\xi_{\text{LO}}^2 + \xi_{\text{TR}}^2} \quad (6.38)$$

which is consistent with the relationship used in Refs. [8, 80] for the stripe-type spin fluctuations.

6.6.2 Diffusive model for the Néel-type antiferromagnet

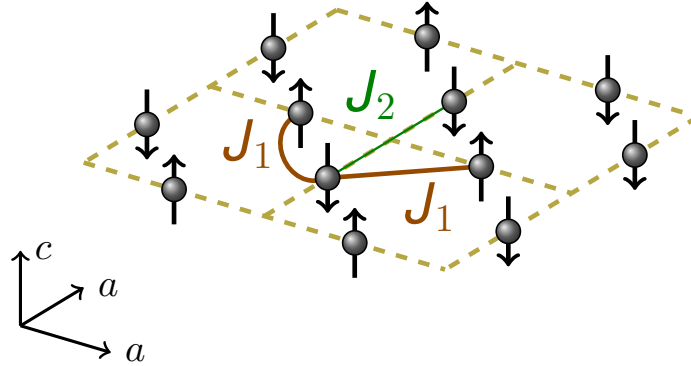


Figure 6.16 Two-dimensional arrangement of spins/moments in Néel-type order.

For the Néel-type on a square lattice of the $I4/mmm$ cell with a lattice parameter a as shown in Fig. 6.16, $J(0) = J(2\pi, 0)$ in Eq. (6.9). So, $J(2\pi, 0)$ for Néel-type is

$$J(0) = 4J_2 - 4J_1 \quad (6.39)$$

and $J(\mathbf{q})$ is

$$J(\mathbf{q}) = 2J_1(c_{x+y} + c_{x-y}) + 4J_2(c_{x+y}c_{x-y}) \quad (6.40)$$

So, replacing these values in Eq. (6.9) gives

$$\chi''(\mathbf{q}, \omega) = \frac{\chi_0 \Gamma \omega}{\Gamma^2 \{1 + \chi_0 [2J_1(c_{x+y} + c_{x-y}) + 4J_2 c_{x+y} c_{x-y} + 4J_1 - 4J_2]\}^2 + \omega^2} \quad (6.41)$$

Again, defining anisotropy parameter $\eta = J_1/2J_2$, which is also the definition of the frustration parameter, and an average correlation length $\xi^2/a^2 = J_2\chi_o$ to obtain

$$\chi''(\mathbf{q}, \omega) = \frac{\chi_0 \Gamma \omega}{\Gamma^2 \{1 + (4\xi^2/a^2)[\eta(c_{x+y} + c_{x-y}) + c_{x+y} c_{x-y} + 2\eta - 1]\}^2 + \omega^2} \quad (6.42)$$

CHAPTER 7 EFFECTS OF HOLE DOPING ON SPIN DYNAMICS OF $\text{Ba}_{1-x}\text{K}_x\text{Mn}_2\text{As}_2$

*Part of the content of this chapter has been published in Physical Review B [Phys. Rev. B **95**, 224401 (2017)] [51].*

As discussed in the section 2.5.2 of chapter 2, chemical substitution was employed on BaMn_2As_2 with the expectation of having similar effects as in 122 iron-arsenide and cuprate superconductors. BaMn_2As_2 is isostructural to AFe_2As_2 compounds and has an insulating local-moment AFM magnetic ground[9] (Néel/G-type, as shown in Fig. 2.6) state similar to cuprates, so the substitution is expected to suppress the G-type antiferromagnetism and drive the system towards superconductivity (SC), as observed in the above-mentioned two classes of superconductor[21]. However, most of the doping methods encounter miscibility problems and only K substitution at the Ba site (hole-doping) is successful in this regard. The K substitution alters the property of the parent BaMn_2As_2 . With only 1.6% of K substitution at Ba site, the insulating BaMn_2As_2 is driven to metallic state, thus, indicating the presence of insulator to metal transition[68], as observed in cuprates[163]. This was an indication of the possibility of SC in $\text{Ba}_{1-x}\text{K}_x\text{Mn}_2\text{As}_2$ compounds at higher K concentration, but the SC is found to be absent up to 40% K substitution[69, 70]. Consistently, the suppression of the Néel temperature T_N is also small and changes from 625 K of parent to 480 K for 40% K doped BaMn_2As_2 compound or $\text{Ba}_{1-x}\text{K}_x\text{Mn}_2\text{As}_2$ with $x = 0.40$ [69, 70].

Nevertheless, the doping induces interesting changes in this compound. As, already mentioned above, the doping causes significant changes in the electronic properties, i.e. the system undergoes an insulator-to-metal transition. In addition to this, for $x \geq 0.16$, the ferromagnetism is observed to coexist with the G-type AFM order below the curie temperature[70]. Furthermore, the recent x-ray circular dichroism (XMCD) measurement finds a large signal corresponding to the As K edge, which shows that the ferromagnetic (FM) order originates from the As $4p$ conduction bands[71]. The

FM ordered moment of $\mu_{\text{FM}} = 0.45 \mu_{\text{B}}/\text{f.u.}$ for $\text{Ba}_{1-x}\text{K}_x\text{Mn}_2\text{As}_2$ with $x = 0.40$ is determined from the magnetization measurement[70]. The ordered moment value is very close to $\mu_{\text{FM}} = 0.40 \mu_{\text{B}}/\text{f.u.}$ expected from the spin polarization of 0.40 conduction holes added per f.u. due to substitution by 0.40 K. So, the FM itinerant magnetism seems to mutually co-exist with AFM from Mn atoms without having any effects on it. This is in contrast to the expectations from the significant hybridization between Mn d and As p bands in BaMn_2As_2 [44]. This hybridization indicates that the introduction of the holes in the As p bands should induce changes in the AFM magnetic order and Mn moment size.

Therefore, the results of inelastic neutron scattering (INS) measurement on $\text{Ba}_{1-x}\text{K}_x\text{Mn}_2\text{As}_2$ compounds was performed to find out the effects of the hole doping on spin dynamics and has been discussed below. Moreover, the measurement was carried out to see if the evolution of spin dynamics across the insulator-metal transition is consistent with the decoupled nature of the AFM and FM order (charge transport) in $\text{Ba}_{1-x}\text{K}_x\text{Mn}_2\text{As}_2$ system.

7.1 Experimental details and preliminary sample characterization

INS measurements were performed on powders of BaMn_2As_2 and K-substituted $\text{Ba}_{1-x}\text{K}_x\text{Mn}_2\text{As}_2$ with $x = 0.125$ and 0.25 (with hole concentrations of $\delta = x/2$ per Mn ion) at ARCS spectrometer at Oak Ridge National Laboratory. The measurement were performed on the powders with mass of nearly 7 grams for each concentration. The samples were prepared by conventional solid-state reaction. Each sample was packed into a cylindrical Al sample can for neutron scattering measurements. The measurements were carried out at $T = 5$ K with incident neutron energies of $E_i = 30, 74, 144.7$ and 315 meV. The time-of-flight data were reduced into energy transfer (E) and momentum transfer (Q) profiles and data corrections for detector efficiency and the empty aluminum can were performed. The $S(Q, E)$ scattering profiles and constant energy/momentum cuts were obtained with MSLICE (DAVE) software[162].

The preliminary characterization of the samples were performed using x-ray diffraction, magnetization and magnetic susceptibility measurements. Room temperature powder x-ray diffraction

(XRD) data were obtained using a Rigaku Geigerflex powder diffractometer and Cu-K α radiation. Rietveld refinements of the powder XRD data were carried out using the FULLPROF package [164]. X-ray diffraction data are shown in Fig. 7.1 and the refinements of the data indicate the presence of MnO in the $x = 0.25$ sample. According to the refinement, the weight percentage of MnO in the $x = 0.25$ sample is 0.6(2)% which corresponds to a molar percentage 3(1)%. This is reasonably consistent with the presence of MnO spin waves in the INS data as discussed below. Similarly, for $x = 0.125$, the weight percentage of MnO is much smaller; 0.12(8)% and hence the molar fraction is 0.6(4)%.

Temperature and field dependent magnetic measurements were carried out using a magnetic properties measurement system from Quantum Design, Inc. Magnetization and susceptibility data are shown in Figs. 7.2 and 7.3. The figures suggest that the FM ordering is absent in both $x = 0$ and 0.125 samples, and indicates presence of it in $x = 0.25$ sample. These results are in consistent with the measurements performed on single crystals for K concentration above and below $x = 0.16$ [68, 125].

7.2 Results and analysis

Figure 7.4 shows the results of the inelastic neutron scattering measurements for $\text{Ba}_{1-x}\text{K}_x\text{Mn}_2\text{As}_2$, $x = 0, 0.125$, and 0.25, over the accessible energy and momentum transfer ranges for $E_i = 144.7$ meV. The figures are obtained after the subtraction of the empty can measurement and there are two prominent features in the spectra, (i) steeply dispersive features with higher intensity at low Q [as in Figs. 7.4 (a), (c)–(d)] or 2θ [as in Figs. 7.4 (b)] , and (ii) flat band-like features whose intensity increases with increasing Q or 2θ . These two features corresponds to the magnetic and lattice excitations, respectively, and are apparent because the measurement was performed with unpolarized neutrons. The steeply dispersive features at low Q are identified as magnetic in origin since their intensity falls off with Q consistent with the Mn^{2+} magnetic form factor. In addition, the steep dispersions originate from magnetic Bragg peaks of BaMn_2As_2 , such as $Q_{(101)} = 1.58 \text{ \AA}$ and $Q_{(103)} = 2.06 \text{ \AA}$, as shown in Fig. 7.4 (a), providing additional confirmation of their magnetic

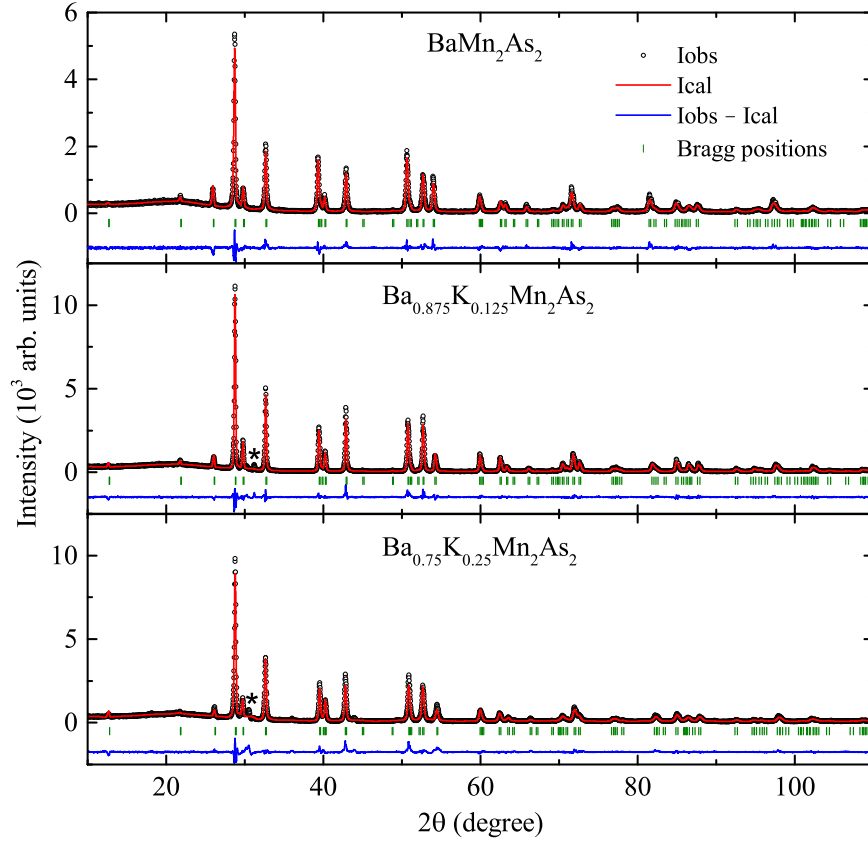


Figure 7.1 X-ray diffraction data for polycrystalline $\text{Ba}_{1-x}\text{K}_x\text{Mn}_2\text{As}_2$ with $x = 0, 0.125$, and 0.25 taken at room temperature. Two-phase refinements of the data including the parent phase and MnO impurities give a molar fraction of 3% MnO for $x = 0.25$ and 0.6% for $x = 0.125$. The figure is reproduced from Ref. [51].

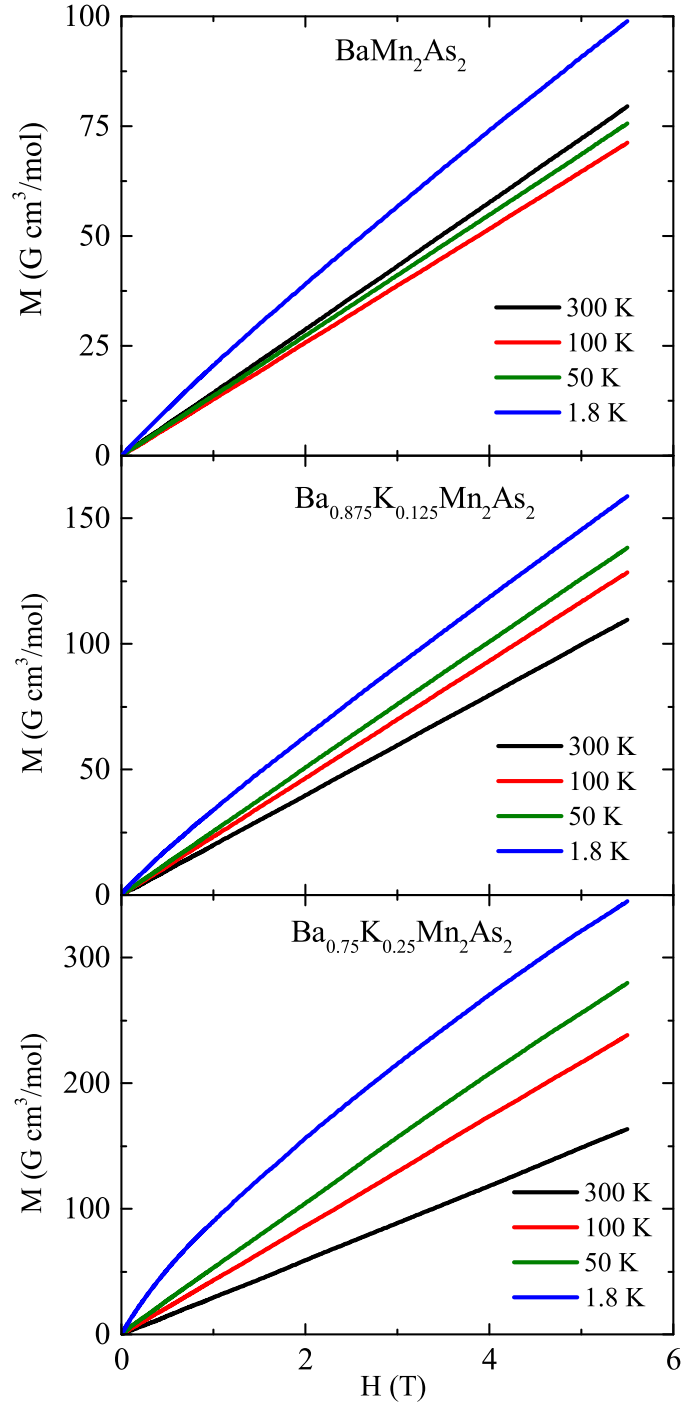


Figure 7.2 Magnetization data for polycrystalline $\text{Ba}_{1-x}\text{K}_x\text{Mn}_2\text{As}_2$ samples as a function of magnetic field at various temperatures. The data show linear behavior without any evidence of ferromagnetism in both $x = 0$ and 0.125 samples except for $x = 0.25$, which shows non-linear feature for $T = 1.8$ K isotherm as a hint of saturation of magnetization observed in ferromagnets. The figure is reproduced from Ref. [51].

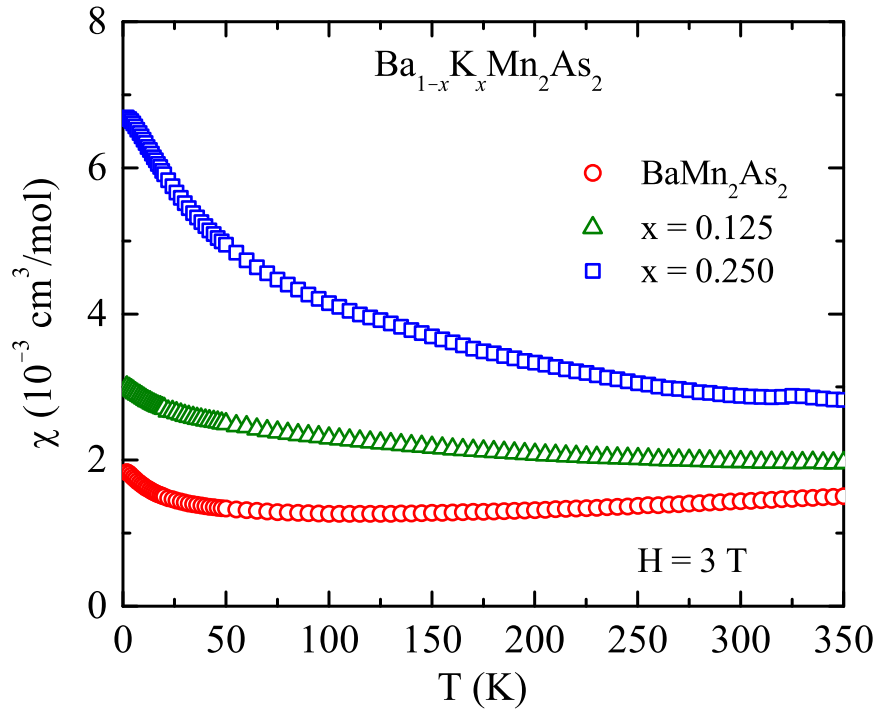


Figure 7.3 Magnetic susceptibility data for polycrystalline samples of $\text{Ba}_{1-x}\text{K}_x\text{Mn}_2\text{As}_2$ taken at a field of 3 T as a function of temperature. The enhancement in the susceptibility for $x = 0.25$ sample is an indication of FM ordering and is consistent with the single crystal measurements for $x > 0.16$ in Ref. [125]. The figure is reproduced from Ref. [51].

character[69]. The second features are phonon which are mainly below 40 meV with intensity increasing as Q^2 . The INS spectra looks qualitatively similar for all concentrations.

So, in addition to the magnetic contribution, $S_{\text{mag}}(Q, E)$, the powder-averaged inelastic neutron scattering intensity is comprised of several other contributions like nuclear (phonon) neutron scattering, $S_{\text{ph}}(Q, E)$, scattering from the empty can, $C(Q, E)$. There are also other instrumental and background contributions, that are combined into a general background function, $B(Q, E)$. Ignoring other experimental complications, such as sample absorption, the total cross-section can be approximated as,

$$I(Q, E) = S_{\text{mag}}(Q, E) + S_{\text{ph}}(Q, E) + B(Q, E) + C(Q, E) \quad (7.1)$$

The general prescription used for analysis of the magnetic scattering is to first subtract off an independent measurement of the empty can, which is performed in all instances discussed below. The next task is to estimate both S_{ph} and B and subtract them as well. In general, both S_{ph} and B can be fairly complicated functions of both Q and E and it is difficult to determine the full functional dependence, especially when impurity phases are present in the samples. So these background contributions are estimated differently in different instances discussed below.

In addition, Fig. 7.4 (d) of $x = 0.25$ shows some extra features at low Q (at lower Q than (101) Bragg peak) below 20 meV, which are from MnO impurities present in the sample. An estimation of the contribution from MnO is done by calculations of the spin wave scattering for pure MnO powder on the basis of published Heisenberg exchange constants[165], as described in the Section 7.3.1.2.

7.2.1 Energy spectrum of the spin waves

The energy spectrum of the spin waves can be obtained from averaging INS data over the low Q region [over a scattering angle range from $2\theta = 2.5$ – 35 degrees, as shown in Fig. 7.4 (b)]. As discussed above, there are background from the phonon scattering as well as other sources contributing to the total scattering intensity at low Q . To get the energy spectrum for the $E_i =$

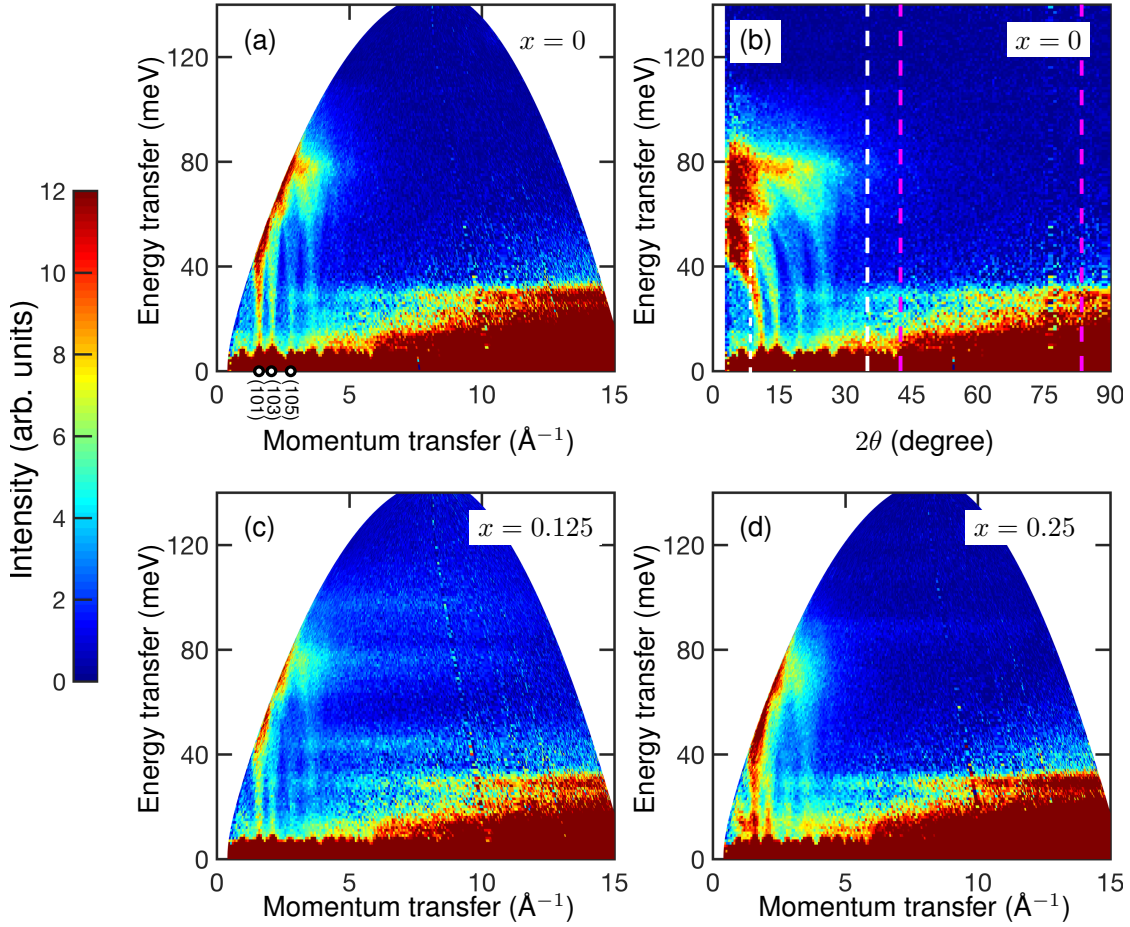


Figure 7.4 Inelastic neutron scattering (INS) data from a powder sample of $\text{Ba}_{1-x}\text{K}_x\text{Mn}_2\text{As}_2$ measured with $E_i = 144.7$ meV and $T = 8$ K. (a), (c) and (d) INS spectra of $\text{Ba}_{1-x}\text{K}_x\text{Mn}_2\text{As}_2$ as function of energy transfer (E) and momentum transfer (Q) for $x = 0, 0.125$ and 0.25 , respectively. (b) INS spectra of $x = 0$ as a function of energy transfer (E) and 2θ . The large white regions correspond to areas that are not accessible by the experiment due to kinematic restrictions of the scattering process. The color scale corresponds to the intensity of scattered neutrons obtained after the scattering from an empty aluminum sample can has been subtracted. Magnetic excitations appear as steeply dispersing modes at low- Q emanating from magnetic Bragg peaks (101), (103), (105), etc., while phonons appear as flat bands below 40 meV whose intensity increases as Q^2 . In (b) the region enclosed by maroon dashed lines corresponds to the high-angle spectra discussed in Section 7.2.1 and similarly white dashed line is the upper limit of the low-angle spectra.

144.7 meV data, as shown in Fig. 7.5, the total background is estimated by scaling the high-angled spectra where the phonon scattering is strong and magnetic scattering is absent. The magnetic spectrum $S_{\text{mag}}(E)$ is given by

$$S_{\text{mag}}(E) = S_{\text{low}}(E) - K S_{\text{high}}(E) \quad (7.2)$$

The high-angle spectrum $S_{\text{high}}(E)$ are averaged from 42.5–83.5 degrees, enclosed by dashed maroon line in Fig. 7.4, and is scaled by K . Then, they are subtracted from the low-angle spectrum $S_{\text{low}}(E)$ averaged from 2.5–35 degrees. Dashed white line in Fig. 7.4 is the 35 degrees mark. It is clear from Fig. 7.5(a) that the $x = 0$ sample is relatively clean from impurities as there are no phonon features found above 40 meV. The scale factor K is chosen by eye to completely eliminate obvious phonon peaks for $x = 0$ and was found to be $K = 0.35$. On the other hand, the $x = 0.125$ and 0.25 samples have additional phonon peaks above 40 meV due to impurity phases in the powder sample. Whereas the low energy phonons (< 50 meV) scale with the same K factor, a different scale factor of 0.6 and 1.4 for the $x = 0.125$ and 0.25 samples, respectively, is employed for the higher energy phonons (> 50 meV) that originate from sample impurities. The low-angle and scaled high-angle spectra are shown in Fig. 7.5, and the difference, $S_{\text{mag}}(E)$ is shown as the shaded region in Fig. 7.5 and also as the data in Fig. 7.6.

The magnetic spectrum for the parent compound is characterized by a peak near 75 meV and an upper cutoff of ~ 115 meV, similar to that published previously [9]. The K-substituted samples, especially the more heavily substituted $x = 0.25$ composition, show some deviations from the parent compound, such as a shift of the main spectral peak to lower energies (~ 70 meV) and some spectral broadening. The mean energy of the distribution, $\langle E \rangle$, (averaged over an energy range from 30 to 110 meV) changes from 66.0 to 59.2 for $x = 0$ and 0.25, respectively, in rough correspondence with the decrease in T_N , as shown in Table 7.1. These doping-dependent effects can arise from a lowering of the average exchange energy with hole doping, disorder, or from damping effects associated with the introduction of hole carriers into the system.

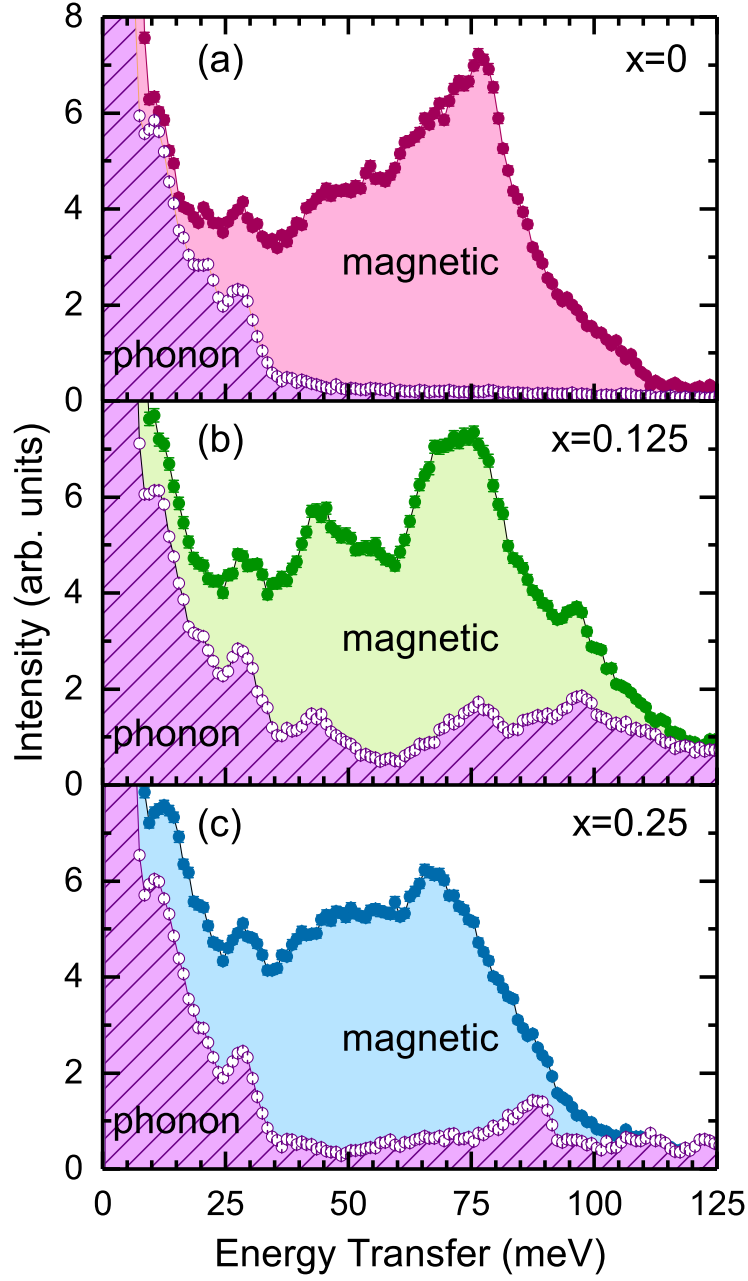


Figure 7.5 High-angle spectra (empty symbols) and scaled low-angle spectra (solid symbols) at $E_i = 144.7$ meV for (a) $x = 0$, (b) 0.125, and (c) 0.25. The shaded region corresponds to the estimated magnetic scattering spectrum $S_{\text{mag}}(E)$ and the hatched shaded area is $KS_{\text{high}}(E) \approx S_{\text{ph}}(E) + B(E)$. The figure is reproduced from Ref. [51].

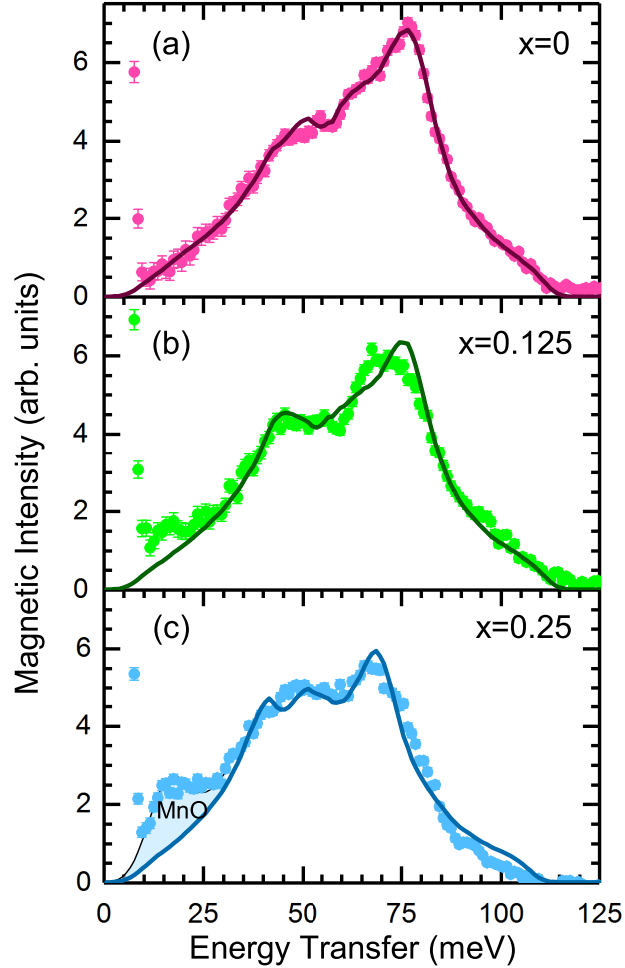


Figure 7.6 Magnetic spectra for $\text{Ba}_{1-x}\text{K}_x\text{Mn}_2\text{As}_2$ as a function of energy for (a) $x = 0$, (b) $x = 0.125$ and (c) $x = 0.25$. Symbols show the neutron data that were obtained with $E_i = 144.7$ meV and summed over a scattering angle range from 2.5 to 35 degrees after subtracting the total background from phonons and other sources as given by Eq. (7.2). Lines correspond to fits obtained using the Heisenberg model described in section 7.2.4. For $x = 0.25$, the additional magnetic scattering observed at low energies (shaded region) is consistent with antiferromagnetic spin wave scattering from MnO[165]. The figure is reproduced from Ref. [51].

Table 7.1 Rough correspondence between relative change of $k_{\text{B}}T_{\text{N}}$ and $\langle E \rangle$ in $\text{Ba}_{1-x}\text{K}_x\text{Mn}_2\text{As}_2$ with doping. $k_{\text{B}}T_{\text{N}}$ is the actual Néel temperature measured by neutron diffraction. Errors are given as one standard deviation. The figure is reproduced from Ref. [51].

Composition	$x = 0$	$x = 0.125$	$x = 0.25$
Hole conc./Mn	$\delta = 0$	$\delta = 0.0625$	$\delta = 0.125$
$k_{\text{B}}T_{\text{N}}$ (meV)[69]	53.9(1)	52.7	49.6(3)
$\langle E \rangle$ (meV)	66.0(3)	64.7(4)	59.2(3)

7.2.2 Spin gap and its evolution with doping

One may not expect a spin gap, Δ , in the BaMn_2As_2 compound if it is considered to have the formal valence state of Mn^{2+} [9, 44]. Mn^{2+} is a spin-only ($S = 5/2$) ion with no magneto-crystalline anisotropy based on the crystal-field effects, hence no spin gap. However, Fig. 7.7 clearly shows the presence of a gap in the spin wave spectrum at the G-type magnetic Bragg peaks for $x = 0.25$ sample. The spin gap likely arises from single-ion anisotropy of the Mn ion. Therefore, the presence of a spin gap and the observation of a smaller ordered moment of $4 \mu_{\text{B}}$ instead of $5 \mu_{\text{B}}$ for $S = 5/2$ suggest that the Mn moment has an orbital component, perhaps more consistent with Mn^+ [9]. The effect of the hole doping is then interesting, because if the doped holes occupy Mn ions, then one would expect more Mn^{2+} character and a closing of the spin gap with doping.

The measurement at 30 meV for which spin gap is clearly visible was not carried out for all concentrations. So, to determine the spin gap for all concentration and its evolution, we first performed constant- Q energy cuts over a small range of Q ($\pm 0.08 \text{ \AA}^{-1}$) centered at $Q_{(101)}$ and $Q_{(103)}$ for the $E_{\text{i}} = 74 \text{ meV}$ data. The background was estimated by similar cuts performed over the range from $Q = 1.75$ to 1.9 \AA^{-1} [in between (101) and (103)] and 2.35 to 2.4 \AA^{-1} [above (103)] and subtracted from the (101) and (103) cuts after accounting for the Q^2 dependence, respectively. The resulting data are shown in Fig. 7.8. A sharp onset of magnetic intensity above $\sim 5 \text{ meV}$ is observed for all compositions. The large errors in the intensity at the lowest energies arise from the subtraction of the strong elastic scattering contribution to the estimated background. The lowest energies background were estimated by fitting the Bragg peak with a Gaussian lineshape.

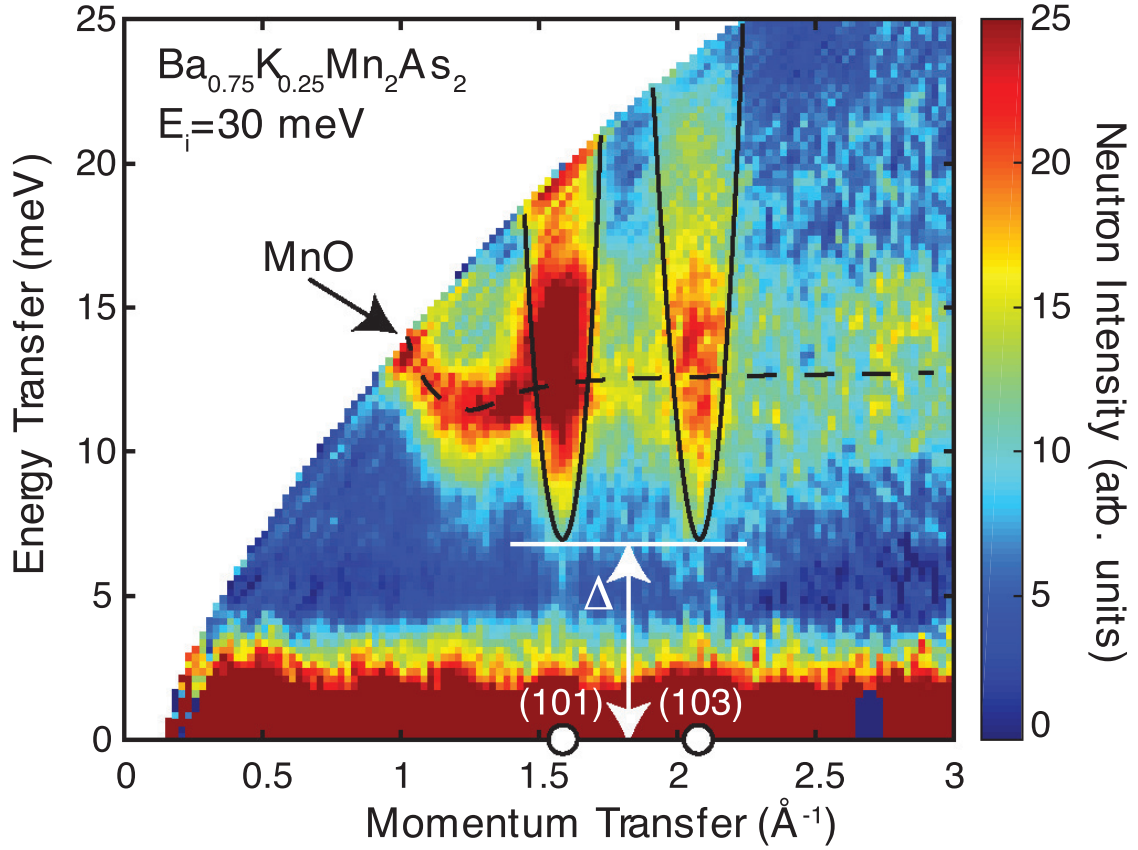


Figure 7.7 $S(Q, E)$ profile of the $\text{Ba}_{0.75}\text{K}_{0.25}\text{Mn}_2\text{As}_2$ sample measured with $E_i = 30$ meV. Steeply dispersive excitations from $Q_{(101)}$ and $Q_{(103)}$ Bragg peaks are highlighted by the solid black outlines. It is evident that a well-defined energy gap (Δ) exists which can be estimated visually to be about $\Delta \approx 6 - 7$ meV. The black dashed line highlights contributions of the spin wave scattering from MnO impurities that can be confirmed from MnO spin wave calculations shown in the Section 7.3.1.2. The figure is reproduced from Ref. [51].

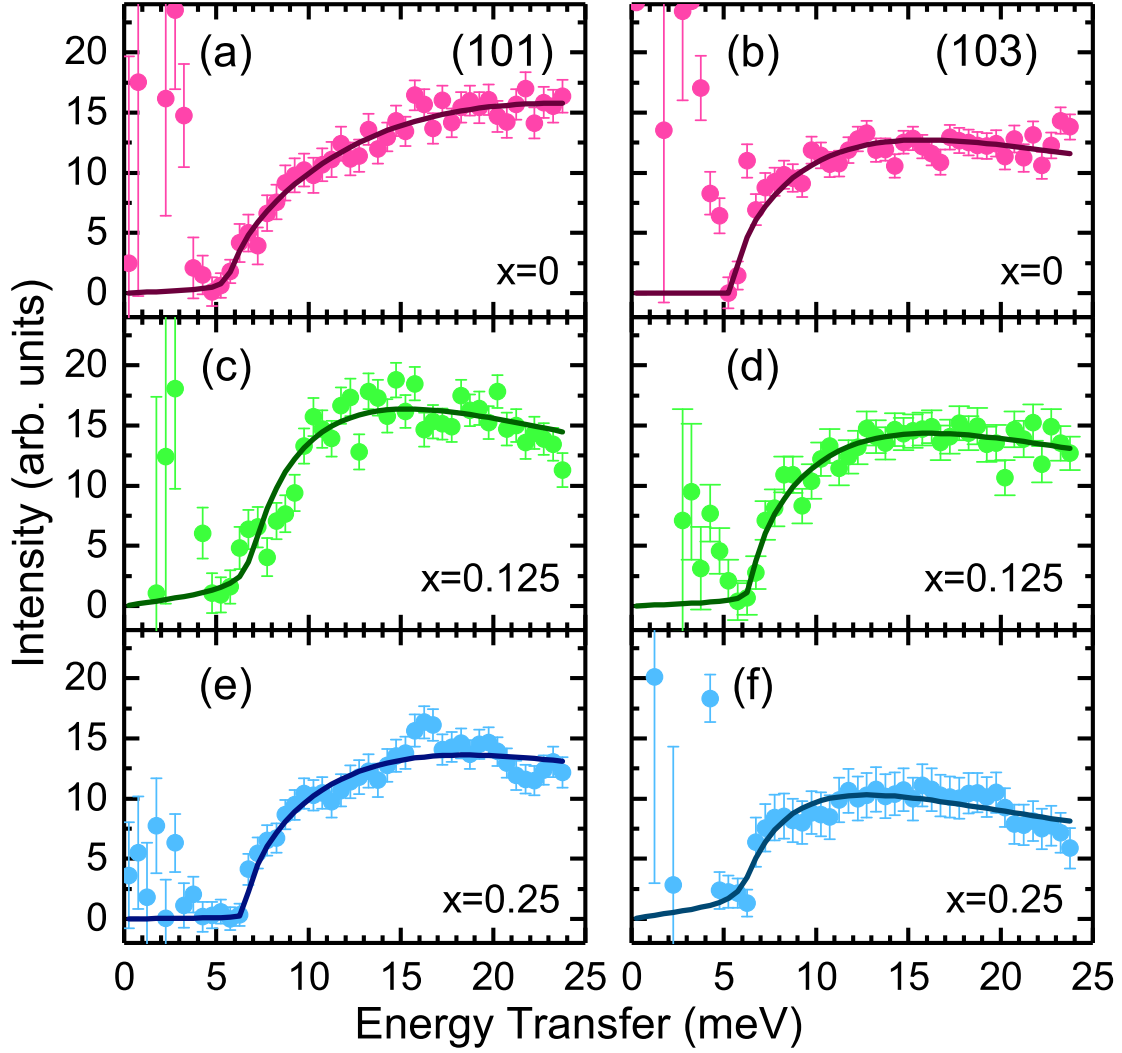


Figure 7.8 Energy cuts from $E_i = 74$ meV data centered at $Q_{(101)}$ [left panels (a), (c), and (e)] and $Q_{(103)}$ [right panels (b), (d) and (f)] are used to determine the spin gap, Δ , for different concentrations of $\text{Ba}_{1-x}\text{K}_x\text{Mn}_2\text{As}_2$ with $x = 0$ [(a) and (b)], $x = 0.125$ [(c) and (d)] and $x = 0.25$ [(e) and (f)]. On each panel, the solid line is obtained by fits of Eq. (7.3) to the data for each composition. The values of the fit parameters are given in Table 7.2. The figure is reproduced from Ref. [51].

Table 7.2 Doping evolution of the spin gap Δ and energy scale Γ of the spin waves in $\text{Ba}_{1-x}\text{K}_x\text{Mn}_2\text{As}_2$. The values are obtained from fits of the constant- Q cuts to the Eqs. (7.3) and (7.4). Errors are given as one standard deviation. The table is reproduced from Ref. [51].

Composition	$x = 0$	$x = 0.125$	$x = 0.25$
Hole conc./Mn	$\delta = 0$	$\delta = 0.0625$	$\delta = 0.125$
Δ (meV)	5.65(15)	6.71(19)	6.28(21)
Γ (meV)	18.1(8)	12.5(8)	12.6(8)

The gap value for each composition is obtained by fitting the low energy spectrum to a damped simple harmonic oscillator expression

$$S(Q, E) = \frac{AE'\Gamma}{\Gamma^2 + E'^2} \quad (7.3)$$

where E' is given by

$$E' = \frac{1}{\sqrt{2}} \left[\left((E^2 - \Gamma_s^2 - \Delta^2)^2 + 4E^2\Gamma_s^2 \right)^{1/2} + (E^2 - \Gamma_s^2 - \Delta^2) \right]^{1/2}. \quad (7.4)$$

Here A is the lineshape amplitude, E is the energy transfer, Δ is the spin gap, Γ_s is a damping constant that describes the sharpness of the gap, and Γ is the energy scale of the spin fluctuations[141]. Preliminary fits in which all parameters are allowed to vary independently generate similar values for Γ and Δ from the (101) and (103) cuts. Thus, global fits to the (101) and (103) cuts for each K-substituted sample were performed to obtain Γ and Δ while allowing the parameter A to vary at each of the wavevectors. The fit values are listed in the Table 7.2.

The results show that the magnitude of the spin gap is almost similar for all the concentrations and the gap is not closing with the addition of holes, thus, do not occupy Mn ions as discussed above. The results is consistent with other observations that doped holes reside primarily in As p bands, and therefore should not dramatically change the single-ion anisotropy of Mn ions. Γ appears to decrease with composition in these fits. However, the physical interpretation of Γ is complicated for several reasons. Steep acoustic spin waves exist above the gap and changes in Γ can arise from changes in the spin wave velocity, damping, or a combination of the two. Also, the presence of MnO impurities in doped compositions can affect the determination of Γ .

The background determined above does not account for the presence of the MnO spectra, which contributes additional intensity around ~ 13 meV to the spin-wave at (101) of $\text{Ba}_{1-x}\text{K}_x\text{Mn}_2\text{As}_2$ $x = 0.25$, measured with $E_i = 74$ meV.

7.2.3 Heisenberg model and other relevant quantities

To ascertain more clearly the effect of hole doping on magnetic exchange interactions between Mn spins (S_i), the full (Q, E) -dependence of the G-type spin wave excitations were analyzed using the $J_1 - J_2 - J_c$ Heisenberg model. Here, J_1 and J_2 are the in-plane NN and NNN exchange interactions and J_c is the out-of-plane NN AFM interaction. This Hamiltonian is written as

$$H = J_1 \sum_{\text{NN}, ab} \mathbf{S}_i \cdot \mathbf{S}_j + J_2 \sum_{\text{NNN}, ab} \mathbf{S}_i \cdot \mathbf{S}_j + J_c \sum_{\text{NN}, c} \mathbf{S}_i \cdot \mathbf{S}_j - D \sum_i (S_i^z)^2 \quad (7.5)$$

The last term in Eq. (7.5) represents the single-ion anisotropy where D is the uniaxial anisotropy parameter appropriate for Mn spins directed along the c -axis.

Similar to Ref. [9], the AFM interactions are represented by positive $J_i > 0$. Within this model, the G-type ground state is only possible when J_1 and J_c are AFM. However, J_2 can be either FM or AFM. A ferromagnetic J_2 stabilizes the G-type order, whereas an AFM J_2 is a frustrating interaction that can destabilize G-type order. When J_2 is AFM, classical G-type and stripe-type AFM ground state are possible and their classical mean-field energies are given by

$$E_G = NS^2(-2J_1 - J_c + 2J_2) \quad (7.6)$$

$$E_{\text{stripe}} = NS^2(-2J_2 - J_c) \quad (7.7)$$

where N is the total number of spins. The G-type state has a lower energy when $J_1 > 2J_2$ as discussed in Section 2.4.1 of Chapter 2.

In order to simulate the full INS spectrum of $S(Q, E)$ for $\text{Ba}_{1-x}\text{K}_x\text{Mn}_2\text{As}_2$, the linear spin wave approximation of the Heisenberg Hamiltonian given in Eq. (7.5) was used. The problem is cast in terms of the Holstein-Primakoff representation involving the boson spin operators. Using the

Fourier transform of boson operators over the Mn sublattice, the following spin-wave dispersion relations are obtained for the G-type AFM structure in the $I4/mmm$ unit cell [9]

$$\left[\frac{\hbar\omega(\mathbf{q})}{2S} \right]^2 = [2J_1 + J_c + D - J_2(2 - \cos q_x a - \cos q_y a)]^2 - \left\{ J_1 \left[\cos \frac{(q_x + q_y)a}{2} + \cos \frac{(q_x - q_y)a}{2} \right] + J_c \cos \left(\frac{q_z c}{2} \right) \right\}^2 \quad (7.8)$$

where \mathbf{q} is the wavevector measured relative to the G-type magnetic Bragg peak.

Various other quantities can be estimated from the Heisenberg spin wave theory. Mean-field analysis shows that the Néel temperature is given by [9]

$$(k_B T_N)_{\text{MF}} = 2(2J_1 - 2J_2 + J_c) \frac{S(S+1)}{3}. \quad (7.9)$$

This mean-field value of T_N will overestimate the actual transition temperature. A more accurate relationship between T_N and the exchange constants can be obtained from fits to the ordering temperature obtained from classical Monte Carlo simulations of the $J_1 - J_2 - J_c$ Heisenberg model[9].

This provides the following relation

$$(k_B T_N)_{\text{MC}} = \frac{A J_1 S(S+1)}{B - \ln(J_c/J_1)} \left[1 - \left(\frac{J_2/J_1}{R_1} \right)^{R_2} \right] \quad (7.10)$$

where $A(S+1) = 26.13$, $B = 6.87$, $R_1 = 0.644$, and $R_2 = 1.082$. After obtaining the exchange constants from fitting the INS data as described below, very good agreement is found between $(k_B T_N)_{\text{MC}}$ and the measured value of $k_B T_N$, but the MF values are a factor of two too high, as shown in Table 7.3.

For analysis of the low-energy spin excitations, one can also derive the value of the spin gap in terms of the single-ion anisotropy and exchange constants.

$$\Delta^2 \approx 8DS^2(2J_1 + J_c) \quad (7.11)$$

The experimentally determined value of $\Delta \approx 6$ meV will allow us to determine the anisotropy parameter, D , after the other exchange constants are determined by fitting (see Table 7.3).

For energies up to about 50 meV, the dispersion is roughly linear above the spin gap. The slope in the linear region is related to the spin wave velocity according to the relation

$$\hbar\omega(\mathbf{q}) = [\Delta^2 + \hbar^2 v_{ab}^2 (q_x^2 + q_y^2) + \hbar^2 v_c^2 q_z^2]^{\frac{1}{2}}, \quad (7.12)$$

where $\hbar\omega(\mathbf{q})$ is the energy of the spin wave mode at wavevector \mathbf{q} close to the center of the first Brillouin zone. v_{ab} and v_c are the two unique spin wave velocities (in the ab -plane and along the c -direction, respectively) that are allowed based on the tetragonal symmetry of the crystal structure.

From Eq. (7.8), these velocities can be written in terms of magnetic exchange constants as

$$\hbar v_{ab} = 2J_1 S a \left[\left(1 - \frac{2J_2}{J_1} \right) \left(1 + \frac{J_c}{2J_1} \right) \right]^{\frac{1}{2}} \quad (7.13)$$

$$\hbar v_c = \sqrt{2} J_1 S c \left[\left(\frac{J_c}{J_1} \right) \left(1 + \frac{J_c}{2J_1} \right) \right]^{\frac{1}{2}}$$

In principle, the spin wave velocity can be estimated in a model-independent fashion by determining the slope from the raw INS data. However, estimates of the spin wave velocity on powder samples are complicated by the averaging over different propagation directions and the sampling of reciprocal space. As described below, since v_{ab} is reasonably well defined from the data, it serves as an excellent fitting parameter for the Heisenberg model.

Solution of the linear spin wave equations-of-motion also produces the spin eigenvectors for each mode. These eigenvectors can be used to calculate the magnetic neutron scattering intensity, $S_{\text{mag}}(\mathbf{Q}, E)$, for each mode (where $\mathbf{Q} = \tau + \mathbf{q}$ with τ a magnetic Bragg peak position). In the case of powder samples, the neutron scattering intensity must be averaged over all directions of \mathbf{Q} . This can be done numerically, providing an intensity function, $S_{\text{mag}}(Q, E)$ that is suitable to compare directly to the background-subtracted magnetic scattering data[9, 166].

7.2.4 Fits to the Heisenberg model

The Heisenberg model spin wave calculations were performed for different sets of SJ_1 , SJ_2 and SJ_c values that were sampled by a Monte Carlo routine and compared with the INS data using

a simple χ^2 test. The evaluations of χ^2 were performed with two methods. In the first method, the full (Q, E) data set [as shown in panels (a)–(c) of Fig. 7.9] were attempted to fit after making estimates of the background throughout. In the second case, the data were summed over a range of angles, the energy dependence of the background were estimated and subtracted and model fits were performed to this energy spectrum [as shown in panels (a)–(c) of Fig. 7.6]. Both methods gave similar results for the exchange constants. However, the second method is preferred as it eliminates issues where background can dominate the evaluation of χ^2 in regions where the magnetic scattering is absent.

Here, the focus is on the results of the second method and discussion of the fits to the spectra in Fig. 7.6. Powder-averaged calculations for a given set of J_i were performed by Monte Carlo sampling 5000 \mathbf{Q} -vectors on a given sphere of magnitude Q , giving the average energy-dependent neutron spectrum on each Q sphere between $Q = 0$ to 6.0 \AA^{-1} with a step of $\Delta Q = 0.015 \text{ \AA}^{-1}$ (this amounts to the sampling of two million different wavevectors for a given set of J_i). The resulting powder-averaged magnetic scattering, $S_{\text{mag}}(Q, E)$, was then averaged over the kinematically allowed Q values for the experimental conditions with $E_i = 144.7 \text{ meV}$ and $2\theta = 2.5\text{--}35$ degrees (as shown in Fig. 7.9). A reduced χ^2 was evaluated by comparing these calculations to the data over the energy range from 30–110 meV after determining an overall scale factor that matched the integrated areas of the experimental and calculated spectra. As many as 35000 different sets of J_i were evaluated for each composition with finer steps in parameter space taken close to minima in χ^2 . In general, fits that constrained the J_i 's to fixed values of v_{ab} produced sharper minima in χ^2 . Error bars in all fitted and derived parameters are reported to one standard deviation. The errors of a given parameter are determined by its extremal values when the reduced χ^2 is projected onto the parameter axis over the interval from χ_{min}^2 to $\chi_{\text{min}}^2 + 3.53$ [167].

This method produced reduced χ_{min}^2 values of 1.8, 6.2 and 12.0 for $x = 0, 0.125$ and 0.25 , respectively, and the corresponding values of the exchange parameters at χ_{min}^2 are listed in Table 7.3. Calculations of the neutron spectra with these parameters, shown in Figs. 7.9 (d)–(f) and as the lines in Fig. 7.6, show reasonable agreement with the data. For BaMn_2As_2 , Figs. 7.9 and

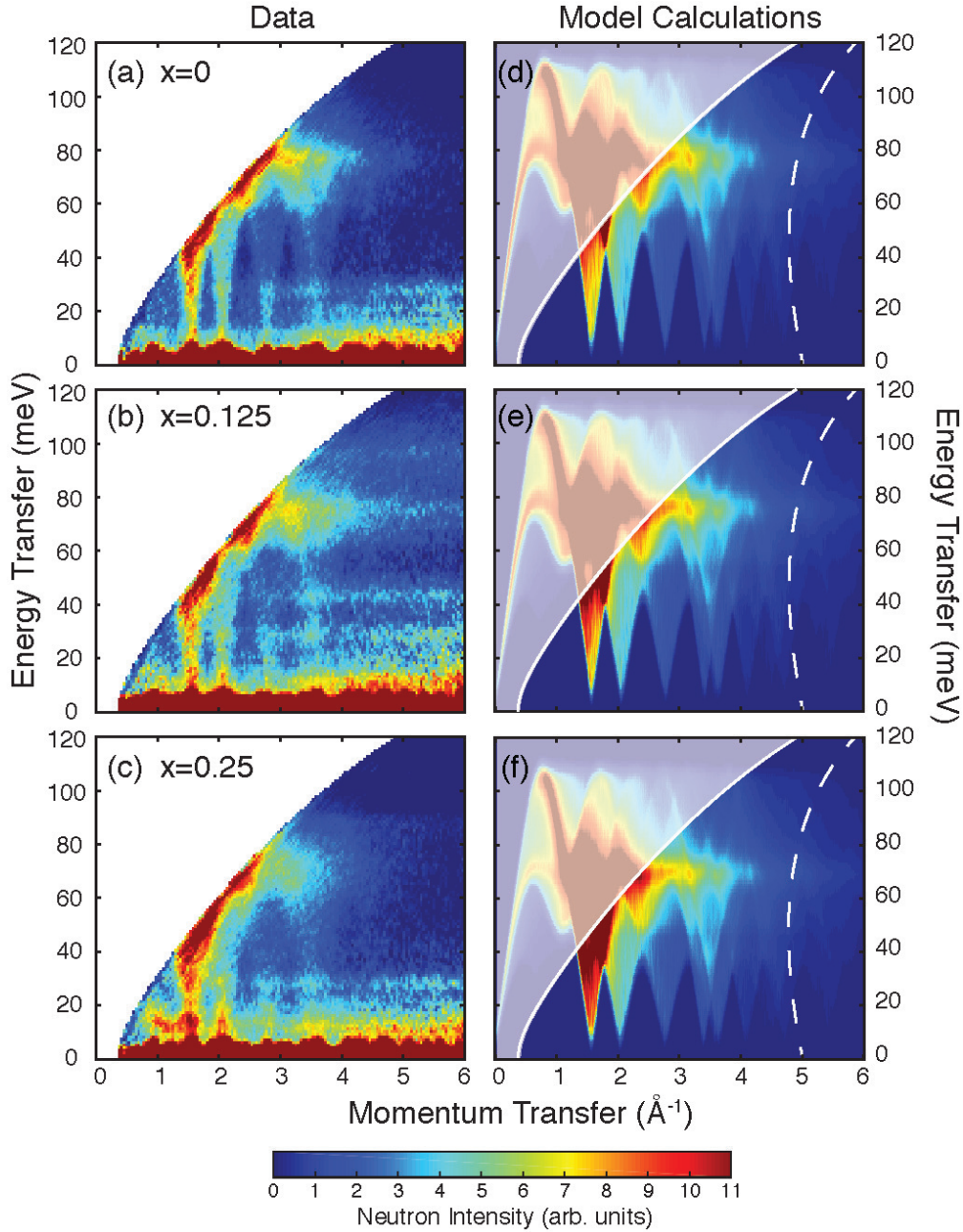


Figure 7.9 Inelastic neutron scattering data measured with $E_i = 144.7$ meV from powders of BaMn₂As₂ in panel (a) and K-doped Ba_{1-x}K_xMn₂As₂ in panels (b) $x = 0.125$ and (c) $x = 0.25$. Data panels are drawn over a smaller Q range as compared to Fig. 7.1. Panels (d), (e) and (f) show neutron intensities calculated using linear spin wave theory of the Heisenberg model for corresponding powders using parameters obtained by fitting the data. Shaded intensities in the upper left of panels (d), (e) and (f) are inaccessible by the experiment due to kinematic constraints defined by the lowest scattering angle of $2\theta_{\min} = 2.5$ degrees. The dashed white line on the right corresponds to a scattering angle of $2\theta = 35$ degrees and was used as a cutoff for the summation of the magnetic spectra shown in Fig. 7.6. The figure is reproduced from Ref. [51].

7.6 show that the Heisenberg model does an excellent job of representing the data. However, the Heisenberg model fits become progressively worse with increased K substitution which is partly due to the higher prevalence of impurity phases that make estimations of the background more difficult. In addition, the poorer fits might also indicate that other interactions that are neglected in the analysis, such as damping, chemical disorder or longer-range interactions, may be present in the metallic samples.

For the parent compound, large values for SJ_1 and SJ_2 are found, consistent with high T_N [69]. A relatively small interlayer exchange ($J_c/J_1 \approx 0.05$) indicates that the magnetism is quasi-two-dimensional in nature. A large AFM NNN interaction (with $J_1/2J_2 \approx 1.5$) highlights that some degree of magnetic frustration is present in BaMn_2As_2 . The exchange values obtained for the parent compound are generally larger than the previous INS results described in Ref. [9], although derived quantities such as v_{ab} and $J_1/2J_2$ show better agreement. This study is likely to be an improvement over the previous work with the better quality data and robust fitting methods.

Generally speaking, relative errors on individual J_i range from 5–20% whereas combined parameters, such as v_{ab} , are much more narrowly defined with relative errors between 1–3%. Essentially, the fits to the INS data are most sensitive to combinations of the exchange parameters due to a high degree of correlation between the individual pairwise exchange constants. Thus, while SJ_1 and SJ_2 do not change with composition within error, SJ_c , v_{ab} and v_c are all reduced by K substitution.

A more quantitative picture of the agreement between the model and data can be ascertained from a series of constant-energy Q -cuts, as shown for BaMn_2As_2 in Fig. 7.10. In these plots, the model calculations (red) are added to an estimate of a quadratic plus constant background contribution (blue). Below 40 meV, the constant-energy Q cuts show a series of peaks in the linear acoustic spin wave regime. The higher-energy cuts correspond to spin waves close to the Brillouin zone boundary. The spin wave dispersion flattens out in these regions of reciprocal space, leading to large contributions to the powder-averaged spin wave scattering intensity and a more continuous Q dependence. The spin wave model calculations capture the position, intensity and Q -width of all features quite well, despite the presence of phonon scattering and other background features

of the data. Certain features of the data are not captured by our model calculations and simple background model. For example, additional scattering is observed at lower Q close to the direct beam at most energy transfers suggesting additional Q -dependent background contributions.

The effect of K substitution on the constant-energy Q -cuts is shown in Fig. 7.11. The main effect is a broadening of the acoustic spin wave peaks most easily observed as broadening of the (101) and (103) acoustic spin wave features in Fig. 7.11 (a) from 30–35 meV. It might be tempting to assume that the spin wave velocity v_{ab} , which mainly contributes to the powder-averaged dispersive features at (101) and (103), is strongly reduced with K substitution. However, Table 7.3 shows that the fitted values of v_{ab} are reduced only 8% from $x = 0$ to $x = 0.25$. Rather, the model fits indicate that this broadening is caused mainly by the reduction of SJ_c . While this reduces v_c by 33%, the main effect of reducing SJ_c on the (101) and (103) dispersive features is to smear out the intensity of the spin wave cone in Q due to powder averaging. This highlights the care that must be taken in interpreting the slope of the dispersive features in powder data, since it is affected by both the velocities and the dimensionality of the magnetic interactions. At higher energies where the spectra are more continuous, the effect of substitution on the Q -dependence is more subtle. In all, the models capture both the energy and momentum dependence of the spin wave scattering for all three compositions and small differences between the spectra are accounted for by minor systematic changes in the exchange constants.

7.3 Discussion of the results

Some of the key results of the INS measurement of the spin waves of $\text{Ba}_{1-x}\text{K}_x\text{Mn}_2\text{As}_2$ powders with $x = 0, 0.125$ and 0.25 are (i) decrease in the mean energy of the energy spectrum of the spin waves, (ii) little or no change in the spin gap, (iii) merely any changes in the in-plane exchange parameters, (iv) a small decrease in $J_1/2J_2$ indicating increase in the in-plane magnetic frustration, and (iv) decrease in the inter-plane exchange parameter J_c and ratio J_c/J_1 indicating increase in the quasi-two dimensionality with increasing K substitution. Furthermore, the overall changes are

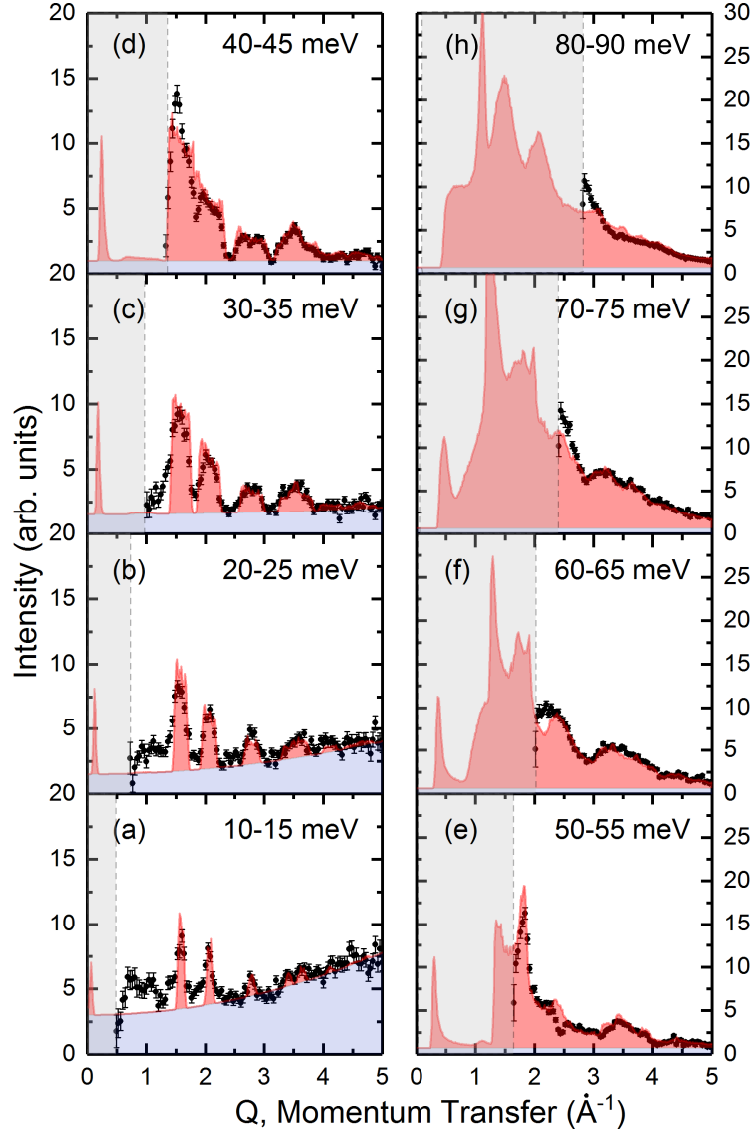


Figure 7.10 Different constant-energy Q -cuts of the BaMn_2As_2 data at $E_i = 144.7$ meV as a function of momentum transfer (black dots) averaged from (a) 10–15 meV, (b) 20–25 meV, (c) 30–35 meV, (d) 40–45 meV, (e) 50–55 meV, (f) 60–65 meV, (g) 70–75 meV and (h) 80–90 meV. The red line and red shaded area correspond to Heisenberg spin wave fits with parameters in Table 7.3. The background (blue shaded area) is estimated by a Q -independent term plus a quadratic term representing the phonon contribution. The gray shaded rectangle on the left represents momentum transfers that are inaccessible kinematically at $E_i = 144.7$ meV. The figure is reproduced from Ref. [51].

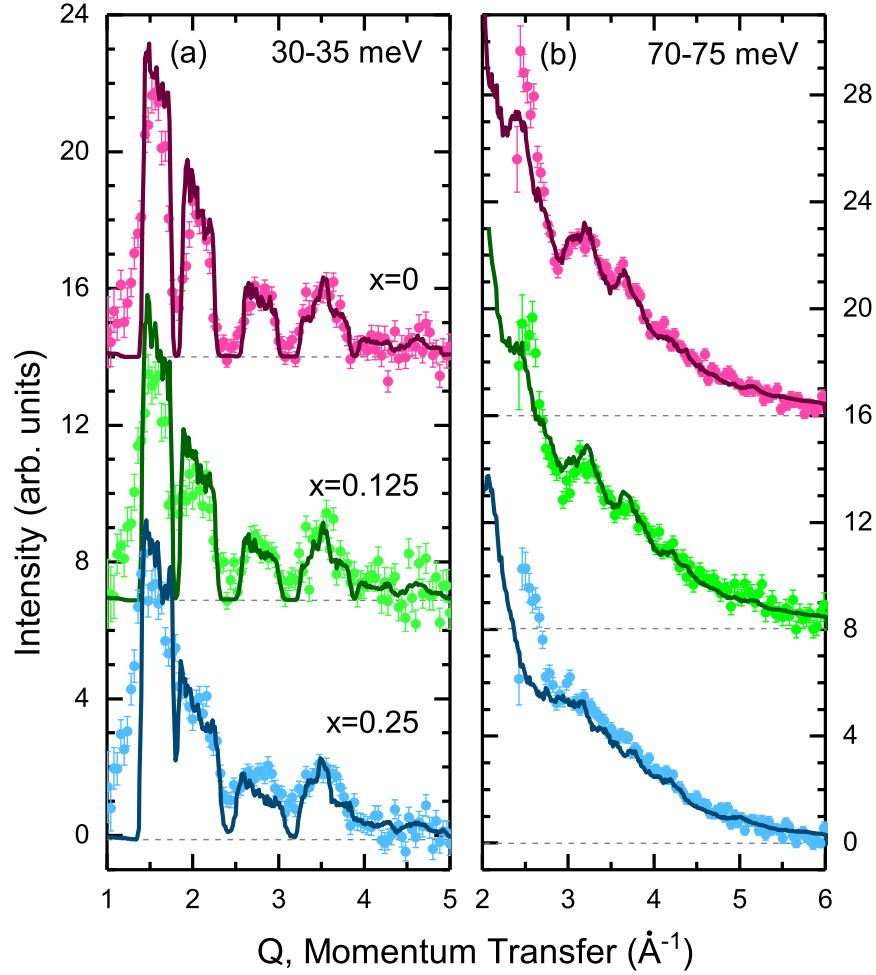


Figure 7.11 A comparison of constant-energy cuts for different compositions of $\text{Ba}_{1-x}\text{K}_x\text{Mn}_2\text{As}_2$ at (a) 30-35 meV and (b) 70-75 meV. Dots correspond to experimental data with the estimated background subtracted. Lines correspond to Heisenberg model calculations of the spin waves. Plots are offset vertically by 7 units in panel (a) and 8 units in panel (b). The figure is reproduced from Ref. [51].

Table 7.3 Energy scales and magnetic parameters of $\text{Ba}_{1-x}\text{K}_x\text{Mn}_2\text{As}_2$ as a function of composition. $k_{\text{B}}T_{\text{N}}$ is the actual Néel temperature measured by neutron diffraction. $\langle E \rangle$ was determined numerically from Fig. 7.6. Values of the spin gap (Δ) and low energy damping (Γ) were determined from fits to Eq. (7.3). Other quantities (exchange constants and related parameters) are determined either directly or indirectly from fittings to the Heisenberg spin wave model as described in the Sections 7.2.3 and 7.2.4. Errors are given as one standard deviation. The table is reproduced from Ref. [51].

Composition	$x = 0$	$x = 0.125$	$x = 0.25$
Hole conc./Mn	$\delta = 0$	$\delta = 0.0625$	$\delta = 0.125$
$k_{\text{B}}T_{\text{N}}$ (meV) [69]	53.9(1)	52.7	49.6(3)
$\langle E \rangle$ (meV)	66.0(3)	64.7(4)	59.2(3)
Δ (meV)	5.65(15)	6.71(19)	6.28(21)
Γ (meV)	18.1(8)	12.5(8)	12.6(8)
SJ_1 (meV)	40.5(2.0)	41(4)	41(5)
SJ_2 (meV)	13.6(1.4)	13.9(2.0)	14.8(3.0)
SJ_c (meV)	1.8(3)	1.4(3)	1.0(2)
SD (meV)	0.048(3)	0.068(7)	0.060(8)
J_c/J_1	0.044(8)	0.034(8)	0.024(6)
$J_1/2J_2$	1.49(7)	1.45 (10)	1.38 (10)
$(k_{\text{B}}T_{\text{N}})_{\text{MF}}$ (meV)	111(4)	111(7)	107(8)
$(k_{\text{B}}T_{\text{N}})_{\text{MC}}$ (meV)	53.9(9)	52.4(1.3)	47.6(1.5)
$\hbar v_{ab}$ (meV Å)	196(3)	195(6)	181(6)
$\hbar v_c$ (meV Å)	166(14)	149(17)	124(15)

small which concludes that the hole doping and the resulting metal-insulator transition has very weak effects on the spin waves, at least up to the hole concentrations of $\delta = x/2 = 12.5\%$.

The small changes in the spin wave is consistent with the fact that T_N decreases by less than 10% between the parent and $x = 0.25$ compounds. Using Eq. (7.10), the observed decrease in T_N with doping has almost equal contributions from an increase in quasi-two-dimensionality (a decrease in J_c/J_1 from 4.4% down to 2.4%) and an increase in the in-plane magnetic frustration (a decrease in $J_1/2J_2$ from 1.49 to 1.37).

The little or no change in the spin gap with composition is in consistent with the absence of the large doping dependence of the Mn magnetic moment[69]. The spin gap is associated with single-ion anisotropy of the Mn ion. The result in combination with the stability of the magnetic moment infers that hole doping does not appreciably change the orbital occupancies of the Mn ion.

All these observations are consistent with doped holes residing primarily in As p bands where they do not directly affect the Mn ion's net magnetic moment or orbital occupancy, but can influence the magnetic exchange interactions. In particular, J_c and J_2 are likely to have significant contributions from superexchange processes mediated through bridging As ions. Any reduction of the electron density on the As sublattice through hole doping would affect these superexchange interactions.

It is interesting to compare INS results described here to similar square lattice Mn-based compounds, such as LaMnAsO[168], LaMnPO[122], BaMn₂Bi₂ [169] and AMnBi₂ (A=Sr,Ca)[170]. Both LaMnAsO and LaMnPO were studied using INS on polycrystalline samples. For LaMnPO, G-type spin excitations are observed up to 100 meV with no observable spin gap. Estimates of the in-plane exchange constants are $SJ_1 = 34$ meV and $SJ_2 = 7\text{--}14$ meV. For LaMnAsO, only low energy spectra were taken and reveal steeply dispersing spin waves with a rather small spin gap of 3.5 meV. Taken together, these results are in reasonable correspondence with magnetic parameters found in BaMn₂As₂.

On the other hand, the magnetic parameters differ considerably between the manganese pnictides and bismuthides. For BaMn₂Bi₂, G-type spin excitations are observed only up to ~ 55 meV,

consistent with the smaller $T_N = 390$ K. Correspondingly smaller in-plane exchange energies of $SJ_1 = 22$ meV and $SJ_2 = 7.8$ meV are determined from the INS data. In addition, a large spin gap of ~ 16 meV indicates that single-ion anisotropy is more than ten times stronger than BaMn_2As_2 . Similar statements can be made for SrMnBi_2 and CaMnBi_2 with $T_N = 287$ K and 264 K, respectively. These compounds have magnetic bandwidth, exchange energies, and single-ion anisotropies comparable to BaMn_2Bi_2 . Presumably, the larger ionic size and larger spin-orbit coupling of Bi in comparison to As results in significantly different magnetic interactions.

Finally, the interesting observation that FM coexists with AFM order in K and Rb doped BaMn_2As_2 with compositions beyond $x \approx 0.16$. The origin of this FM component has been proposed to arise from canting of the Mn spins[69, 171], or from As band ferromagnetism[172]. Recent XMCD measurements support a picture where FM arises from doped holes on the As sublattice, which is at least consistent with the observations here. To go further, it should be possible to observe FM fluctuations directly in the INS experiments and address this controversy. However, there is no evidence of any FM signal in the $x = 0.25$ sample where FM order is expected below ~ 100 K. The small size of the ordered FM moment ($< 0.2 \mu_B$) would make it very difficult to observe a FM signal, especially in powder samples. Also, the presence of MnO magnetic impurities in the $x = 0.25$ sample further hampers any search for a definitive signal from FM fluctuations at energies below 25 meV. Additional INS measurements on single-crystal samples with higher K or Rb compositions are necessary to explore this point further.

7.3.1 Additional information related to the data analysis

7.3.1.1 Estimation of background for the constant-energy cuts

For the constant-energy Q cuts shown in Fig. 7.10, a simple form is chosen to represent the Q -dependent background for each independent cut at an average energy transfer of E . This form is simply a quadratic term intended to represent phonon scattering plus a constant term, $S_{\text{ph}}^E(Q) + B^E(Q) = UQ^2 + F$. The parameters U and F are given in Table 7.4 and were chosen for each Q cut in Figs. 7.10 and 7.11 as a guide to the eye.

Table 7.4 Parameters (U , F) employed in the background estimates for constant-energy Q cuts. The table is reproduced from Ref. [51].

Energy range	$x = 0$	$x = 0.125$	$x = 0.25$
10-15 meV	(3, 0.19)	-	-
20-25 meV	(1.5, 0.1)	-	-
30-35 meV	(1.5, 0.02)	(1.6, 0.08)	(1.3, 0.04)
40-45 meV	(1, 0)	-	-
50-55 meV	(0.7, 0)	-	-
60-65 meV	(0.6, 0)	-	-
70-75 meV	(0.6, 0)	(1.3, 0.04)	(0.7, 0)
80-90 meV	(0.7, 0)	-	-

7.3.1.2 Spin wave scattering from MnO impurities

The MnO impurities were discovered in the doped samples, most notably in the $x = 0.25$ sample. MnO is an antiferromagnet at the temperatures studied and clear spin wave scattering is observed below 25 meV from MnO impurities. MnO spin waves have been studied in detail by inelastic neutron scattering and the data have been fit with linear spin wave theory. Using the exchange parameters determined in Ref. [165], the expected scattering from polycrystalline MnO impurities were calculated for $E_i = 144.7$ meV, as shown in Fig. 7.12. Figure 7.12(a) shows that the spin waves contribute strongly below 25 meV and display dispersive features up to about 3 \AA^{-1} . The angle-averaged spectrum is shown in Fig. 7.12(b) and can be compared to Fig. 7.6(c), where the peak corresponding to MnO spin wave scattering is apparent in the data.

7.3.1.3 Uniqueness of fitted exchange values

Modeling using the spin wave approximation to the Heisenberg model was performed against a set of exchange parameters SJ_1, SJ_2 and SJ_c as explained in the main text. It was discovered that SJ_1 and SJ_2 are highly correlated and different combinations of these parameters (such as v_{ab}) result in more sharply defined minima in χ^2 . This is mainly due to the fact that v_{ab} is reasonably well determined by the slope of the acoustic spin waves at low energies with a value of roughly 200 meV \AA . A reasonable range of v_{ab} from 165-210 meV \AA was chosen for fitting, which

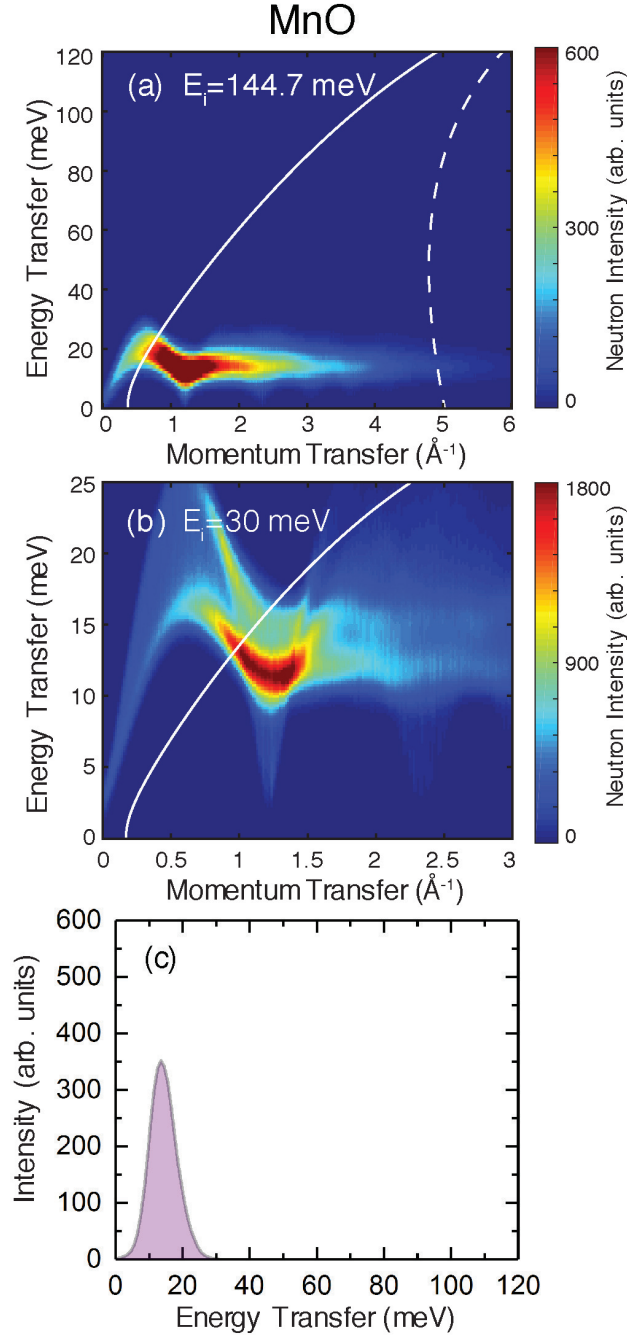


Figure 7.12 Calculations of the powder-averaged spin wave scattering from MnO. The full neutron intensity $S(Q, E)$ is shown for an incident energy of (a) 144.7 meV and (b) 30 meV. The solid line denotes the kinematic limit near forward scattering ($2\theta = 2.5$ degrees) and the dashed line in panel (a) corresponds to a scattering angle of $2\theta = 35$ degrees. Panel (c) shows the MnO spin wave spectrum obtained at $E_i = 144.7$ meV after averaging over the angle range in (a). The figure is reproduced from Ref. [51].

dramatically reduces the necessary $SJ_1 - SJ_2$ parameter space that needs to be explored, as shown in Fig. 7.13.

Therefore, three independent parameters, SJ_1, v_{ab} and SJ_c were chosen as the main parameter set for fitting. The dependence of χ^2 on these parameters is shown for different cuts in this three-dimensional parameter space when either SJ_c [Fig. 7.14 (a) - (c)] or v_{ab} [Fig. 7.14 (d) - (f)] is held fixed at the value that minimizes χ^2 . For $x = 0$, a strong and deep local minimum exists in χ^2 . For $x = 0.125$ and 0.25 , the minimum value of χ^2 is higher, and therefore the goodness of fit is worse. In addition, another local minimum in χ^2 develops at higher values of SJ_1 and SJ_c [see Fig. 7.14 (e)]. However, the parameters are not expected to change too drastically, so the best parameters relative to the local minimum found in the $x = 0$ data are reported. In addition, parameters in the second minima have values of $(k_B T_N)_{MC}$ [Eq. (7.10)] that do not conform to the observed Néel temperature.

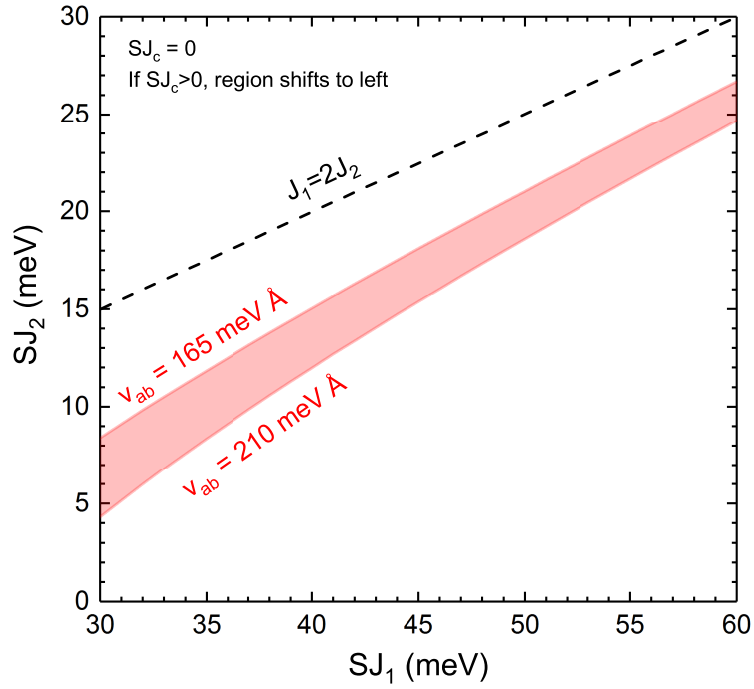


Figure 7.13 Region of $SJ_1 - SJ_2$ parameter space delineated by boundaries of v_{ab} from 165 to 210 meV Å with $SJ_c = 0$ is shown as the shaded region. For a G-type ground state, values of (SJ_1, SJ_2) above the dashed line correspond to the condition $J_1 < 2J_2$ and are not allowed. The figure is reproduced from Ref. [51].

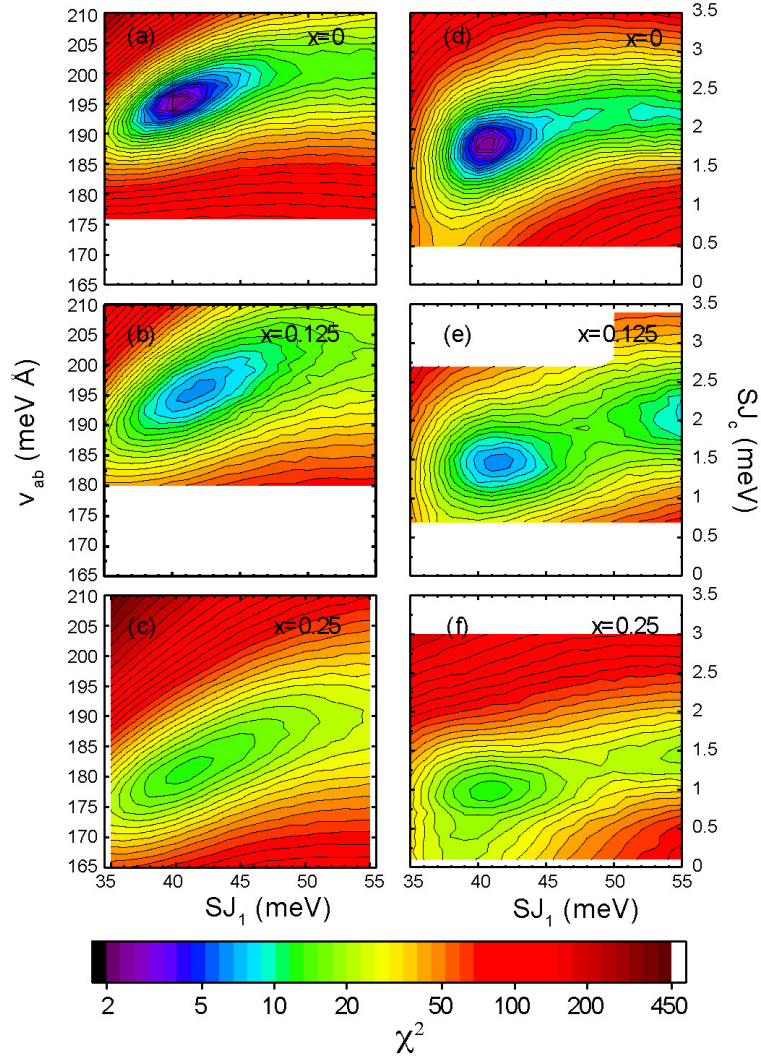


Figure 7.14 Goodness of the fit, χ^2 , plotted in the SJ_1 - v_{ab} plane for fixed SJ_c [panels (a) - (c)] and the SJ_1 - SJ_c plane for fixed v_{ab} [panels (d) - (f)]. Plots are shown for each composition $x = 0$ [panels (a) and (b)], $x = 0.125$ [panels (c) and (d)], and $x = 0.25$ [panels (e) and (f)]. Minima in χ^2 are apparent for the cuts shown. In panels (a) - (c), the parameter SJ_c is held fixed at 1.8, 1.4, and 1.0 meV, respectively. In panels (d)-(f), the parameter v_{ab} is held fixed at 196, 195 and 181 meV Å, respectively. The value of χ^2 is indicated by the logarithmic color scale. The figure is reproduced from Ref. [51].

CHAPTER 8 SUMMARY AND FUTURE WORK

In this work, I have discussed spin dynamics of three members of 3d transition-metal 122 ternary compounds studied using inelastic neutron scattering technique. One of the compound, $\text{Ca}(\text{Fe}_{1-x}\text{Co}_x)_2\text{As}_2$, is a member of the high-temperature iron-based superconductors and the other two are variant compounds with Co and Mn at the TM site. In iron-based superconductors, a generic phase diagram shows the suppression of antiferromagnetism and appearance of superconductivity. The magnetism is closely related to superconductivity and the low-energy overdamped spin fluctuations are established as the necessary component for the electron pairing for superconductivity. The $\text{Ca}(\text{Fe}_{1-x}\text{Co}_x)_2\text{As}_2$ compound is unique compared to other extensively studied 122 compounds and the evolution of its spin fluctuations with Co doping was studied to further understand the link between the overdamped spin fluctuations and superconductivity. Next, the $\text{CaCo}_{1.86}\text{As}_2$ compounds, which is the end member of $\text{Ca}(\text{Fe}_{1-x}\text{Co}_x)_2\text{As}_2$ series was studied to understand its diverse magnetic behavior and a novel property has been revealed. Finally, the evolution of spin fluctuations in $\text{Ba}_{1-x}\text{K}_x\text{Mn}_2\text{As}_2$ compound, in which chemical substitution was employed similar to $\text{Ba}_{1-x}\text{K}_x\text{Fe}_2\text{As}_2$ compound, was studied across the insulator-metal transition to further elucidate the correlation between the magnetism and hole doping.

The evolution of spin fluctuations in $\text{Ca}(\text{Fe}_{1-x}\text{Co}_x)_2\text{As}_2$ compound with Co-substitution was studied and compared with other electron-doped $A\text{Fe}_2\text{As}_2$ compounds, especially $\text{Ba}(\text{Fe}_{1-x}\text{Co}_x)_2\text{As}_2$. The results show that spin fluctuations and its evolution in $\text{Ca}(\text{Fe}_{1-x}\text{Co}_x)_2\text{As}_2$ display some similar characteristics to other 122-iron-arsenide compounds, but also possess some key differences pertaining to its unique character (strong first-order magnetic and structural transition and extreme sensitivity to pressure). Most importantly, the result validates the link between the overdamped spin fluctuations and superconductivity discovered in the $\text{Ba}(\text{Fe}_{1-x}\text{Co}_x)_2\text{As}_2$ compounds. In addition, a peculiar suppression of the spin fluctuations was observed with decreasing temperature

for $\text{Ca}(\text{Fe}_{1-x}\text{Co}_x)_2\text{As}_2$ $x = 0.030$. To explain this, I discussed two possible interesting scenarios, opening of a pseudogap and the proximity to the collapsed tetragonal (cT) phase. The proximity to the collapsed tetragonal phase highlights the importance of the magnetoelastic coupling between the interlayer As-As bond and magnetism in these system.

The anomalous suppression of the spin fluctuations observed in the $\text{Ca}(\text{Fe}_{1-x}\text{Co}_x)_2\text{As}_2$ $x = 0.030$ sample is associated with either the opening of a pseudogap or the proximity to the cT phase. The pseudogap, whose origin is still under debate in extensively studied cuprates, is very poorly understood in iron-based superconductors. Furthermore, their existence in the iron based superconductors is not clear so far. Therefore, further experiments are necessary to elucidate the reason behind the suppression, establish the effect of the magnetoelastic coupling, confirm or rule out the presence of a pseudogap and its role in the suppression. The confirmation of the pseudogap by the inelastic neutron scattering measurements will provide new understanding of these unconventional superconductors. The current measurement was also inconclusive about the existence of a spin-resonance peak, which verifies the unconventional nature of superconductivity as well as can verify the presence of the pseudogap. Therefore, it is necessary to measure the spin resonance and their temperature dependence.

Other compounds such as La doped CaFe_2As_2 also exhibit suppression of the Fe moment corresponding to the reduction in the c lattice parameter[158]. So, their study will also highlight and elucidate the effect of the magnetoelastic coupling on spin dynamics of these 122 compounds.

Next, the inelastic neutron scattering measurement on $\text{CaCo}_{1.86}\text{As}_2$ compounds showed the presence of the unique spin fluctuations in $\text{CaCo}_{1.86}\text{As}_2$ at $E \gtrsim 10$ meV. I have discussed that these unique and extremely anisotropic, one-dimensional wall-like, spin fluctuations arise due to extreme magnetic frustration in $\text{CaCo}_{1.86}\text{As}_2$ compound. The magnetic frustration was discussed in terms of J_1 - J_2 model and it is found that the $\text{CaCo}_{1.86}\text{As}_2$ compound is a unique case of the square-lattice system. First, the magnetic frustration ratio $J_1/2J_2$ is close to the value of maximum frustration, at which the possibility of exotic physics like spin liquids are discussed, and second, it is an itinerant system (moderately-correlated), in which the frustration is very-poorly understood.

Additionally, I also showed that the magnetic frustration can be quantitatively obtained from the spatial anisotropy of the spin fluctuations, measured using inelastic neutron scattering.

This result motivates to identify other potential candidates of maximally-frustrated and moderately correlated itinerant system to elucidate the role of magnetic frustration in itinerant magnets. A way to do that could be a chemical substitution as discussed in section 2.4.1 of chapter 2. In case of spin liquids, the system does not order magnetically down to 0 K, so as a logical step towards this exotic physics, one should look for the chemical substitution that suppresses the A-type antiferromagnetic (AFM) order in $\text{CaCo}_{1.86}\text{As}_2$ compound. In Ref. [156], it is discussed that Fe substitution at the Co site suppresses the magnetic order. In these potential compounds, novel electronic and/or magnetic phenomena may be found and their measurement is another step in understanding novel phenomena due to competing interactions. In addition, the result also motivates to further the theoretical understanding of magnetic frustration in moderately correlated itinerant system.

Finally, the results of the inelastic neutron scattering measurements on the $\text{Ba}_{1-x}\text{K}_x\text{Mn}_2\text{As}_2$ compounds across the insulator-metal transition indicate that changes in the spin dynamics of the Néel-type AFM state across the insulator-metal transition is small. The result is consistent with other measurements which suggest that the hole-doping induces ferromagnetic (FM) order and metallic behavior which are decoupled from the existing Néel-type AFM order. So, the Néel magnetic order is robust against the K substitution(hole doping), at least up to 40% of K. However, no additional sign of the FM spin fluctuations were observed, which was attributed to the small FM moment of the currently measured sample. As the FM moment increases with the higher K doping, additional inelastic neutron scattering measurement on single crystals of higher K concentration is necessary to verify the existence of the FM spin fluctuations.

BIBLIOGRAPHY

- [1] Y. Kamihara, H. Hiramatsu, M. Hirano, R. Kawamura, H. Yanagi, T. Kamiya, and H. Hosono, “Iron-Based Layered Superconductor: LaOFeP,” [J. Am. Chem. Soc. **128**, 10012 \(2006\)](#).
- [2] Y. Kamihara, T. Watanabe, M. Hirano, and H. Hosono, “Iron-Based Layered Superconductor La[O_{1-x}Fx]FeAs ($x = 0.05 - 0.12$) with $T_c = 26$ K,” [J. Am. Chem. Soc. **130**, 3296 \(2008\)](#).
- [3] P. Dai, “Antiferromagnetic order and spin dynamics in iron-based superconductors,” [Rev. Mod. Phys. **87**, 855 \(2015\)](#).
- [4] S. Nandi, M. G. Kim, A. Kreyssig, R. M. Fernandes, D. K. Pratt, A. Thaler, N. Ni, S. L. Bud’ko, P. C. Canfield, J. Schmalian, R. J. McQueeney, and A. I. Goldman, “Anomalous Suppression of the Orthorhombic Lattice Distortion in Superconducting Ba(Fe_{1-x}Co_x)₂As₂ Single Crystals,” [Phys. Rev. Lett. **104**, 057006 \(2010\)](#).
- [5] G. S. Tucker, R. M. Fernandes, D. K. Pratt, A. Thaler, N. Ni, K. Marty, A. D. Christianson, M. D. Lumsden, B. C. Sales, A. S. Sefat, S. L. Bud’ko, P. C. Canfield, A. Kreyssig, A. I. Goldman, and R. J. McQueeney, “Crossover from spin waves to diffusive spin excitations in underdoped Ba(Fe_{1-x}Co_x)₂As₂,” [Phys. Rev. B **89**, 180503 \(2014\)](#).
- [6] D. G. Quirinale, V. K. Anand, M. G. Kim, A. Pandey, A. Huq, P. W. Stephens, T. W. Heitmann, A. Kreyssig, R. J. McQueeney, D. C. Johnston, and A. I. Goldman, “Crystal and magnetic structure of CaCo_{1.86}As₂ studied by x-ray and neutron diffraction,” [Phys. Rev. B **88**, 174420 \(2013\)](#).
- [7] A. I. Goldman, A. Kreyssig, K. Prokeš, D. K. Pratt, D. N. Argyriou, J. W. Lynn, S. Nandi, S. A. J. Kimber, Y. Chen, Y. B. Lee, G. Samolyuk, J. B. Leão, S. J. Poulton, S. L. Bud’ko, N. Ni, P. C. Canfield, B. N. Harmon, and R. J. McQueeney, “Lattice collapse and quenching of magnetism in CaFe₂As₂ under pressure: A single-crystal neutron and x-ray diffraction investigation,” [Phys. Rev. B **79**, 024513 \(2009\)](#).
- [8] W. Jayasekara, Y. Lee, A. Pandey, G. S. Tucker, A. Sapkota, J. Lamsal, S. Calder, D. L. Abernathy, J. L. Niedziela, B. N. Harmon, A. Kreyssig, D. Vaknin, D. C. Johnston, A. I. Goldman, and R. J. McQueeney, “Stripe Antiferromagnetic Spin Fluctuations in SrCo₂As₂,” [Phys. Rev. Lett. **111**, 157001 \(2013\)](#).
- [9] D. C. Johnston, R. J. McQueeney, B. Lake, A. Honecker, M. E. Zhitomirsky, R. Nath, Y. Furukawa, V. P. Antropov, and Y. Singh, “Magnetic exchange interactions in BaMn₂As₂: A case study of the J_1 - J_2 - J_c Heisenberg model,” [Phys. Rev. B **84**, 094445 \(2011\)](#).

- [10] H. K. Onnes, “Further experiments with Liquid Helium. C. On the change of Electrical Resistance of Pure Metals at very low Temperatures, etc. IV. The resistance of pure mercury at helium temperatures,” [Proceedings of Royal Netherlands Academy of Arts and Sciences](#) **13**, 1274 (1911).
- [11] H. K. Onnes, “Further experiments with Liquid Helium. D. On the change of Electrical Resistance of Pure Metals at very low Temperatures, etc. V. The Disappearance of the resistance of mercury,” [Proceedings of Royal Netherlands Academy of Arts and Sciences](#) **14**, 113 (1911).
- [12] M. Tinkham, *Introduction to Superconductivity* (McGraw-Hill, 1996).
- [13] N. W. Ashcroft and N. D. Mermin, *Solid State Physics* (Brooks/Cole, Cengage Learning, 1976).
- [14] H. K. Onnes, “Further experiments with Liquid Helium G. On the electrical resistance of Pure Metals etc. VI. On the Sudden Change in the Rate at which the Resistance of Mercury Disappears,” [Proceedings of Royal Netherlands Academy of Arts and Sciences](#) **14**, 818 (1912).
- [15] J. Schmalian, “FAILED THEORIES OF SUPERCONDUCTIVITY,” [Mod. Phys. Lett. B](#) **24**, 2679 (2010).
- [16] H. Fröhlich, “Theory of the Superconducting State. I. The Ground State at the Absolute Zero of Temperature,” [Phys. Rev.](#) **79**, 845 (1950).
- [17] J. Bardeen, “Zero-Point Vibrations and Superconductivity,” [Phys. Rev.](#) **79**, 167 (1950).
- [18] H. Fröhlich, “Isotope Effect in Superconductivity,” [Proceedings of the Physical Society. Section A](#) **63**, 778 (1950).
- [19] J. Bardeen, L. N. Cooper, and J. R. Schrieffer, “Theory of Superconductivity,” [Phys. Rev.](#) **108**, 1175 (1957).
- [20] J. Bardeen, L. N. Cooper, and J. R. Schrieffer, “Microscopic Theory of Superconductivity,” [Phys. Rev.](#) **106**, 162 (1957).
- [21] G. R. Stewart, “Unconventional superconductivity,” [Adv. Phys.](#) **66**, 75 (2017).
- [22] G. R. Stewart, “Heavy-fermion systems,” [Rev. Mod. Phys.](#) **56**, 755 (1984).
- [23] B. D. White, J. D. Thompson, and M. B. Maple, “Unconventional superconductivity in heavy-fermion compounds,” [Physica C: Superconductivity and its Applications](#) **514**, 246 (2015).
- [24] P. A. Lee, N. Nagaosa, and X.-G. Wen, “Doping a Mott insulator: Physics of high-temperature superconductivity,” [Rev. Mod. Phys.](#) **78**, 17 (2006).
- [25] P. C. Canfield and S. L. Bud’ko, “FeAs-Based Superconductivity: A Case Study of the Effects of Transition Metal Doping on BaFe₂As₂,” [Annu. Rev. Condens. Matter Phys.](#) **1**, 27 (2010).

- [26] D. C. Johnston, “The puzzle of high temperature superconductivity in layered iron pnictides and chalcogenides,” [Adv. Phys. **59**, 803 \(2010\)](#).
- [27] H. Hosono and K. Kuroki, “Iron-based superconductors: Current status of materials and pairing mechanism,” [Physica C: Superconductivity and its Applications **514**, 399 \(2015\)](#).
- [28] G. Seyfarth, A.-S. Rüetschi, K. Sengupta, A. Georges, D. Jaccard, S. Watanabe, and K. Miyake, “Heavy fermion superconductor CeCu_2Si_2 under high pressure: Multiprobing the valence crossover,” [Phys. Rev. B **85**, 205105 \(2012\)](#).
- [29] F. Steglich, J. Aarts, C. D. Bredl, W. Lieke, D. Meschede, W. Franz, and H. Schäfer, “Superconductivity in the Presence of Strong Pauli Paramagnetism: CeCu_2Si_2 ,” [Phys. Rev. Lett. **43**, 1892 \(1979\)](#).
- [30] J. G. Bednorz and K. A. Müller, “Possible high T_c superconductivity in the Ba–La–Cu–O system,” [Zeitschrift für Physik B Condensed Matter **64**, 189 \(1986\)](#).
- [31] I. I. Mazin, “Superconductivity gets an iron boost,” [Nature **464**, 183 \(2010\)](#).
- [32] L. Gao, Y. Y. Xue, F. Chen, Q. Xiong, R. L. Meng, D. Ramirez, C. W. Chu, J. H. Eggert, and H. K. Mao, “Superconductivity up to 164 K in $\text{HgBa}_2\text{Ca}_{m-1}\text{Cu}_m\text{O}_{2m+2+\delta}$ ($m=1, 2$, and 3) under quasihydrostatic pressures,” [Phys. Rev. B **50**, 4260 \(1994\)](#).
- [33] J.-F. Ge, Z.-L. Liu, C. Liu, C.-L. Gao, D. Qian, Q.-K. Xue, Y. Liu, and J.-F. Jia, “Superconductivity above 100 K in single-layer FeSe films on doped SrTiO_3 ,” [Nature Mater. **14**, 285 \(2015\)](#).
- [34] J. Paglione and R. L. Greene, “High-temperature superconductivity in iron-based materials,” [Nature Phys. **6**, 645 \(2010\)](#).
- [35] K. Kothapalli, A. E. Böhmer, W. T. Jayasekara, B. G. Ueland, P. Das, A. Sapkota, V. Taufour, Y. Xiao, E. Alp, S. L. Bud’ko, P. C. Canfield, A. Kreyssig, and A. I. Goldman, “Strong cooperative coupling of pressure-induced magnetic order and nematicity in FeSe,” [Nature Commun. **7**, 12728 \(2016\)](#).
- [36] W. R. Meier, T. Kong, U. S. Kaluarachchi, V. Taufour, N. H. Jo, G. Drachuck, A. E. Böhmer, S. M. Saunders, A. Sapkota, A. Kreyssig, M. A. Tanatar, R. Prozorov, A. I. Goldman, F. F. Balakirev, A. Gurevich, S. L. Bud’ko, and P. C. Canfield, “Anisotropic thermodynamic and transport properties of single-crystalline $\text{CaKFe}_4\text{As}_4$,” [Phys. Rev. B **94**, 064501 \(2016\)](#).
- [37] N. Ni, J. M. Allred, B. C. Chan, and R. J. Cava, “High T_c electron doped $\text{Ca}_{10}(\text{Pt}_3\text{As}_8)(\text{Fe}_2\text{As}_2)_5$ and $\text{Ca}_{10}(\text{Pt}_4\text{As}_8)(\text{Fe}_2\text{As}_2)_5$ superconductors with skutterudite intermediary layers,” [Proc. Natl. Acad. Sci. **108**, E1019 \(2011\)](#).
- [38] Z. Ban and M. Sikirica, “The crystal structure of ternary silicides ThM_2Si_2 ($M = \text{Cr}, \text{Mn}, \text{Fe}, \text{Co}, \text{Ni}$ and Cu),” [Acta Cryst. **18**, 594 \(1965\)](#).

- [39] D. Johrendt, C. Felser, O. Jepsen, O. K. Andersen, A. Mewis, and J. Rouxel, “LMTO Band Structure Calculations of ThCr_2Si_2 -Type Transition Metal Compounds,” *J. Solid State Chem.* **130**, 254 (1997).
- [40] R. Hoffmann and C. Zheng, “Making and breaking bonds in the solid state: the thorium chromium silicide (ThCr_2Si_2) structure,” *J. Phys. Chem.* **89**, 4175 (1985).
- [41] M. D. Lumsden and A. D. Christianson, “Magnetism in Fe-based superconductors,” *J. Phys.: Condens. Matter* **22**, 203203 (2010).
- [42] A. I. Goldman, D. N. Argyriou, B. Ouladdiaf, T. Chatterji, A. Kreyssig, S. Nandi, N. Ni, S. L. Bud’ko, P. C. Canfield, and R. J. McQueeney, “Lattice and magnetic instabilities in CaFe_2As_2 : A single-crystal neutron diffraction study,” *Phys. Rev. B* **78**, 100506 (2008).
- [43] Y. Singh, M. A. Green, Q. Huang, A. Kreyssig, R. J. McQueeney, D. C. Johnston, and A. I. Goldman, “Magnetic order in BaMn_2As_2 from neutron diffraction measurements,” *Phys. Rev. B* **80**, 100403 (2009).
- [44] J. An, A. S. Sefat, D. J. Singh, and M.-H. Du, “Electronic structure and magnetism in BaMn_2As_2 and BaMn_2Sb_2 ,” *Phys. Rev. B* **79**, 075120 (2009).
- [45] M. A. Kastner, R. J. Birgeneau, G. Shirane, and Y. Endoh, “Magnetic, transport, and optical properties of monolayer copper oxides,” *Rev. Mod. Phys.* **70**, 897 (1998).
- [46] R. J. McQueeney, S. O. Diallo, V. P. Antropov, G. D. Samolyuk, C. Broholm, N. Ni, S. Nandi, M. Yethiraj, J. L. Zarestky, J. J. Pulikotil, A. Kreyssig, M. D. Lumsden, B. N. Harmon, P. C. Canfield, and A. I. Goldman, “Anisotropic Three-Dimensional Magnetism in CaFe_2As_2 ,” *Phys. Rev. Lett.* **101**, 227205 (2008).
- [47] S. O. Diallo, V. P. Antropov, T. G. Perring, C. Broholm, J. J. Pulikotil, N. Ni, S. L. Bud’ko, P. C. Canfield, A. Kreyssig, A. I. Goldman, and R. J. McQueeney, “Itinerant Magnetic Excitations in Antiferromagnetic CaFe_2As_2 ,” *Phys. Rev. Lett.* **102**, 187206 (2009).
- [48] L. W. Harriger, A. Schneidewind, S. Li, J. Zhao, Z. Li, W. Lu, X. Dong, F. Zhou, Z. Zhao, J. Hu, and P. Dai, “Transition from Three-Dimensional Anisotropic Spin Excitations to Two-Dimensional Spin Excitations by Electron Doping the FeAs-Based $\text{BaFe}_{1.96}\text{Ni}_{0.04}\text{As}_2$ Superconductor,” *Phys. Rev. Lett.* **103**, 087005 (2009).
- [49] J. Zhao, D. T. Adroja, D.-X. Yao, R. Bewley, S. Li, X. F. Wang, G. Wu, X. H. Chen, J. Hu, and P. Dai, “Spin waves and magnetic exchange interactions in CaFe_2As_2 ,” *Nat. Phys.* **5**, 555 (2009).
- [50] A. Sapkota, B. G. Ueland, V. K. Anand, N. S. Sangeetha, D. L. Abernathy, M. B. Stone, J. L. Niedziela, D. C. Johnston, A. Kreyssig, A. I. Goldman, and R. J. McQueeney, “Effective One-Dimensional Coupling in the Highly Frustrated Square-Lattice Itinerant Magnet $\text{CaCo}_{2-y}\text{As}_2$,” *Phys. Rev. Lett.* **119**, 147201 (2017).

- [51] M. Ramazanoglu, A. Sapkota, A. Pandey, J. Lamsal, D. L. Abernathy, J. L. Niedziela, M. B. Stone, A. Kreyssig, A. I. Goldman, D. C. Johnston, and R. J. McQueeney, “Robust antiferromagnetic spin waves across the metal-insulator transition in hole-doped BaMn_2As_2 ,” [Phys. Rev. B **95**, 224401 \(2017\)](#).
- [52] N. Shannon, B. Schmidt, K. Penc, and P. Thalmeier, “Finite temperature properties and frustrated ferromagnetism in a square lattice Heisenberg model,” [Eur. Phys. J. B **38**, 599 \(2004\)](#).
- [53] N. Shannon, T. Momoi, and P. Sindzingre, “Nematic Order in Square Lattice Frustrated Ferromagnets,” [Phys. Rev. Lett. **96**, 027213 \(2006\)](#).
- [54] L. Balents, “Spin liquids in frustrated magnets,” [Nature **464**, 199 \(2010\)](#).
- [55] L. Savary and L. Balents, “Quantum spin liquids: a review,” [Rep. Prog. Phys. **80**, 016502 \(2017\)](#).
- [56] W. R. Meier, Q.-P. Ding, A. Kreyssig, S. L. Budko, A. Sapkota, K. Kothapalli, V. Borisov, R. Valentí, C. D. Batista, P. P. Orth, R. M. Fernandes, A. I. Goldman, Y. Furukawa, A. E. Böhmer, and P. C. Canfield, “Hedgehog spin-vortex crystal stabilized in a hole-doped iron-based superconductor,” [npj Quantum Materials **3**, 5 \(2018\)](#).
- [57] O. J. Lipscombe, G. F. Chen, C. Fang, T. G. Perring, D. L. Abernathy, A. D. Christianson, T. Egami, N. Wang, J. Hu, and P. Dai, “Spin Waves in the $(\pi, 0)$ Magnetically Ordered Iron Chalcogenide $\text{Fe}_{1.05}\text{Te}$,” [Phys. Rev. Lett. **106**, 057004 \(2011\)](#).
- [58] A. L. Wysocki, K. D. Belashchenko, and V. P. Antropov, “Consistent model of magnetism in ferropnictides,” [Nature Phys. **7**, 485 \(2011\)](#).
- [59] J. Hu, B. Xu, W. Liu, N.-N. Hao, and Y. Wang, “Unified minimum effective model of magnetic properties of iron-based superconductors,” [Phys. Rev. B **85**, 144403 \(2012\)](#).
- [60] N. Ni, M. E. Tillman, J.-Q. Yan, A. Kracher, S. T. Hannahs, S. L. Bud’ko, and P. C. Canfield, “Effects of Co substitution on thermodynamic and transport properties and anisotropic H_{c2} in $\text{Ba}(\text{Fe}_{1-x}\text{Co}_x)_2\text{As}_2$ single crystals,” [Phys. Rev. B **78**, 214515 \(2008\)](#).
- [61] M. Rotter, M. Tegel, and D. Johrendt, “Superconductivity at 38 K in the Iron Arsenide $(\text{Ba}_{1-x}\text{K}_x)\text{Fe}_2\text{As}_2$,” [Phys. Rev. Lett. **101**, 107006 \(2008\)](#).
- [62] A. Leithe-Jasper, W. Schnelle, C. Geibel, and H. Rosner, “Superconducting State in $\text{SrFe}_{2-x}\text{Co}_x\text{As}_2$ by Internal Doping of the Iron Arsenide Layers,” [Phys. Rev. Lett. **101**, 207004 \(2008\)](#).
- [63] L. Harnagea, S. Singh, G. Friemel, N. Leps, D. Bombor, M. Abdel-Hafiez, A. U. B. Wolter, C. Hess, R. Klingeler, G. Behr, S. Wurmehl, and B. Büchner, “Phase diagram of the iron arsenide superconductors $\text{Ca}(\text{Fe}_{1-x}\text{Co}_x)_2\text{As}_2$ ($0 \leq x \leq 0.2$),” [Phys. Rev. B **83**, 094523 \(2011\)](#).

- [64] R. M. Fernandes, D. K. Pratt, W. Tian, J. Zarestky, A. Kreyssig, S. Nandi, M. G. Kim, A. Thaler, N. Ni, P. C. Canfield, R. J. McQueeney, J. Schmalian, and A. I. Goldman, “Unconventional pairing in the iron arsenide superconductors,” [Phys. Rev. B **81**, 140501 \(2010\)](#).
- [65] D. S. Inosov, J. T. Park, P. Bourges, D. L. Sun, Y. Sidis, A. Schneidewind, K. Hradil, D. Haug, C. T. Lin, B. Keimer, and V. Hinkov, “Normal-state spin dynamics and temperature-dependent spin-resonance energy in optimally doped $\text{BaFe}_{1.85}\text{Co}_{0.15}\text{As}_2$,” [Nat. Phys. **6**, 178 \(2010\)](#).
- [66] D. S. Inosov, “Spin fluctuations in iron pnictides and chalcogenides: From antiferromagnetism to superconductivity,” [Comptes Rendus Physique **17**, 60 \(2016\)](#).
- [67] A. Pandey, V. K. Anand, and D. C. Johnston, “Large miscibility gap in the $\text{Ba}(\text{Mn}_x\text{Fe}_{1-x})_2\text{As}_2$ system,” [Phys. Rev. B **84**, 014405 \(2011\)](#).
- [68] A. Pandey, R. S. Dhaka, J. Lamsal, Y. Lee, V. K. Anand, A. Kreyssig, T. W. Heitmann, R. J. McQueeney, A. I. Goldman, B. N. Harmon, A. Kaminski, and D. C. Johnston, “ $\text{Ba}_{1-x}\text{K}_x\text{Mn}_2\text{As}_2$: An Antiferromagnetic Local-Moment Metal,” [Phys. Rev. Lett. **108**, 087005 \(2012\)](#).
- [69] J. Lamsal, G. S. Tucker, T. W. Heitmann, A. Kreyssig, A. Jesche, A. Pandey, W. Tian, R. J. McQueeney, D. C. Johnston, and A. I. Goldman, “Persistence of local-moment antiferromagnetic order in $\text{Ba}_{1-x}\text{K}_x\text{Mn}_2\text{As}_2$,” [Phys. Rev. B **87**, 144418 \(2013\)](#).
- [70] A. Pandey, B. G. Ueland, S. Yeninas, A. Kreyssig, A. Sapkota, Y. Zhao, J. S. Helton, J. W. Lynn, R. J. McQueeney, Y. Furukawa, A. I. Goldman, and D. C. Johnston, “Co-existence of Half-Metallic Itinerant Ferromagnetism with Local-Moment Antiferromagnetism in $\text{Ba}_{0.60}\text{K}_{0.40}\text{Mn}_2\text{As}_2$,” [Phys. Rev. Lett. **111**, 047001 \(2013\)](#).
- [71] B. G. Ueland, A. Pandey, Y. Lee, A. Sapkota, Y. Choi, D. Haskel, R. A. Rosenberg, J. C. Lang, B. N. Harmon, D. C. Johnston, A. Kreyssig, and A. I. Goldman, “Itinerant Ferromagnetism in the As 4*p* Conduction Band of $\text{Ba}_{0.6}\text{K}_{0.4}\text{Mn}_2\text{As}_2$ Identified by X-Ray Magnetic Circular Dichroism,” [Phys. Rev. Lett. **114**, 217001 \(2015\)](#).
- [72] N. Ni, S. Nandi, A. Kreyssig, A. I. Goldman, E. D. Mun, S. L. Bud’ko, and P. C. Canfield, “First-order structural phase transition in CaFe_2As_2 ,” [Phys. Rev. B **78**, 014523 \(2008\)](#).
- [73] J.-Q. Yan, A. Kreyssig, S. Nandi, N. Ni, S. L. Bud’ko, A. Kracher, R. J. McQueeney, R. W. McCallum, T. A. Lograsso, A. I. Goldman, and P. C. Canfield, “Structural transition and anisotropic properties of single-crystalline SrFe_2As_2 ,” [Phys. Rev. B **78**, 024516 \(2008\)](#).
- [74] M. G. Kim, R. M. Fernandes, A. Kreyssig, J. W. Kim, A. Thaler, S. L. Bud’ko, P. C. Canfield, R. J. McQueeney, J. Schmalian, and A. I. Goldman, “Character of the structural and magnetic phase transitions in the parent and electron-doped BaFe_2As_2 compounds,” [Phys. Rev. B **83**, 134522 \(2011\)](#).

- [75] J. Zhao, W. Ratcliff, J. W. Lynn, G. F. Chen, J. L. Luo, N. L. Wang, J. Hu, and P. Dai, “Spin and lattice structures of single-crystalline SrFe_2As_2 ,” [*Phys. Rev. B* **78**, 140504 \(2008\)](#).
- [76] Q. Huang, Y. Qiu, W. Bao, M. A. Green, J. W. Lynn, Y. C. Gasparovic, T. Wu, G. Wu, and X. H. Chen, “Neutron-Diffraction Measurements of Magnetic Order and a Structural Transition in the Parent BaFe_2As_2 Compound of FeAs-Based High-Temperature Superconductors,” [*Phys. Rev. Lett.* **101**, 257003 \(2008\)](#).
- [77] S. Ran, S. L. Bud’ko, W. E. Straszheim, and P. C. Canfield, “Combined effects of transition metal (Ni and Rh) substitution and annealing/quenching on the physical properties of CaFe_2As_2 ,” [*Phys. Rev. B* **90**, 054501 \(2014\)](#).
- [78] R. A. Ewings, T. G. Perring, J. Gillett, S. D. Das, S. E. Sebastian, A. E. Taylor, T. Guidi, and A. T. Boothroyd, “Itinerant spin excitations in SrFe_2As_2 measured by inelastic neutron scattering,” [*Phys. Rev. B* **83**, 214519 \(2011\)](#).
- [79] L. W. Harriger, H. Q. Luo, M. S. Liu, C. Frost, J. P. Hu, M. R. Norman, and P. Dai, “Nematic spin fluid in the tetragonal phase of BaFe_2As_2 ,” [*Phys. Rev. B* **84**, 054544 \(2011\)](#).
- [80] S. O. Diallo, D. K. Pratt, R. M. Fernandes, W. Tian, J. L. Zarestky, M. Lumsden, T. G. Perring, C. L. Broholm, N. Ni, S. L. Bud’ko, P. C. Canfield, H.-F. Li, D. Vaknin, A. Kreyssig, A. I. Goldman, and R. J. McQueeney, “Paramagnetic spin correlations in CaFe_2As_2 single crystals,” [*Phys. Rev. B* **81**, 214407 \(2010\)](#).
- [81] K. Matan, R. Morinaga, K. Iida, and T. J. Sato, “Anisotropic itinerant magnetism and spin fluctuations in BaFe_2As_2 : A neutron scattering study,” [*Phys. Rev. B* **79**, 054526 \(2009\)](#).
- [82] L. W. Harriger, M. Liu, H. Luo, R. A. Ewings, C. D. Frost, T. G. Perring, and P. Dai, “Temperature dependence of the paramagnetic spin excitations in BaFe_2As_2 ,” [*Phys. Rev. B* **86**, 140403 \(2012\)](#).
- [83] D. K. Pratt, W. Tian, A. Kreyssig, J. L. Zarestky, S. Nandi, N. Ni, S. L. Bud’ko, P. C. Canfield, A. I. Goldman, and R. J. McQueeney, “Coexistence of Competing Antiferromagnetic and Superconducting Phases in the Underdoped $\text{Ba}(\text{Fe}_{0.953}\text{Co}_{0.047})_2\text{As}_2$ Compound Using X-ray and Neutron Scattering Techniques,” [*Phys. Rev. Lett.* **103**, 087001 \(2009\)](#).
- [84] S. Ran, S. L. Bud’ko, W. E. Straszheim, J. Soh, M. G. Kim, A. Kreyssig, A. I. Goldman, and P. C. Canfield, “Control of magnetic, nonmagnetic, and superconducting states in annealed $\text{Ca}(\text{Fe}_{1-x}\text{Co}_x)_2\text{As}_2$,” [*Phys. Rev. B* **85**, 224528 \(2012\)](#).
- [85] S. Ran, *Combined effects of post-growth thermal and chemical substitution on physical properties of CaFe_2As_2* , [Graduate theses and dissertations](#) (2014), 14274.
- [86] S. Ran, S. L. Bud’ko, D. K. Pratt, A. Kreyssig, M. G. Kim, M. J. Kramer, D. H. Ryan, W. N. Rowan-Weetaluktuk, Y. Furukawa, B. Roy, A. I. Goldman, and P. C. Canfield, “Stabilization of an ambient-pressure collapsed tetragonal phase in CaFe_2As_2 and tuning

- of the orthorhombic-antiferromagnetic transition temperature by over 70 K via control of nanoscale precipitates,” *Phys. Rev. B* **83**, 144517 (2011).
- [87] K. Ali and K. Maiti, “Emergent electronic structure of CaFe_2As_2 ,” *Sci. Rep.* **7**, 6298 (2017).
 - [88] A. van Roekeghem, P. Richard, X. Shi, S. Wu, L. Zeng, B. Scharov, Y. Ohtsubo, T. Qian, A. S. Sefat, S. Biermann, and H. Ding, “Tetragonal and collapsed-tetragonal phases of CaFe_2As_2 : A view from angle-resolved photoemission and dynamical mean-field theory,” *Phys. Rev. B* **93**, 245139 (2016).
 - [89] C. Liu, T. Kondo, R. M. Fernandes, A. D. Palczewski, E. D. Mun, N. Ni, A. N. Thaler, A. Bostwick, E. Rotenberg, J. Schmalian, S. L. Budko, P. C. Canfield, and A. Kaminski, “Evidence for a Lifshitz transition in electron-doped iron arsenic superconductors at the onset of superconductivity,” *Nature Phys.* **6**, 419 (2010).
 - [90] T. Kondo, R. M. Fernandes, R. Khasanov, C. Liu, A. D. Palczewski, N. Ni, M. Shi, A. Bostwick, E. Rotenberg, J. Schmalian, S. L. Bud’ko, P. C. Canfield, and A. Kaminski, “Unexpected Fermi-surface nesting in the pnictide parent compounds BaFe_2As_2 and CaFe_2As_2 revealed by angle-resolved photoemission spectroscopy,” *Phys. Rev. B* **81**, 060507 (2010).
 - [91] G. S. Tucker, R. M. Fernandes, H.-F. Li, V. Thampy, N. Ni, D. L. Abernathy, S. L. Bud’ko, P. C. Canfield, D. Vaknin, J. Schmalian, and R. J. McQueeney, “Magnetic excitations in underdoped $\text{Ba}(\text{Fe}_{1-x}\text{Co}_x)_2\text{As}_2$ with $x = 0.047$,” *Phys. Rev. B* **86**, 024505 (2012).
 - [92] T. J. Sato, K. Matan, S. Ibuka, R. Morinaga, S. Chi, J. W. Lynn, A. D. Christianson, and M. D. Lumsden, “Doping dependence of spin dynamics in electron-doped $\text{Ba}(\text{Fe}_{1-x}\text{Co}_x)_2\text{As}_2$,” *Phys. Rev. B* **83**, 059901 (2011).
 - [93] M. Wang, C. Zhang, X. Lu, G. Tan, H. Luo, Y. Song, M. Wang, X. Zhang, E. A. Goremychkin, T. G. Perring, T. A. Maier, Z. Yin, K. Haule, G. Kotliar, and P. Dai, “Doping dependence of spin excitations and its correlations with high-temperature superconductivity in iron pnictides,” *Nature Commun.* **4**, 2874 (2013).
 - [94] M. M. Korshunov and I. Eremin, “Theory of magnetic excitations in iron-based layered superconductors,” *Phys. Rev. B* **78**, 140509 (2008).
 - [95] T. A. Maier and D. J. Scalapino, “Theory of neutron scattering as a probe of the superconducting gap in the iron pnictides,” *Phys. Rev. B* **78**, 020514 (2008).
 - [96] M. S. Torikachvili, S. L. Bud’ko, N. Ni, and P. C. Canfield, “Pressure Induced Superconductivity in CaFe_2As_2 ,” *Phys. Rev. Lett.* **101**, 057006 (2008).
 - [97] W. Yu, A. A. Aczel, T. J. Williams, S. L. Bud’ko, N. Ni, P. C. Canfield, and G. M. Luke, “Absence of superconductivity in single-phase CaFe_2As_2 under hydrostatic pressure,” *Phys. Rev. B* **79**, 020511 (2009).

- [98] E. Colombier, S. L. Bud'ko, N. Ni, and P. C. Canfield, "Complete pressure-dependent phase diagrams for SrFe_2As_2 and BaFe_2As_2 ," *Phys. Rev. B* **79**, 224518 (2009).
- [99] W. J. Duncan, O. P. Welzel, C. Harrison, X. F. Wang, X. H. Chen, F. M. Grosche, and P. G. Niklowitz, "High pressure study of BaFe_2As_2 —the role of hydrostaticity and uniaxial stress," *J. Phys.: Condens. Matter* **22**, 052201 (2010).
- [100] H. Kotegawa, T. Kawazoe, H. Sugawara, K. Murata, and H. Tou, "Effect of Uniaxial Stress for Pressure-Induced Superconductor SrFe_2As_2 ," *J. Phys. Soc. Jpn.* **78**, 083702 (2009).
- [101] W. Uchaya, A. Stemshorn, G. Tsoi, Y. K. Vohra, A. S. Sefat, B. C. Sales, K. M. Hope, and S. T. Weir, "Collapsed tetragonal phase and superconductivity of BaFe_2As_2 under high pressure," *Phys. Rev. B* **82**, 144118 (2010).
- [102] W. O. Uchaya, J. M. Montgomery, G. M. Tsoi, Y. K. Vohra, M. A. McGuire, A. S. Sefat, B. C. Sales, and S. T. Weir, "Phase transition and superconductivity of SrFe_2As_2 under high pressure," *J. Phys.: Condens. Matter* **23**, 122201 (2011).
- [103] K. Prokeš, A. Kreyssig, B. Ouladdiaf, D. K. Pratt, N. Ni, S. L. Bud'ko, P. C. Canfield, R. J. McQueeney, D. N. Argyriou, and A. I. Goldman, "Evidence from neutron diffraction for superconductivity in the stabilized tetragonal phase of CaFe_2As_2 under uniaxial pressure," *Phys. Rev. B* **81**, 180506 (2010).
- [104] A. Kreyssig, M. A. Green, Y. Lee, G. D. Samolyuk, P. Zajdel, J. W. Lynn, S. L. Bud'ko, M. S. Torikachvili, N. Ni, S. Nandi, J. B. Leão, S. J. Poulton, D. N. Argyriou, B. N. Harmon, R. J. McQueeney, P. C. Canfield, and A. I. Goldman, "Pressure-induced volume-collapsed tetragonal phase of CaFe_2As_2 as seen via neutron scattering," *Phys. Rev. B* **78**, 184517 (2008).
- [105] T. Yildirim, "Strong Coupling of the Fe-Spin State and the As-As Hybridization in Iron-Pnictide Superconductors from First-Principle Calculations," *Phys. Rev. Lett.* **102**, 037003 (2009).
- [106] D. K. Pratt, Y. Zhao, S. A. J. Kimber, A. Hiess, D. N. Argyriou, C. Broholm, A. Kreyssig, S. Nandi, S. L. Bud'ko, N. Ni, P. C. Canfield, R. J. McQueeney, and A. I. Goldman, "Suppression of antiferromagnetic spin fluctuations in the collapsed phase of CaFe_2As_2 ," *Phys. Rev. B* **79**, 060510 (2009).
- [107] J. H. Soh, G. S. Tucker, D. K. Pratt, D. L. Abernathy, M. B. Stone, S. Ran, S. L. Bud'ko, P. C. Canfield, A. Kreyssig, R. J. McQueeney, and A. I. Goldman, "Inelastic Neutron Scattering Study of a Nonmagnetic Collapsed Tetragonal Phase in Nonsuperconducting CaFe_2As_2 : Evidence of the Impact of Spin Fluctuations on Superconductivity in the Iron-Arsenide Compounds," *Phys. Rev. Lett.* **111**, 227002 (2013).
- [108] R. S. Dhaka, R. Jiang, S. Ran, S. L. Bud'ko, P. C. Canfield, B. N. Harmon, A. Kaminski, M. Tomić, R. Valentí, and Y. Lee, "Dramatic changes in the electronic structure upon transition to the collapsed tetragonal phase in CaFe_2As_2 ," *Phys. Rev. B* **89**, 020511 (2014).

- [109] S. E. Hahn, Y. Lee, N. Ni, P. C. Canfield, A. I. Goldman, R. J. McQueeney, B. N. Harmon, A. Alatas, B. M. Leu, E. E. Alp, D. Y. Chung, I. S. Todorov, and M. G. Kanatzidis, “Influence of magnetism on phonons in CaFe_2As_2 as seen via inelastic x-ray scattering,” *Phys. Rev. B* **79**, 220511 (2009).
- [110] R. Mittal, L. Pintschovius, D. Lamago, R. Heid, K.-P. Bohnen, D. Reznik, S. L. Chaplot, Y. Su, N. Kumar, S. K. Dhar, A. Thamizhavel, and T. Brueckel, “Measurement of Anomalous Phonon Dispersion of CaFe_2As_2 Single Crystals Using Inelastic Neutron Scattering,” *Phys. Rev. Lett.* **102**, 217001 (2009).
- [111] S. L. Bud’ko, S. Ran, and P. C. Canfield, “Thermal expansion of CaFe_2As_2 : Effect of cobalt doping and postgrowth thermal treatment,” *Phys. Rev. B* **88**, 064513 (2013).
- [112] M. Chefki, M. M. Abd-Elmeguid, H. Micklitz, C. Huhnt, W. Schlabititz, M. Reehuis, and W. Jeitschko, “Pressure-induced Transition of the Sublattice Magnetization in EuCo_2P_2 : Change from Local Moment $\text{Eu}(4f)$ to Itinerant $\text{Co}(3d)$ Magnetism,” *Phys. Rev. Lett.* **80**, 802 (1998).
- [113] M. Reehuis, W. Jeitschko, G. Kotzyba, B. Zimmer, and X. Hu, “Antiferromagnetic order in the ThCr_2Si_2 type phosphides CaCo_2P_2 and CeCo_2P_2 ,” *J. Alloys Cmpd.* **266**, 54 (1998).
- [114] V. K. Anand, P. K. Perera, A. Pandey, R. J. Goetsch, A. Kreyssig, and D. C. Johnston, “Crystal growth and physical properties of SrCu_2As_2 , SrCu_2Sb_2 , and BaCu_2Sb_2 ,” *Phys. Rev. B* **85**, 214523 (2012).
- [115] A. Pandey, D. G. Quirinale, W. Jayasekara, A. Sapkota, M. G. Kim, R. S. Dhaka, Y. Lee, T. W. Heitmann, P. W. Stephens, V. Ogloblichev, A. Kreyssig, R. J. McQueeney, A. I. Goldman, A. Kaminski, B. N. Harmon, Y. Furukawa, and D. C. Johnston, “Crystallographic, electronic, thermal, and magnetic properties of single-crystal SrCo_2As_2 ,” *Phys. Rev. B* **88**, 014526 (2013).
- [116] V. K. Anand, R. S. Dhaka, Y. Lee, B. N. Harmon, A. Kaminski, and D. C. Johnston, “Physical properties of metallic antiferromagnetic $\text{CaCo}_{1.86}\text{As}_2$ single crystals,” *Phys. Rev. B* **89**, 214409 (2014).
- [117] A. S. Sefat, D. J. Singh, R. Jin, M. A. McGuire, B. C. Sales, and D. Mandrus, “Renormalized behavior and proximity of BaCo_2As_2 to a magnetic quantum critical point,” *Phys. Rev. B* **79**, 024512 (2009).
- [118] R. S. Dhaka, Y. Lee, V. K. Anand, D. C. Johnston, B. N. Harmon, and A. Kaminski, “Angle-resolved photoemission spectroscopy study of BaCo_2As_2 ,” *Phys. Rev. B* **87**, 214516 (2013).
- [119] V. K. Anand, D. G. Quirinale, Y. Lee, B. N. Harmon, Y. Furukawa, V. V. Ogloblichev, A. Huq, D. L. Abernathy, P. W. Stephens, R. J. McQueeney, A. Kreyssig, A. I. Goldman, and D. C. Johnston, “Crystallography and physical properties of BaCo_2As_2 , $\text{Ba}_{0.94}\text{K}_{0.06}\text{Co}_2\text{As}_2$, and $\text{Ba}_{0.78}\text{K}_{0.22}\text{Co}_2\text{As}_2$,” *Phys. Rev. B* **90**, 064517 (2014).

- [120] M. Baldini, T. Muramatsu, M. Sherafati, H.-k. Mao, L. Malavasi, P. Postorino, S. Satpathy, and V. V. Struzhkin, “Origin of colossal magnetoresistance in LaMnO_3 manganite,” [Proc. Natl. Acad. Sci. **112**, 10869 \(2015\)](#).
- [121] Y. Singh, A. Ellern, and D. C. Johnston, “Magnetic, transport, and thermal properties of single crystals of the layered arsenide BaMn_2As_2 ,” [Phys. Rev. B **79**, 094519 \(2009\)](#).
- [122] D. E. McNally, S. Zellman, Z. P. Yin, K. W. Post, H. He, K. Hao, G. Kotliar, D. Basov, C. C. Homes, and M. C. Aronson, “From Hund’s insulator to Fermi liquid: Optical spectroscopy study of K doping in BaMn_2As_2 ,” [Phys. Rev. B **92**, 115142 \(2015\)](#).
- [123] P. Fazekas, *Lecture Notes on Electron Correlation and Magnetism* (World Scientific Publishing Co. Pte. Ltd., 5 Toh Tuck Link, Singapore, 1999).
- [124] A. Georges, L. de’ Medici, and J. Mravlje, “Strong Correlations from Hunds Coupling,” [Annu. Rev. Condens. Matter Phys. **4**, 137 \(2013\)](#).
- [125] J.-K. Bao, H. Jiang, Y.-L. Sun, W.-H. Jiao, C.-Y. Shen, H.-J. Guo, Y. Chen, C.-M. Feng, H.-Q. Yuan, Z.-A. Xu, G.-H. Cao, R. Sasaki, T. Tanaka, K. Matsubayashi, and Y. Uwatoko, “Weakly ferromagnetic metallic state in heavily doped $\text{Ba}_{1-x}\text{K}_x\text{Mn}_2\text{As}_2$,” [Phys. Rev. B **85**, 144523 \(2012\)](#).
- [126] G. Shirane, S. M. Shapiro, and J. M. Tranquada, *Neutron Scattering with a Triple-Axis Spectrometer: Basic Techniques* (Cambridge University Press, New York, 2002).
- [127] G. L. Squires, *Introduction to the Theory of Thermal Neutron Scattering* (Cambridge University Press, Cambridge., 1978).
- [128] T. Chatterji, *Neutron Scattering from Magnetic Materials* (Elsevier B. V., Amsterdam, Netherlands, 2006).
- [129] J. M. Carpenter and C.-K. Loong, *Elements of Slow-Neutron Scattering: Basics, Techniques, and Applications* (Cambridge University Press, Cambridge, 2015).
- [130] D. L. Abernathy, M. B. Stone, M. J. Loguillo, M. S. Lucas, O. Delaire, X. Tang, J. Y. Y. Lin, and B. Fultz, “Design and operation of the wide angular-range chopper spectrometer ARCS at the Spallation Neutron Source,” [Rev. Sci. Instrum. **83**, 015114 \(2012\)](#).
- [131] S. Itoh, K. Ueno, and T. Yokoo, “Fermi chopper developed at KEK,” [Nucl. Instrum. Methods Phys. Res. Sec. A **661**, 58 \(2012\)](#).
- [132] J. A. Rodriguez, D. M. Adler, P. C. Brand, C. Broholm, J. C. Cook, C. Brocker, R. Hammond, Z. Huang, P. Hundertmark, J. W. Lynn, N. C. Maliszewskyj, J. Moyer, J. Orndorff, D. Pierce, T. D. Pike, G. Scharfstein, S. A. Smee, and R. Vilaseca, “MACS—a new high intensity cold neutron spectrometer at NIST,” [Meas. Sci. Technol. **19**, 034023 \(2008\)](#).

- [133] A. Sapkota, P. Das, A. E. Böhmer, B. G. Ueland, D. L. Abernathy, S. L. Bud'ko, P. C. Canfield, A. Kreyssig, A. I. Goldman, and R. J. McQueeney, "Doping evolution of spin fluctuations and their peculiar suppression at low temperatures in $\text{Ca}(\text{Fe}_{1-x}\text{Co}_x)_2\text{As}_2$," *Phys. Rev. B* (Forthcoming 2018).
- [134] G. R. Stewart, "Superconductivity in iron compounds," *Rev. Mod. Phys.* **83**, 1589 (2011).
- [135] M. D. Lumsden, A. D. Christianson, D. Parshall, M. B. Stone, S. E. Nagler, G. J. MacDougall, H. A. Mook, K. Lokshin, T. Egami, D. L. Abernathy, E. A. Goremychkin, R. Osborn, M. A. McGuire, A. S. Sefat, R. Jin, B. C. Sales, and D. Mandrus, "Two-dimensional resonant magnetic excitation in $\text{BaFe}_{1.84}\text{Co}_{0.16}\text{As}_2$," *Phys. Rev. Lett.* **102**, 107005 (2009).
- [136] S. Chi, A. Schneidewind, J. Zhao, L. W. Harriger, L. Li, Y. Luo, G. Cao, Z. Xu, M. Loewenhaupt, J. Hu, and P. Dai, "Inelastic Neutron-Scattering Measurements of a Three-Dimensional Spin Resonance in the FeAs-Based $\text{BaFe}_{1.9}\text{Ni}_{0.1}\text{As}_2$ Superconductor," *Phys. Rev. Lett.* **102**, 107006 (2009).
- [137] A. D. Christianson, E. A. Goremychkin, R. Osborn, S. Rosenkranz, M. D. Lumsden, C. D. Malliakas, I. S. Todorov, H. Claus, D. Y. Chung, M. G. Kanatzidis, R. I. Bewley, and T. Guidi, "Unconventional superconductivity in $\text{Ba}_{0.6}\text{K}_{0.4}\text{Fe}_2\text{As}_2$ from inelastic neutron scattering," *Nature* **456**, 930 (2008).
- [138] A. E. Böhmer, A. Sapkota, A. Kreyssig, S. L. Bud'ko, G. Drachuck, S. M. Saunders, A. I. Goldman, and P. C. Canfield, "Effect of Biaxial Strain on the Phase Transitions of $\text{Ca}(\text{Fe}_{1-x}\text{Co}_x)_2\text{As}_2$," *Phys. Rev. Lett.* **118**, 107002 (2017).
- [139] R. Coldea, (1998), developed by Radu Coldea: 1998-2001 & ISIS addons and enhancements: 2001-2014. <http://mslice.isis.rl.ac.uk/>.
- [140] R. A. Ewings, A. Buts, M. D. Le, J. van Duijn, I. Bustinduy, and T. G. Perring, "Horace: Software for the analysis of data from single crystal spectroscopy experiments at time-of-flight neutron instruments," *Nucl. Instrum. Methods Phys. Res. Sec. A* **834**, 132 (2016).
- [141] B. Lake, G. Aeppli, T. E. Mason, A. Schröder, D. F. McMorrow, K. Lefmann, M. Isshiki, M. Nohara, H. Takagi, and S. M. Hayden, "Spin gap and magnetic coherence in a clean high-temperature superconductor," *Nature* **400**, 43 (1999).
- [142] G. Ehlers, A. A. Podlesnyak, J. L. Niedziela, E. B. Iverson, and P. E. Sokol, "The new cold neutron chopper spectrometer at the Spallation Neutron Source: Design and performance," *Rev. Sci. Instrum.* **82**, 085108 (2011).
- [143] R. A. Ewings, T. G. Perring, R. I. Bewley, T. Guidi, M. J. Pitcher, D. R. Parker, S. J. Clarke, and A. T. Boothroyd, "High-energy spin excitations in BaFe_2As_2 observed by inelastic neutron scattering," *Phys. Rev. B* **78**, 220501 (2008).
- [144] R. M. Fernandes and J. Schmalian, "Competing order and nature of the pairing state in the iron pnictides," *Phys. Rev. B* **82**, 014521 (2010).

- [145] J. Cui, B. Roy, M. A. Tanatar, S. Ran, S. L. Bud'ko, R. Prozorov, P. C. Canfield, and Y. Furukawa, "Antiferromagnetic spin correlations and pseudogaplike behavior in $\text{Ca}(\text{Fe}_{1-x}\text{Co}_x)_2\text{As}_2$ studied by ^{75}As nuclear magnetic resonance and anisotropic resistivity," [Phys. Rev. B **92**, 184504 \(2015\)](#).
- [146] K. Matan, S. Ibuka, R. Morinaga, S. Chi, J. W. Lynn, A. D. Christianson, M. D. Lumsden, and T. J. Sato, "Doping dependence of spin dynamics in electron-doped $\text{Ba}(\text{Fe}_{1-x}\text{Co}_x)_2\text{As}_2$," [Phys. Rev. B **82**, 054515 \(2010\)](#).
- [147] T. Timusk and B. Statt, "The pseudogap in high-temperature superconductors: an experimental survey," [Rep. Prog. Phys. **62**, 61 \(1999\)](#).
- [148] M. R. Norman, D. Pines, and C. Kallin, "The pseudogap: friend or foe of high T_c ?" [Adv. Phys. **54**, 715 \(2005\)](#).
- [149] A. A. Kordyuk, "Pseudogap from ARPES experiment: Three gaps in cuprates and topological superconductivity (Review Article)," [Low Temp. Phys. **41**, 319 \(2015\)](#).
- [150] W. W. Warren, R. E. Walstedt, G. F. Brennert, R. J. Cava, R. Tycko, R. F. Bell, and G. Dabbagh, "Cu spin dynamics and superconducting precursor effects in planes above T_c in $\text{YBa}_2\text{Cu}_3\text{O}_{6.7}$," [Phys. Rev. Lett. **62**, 1193 \(1989\)](#).
- [151] R. E. Walstedt, W. W. Warren, R. F. Bell, R. J. Cava, G. P. Espinosa, L. F. Schneemeyer, and J. V. Waszczak, " ^{63}Cu NMR shift and linewidth anomalies in the $T_c = 60$ K phase of Y-Ba-Cu-O," [Phys. Rev. B **41**, 9574 \(1990\)](#).
- [152] C. Stock, W. J. L. Buyers, R. Liang, D. Peets, Z. Tun, D. Bonn, W. N. Hardy, and R. J. Birgeneau, "Dynamic stripes and resonance in the superconducting and normal phases of $\text{YBa}_2\text{Cu}_3\text{O}_{6.5}$ ortho-II superconductor," [Phys. Rev. B **69**, 014502 \(2004\)](#).
- [153] M. A. Surmach, F. Brückner, S. Kamusella, R. Sarkar, P. Y. Portnichenko, J. T. Park, G. Ghambashidze, H. Luetkens, P. K. Biswas, W. J. Choi, Y. I. Seo, Y. S. Kwon, H.-H. Klauss, and D. S. Inosov, "Superconducting properties and pseudogap from preformed Cooper pairs in the triclinic $(\text{CaFe}_{1-x}\text{Pt}_x\text{As})_{10}\text{Pt}_3\text{As}_8$," [Phys. Rev. B **91**, 104515 \(2015\)](#).
- [154] P. Dai, H. A. Mook, R. D. Hunt, and F. Doğan, "Evolution of the resonance and incommensurate spin fluctuations in superconducting $\text{YBa}_2\text{Cu}_3\text{O}_{6+x}$," [Phys. Rev. B **63**, 054525 \(2001\)](#).
- [155] W. T. Jayasekara, U. S. Kaluarachchi, B. G. Ueland, A. Pandey, Y. B. Lee, V. Taufour, A. Sapkota, K. Kothapalli, N. S. Sangeetha, G. Fabbri, L. S. I. Veiga, Y. Feng, A. M. dos Santos, S. L. Bud'ko, B. N. Harmon, P. C. Canfield, D. C. Johnston, A. Kreyssig, and A. I. Goldman, "Pressure-induced collapsed-tetragonal phase in SrCo_2As_2 ," [Phys. Rev. B **92**, 224103 \(2015\)](#).
- [156] W. T. Jayasekara, A. Pandey, A. Kreyssig, N. S. Sangeetha, A. Sapkota, K. , V. K. Anand, W. Tian, D. Vaknin, D. C. Johnston, R. J. McQueeney, A. I. Goldman, and B. G. Ueland,

- “Suppression of magnetic order in $\text{CaCo}_{1.86}\text{As}_2$ with Fe substitution: Magnetization, neutron diffraction, and x-ray diffraction studies of $\text{Ca}(\text{Co}_{1-x}\text{Fe}_x)_y\text{As}_2$,” *Phys. Rev. B* **95**, 064425 (2017).
- [157] M. Reehuis and W. Jeitschko, “Structure and magnetic properties of the phosphides CaCo_2P_2 and LnT_2P_2 with ThCr_2Si_2 structure and LnTP with PbFCl structure (Ln = Lanthanoids, T = Fe, Co, Ni),” *J. Phys. Chem. Solids* **51**, 961 (1990).
- [158] L. Ortenzi, H. Gretarsson, S. Kasahara, Y. Matsuda, T. Shibauchi, K. D. Finkelstein, W. Wu, S. R. Julian, Y.-J. Kim, I. I. Mazin, and L. Boeri, “Structural Origin of the Anomalous Temperature Dependence of the Local Magnetic Moments in the CaFe_2As_2 Family of Materials,” *Phys. Rev. Lett.* **114**, 047001 (2015).
- [159] E. Manousakis, J. Ren, S. Meng, and E. Kaxiras, “Is the nature of magnetic order in copper-oxides and in iron-pnictides different?” *Solid State Commun.* **150**, 62 (2010).
- [160] J. Knolle, I. Eremin, A. V. Chubukov, and R. Moessner, “Theory of itinerant magnetic excitations in the spin-density-wave phase of iron-based superconductors,” *Phys. Rev. B* **81**, 140506 (2010).
- [161] R. Nath, A. A. Tsirlin, H. Rosner, and C. Geibel, “Magnetic properties of $\text{BaCdVO}(\text{PO}_4)_2$: A strongly frustrated spin- $\frac{1}{2}$ square lattice close to the quantum critical regime,” *Phys. Rev. B* **78**, 064422 (2008).
- [162] R. T. Azuah, L. R. Kneller, Y. Qiu, P. L. W. Tregenna-Piggott, C. M. Brown, J. R. D. Copley, and R. M. Dimeo, “DAVE: A Comprehensive Software Suite for the Reduction, Visualization, and Analysis of Low Energy Neutron Spectroscopic Data,” *J. Res. Natl. Inst. Stan. Technol.* **114**, 341 (2009).
- [163] J. M. Tranquada, “Spins, stripes, and superconductivity in hole-doped cuprates,” *AIP Conference Proceedings* **1550**, 114 (2013).
- [164] J. Rodriguez-Carvajal, “Recent advances in magnetic structure determination by neutron powder diffraction,” *Physica B: Condens. Matter* **192**, 55 (1993).
- [165] M. Kohgi, Y. Ishikawa, and Y. Endoh, “Inelastic neutron scattering study of spin waves in MnO ,” *Solid State Commun.* **11**, 391 (1972).
- [166] R. J. McQueeney, J.-Q. Yan, S. Chang, and J. Ma, “Determination of the exchange anisotropy in perovskite antiferromagnets using powder inelastic neutron scattering,” *Phys. Rev. B* **78**, 184417 (2008).
- [167] W. H. Press, S. A. Teukolsky, W. T. Vetterling, and B. P. Flannery, *Numerical Recipes in C: The Art of Scientific Computing* (Cambridge University Press, Cambridge, 1998).
- [168] M. A. McGuire and V. O. Garlea, “Short- and long-range magnetic order in LaMnAsO ,” *Phys. Rev. B* **93**, 054404 (2016).

- [169] S. Calder, B. Saparov, H. B. Cao, J. L. Niedziela, M. D. Lumsden, A. S. Sefat, and A. D. Christianson, “Magnetic structure and spin excitations in BaMn_2Bi_2 ,” [Phys. Rev. B **89**, 064417 \(2014\)](#).
- [170] M. C. Rahn, A. J. Princep, A. Piovano, J. Kulda, Y. F. Guo, Y. G. Shi, and A. T. Boothroyd, “Spin dynamics in the antiferromagnetic phases of the Dirac metals $AMnBi_2$ ($A = \text{Sr}, \text{Ca}$),” [Phys. Rev. B **95**, 134405 \(2017\)](#).
- [171] J. K. Glasbrenner and I. I. Mazin, “First-principles evidence of Mn moment canting in hole-doped $\text{Ba}_{1-2x}\text{K}_{2x}\text{Mn}_2\text{As}_2$,” [Phys. Rev. B **89**, 060403 \(2014\)](#).
- [172] S. M. Griffin and J. B. Neaton, “Prediction of a new class of half-metallic ferromagnets from first principles,” [Phys. Rev. Mater. **1**, 044401 \(2017\)](#).